Volume 14 Number 4 2004

ISBN 0-86176-958-9 ISSN 0961-5539

International Journal of

Numerical Methods for Heat & Fluid Flow

Numerical methods in aerospace: civil aviation and space exploration

Guest Editor: Dr Mike Keavey

Emerald

www.emeraldinsight.com

International Journal of
Numerical Methods for Heat & Fluid Flow

ISSN 0961-5539

Volume 14
Number 4
2004

Numerical methods in aerospace: civil aviation and space exploration

Guest Editor
Dr Mike Keavey

CONTENTS

CONTENTS
continued

Access this journal online

www.emeraldinsight.com/hff.htm

As a subscriber to this journal, you can benefit from instant, electronic access to this title via Emerald Fulltext. Your access includes a variety of features that increase the value of your journal subscription.

How to access this journal electronically

To benefit from electronic access to this journal you first need to register via the Internet. Registration is simple and full instructions are available online at **www.emeraldinsight.com/rpsv/librariantoolkit/emeraldadmin** Once registration is completed, your institution will have instant access to all articles through the journal's Table of Contents page at **www.emeraldinsight.com/0961-5539.htm** More information about the journal is also available at **www.emeraldinsight.com/hff.htm**

Our liberal institution-wide licence allows everyone within your institution to access your journal electronically, making your subscription more cost effective. Our Web site has been designed to provide you with a comprehensive, simple system that needs only minimum administration. Access is available via IP authentication or username and password.

Key features of Emerald electronic journals

Automatic permission to make up to 25 copies of individual articles

This facility can be used for training purposes, course notes, seminars etc. This only applies to articles of which Emerald owns copyright. For further details visit **www.emeraldinsight.com/copyright**

Online publishing and archiving

As well as current volumes of the journal, you can also gain access to past volumes on the internet via Emerald Fulltext. Archives go back to 1994 and abstracts back to 1989. You can browse or search the database for relevant articles.

Key readings

This feature provides abstracts of related articles chosen by the journal editor, selected to provide readers with current awareness of interesting articles from other publications in the field.

Reference linking

Direct links from the journal article references to abstracts of the most influential articles cited. Where possible, this link is to the full text of the article.

E-mail an article

Allows users to e-mail links to relevant and interesting articles to another computer for later use, reference or printing purposes.

Additional complementary services available

Your access includes a variety of features that add to the functionality and value of your journal subscription:

E-mail alert services

These services allow you to be kept up to date with the latest additions to the journal via e-mail, as soon as new material enters the database. Further information about the services available can be found at **www.emeraldinsight.com/usertoolkit/emailalerts**

Research register

A web-based research forum that provides insider information on research activity world-wide located at **www.emeraldinsight.com/researchregister** You can also register your research activity here.

User services

Comprehensive librarian and user toolkits have been created to help you get the most from your journal subscription. For further information about what is available visit **www.emeraldinsight.com/usagetoolkit**

Choice of access

Electronic access to this journal is available via a number of channels. Our Web site **www.emeraldinsight.com** is the recommended means of electronic access, as it provides fully searchable and value added access to the complete content of the journal. However, you can also access and search the article content of this journal through the following journal delivery services:

EBSCOHost Electronic Journals Service
ejournals.ebsco.com

Huber E-Journals
e-journals.hanshuber.com/english/index.htm

Ingenta
www.ingenta.com

Minerva Electronic Online Services
www.minerva.at

OCLC FirstSearch
www.oclc.org/firstsearch

SilverLinker
www.ovid.com

SwetsWise
www.swetswise.com

Emerald Customer Support

For customer support and technical help contact:
E-mail **support@emeraldinsight.com**
Web **www.emeraldinsight.com/customercharter**
Tel +44 (0) 1274 785278
Fax +44 (0) 1274 785204

EDITORIAL ADVISORY BOARD

International Journal of Numerical Methods for Heat & Fluid Flow
Vol. 14 No. 4, 2004
p. 408

0961-5539

Simulation of transonic flutter and active shockwave control

L. Djayapertapa and C.B. Allen

Keywords Elasticity, Flight control, Flight dynamics, Aerodynamics

Transonic flutter and active flap control, in two dimensions, are simulated by coupling independent structural dynamic and inviscid aerodynamic models, in the time domain. A flight control system, to actively control the trailing edge flap motion, has also been incorporated and, since this requires perfect synchronisation of fluid, structure and control signal, the "strong" coupling approach is adopted. The computational method developed is used to perform transonic aeroelastic and aeroservoelastic calculations in the time domain, and used to compute stability (flutter) boundaries of 2D wing sections. Open and closed loop simulations show that active control can successfully suppress flutter and results in a significant increase in the allowable speed index in the transonic regime. It is also shown that active control is still effective when there is free-play in the control surface hinge. Flowfield analysis is used to investigate the nature of flutter and active control, and the fundamental importance of shock wave motion in the vicinity of the flap is demonstrated.

Numerical study of active shock control for transonic aerodynamics

N. Qin, Y. Zhu and S.T. Shaw

Keywords Aerodynamics, Waveforms, Flow, Differential equations, Numerical analysis

In this paper, the effectiveness of a number of active devices for the control of shock waves on transonic aerofoils is investigated using numerical solutions of the Reynolds-averaged Navier-Stokes equations. A brief description of the flow model and the numerical method is presented including, in particular, the boundary condition modelling and the numerical treatment for surface mass transfer. Comparisons with experimental data have been made where possible to validate the numerical study before some systematic numerical simulations for a parametric study. The effects of surface suction, blowing, and local modification of the surface contour (bump) on aerofoil aerodynamic performance have been studied extensively regarding the control location, the mass flow strength and the bump height. The numerical simulations highlight the benefits and drawbacks of the various control devices for transonic aerodynamic performance and identify the key design parameters for optimisation.

Dynamic modeling in large-eddy simulation of turbulent channel flow: investigation of two-dimensional versus three-dimensional test filtering

Jessica Gullbrand

Keywords Simulation, Turbulent flow, Eddy currents, Tests and testing

Large-eddy simulation (LES) of a turbulent channel flow is performed using different subfilter-scale (SFS) models and test filter functions. The SFS models used are the dynamic Smagorinsky model (DSM) and the dynamic mixed model (DMM). The DMM is a linear combination between the scale-similarity model and the DSM. The test filter functions investigated are the sharp cut-off (in spectral space) and smooth filter that is commutative up to fourth-order. The filters are applied either in the homogeneous directions or in all three spatial directions. The governing equations are discretized using a fourth-order energy-conserving finite-difference scheme. The influence from the test filter function and the SFS model on the LES results are investigated and the effect of two-dimensional versus three-dimensional test filtering are investigated. The study shows that the combination of SFS model and filter function highly influences the computational results; even the effect on the zeroth-order moment is large.

The role of endothermic gasification in propellant ignition

Caroline Lowe

Keywords Compressible flow, Ignition systems, Differential equations, Gases

This study explores a reactor model designed to describe the decomposition, ignition and combustion of energetic materials in combination with real experimental data for these energetic materials. Spatial uniformity is initially assumed which reduces the system of partial-differential-equations to a system

0961-5539

of ordinary-differential-equations that can be easily solved numerically. The phase-plane is explicitly presented and examined to illustrate how chemistry and temperature evolve in time. The computations provide an understanding of the vast different timescales that exist and illustrate the singularity structure. Following this the effect of including this chemical regime in an environment typically induced by the combustion of these materials, that is within a compressible fluid flow, is pursued.

Rarefied, superorbital flows in an expansion tube

V. Wheatley, H.S. Chiu, P.A. Jacobs, M.N. Macrossan, D.J. Mee and R.G. Morgan

Keywords Rarefied flow, Expansion tube, Computational modelling, Modelling, Flow, Numerical analysis

This paper describes a free-piston driven expansion tube and its instrumentation. The facility is used to generate rarefied flows at speeds of approximately 10 km/s. Although the flow in the tube itself is in the continuum regime, rarefied flow conditions are achieved by allowing the test gas to further expand as a free jet into the facility's test section. The test flow is surveyed to provide bar-gauge pressure measurements. Numerical simulation is then used to describe more fully the test flow properties. The flows produced are suitable for the aerodynamic testing of small models at superorbital speeds and should provide data that are suitable for the calibration of Direct Simulation Monte-Carlo codes.

Numerical simulation of inductively coupled plasma flows under chemical non-equilibrium

Gérard Degrez, David Vanden Abeele, Paolo Barbante and Benot Bottin

Keywords Numerical analysis, Plasma physics, Flow, Equilibrium methods

This paper presents a detailed review of the numerical modeling of inductively coupled air plasmas under local thermodynamic equilibrium and under chemical non-equilibrium. First, the physico-chemical models are described, i.e. the thermodynamics, transport phenomena and chemical kinetics models. Particular attention is given to the correct modelling of ambipolar diffusion in multi-component chemical non-equilibrium plasmas. Then, the numerical aspects are discussed, i.e. the space discretization and iterative solution strategies. Finally, computed results are presented for the flow, temperature and chemical concentration fields in an air inductively coupled plasma torch. Calculations are performed assuming local thermodynamic equilibrium and under chemical non-equilibrium, where two different finite-rate chemistry models are used. Besides important non-equilibrium effects, we observe significant demixing of oxygen and nitrogen nuclei, which occurs due to diffusion regardless of the degree of non-equilibrium in the plasma.

Discretization of the magnetic field in MPD thrusters

Jörg Heiermann and Monika Auweter-Kurtz

Keywords Plasma physics, Aerodynamics, Flow, Electromagnetic radiation

For the numerical simulation of magnetoplasmadynamic (MPD) self-field thruster flow, the solution of one of the two dynamical Maxwell equations – Faraday's law – is required. The Maxwell equations and Ohm's law for plasmas can be summarized in one equation for the stream function so that the two-dimensional, axisymmetric magnetic field can be calculated. The finite volume (FV) discretization of the equation on unstructured, adaptive meshes is presented in detail and solutions for different thruster currents are shown. The calculated thrust is compared with the experimental data.

Editorial

Early in 2001, when the idea of a Special Aerospace Issue was first conceived, the Airbus A3XX had just officially become the A380 and the possibility of a new supersonic transport, possibly to be built in collaboration with Boeing, was also under discussion. The civil aircraft industry looked set for expansion in the new millennium, and in the space sector there was even talk of a manned mission to Mars. Here in the UK, the Association of Aerospace Universities had just been formed to harness the enthusiasm of the younger generation and to ensure that the experience of those of us who were a little older was passed on. This issue now comes to print when it is perhaps even more important that the scientific community strives towards the goal of safe and efficient air transport and does not lose the longer term vision of man's eventual exploration of the planets.

After decades of trying to take subsonic civil aviation closer and closer to Mach 1, the advent of the mass market in air travel eventually led to a reduction in speed and a much greater emphasis on fuel economy and efficiency. Currently, researchers in the field of transonic aerodynamics are trying to achieve the best of both worlds by addressing the subject of active shockwave control. The first two papers deal with this issue in slightly different ways. The paper by Djayapertapa and Allen from the University of Bristol couples a model of flow over an aerofoil with aeroelasticity and a system to control the angle of the control surfaces. The second paper, by Qin, Zhu and Shaw, from Sheffield, Brunel and Cranfield, models the use of bumps, suction and blowing to move the point at which a shock occurs and reduce its strength.

Turbulence modelling is one of the "Grand Challenges" of mathematical physics, with emphasis on direct numerical simulation, large eddy simulation and traditional Reynolds averaging approaches. The paper by Gullbrand from Stanford examines the subtle subject of filtering and sub-filter scale modelling in LES. Still towards a more pure mathematical end of the spectrum, the paper by Lowe, at the new Centre for Mathematical Sciences in Cambridge, examines the properties of equations representing propellant ignition and the behaviour of propagating shock waves.

Moving to the limits of flows that can be modelled using continuum representations, the paper by Wheatley *et al.* at the University of Queensland describes and models a hypersonic test facility capable of generating non-continuous flows at close to 10 km/s, for the testing of small aerodynamic models under aerobraking conditions. It is important to remember that numerical modelling can only be taken so far without some form of experimental validation.

International Journal of Numerical Methods for Heat & Fluid Flow
Vol. 14 No. 4, 2004
pp. 411-412

0961-5539

The last two papers deal with different aspects of plasma flow and magnetohydrodynamics. The paper by Degrez, Vanden Abeele, Barbante and Bottin from the von Karman Institute, the Université Libre de Bruxelles, the Politecnico de Milano and the Institut Suprieur Industriel de Bruxelles describes another experimental facility dealing with re-entry flows, in this case, an inductively coupled plasma wind tunnel. This paper considers not only the gas dynamics and electromagnetic behaviour, but also non-equilibrium chemistry. The final paper by Heiermann and Auweter-Kurz from the Institut für Raumfahrtsysteme at the University of Stuttgart analyses the magnetic field in MPD thrusters. These are actual candidates for the propulsion of manned spacecraft to Mars. A clear explanation of the principle of such devices is given, followed by the equations needed to model them, methods for their numerical solution, and comparisons with an actual thruster in the laboratory.

I have to say that, as someone who became an academic associated with aerospace just 10 years back, after half a lifetime of research in the electricity supply industry, it has been a great and undeserved privilege to edit this issue and collaborate with authors from some of the world's most prestigious aerospace institutions. I would like to take this opportunity to thank the authors for their contributions and also for their fortitude and patience as they waited for everything to come together. I would also like to thank the anonymous referees, without whose commitment all this would not have been possible. Finally, if I can be allowed one small personal indulgence, I would like to conclude with two quotations from Apollo 13: firstly, the words attributed to Jim Lovell in the film of that name, "I look up at the moon and wonder – when will we be going back"; secondly, the words of flight director Gene Kranz, which I commend to the younger generation everywhere, "Failure is not an option".

Mike Keavey

Simulation of transonic flutter and active shockwave control

L. Djayapertapa and C.B. Allen
Department of Aerospace Engineering, University of Bristol, Bristol, Avon, UK

Keywords *Elasticity, Flight control, Flight dynamics, Aerodynamics*

Received August 2001
Revised August 2002
Accepted October 2002

Abstract *Transonic flutter and active flap control, in two dimensions, are simulated by coupling independent structural dynamic and inviscid aerodynamic models, in the time domain. A flight control system, to actively control the trailing edge flap motion, has also been incorporated and, since this requires perfect synchronisation of fluid, structure and control signal, the "strong" coupling approach is adopted. The computational method developed is used to perform transonic aeroelastic and aeroservoelastic calculations in the time domain, and used to compute stability (flutter) boundaries of 2D wing sections. Open and closed loop simulations show that active control can successfully suppress flutter and results in a significant increase in the allowable speed index in the transonic regime. It is also shown that active control is still effective when there is free-play in the control surface hinge. Flowfield analysis is used to investigate the nature of flutter and active control, and the fundamental importance of shock wave motion in the vicinity of the flap is demonstrated.*

Nomenclature

a_∞ = freestream speed of sound
a_h = non-dimensional distance of the elastic axis from midchord, positive aft of midchord
ACT = active control technology
b = aerofoil semi-chord
c = $2b$, aerofoil chord
c_β = non-dimensional distance of hinge axis from midchord, positive aft of midchord
CHM = control hinge moment, non-dimensional
C_L = lift coefficient
C_D = drag coefficient
$C_{M_{ea}}$ = pitching moment coefficient about the elastic axis
e = total specific energy
EA = elastic axis
$\mathbf{F}$ = convective aerodynamic flux
$\mathbf{f_a}$ = non-dimensional aerodynamic loads
$\mathbf{f_c}$ = non-dimensional active control force
$\mathbf{f_{fp}}$ = non-dimensional free-play force
FPM = free-play moment about EA, non-dimensional
FPHM = free-play hinge moment about hinge axis, non-dimensional
G = control law gains
h = plunging displacement (measured +ve downwards)
HA = hinge axis
I_α = polar moment of inertia of aerofoil mass about EA
I_β = polar moment of inertia of control surface mass about EA
$[\mathbf{K}]$ = non-dimensional stiffness matrix
K_h = $m\omega_h^2$, bending stiffness corresponding to plunging displacement
K_α = $I_\alpha\omega_\alpha^2$, torsional stiffness corresponding to pitching rotation
K_β = $I_\beta\omega_\beta^2$, torsional stiffness corresponding to control surface rotation
L = $q_\infty c C_L$, aerodynamic lift

The authors would like to acknowledge the contribution of Professor S.P. Fiddes, who originally supervised Mr Djayapertapa's PhD research, to this work.

International Journal of Numerical Methods for Heat & Fluid Flow
Vol. 14 No. 4, 2004
pp. 413-443

0961-5539
DOI 10.1108/09615530410532231

LCO = limit cycle oscillations
m = mass of the aerofoil per unit span
$[\mathbf{M}]$ = non-dimensional mass matrix
M_∞ = free-stream Mach number
M_{ea} = $q_\infty c^2 C_{M_{ea}}$ pitching moment about elastic axis (EA)
$\mathbf{n}$ = cell face outward unit normal
q_∞ = $1/2\rho_\infty U_\infty^2$, free-stream dynamic pressure
r_α = I_α/mb^2, aerofoil radius of gyration about EA in semi-chords, non-dimensional
r_β = I_β/mb^2, control surface radius of gyration about HA in semi-chords, non-dimensional
$\mathbf{R}$ = residual vector
$\mathbf{U}$ = vector of conserved variables
$\mathbf{u}$ = velocity vector
S_α = aerofoil static moment about **EA**
S_β = control surface static moment about hinge axis
t = real time
u, v = cartesian velocity components
$\mathbf{q}$ = structural displacement vector
U_∞ = free-stream velocity
U^* = $U_\infty/\omega_\alpha\sqrt[3]{\mu}$ speed index
V = volume of cell
x, y = cartesian coordinates
x_t, y_t = grid cartesian velocity
$\mathbf{X_t}$ = grid velocity vector
x_α = off-set distance of the aerofoil centre of gravity (CG) from EA, positive aft of EA
x_β = off-set distance of the control surface centre of gravity (CG) from HA, positive aft of HA
α = pitching displacement (positive nose-up)
γ = ratio of specific heats
ρ = density
μ = $m/\pi\rho b^2$, aerofoil-air mass ratio
ξ = h/b, non-dimensional plunging displacement
ω_h = K_h/m, uncoupled plunging natural frequency
ω_α = K_α/I_α, uncoupled pitching natural frequency
ω_β = $K_\beta I_\beta$, uncoupled control surface rotation natural frequency
τ = fictitious pseudo time

1. Introduction

The design cruising speed of civil aircraft often falls within the transonic region, where the structural loads, and hence aeroelastic behaviour, are greatly affected by the presence and motion of shock waves. Hence, the accurate prediction of flutter characteristics of aerofoils in transonic flow is a critical design consideration for most modern civil and high performance aircraft.

In the pure subsonic or supersonic regimes, it has been a normal industry practice to use linear aerodynamic theory, such that the aerodynamic forces depend upon the body motion in linear fashion, thus permitting uncoupling of the structural and fluid equations (MacNeal Schwendler Corporation, 1995). However, this cannot be applied in the transonic regime due to the high non-linearity of the flow field. The aerofoil thickness was often neglected in linear theory, but the aerofoil geometry plays an important role in the development and motion of shock waves in the transonic region (Bland and Edwards, 1984). There are other non-linear phenomena associated with aeroelastics, for example, aileron buzz or limit cycle oscillations (LCO), and none of these phenomena can be predicted directly by traditional linear theoretical methods, since they are interactions between non-linear aerodynamic forces and structures. Hence, more advanced aeroelastic simulation methods, applicable to transonic flows, are essential.

Computational aeroelastics (and aeroservoelastics) often involves two computational models, namely independent aerodynamic and structural

models. In the former, the aircraft surface and the surrounding flow field are discretised, before the governing fluid flow equations are solved. The latter involves solving the structural equations with aerodynamic forces as source terms. (For aeroservoelastics a flight control system is also required.) Coupling these two models in the time domain allows time-accurate simulation of aeroelastic response, and the possibility of identifying flutter boundaries.

It is possible, with current computational power, to develop coupled aerodynamic-structural dynamic methods using the Euler and Navier-Stokes equations as the aerodynamic model. Earlier, euler solvers have been coupled with structural models (Alonso and Jameson, 1994; Bendiksen and Kousen, 1987; Guruswamy, 1990; Kousen and Bendiksen, 1988, 1994; Robinson *et al.*, 1991). The Navier-Stokes equations are still rarely used in computational transonic aeroelasticity mainly due to their excessive CPU demands. Simplified forms of the Navier-Stokes equations have been used for aeroelastic applications (Badcock *et al.*, 1995; Meijer *et al.*, 1998; Prananta and Hounjet, 1996; Prananta *et al.*, 1995; Schuster *et al.*, 1998), but results show that for two degrees of freedom aerofoil motions, little difference was found between using inviscid and viscous aerodynamic models. Reviews of computational aeroelasticity are presented in Bennett and Edwards (1998) and Försching (1995).

The time-accurate interaction between structural dynamics, the flight control system and aerodynamics, known as aeroservoelasticity, has recently received attention, (Batina and Yang, 1984; Edwards *et al.*, 1978; Guillot and Friedman, 1994, 1995; Guruswamy, 1989a, Guruswamy and Tu, 1989b; Horikawa and Dowell, 1979; Karpel, 1982; Nissim, 1971, 1977, 1990; Nissim and Abel, 1978; Nissim *et al.*, 1978; Noll, 1993; Pak *et al.*, 1991; Whalley and Ebrahimi, 1998). Active control technology (ACT) can be implemented within an aeroelastic solver in order to simulate any of the following: flutter suppression, gust alleviation or manoeuver enhancement. Earlier work has relied mainly on transonic small disturbance theory as the aerodynamic solver (Batina and Yang, 1984; Guruswamy, 1989a; Guruswamy and Tu, 1989b) or has been performed in the frequency domain (Batina and Yang, 1984; Edwards *et al.*, 1978; Guillot and Friedman, 1994, 1995; Guruswamy, 1989a, Guruswamy and Tu, 1989b; Horikawa and Dowell, 1979; Karpel, 1982; Nissim, 1990; Pak *et al.*, 1991; Whalley and Ebrahimi, 1998). For example, Nissim (1990, 1971) performed flutter boundary calculations in the frequency domain by considering the sign of the work done by the structural system on its surroundings. There are limitations to this approach, but the energy analysis is extremely useful and is used here.

Active control systems normally have constant (with time) control laws. However, the use of adaptive control in active flutter suppression has started to appear in the literature (Guillot and Friedman, 1994, 1995; Pak *et al.*, 1991). This approach is attractive since the parameters of the system often change with

time or under load, which are the usual limitations of control using fixed-structures and fixed-parameter controllers. The added complexity of adaptive control is often justified by reduced hardware requirements, but it is very difficult to prove the stability properties of controllers whose parameters can vary. In addition, it is almost impossible to get certification for civil aircraft equipped with adaptive control. Hence, the approach of using fixed-parameter controllers is preferred in this research, although it should also be noted that fixed-parameter active controllers are also difficult to certify.

This paper presents a computational method to simulate the aeroelastic and aeroservoelastic behaviour of a two and three degrees of freedom aerofoil. The motions considered are plunge, pitch and control surface (flap) rotation about the hinge axis. The aerodynamic model is described by the Euler equations, which is coupled with a structural model in the time domain, using the "strong" coupling approach. A control law is implemented within the aeroelastic solver to investigate the active means of flutter suppression via control surface (flap) motion, and the effect on the stability (flutter) boundary presented. The mechanics of flutter are examined by considering the phase difference between the plunge and pitch motions for a two degree of freedom model. Transonic flutter is examined using the time-dependent flowfield plots, to demonstrate the effect of active control on shock motion. The effects of free-play in the control surface hinge are also considered.

2. Structural model

Figure 1 shows the typical wing section used to derive the structural equations of motion. This model has been well established for two-dimensional aeroelastic analysis (Dowell *et al.*, 1994; Fung, 1955; Glaser, 1987). The degrees of freedom associated with the aerofoil are shown in Figure 1. The pitching and plunging displacements are restrained by a pair of springs attached to the elastic axis (EA) with spring constants K_α and K_h, respectively. A torsional spring is also attached at the hinge axis whose spring constant is K_β.

Djayapertapa (2001) and Scanlan and Rosenbaum (1951) describe the derivation of the two degrees of freedom aeroelastic equation of motion from Lagrange's equation, and the same principal can be applied to a three degree of freedom system. The resulting governing equations are given by:

$$m\ddot{h} + S_\alpha b\ddot{\alpha} + S_\beta b\ddot{\beta} + K_h h = -L \tag{1}$$

$$S_\alpha b\ddot{h} + I_\alpha\ddot{\alpha} + [(C_\beta - a_h)bS_\beta + I_\beta]\ddot{\beta} + K_\alpha\alpha = M_{\text{ea}} \tag{2}$$

$$S_\beta\ddot{h} + [(C_\beta - a_h)bS_\beta + I_\beta]\ddot{\alpha} + I_\beta\ddot{\beta} + K_\beta\beta = H_\beta \tag{3}$$

where the symbol definitions are shown in Figure 1. S_α is the static moment of the aerofoil about the EA and is given by $S_\alpha = mX_\alpha b$. S_β is the static moment of the control surface about the hinge axis and is given by $S_\beta = mX_\beta b$.

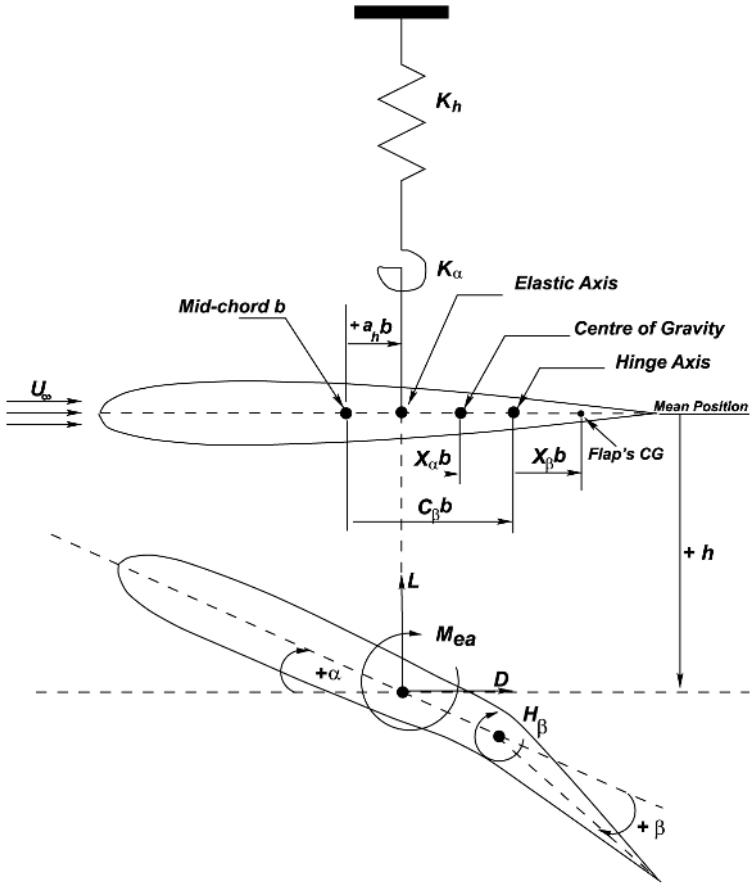

Figure 1.
Aeroelastic parameter definition

$I_\alpha = mr_\alpha^2 b^2$ is the aerofoil moment of inertia about the EA, and $I_\beta = mr_\beta^2 b^2$ is the control surface moment of inertia about the EA.

In order to obtain the full non-dimensional form of the equation, non-dimensional plunge ($\xi = h/b$) and non-dimensional time are introduced. Following the results in the work Djayapertapa (2001), the full non-dimensional form of the aeroelastic equations can be written in the form

$$[\mathbf{M}]\mathbf{q}'' + [\mathbf{K}]\mathbf{q} = \mathbf{f_a} \tag{4}$$

where

$$[\mathbf{M}] = \begin{bmatrix} 1 & x_\alpha & x_\beta \\ x_\alpha & r_\alpha^2 & (C_\beta - a_h)x_\beta + r_\beta^2 \\ x_\beta & (C_\beta - a_h)x_\beta + r_\beta^2 & r_\beta^2 \end{bmatrix} \tag{5}$$

$$[\mathbf{K}] = \frac{4M_\infty^2\gamma}{U^{*2}\mu}\begin{bmatrix} \frac{\omega_h^2}{\omega_\alpha^2} & 0 & 0 \\ 0 & r_\alpha^2 & 0 \\ 0 & 0 & r_\beta^2\frac{\omega_\beta^2}{\omega_\alpha^2} \end{bmatrix}, \tag{6}$$

$$\mathbf{q} = \begin{Bmatrix} \xi \\ \alpha \\ \beta \end{Bmatrix}, \quad \mathbf{f_a} = \frac{4M_\infty^2\gamma}{\pi\mu}\begin{Bmatrix} -C_{\mathrm{L}} \\ 2C_{\mathrm{M_{ea}}} \\ 2C_{\mathrm{H}} \end{Bmatrix} \tag{7}$$

U^* and μ are the non-dimensional speed (the speed index) and mass ratio of aerofoil to air, respectively, and their expressions are given by

$$U^* = \frac{U_\infty}{b\omega_\alpha\sqrt{\mu}}; \qquad \mu = \frac{m}{\pi\rho b^2} \tag{8}$$

2.1 Structural time integration

Equation (4) is solved by approximating it at time level $n+1$, and an implicit Newmark scheme (Bathe, 1982) is used to integrate the equation. Details of the step by step procedure can be found in the work of Djayapertapa (2001).

The choice of time-step in the integration is conditional on accuracy not stability, as the Newmark scheme is unconditionally stable. The size of the time step is governed by the smallest period of the free vibration system (T_{s}). The number of time-steps used per cycle is labelled nspc and so $\Delta t = T_{\mathrm{s}}/\mathrm{nspc}$. The time-step requirements of the Newmark scheme were assessed using a two degree of freedom system, a test case from the works of Bathe (1982). The equations of motion are by

$$\begin{bmatrix} 2.0 & 0.0 \\ 0.0 & 1.0 \end{bmatrix}\begin{Bmatrix} Y_1'' \\ Y_2'' \end{Bmatrix} + \begin{bmatrix} 6.0 & -2.0 \\ -2.0 & 1.0 \end{bmatrix}\begin{Bmatrix} Y_1 \\ Y_2 \end{Bmatrix} = \begin{Bmatrix} 0.0 \\ 10.0 \end{Bmatrix} \tag{9}$$

and the initial conditions are $\mathbf{Y} = \{0,0\}^{\mathrm{T}}$, $\mathbf{Y}' = \{0,0\}^{\mathrm{T}}$. The exact solution of these equations is

$$Y_1 = \frac{5}{3}\left(1 - \cos(\sqrt{2}t)\right) - \frac{2}{3}\left(1 - \cos(\sqrt{5}t)\right) \tag{10}$$

$$Y_2 = \frac{5}{3}\left(1 - \cos(\sqrt{2}t)\right) + \frac{4}{3}\left(1 + \cos(\sqrt{5}t)\right) \tag{11}$$

Figure 2 shows the responses for nspc = 20 and 30. It is clear that 30 time-steps per cycle gives acceptable accuracy, and this is not an excessive number,

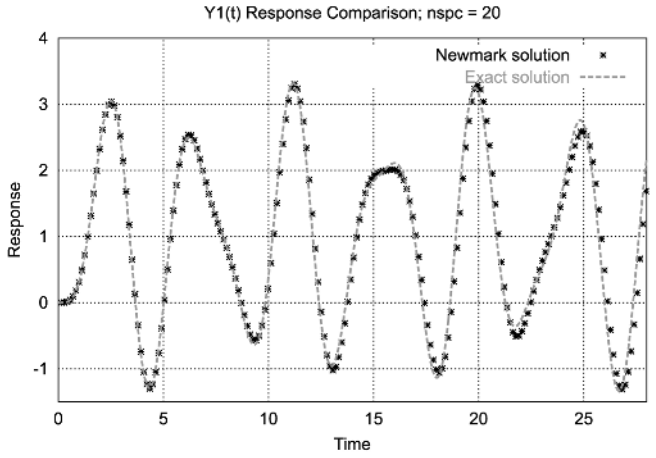

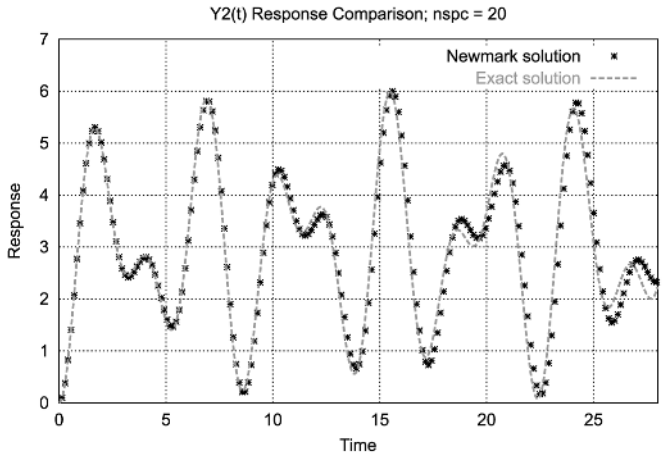

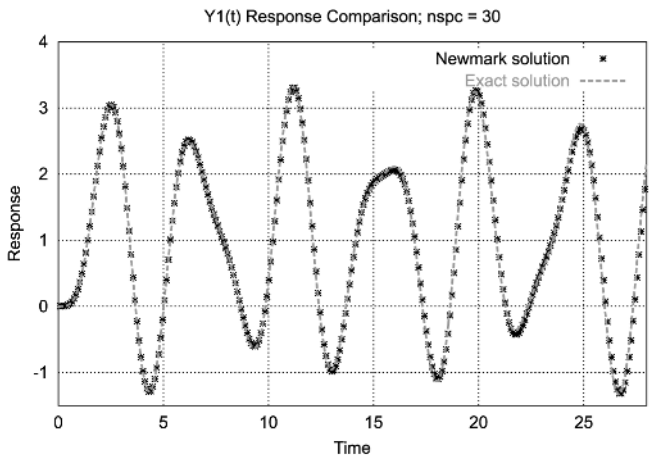

(*continued*)

Figure 2.
Response comparison
Newmark scheme

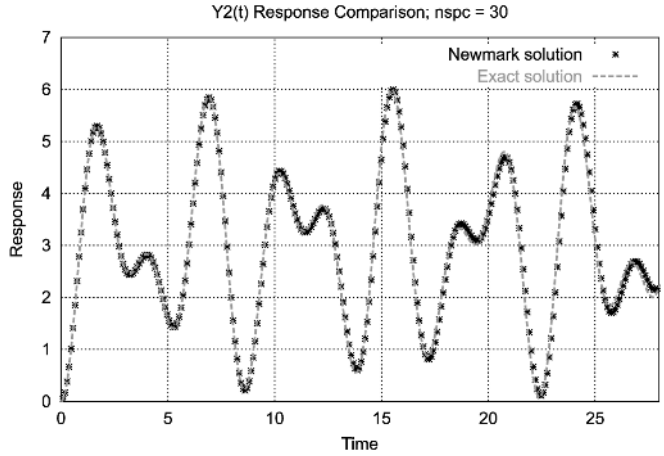

Figure 2.

particularly when one considers how cheap the structural equations are to solve compared to the fluid.

3. Aerodynamic model

A finite-volume Euler code is used for the aerodynamic model. The two-dimensional unsteady Euler equations on a moving grid in integral form are:

$$\frac{\partial}{\partial t}\iint_V \mathbf{U}\,\mathrm{d}x\,\mathrm{d}y + \int_{\partial V} \mathbf{F}\cdot\mathbf{n}\,\mathrm{d}S = 0 \tag{12}$$

where $\mathbf{U}$ is the vector of conserved variables, $\mathbf{F}$ is the flux vector, $\mathbf{n}$ is the outward cell face unit normal, and S the peripheral length of the cell face. $\mathbf{U}$ and $\mathbf{F}$ are given by:

$$\mathbf{U} = \begin{Bmatrix} \rho \\ \rho u \\ \rho v \\ \rho e \end{Bmatrix}, \qquad \mathbf{F} = \begin{Bmatrix} \rho(\mathbf{u} - \mathbf{X_t}) \\ \rho u(\mathbf{u} - \mathbf{X_t}) + P\mathbf{i} \\ \rho v(\mathbf{u} - \mathbf{X_t}) + P\mathbf{j} \\ \rho e(\mathbf{u} - \mathbf{X_t}) + P\mathbf{u} \end{Bmatrix} \tag{13}$$

where $\mathbf{u}$ is the velocity vector, $\mathbf{X_t}$ the grid velocity vector, and P, ρ, u, v and e are pressure, density, Cartesian x- and y-component velocities and total specific energy, respectively. The equation set is closed by

$$P = (\gamma - 1)\left(\rho e - \frac{\rho \mathbf{u}^2}{2}\right) \tag{14}$$

3.1 Discretisation

The unsteady Euler equations are solved using a Jameson (Jameson *et al.*, 1981) type cell-centred finite-volume method. Equation (12) is applied to each cell of the mesh. Following Jameson *et al.* (1981), the spatial and time dependent terms are decoupled and a set of ordinary differential equations are obtained. Artificial dissipation needs to be added to stabilise the solution (Jameson *et al.*, 1981; Kroll and Jain, 1987).

3.2 Aerodynamic time integration

It is expensive to use explicit time-stepping for unsteady flows. To maintain time-accuracy the whole domain must be integrated by the same time-step, and this is limited to the smallest value over the domain. Hence, an implicit scheme is used, based on that proposed by Jameson (1991). This solves the unsteady flows as a series of pseudo-steady cases, and is extremely efficient compared to an explicit scheme (Allen, 1997b; Gaitonde, 1994). Equation (1) is approximated for each computational cell at time level $(n+1)$ by

$$\frac{\mathrm{d}(V^{n+1}\mathbf{U}^{n+1})}{\mathrm{d}t} + \mathbf{R}^{n+1} = 0 \tag{15}$$

where V is the cell area, $\mathbf{R}$ is the flux integral, and the superscript $(n+1)$ denotes the time level $(n+1)\Delta t$. The $\mathrm{d}/\mathrm{d}t$ operator is approximated by an implicit second-order backward difference to give

$$\frac{3V^{n+1}\mathbf{U}^{n+1} - 4V^{n}\mathbf{U}^{n} + V^{n-1}\mathbf{U}^{n-1}}{2\Delta t} + \mathbf{R}(\mathbf{U}^{n+1}) = 0 \tag{16}$$

or

$$\mathbf{R}^{*}(\mathbf{U}^{n+1}) = \mathbf{R}(\mathbf{U}^{n+1}) + \frac{3V^{n+1}\mathbf{U}^{n+1} - 4V^{n}\mathbf{U}^{n} + V^{\mathrm{n}-1}\mathbf{U}^{n-1}}{2\Delta t} = 0 \tag{17}$$

To solve this $\mathbf{U}^{n+1}$ must be iterated upon until equation (17) $\rightarrow 0$. Hence, a fictitious derivative with respect to "pseudo time" τ can be introduced to the equation to give

$$V^{n+1}\frac{\mathrm{d}\mathbf{U}}{\mathrm{d}\tau} + \mathbf{R}^{*}(\mathbf{U}) = 0 \tag{18}$$

and the solution of equation (17) is then equivalent to marching equation (18) to a steady state in pseudo time, i.e. when $\mathbf{U}$ has been found such that $\mathrm{d}\mathbf{U}/\mathrm{d}\tau \rightarrow 0$ then $\mathbf{U}^{n+1} = \mathbf{U}$. There is no limit on the real time-step allowed, and steady acceleration techniques can be used in pseudo time. Equation (18) is solved using a multi-stage Runge-Kutta method with local time-stepping.

3.3 Moving mesh algorithm

The flow-solver is used in conjunction with a structured moving mesh, which allows the cell volumes to distort as the aerofoil moves or deforms. An algebraic moving grid generator based on transfinite interpolation (Eriksson, 1982; Gordon and Hall, 1973; Gordon and Thiel, 1982) is used. This approach is extremely efficient, as it allows instantaneous grid positions and speeds to be computed directly at any time (Allen, 1995, 1997a; Gaitonde and Fiddes, 1993).

The cell areas required in the time-stepping scheme can be calculated exactly in terms of the coordinates of the grid nodes. However, if the areas are calculated in this manner, errors will be introduced by the moving mesh. In order to avoid such errors, a geometric conservation law needs to be satisfied numerically, in addition to the mass, momentum and energy conservation laws that govern the physics of the flow (Thomas and Lombard, 1979). The areas must be integrated forward using the same numerical scheme as for the flow.

Figure 3 shows an example of a moving C-grid generated by the present method. A sequence of grids is shown for NACA 64A010 aerofoil pitching up 20°.

More details of the flow-solver can be found in the works Djayapertapa (2001) and Djayapertapa and Allen (2001).

4. Aero-structural coupling

There are two options when coupling separate aerodynamic and structural dynamic codes. The simplest method to couple separate aerodynamic and structural dynamic codes is "weak" coupling, wherein there is no intermediate

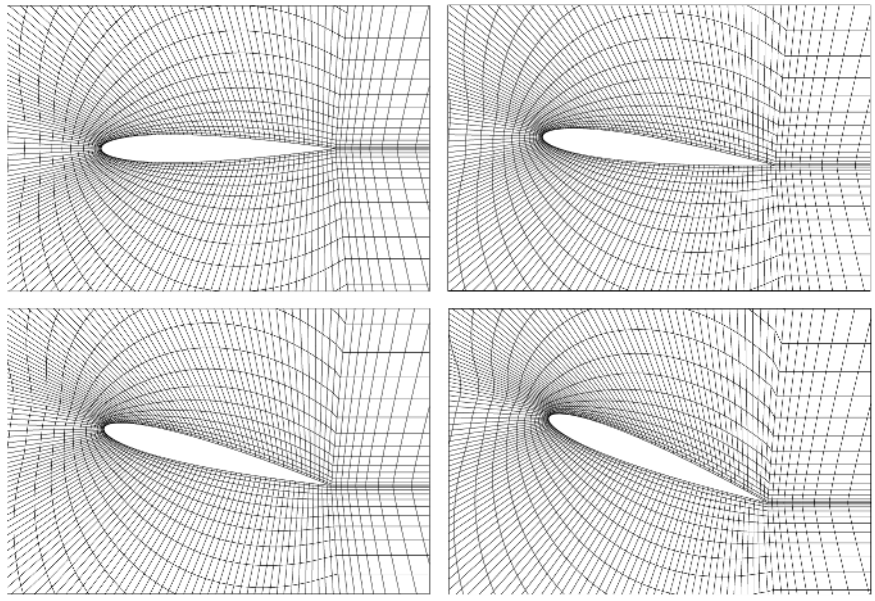

Figure 3.
Moving C-grid, NACA0012 aerofoil

exchange of information between the two solvers at each time level. At each time level the fluid is solved using the current structural position to give aerodynamic loads on the structure, and these are then used to solve for a new structural position. This is simply repeated for each time level. Hence, the fluid and structure are not synchronised in time, and there is always a phase lag between the two. This phase lag will be time-step dependent, and this has been examined earlier.

Alternatively "strong" coupling can be used, wherein there is exchange of information between the two solvers. At each real time level the aerodynamic loads are computed, then the structural position that results from those loads are computed. The aerodynamic loads around this new structural position are then recomputed, and this iterative procedure is repeated until the fluid and structure are perfectly synchronised at each real time level. This is more complex to code than weak coupling, but ensures there is no phase lag between fluid and structure. A flight control system is integrated with the aero-structural code in the next section, and it is clearly desirable that no phase lag is present in this case.

In fact, earlier it has been shown (Djayapertapa and Allen, 2001) that only for low numbers of real time-steps per period is the strong coupling scheme more expensive, in terms of CPU requirements, than the weak coupling scheme. However, in this region the phase lag is such that weak coupling is not of acceptable accuracy. As a flight control system is to be integrated which cannot function with inherent phase lag, the strong coupling scheme was chosen.

It has also been shown (Djayapertapa and Allen, 2001) that computations performed on a grid of density 147×32 points, using 60 real time-steps per cycle gave acceptable accuracy. Increasing either grid density or number of time-steps gave only small increases in accuracy, which were far outweighed by the increased computational cost.

4.1 Energy considerations

During an unsteady coupled calculation there will be energy transfer from fluid to structure, and vice versa, and it is useful to examine this energy transfer. The general energy identity (derivable from Lagrange's equation) is given by

$$E_{\text{total}} = \text{KE} + \text{PE} = E_{\text{o}} + W_{\text{ext}} \tag{19}$$

where E_{total} is the total mechanical energy of the structure, consisting of kinetic energy (KE) and potential energy (PE). E_{o} is the initial energy of the structure, i.e. the energy that the structure has at time $= 0$, and W_{ext} is the work done by external forces such as the aerodynamic forces.

$W_{\text{ext}} > 0$ indicates that work is being done by the fluid. If the amplitude of the structural oscillation grows then W_{ext} and E_{total} will also grow, but following the energy identity given by equation (19), the difference between the total energy and the work done by the aerodynamic forces should be constant. That identity can also be used to check the time integration scheme used. If the

difference is constant then no amplitude error or period elongation are introduced by the time integration scheme.

4.2 Computed responses for Isogai model

A two degree of freedom test case due to Isogai (1979) was first considered. The aeroelastic parameters used are

$$a_h = -2.0, \quad x_\alpha = 1.8, \quad r_\alpha = 1.87, \quad \frac{\omega_h}{\omega_\alpha} = 1.0, \quad \mu = 60. \tag{20}$$

This represents a typical section of a swept back wing, since the elastic axis is ahead of the leading edge.

Aeroelastic responses for plunge and pitch for speed index, U^*, values of 0.30, 0.5025 and 0.70 at a Mach number of 0.85 are shown in Figure 4. At the lower value of speed index the responses are decayed. These decayed responses are produced because the structural stiffness overpowers the work done by the fluids. As U^* increases the response reaches a neutrally stable condition in which the structural stiffness is just sufficient to dissipate the extracted energy – this is termed the flutter point (0.5025 in this case). When the speed index is increased further, the extracted energy overpowers the structural stiffness, hence diverging responses are obtained. The character of this divergent response then can be benign, i.e. small amplitude flutter or catastrophic, i.e. explosive flutter. The analysis of this character should be based on Hopf bifurcation or stability/instability of the LCO. For panel flutter, this analysis was performed by Librescu (1965, 1967), where the flutter character was termed "undangerous" or "dangerous", and was determined by the sign of the first Liapounov magnitude (Bautin, 1949).

Figure 5 displays the energy variations for the above three cases. The energy is non-dimensionalised by the initial energy E_0, so that the difference of the total energy and the work done by external forces should be equal to 1 as time increases. From Figure 5 we see that this difference remains constant and equal to the initial energy E_0, thus proving that the numerical scheme used is energy conserving.

The flutter point is located for a particular Mach number by computing the time-response for several values of speed index, and analysing the rate of decay for each one. When the speed index is found at which the rate of decay is zero, this is the flutter speed index at that Mach number. If the process of locating the flutter point is repeated for several Mach numbers the flutter boundary of the aerofoil can be computed. Therefore, it should be noted that the coupled code is not a "prediction" tool, but a simulation tool which, if required, can be used in a brute force way to compute flutter boundaries. The computed flutter boundary is shown in Figure 6, which also shows results due to Alonso and Jameson (1994), Isogai (1979) and Kousen and Bendiksen (1994). The results compare well.

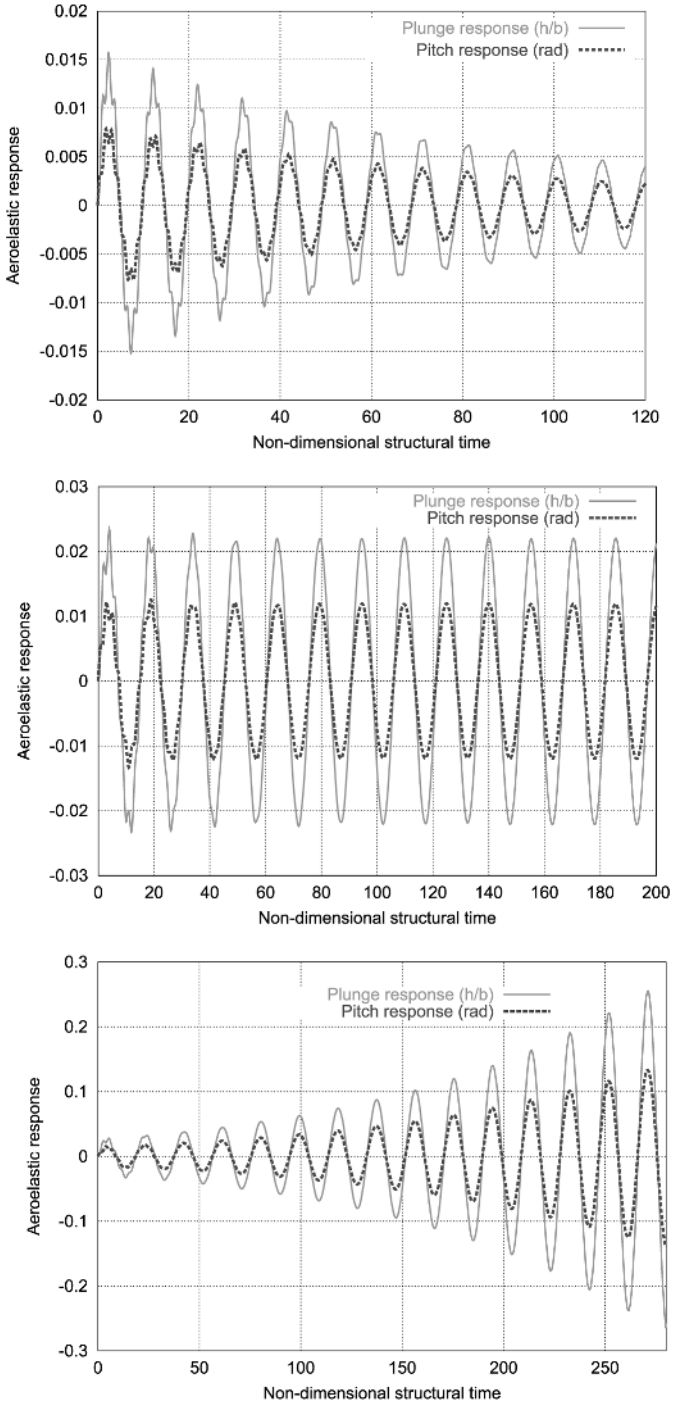

Figure 4.
Aeroelastic response, $U^* = 0.30$, 0.5025, 0.7, and Mach = 0.85

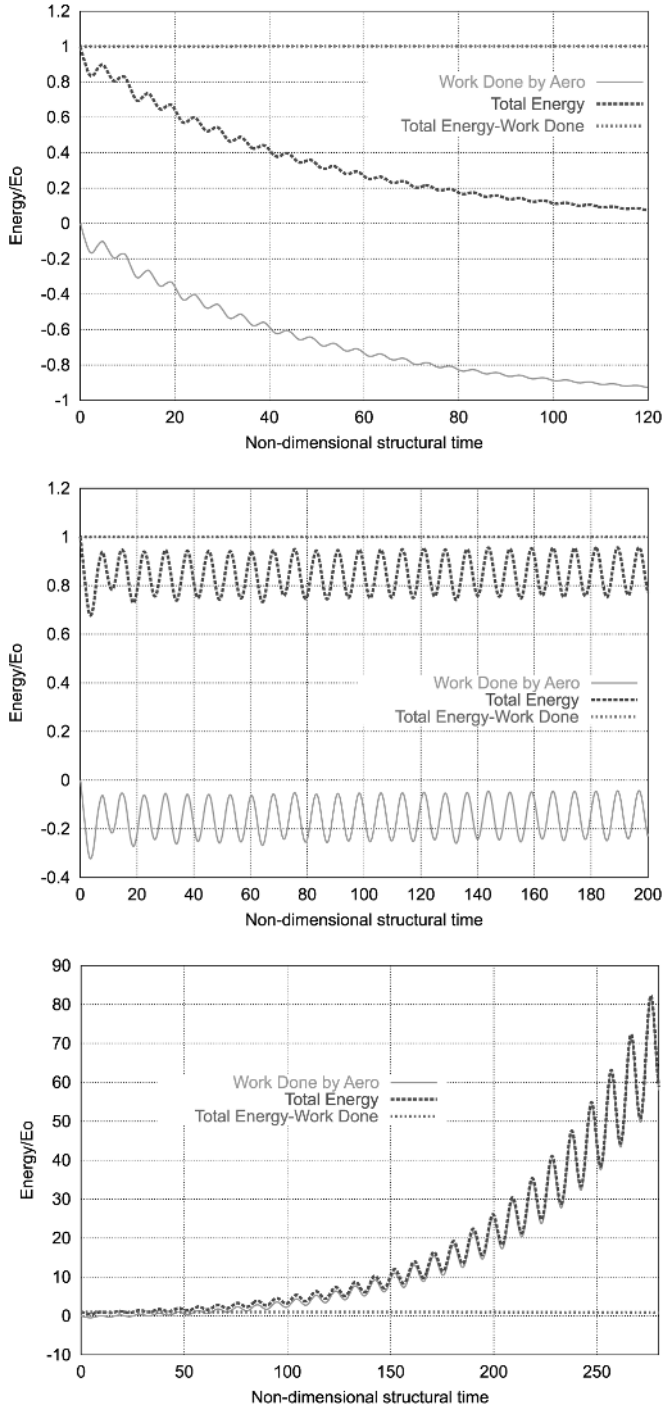

Figure 5.
Energy variations, $U^* = 0.30$, 0.5025, 0.7, and Mach = 0.85

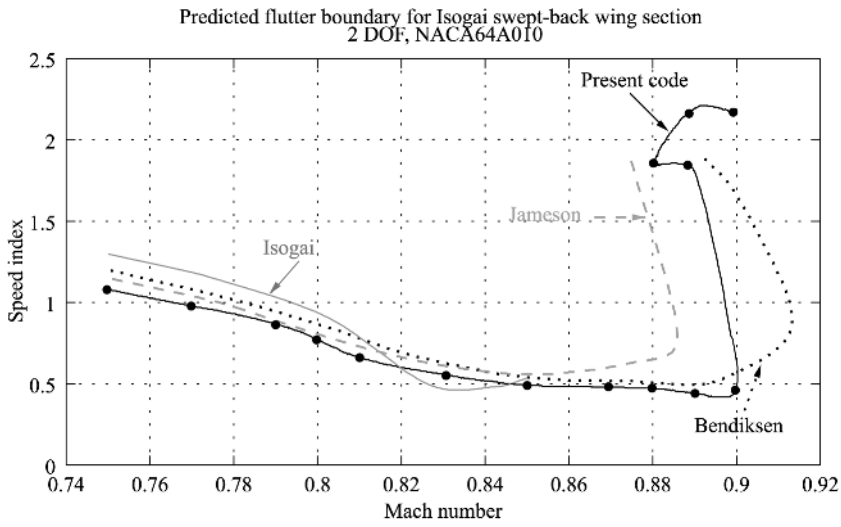

Figure 6.
Isogai model predicted flutter boundary

One interesting point to consider is the phase difference between the plunge and pitch motion. Figure 7 shows the phase difference for varying Mach number and speed index. This shows that in the lower transonic region the plunge and pitch motion are in phase even far above the flutter point. As the Mach number and speed index increase, this difference increases almost linearly, until there is a rapid change to antiphase motion at high Mach number. It is believed that once the Mach number becomes high enough, or the amplitude of oscillation becomes large enough (i.e. the speed index becomes large enough), the shockwaves on one or both sides will move to the trailing edge. Once this occurs the motion of the shocks becomes limited, and hence the section motion must change since the applied aerodynamic load variation changes.

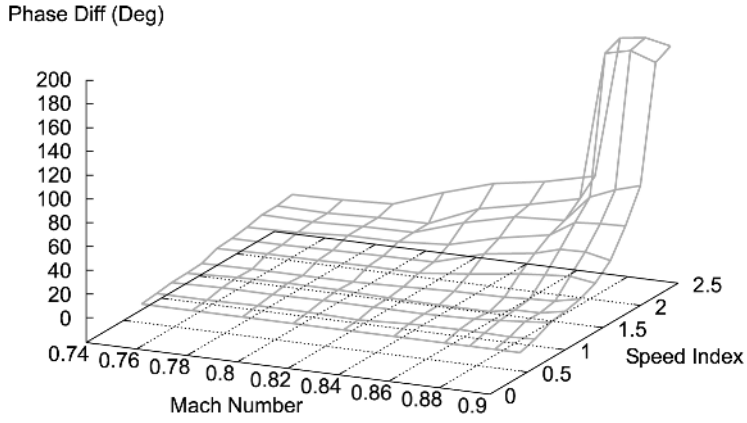

Figure 7.
Phase difference plot, Isogai model

4.3 Computed three degree of freedom response

A three degree of freedom was added to the NACA64A010 case used earlier. The structural parameters used for the calculations are as follows (Schulze, 1998):

$$a_h = -0.2, \quad x_\alpha = 0.2, \quad r_\alpha = 0.5, \quad \frac{\omega_h}{\omega_\alpha} = 0.3, \quad \mu = 23.48,$$

$$x_\beta = 0.008, \quad r_\beta = 0.06, \quad \frac{\omega_\beta}{\omega_\alpha} = 1.5, \quad C_\beta = 0.5 \tag{21}$$

The computed flutter boundary of the aerofoil is shown in Figure 8. The figure also shows results obtained by DLR (Schulze, 1998), and the two flutter boundaries compare very well.

5. Aeroservoelastic coupling

The trailing edge flap may be moved according to the instantaneous aerofoil state to attempt to reduce the structural deformation. Hence, active control has been implemented within the aeroelastic solver, in order to investigate active means of transonic flutter suppression via control surface (flap) and motion-aeroservoelasticity (closed loop calculations). A simple control law is used which relates the required flap deflection angle, β_c, to the motion of the main aerofoil surface (plunge and pitch degrees of freedom). Hence, β_c is evaluated according to the following equation

$$\beta_c = G_1\xi + G_2\alpha + G_3\dot{\xi} + G_4\dot{\alpha} + G_5\ddot{\xi} + G_6\ddot{\alpha} \tag{22}$$

where the G's are the gains of the system.

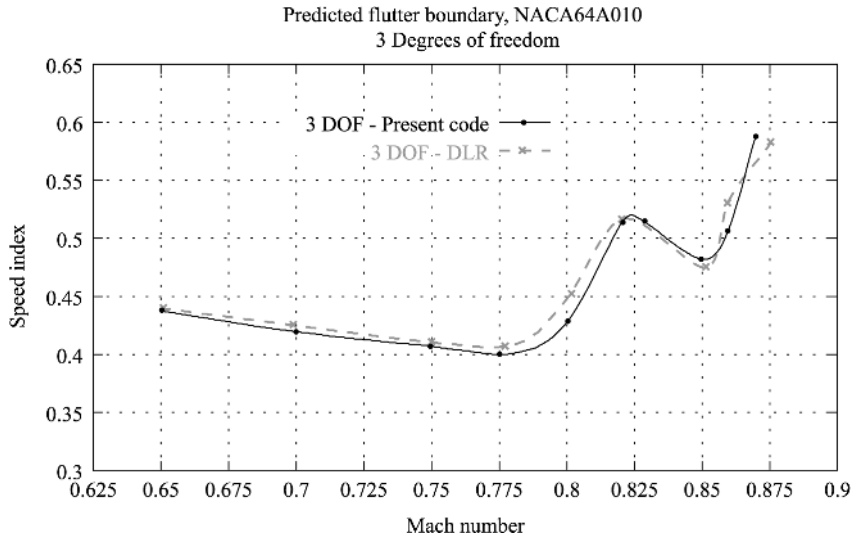

Figure 8.
Predicted flutter boundary for three degrees of freedom

The flap is moved according to the demanded deflection angle β_c. However, instead of moving the flap by β_c degrees within a certain amount of time (according to the flap deflection rate), the required angle is converted into equivalent control hinge moment (CHM) which is blended into the open loop aeroelastic equations as the external moment acting on the hinge axis, hence only affecting the β degree of freedom. There are two hinge moments on the right hand side of the aeroservoelastic equation, the aerodynamic hinge moment (AHM) and the CHM as shown by equation (23)

$$x_\beta \ddot{\xi} + \left[(C_\beta - a_h)x_\beta + r_\beta^2\right]\ddot{\alpha} + r_\beta^2 \ddot{\beta} + \frac{4M_\infty^2 \gamma}{U^{*2}\mu} r_\beta^2 \left(\frac{\omega_\beta}{\omega_\alpha}\right)^2 \beta = \underbrace{\frac{8M_\infty^2 \gamma}{\pi\mu} C_{\mathrm{H}}}_{\mathrm{AHM}} + \underbrace{\frac{4M_\infty^2 \gamma}{U^{*2}\mu} r_\beta^2 \left(\frac{\omega_\beta}{\omega_\alpha}\right)^2 \beta_c}_{\mathrm{CHM}} \tag{23}$$

This is because it is impossible to guarantee that the flap will move from β to $\beta + \beta_c$ within a certain amount of time. By converting the required angle to the equivalent CHM the flap dynamics are accounted for. Furthermore, from the open loop three degree of freedom case, it was seen that the flap motion also influences the pitch and plunge motion. That influence has already been included when the CHM was blended into the open loop aeroelastic equation.

The same time marching scheme is used to integrate the aeroservoelastic equation of motion, the only change lies in the representation of the right hand side force. It is now given by $\mathbf{f} = \mathbf{f_a} + \mathbf{f_c}$ where $\mathbf{f_c}$ is the control forces and is given by $\mathbf{f_c} = \{0, 0, \mathrm{CHM}\}^{\mathrm{T}}$.

The energy identity given by equation (19) should still hold, and the work done by external forces includes an extra term due to the control surface.

5.1 Computed closed loop responses

Closed loop simulations were performed using the active control. A Mach number of 0.85 was chosen, and the speed index was 5 per cent above the flutter speed, i.e. corresponding to an unstable response.

Different gain combinations were first considered in order to determine the optimum gain combinations to be used. From a series of calculations it was found that G_1, G_2, G_5 and G_6 fail to suppress the flutter, whereas G_3 and G_4 successfully suppressed the motion. The most effective combination was to use G_3 and G_4 together. Figure 9 shows the plunge, pitch and flap responses for $M = 0.85$, and $U^* = 1.05U^*_{\mathrm{flutter}}$. The initial disturbance was $\dot{\xi} = \dot{\alpha} = 0.01$ and the gains were $G_3 = G_4 = 1.0$. Two situations were considered: implementing the active control immediately, and at some later time. It is clear that the active control has managed to "drain" the

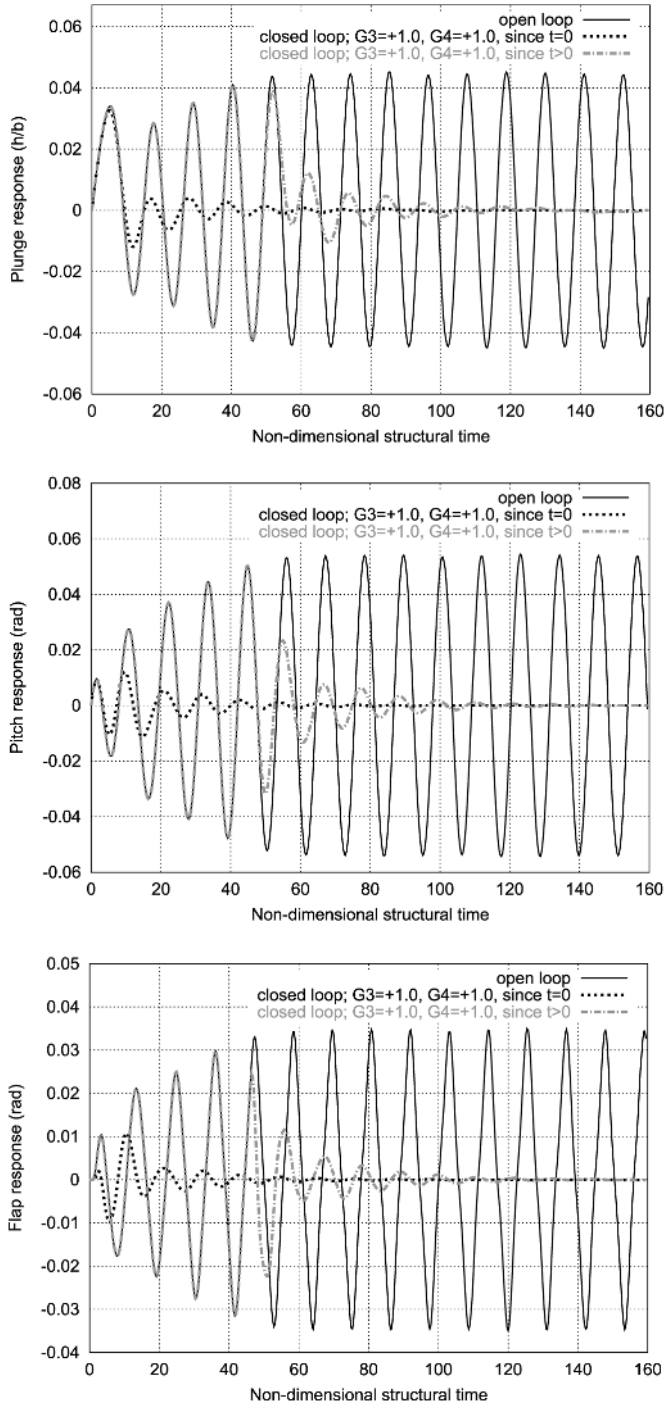

Figure 9.
Positive velocity feedback; $G_3 = +1.0$, $G_4 = +1.0$, and $U^* = 1.05\ U_f^*$

structural energy very quickly, even when the disturbance has sufficient time to grow.

The effect of the control law on the flutter boundary was then considered. The open and closed loop flutter boundaries are shown in Figure 10. The control law works very effectively within the transonic region, where the shock position can be affected by the flap. An increase of upto 19 per cent in the allowable speed index can be achieved with this control law.

The mechanics of transonic flutter and active control were investigated by considering a more unstable case. Figure 11 shows a series of flowfield Mach contours for $M = 0.85$, and $U^* = 1.10U^*_{\text{flutter}}$ without active control. The same aerofoil was used, but the grid density was increased to 211×40 to capture the shock more sharply. Contours are plotted every quarter period, for six periods. These show how the out of phase shock motion across the flap causes the oscillation to grow. Figure 12 shows Mach contours for the same case with active control switched on just before the end of the third cycle. The flap is clearly effective in controlling the shock motion in this case.

It should be remembered that an inviscid aerodynamic model is used here, and that viscous effects are likely to be significant for this type of flow, where there are shock waves present and a moving control surface.

5.2 Effect of sampling frequency

A real flight control system would sample the aerofoil state continuously, whereas it is only sampled at discrete points in time here. Hence, the effect of time-step size on the active control was considered. The above computations were performed with 60 real time-steps per period. The above case was run again with 240 time-steps per period. Figure 13 shows the plunge, pitch, and

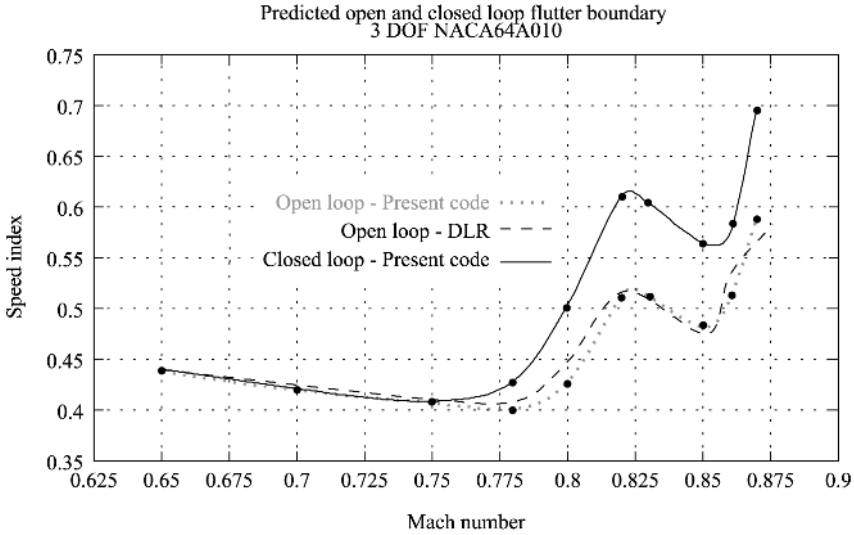

Figure 10.
Control law effectiveness

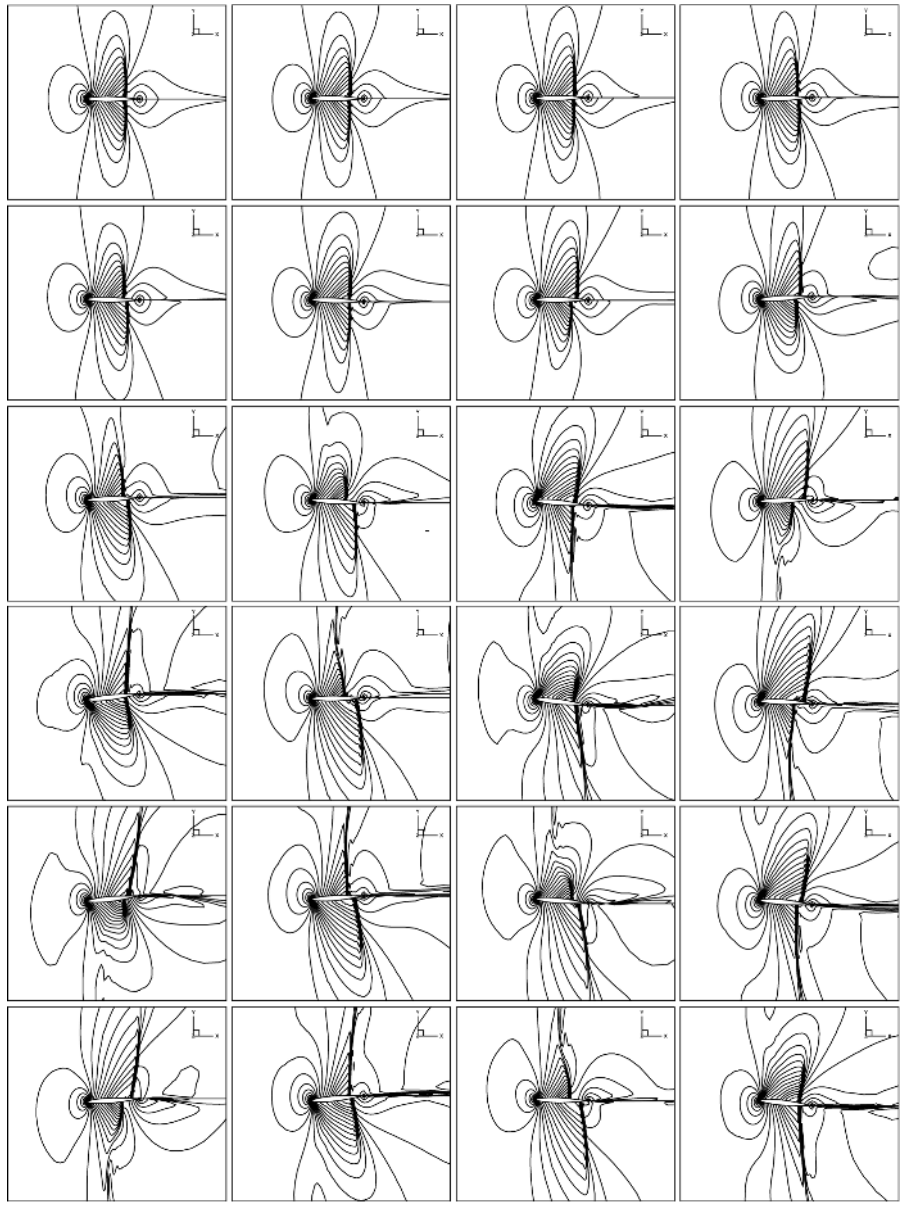

Figure 11.
Open loop flowfield mach contours

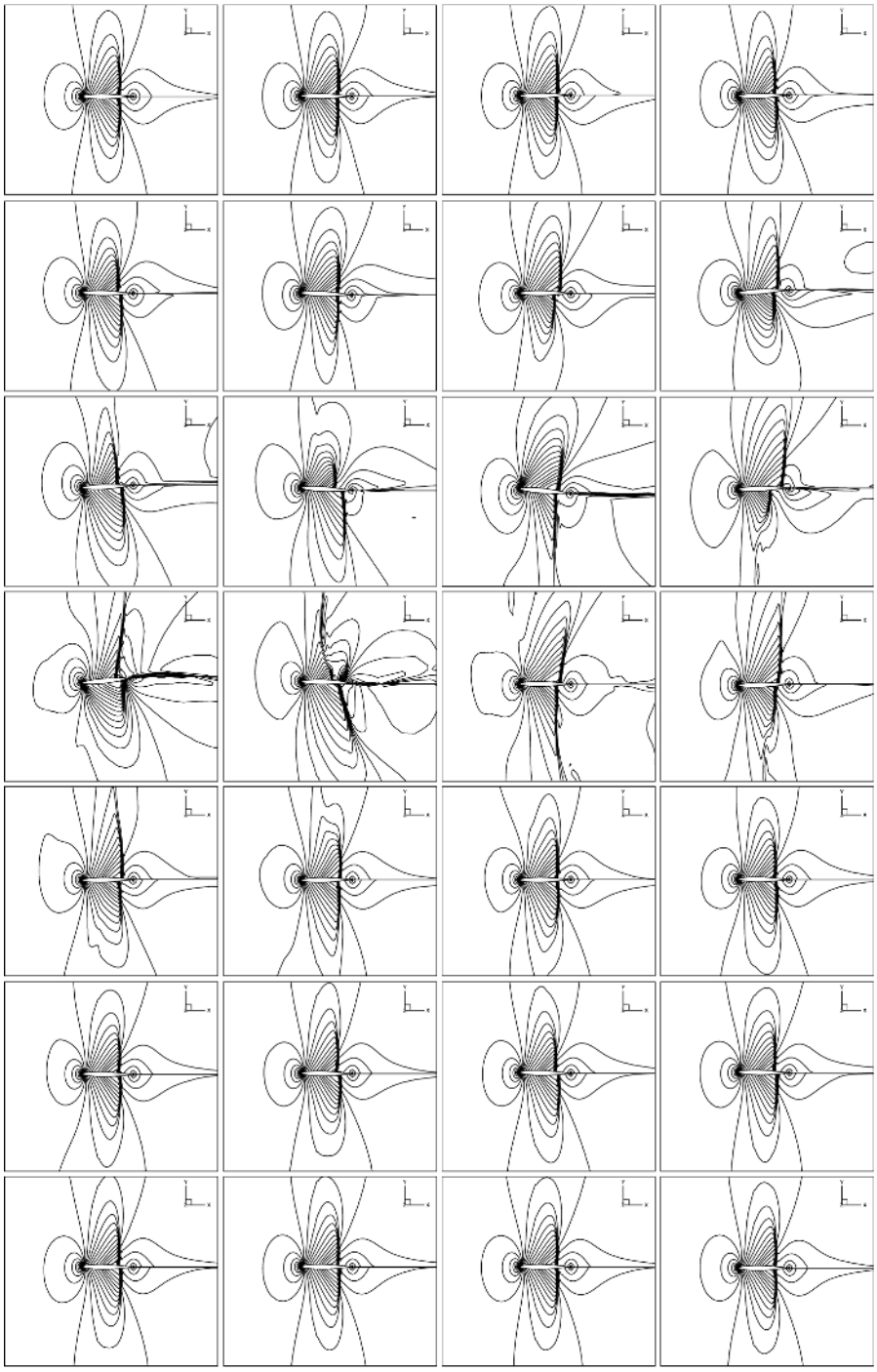

Figure 12.
Closed loop flowfield mach contours

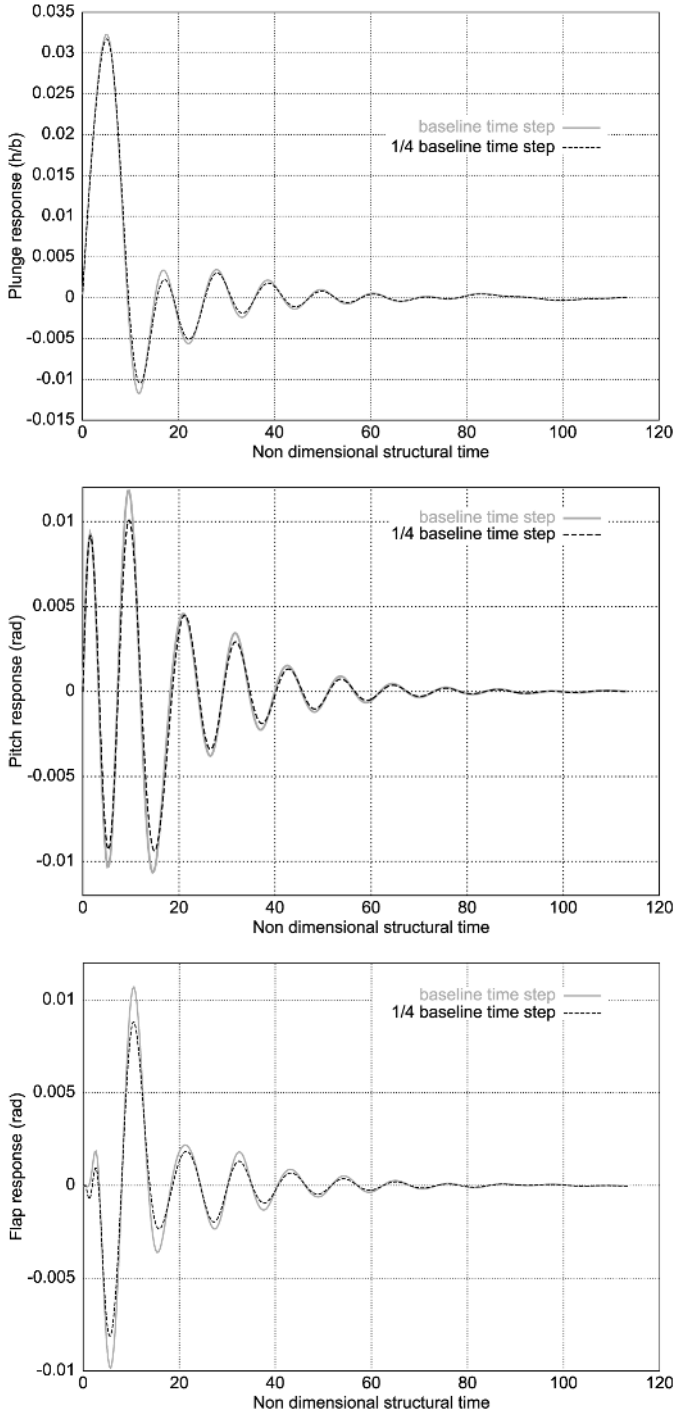

Figure 13.
Effect of reducing the real time-step size

flap variations for the two sampling frequencies. It is clear that there is very little difference between the two cases.

6. Non-linear structural model

The effect of structural non-linearity on aeroservoelastic calculations has also been considered. Backlash (free-play) in the torsional spring of the control surface motion was considered.

Figure 14 plots the variation of the hinge moment against the flap deflection angle. The solid line represents the linear variation that has been used so far, and the dashed line shows the typical non-linear characteristics for backlash. There is a range of rotational amplitude where the restoring hinge moment is zero, outside this range a linear relationship between the restoring hinge moment and flap deflection angle exists.

Free-play of the hinge axis modifies the aeroelastic and aeroservoelastic equation only for the β (flap) degree of freedom. Outside the free-play region the equation of motion for the flap degree of freedom is given by

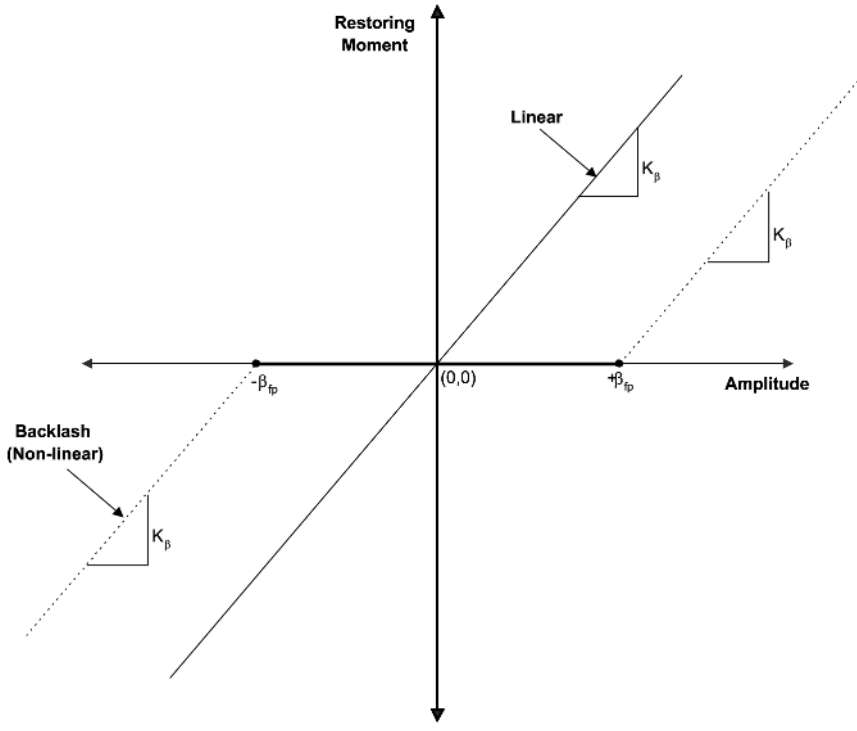

Figure 14.
Linear and non-linear moment relation

$$x_\beta \ddot{\xi} + \left[(C_\beta - a_h)x_\beta + r_\beta^2\right]\ddot{\alpha} + r_\beta^2 \ddot{\beta} + \frac{4M_\infty^2 \gamma}{U^{*2}\mu} r_\beta^2 \left(\frac{\omega_\beta}{\omega_\alpha}\right)^2 \beta = \underbrace{\frac{8M_\infty^2 \gamma}{\pi\mu} C_H}_{\text{AHM}} + \underbrace{\frac{4M_\infty^2 \gamma}{U^{*2}\mu} r_\beta^2 \left(\frac{\omega_\beta}{\omega_\alpha}\right)^2 \beta_c}_{\text{CHM}} \pm \underbrace{\frac{4M_\infty^2 \gamma}{U^{*2}\mu} r_\beta^2 \left(\frac{\omega_\beta}{\omega_\alpha}\right)^2 \beta_{\text{fp}}}_{\text{FPHM}} \quad (24)$$

where the positive sign is used when $\beta > \beta_{\text{fp}}$ and negative sign is used when $\beta < -\beta_{\text{fp}}$ to evaluate free-play hinge moment (FPHM). The same time-marching scheme can be used again to integrate equation (24), as only change lies in the representation of the right hand side force. It is now given by $\mathbf{f} = \mathbf{f_a} + \mathbf{f_c} + \mathbf{f_{fp}}$ where $\mathbf{f_{fp}}$ is the free play hinge moment and is given by $\mathbf{f_{fp}} = \{0, 0, \text{FPHM}\}^{\text{T}}$.

As before the energy identity given by equation (19) should still hold. The work done by the external forces includes an extra term when β is outside the free-play region. Inside the free-play region this term and the control surface term are both zero.

6.1 Computed responses

Open and closed loop calculations were performed for the three degree of freedom case presented above, now with the non-linear CHM. The aerofoil is the NACA64A010 section, the Mach number is 0.85 and the flutter speed index was chosen. The effects of the free-play of 1.0° in the hinge axis torsional spring on the aeroelastic responses are shown in Figure 15. From the figure it can be seen that free-play actually causes the responses to grow and settle into a limit cycle oscillation, i.e. the effect is destabilising.

Results for active control calculations with backlash are shown in Figure 15. It can be seen that the responses are damped when the required flap angle β_c falls outside the free-play area. However, once the response has settled, and β_c lies within the free-play area, there is not much that the control law can do, since it is utilising the CHM to suppress the motions, and within the free-play area the control hinge moment is zero. From the plot of energy it is clear that the control law drains the energy until β_c falls within the free-play area.

Figure 16 shows the open loop phase plane plots for plunge, pitch and flap deflection for the linear structural model and free-play of one degree. Figure 17 shows flap deflection phase plane plots for closed loop calculations with and without free-play. With free-play the flap settles into a periodic motion.

It should also be noted here that the effect of signal sampling frequency, i.e. size of the real time-step used, was also considered in the free-play region.

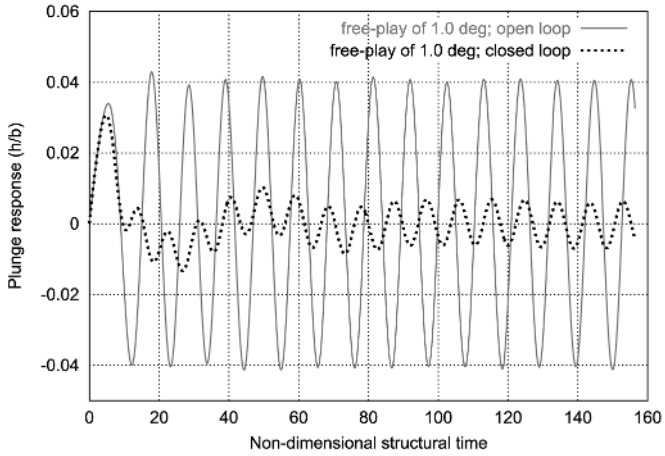

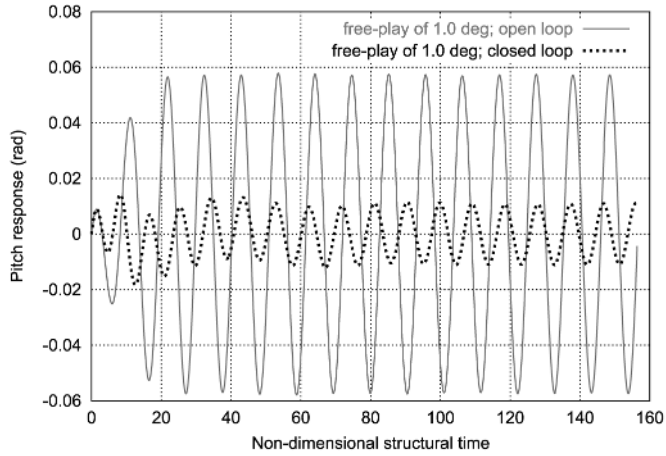

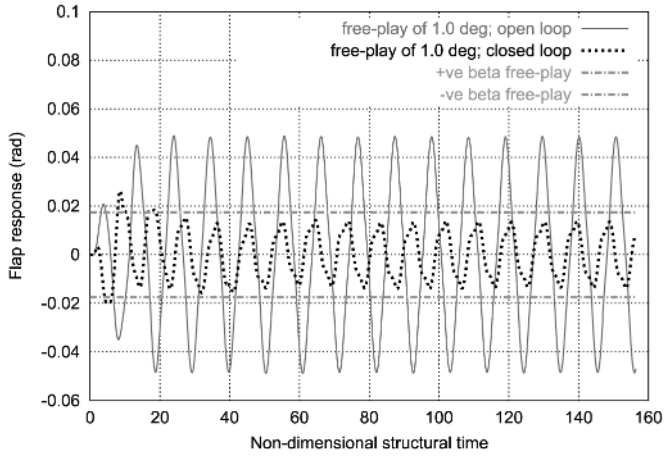

(*continued*)

Figure 15.
The effects of free-play of 1.0 deg

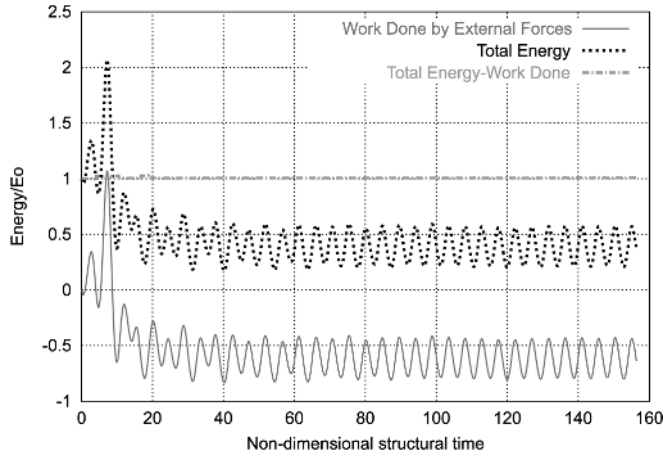

Figure 15.

Again there was only a small amplitude dependence on the time-step size, and no frequency dependence, as in Section 5.2.

7. Conclusions

Numerical simulations of transonic flutter and active control have been performed, by coupling independent aerodynamic and structural dynamic codes in the time domain. A simple control system has also been integrated with the coupled code, and since this requires perfect synchronisation of fluid, structure and control signal, the "strong" approach to coupling has been adopted. Two and three degree of freedom two-dimensional structural models have been considered. The consistency of the coupling has been demonstrated by considering the total energy of the structure and work done by the fluid. The difference between the two remains constant with time regardless of the structural motion.

The coupled scheme has been used to simulate time responses to structural disturbances for various Mach numbers and speed indices, to attempt to compute flutter boundaries for the two and three degree of freedom cases, and the results compare well with other published data. Furthermore, the structural model has been extended to include an actively controlled trailing edge flap, and this has succesfully been used to increase the stability margin by means of control surface motion. The aerofoil velocity feedback signal was found to give the best suppression results, and for the NACA64A010 aerofoil an increase of up to 19 per cent in the allowable speed index can be achieved within the transonic region. Furthermore, it has been shown that active control is still effective when there is free-play in the control hinge – the aerofoil response is supressed to within the free-play region.

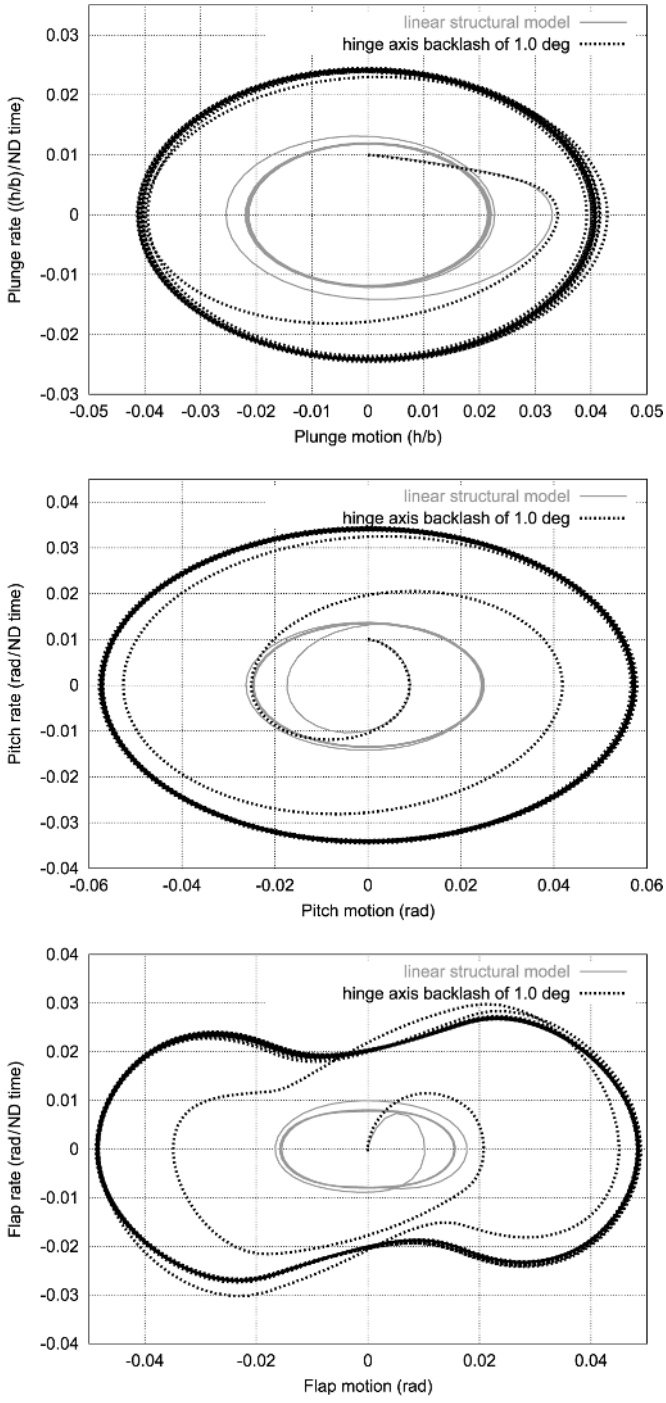

Figure 16.
Phase plane plots for linear and non-linear structure

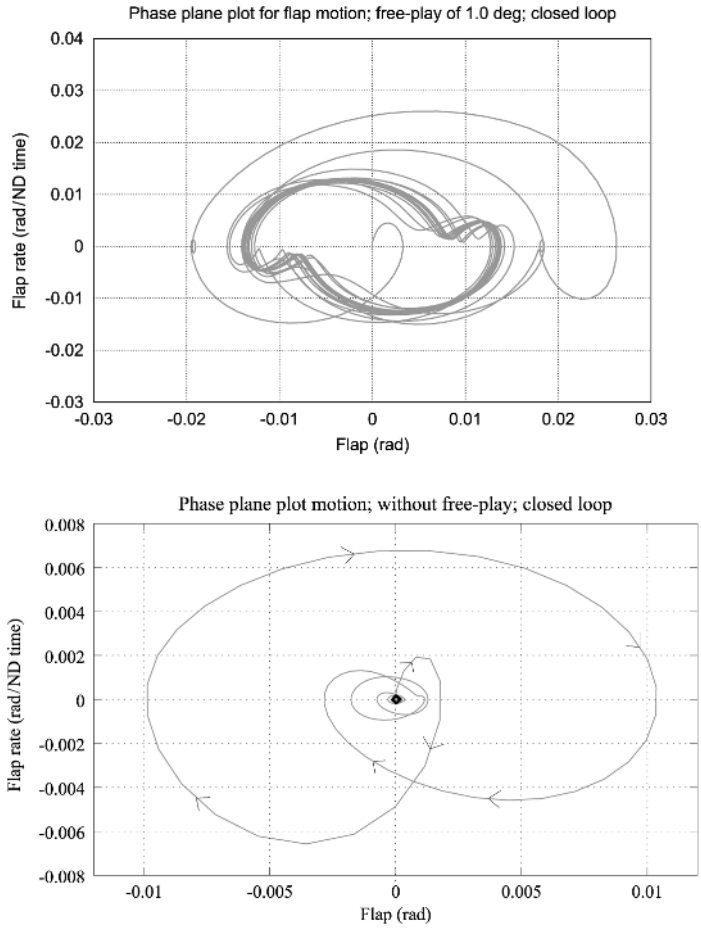

Figure 17.
Closed loop flap phase plane comparison with and without free-play

The mechanics of transonic flutter and active control have been examined by considering time-dependent flowfield data, and the fundamental importance of shock wave motion has been clearly demonstrated.

References

Allen, C.B. (1995), "Central-difference and upwind biased schemes for steady and unsteady Euler aerofoil flows", *Aeronautical Journal*, Vol. 99, pp. 52-62.

Allen, C.B. (1997a), "The reduction of numerical entropy generated by unsteady shockwaves", *Aeronautical Journal*, Vol. 101 No. 1001, pp. 9-16.

Allen, C.B. (1997b), "Grid adaptation for unsteady flow computations", *I. Mech. E. J. of Aerospace Eng.,* Part G4, Vol. 211, pp. 237-50.

Alonso, J.J. and Jameson, A. (1994), "Fully-implicit time-marching aeroelastic solutions", *AIAA Paper No. 94-0056*, Reno, NV.

Badcock, K.J., Sim, G. and Richards, B.E. (1995), "Aeroelastic studies using transonic flow CFD modelling", *Proceedings International Forum on Aeroelasticity and Structural Dynamics*, June 1995, Manchester, pp. 18.1-18.12.

Bathe, K.J. (1982), *Finite Element Procedures in Engineering Analysis*, Prentice-Hall, Englewood Cliffs, NJ.

Batina, J.T. and Yang, T.Y. (1984), "Application of transonic codes to aeroelastic modelling of airfoils including active controls", *Journal of Aircraft*, Vol. 21 No. 8, pp. 623-30.

Bautin, N.N. (1949), *Behaviours of Dynamic Systems in the Vicinity of the Boundary of the Stability Domain*, Gostekizdat, Moscow.

Bendiksen, O.O. and Kousen, K.A. (1987), "Transonic flutter analysis using the Euler equations", *AIAA Paper No. 87-0911-CP*, Reno, NV.

Bennett, R.M. and Edwards, J.W. (1998), "An overview of recent development in computational aeroelasticity", *AIAA 98-2421, 29th AIAA Fluid Dynamics Conference*, Albuquerque, NM.

Bland, S.R. and Edwards, J.W. (1984), "Airfoil shape and thickness effects on transonic airloads and flutter", *Journal of Aircraft*, Vol. 21, pp. 209-17.

Djayapertapa, L. (2001), "A computational method for coupled aerodynamic-structural calculations in unsteady transonic flow with active control study", PhD thesis, Aerospace Engineering Department, Bristol University.

Djayapertapa, L. and Allen, C.B. (2001), "Time-marching analysis of aeroservoelasticity", *Paper 1, Proceedings RAeS Aerodynamics Conference*, London.

Dowell, E.H., *et al.* (Eds) (1994), *A Modern Course in Aeroelasticity*, 3rd revision and enlarged edition, Kluwer Academic Publishers, Boston, MA.

Edwards, J.W., Breakwell, J.V. and Bryon, A.E. Jr (1978), "Active flutter control using generalized unsteady aerodynamic theory", *Journal of Guidance and Control*, Vol. 1 No. 1, pp. 32-40.

Eriksson, L.E. (1982), "Generation of boundary conforming grids around wing-body configurations using transfinite interpolation", *AIAA Journal*, Vol. 20 No. 10, pp. 1313-20.

Försching, H. (1995), "Challenges and perspectives in computational aeroelasticity", *Proceedings International Forum on Aeroelasticity and Structural Dynamics*, June 1995, Manchester, pp. 11.1-11.9.

Fung, Y.C. (1955), *An Introduction To the Theory of Aeroelasticity*, Wiley, New York, NY.

Gaitonde, A.L. (1994), "A dual-time method for the solution of the unsteady Euler equations", *The Aeronautical Journal*, Vol. 98, pp. 283-91.

Gaitonde, A.L. and Fiddes, S.P. (1993), "A three dimensional moving mesh method for the calculations of unsteady transonic flows", *Paper 13 in Proceedings of the 1993 European Forum for Recent Developments and Applications in Aeronautical CFD*, Bristol.

Glaser, J. (1987), *Seminar on Aeroelasticity*, de Havilland, Canada.

Gordon, W.J. and Hall, C.A. (1973), "Construction of curvilinear co-ordinates systems and applications to mesh generation", *International Journal for Numerical Methods in Engineering*, Vol. 7, pp. 461-77.

Gordon, W.J. and Thiel, L.C. (1982), "Transfinite mappings and their application to grid generation", in Thompson, J.F. (Ed.), *Numerical Grid Generation*, North Holland.

Guillot, D. and Friedman, P.P. (1994), "A fundamental aeroservoelastic study combining unsteady CFD with adaptive control", *AIAA 94-1721*, Reno, NV.

Guillot, D. and Friedman, P.P. (1995), "Adaptive control of aeroelastic instabilities in transonic flow using CFD based loads", *Proceedings International Forum on Aeroelasticity and Structural Dynamics*, June 1995, Manchester, pp. 73.1-73.13.

Guruswamy, G.P. (1989a), "Integrated approach for active coupling of structures and fluids", *AIAA Journal*, Vol. 27 No. 6, pp. 788-93.

Guruswamy, G.P. (1990), "Unsteady aerodynamic and aeroelastic calculations for wings using Euler equations", *AIAA Journal*, Vol. 28 No. 3, pp. 461-9.

Guruswamy, G.P. and Tu, E.L. (1989b), "Transonic aeroelasticity of fighter wings with active control surfaces", *Journal of Aircraft*, Vol. 26 No. 7, pp. 682-4.

Horikawa, H. and Dowell, E.A. (1979), "An elementary explanation of the flutter mechanism with active feedback controls", *Journal of Aircraft*, Vol. 16 No. 4, pp. 225-32.

Isogai, K. (1979), "On the transonic-dip mechanism of flutter of a sweptback wing", *AIAA Journal*, Vol. 17 No. 7, pp. 793-5.

Jameson, A. (1991), "Time dependent calculations using multigrid, with applications to unsteady flows past airfoils and wings", *AIAA Paper 91-1596*, Reno, NV.

Jameson, A., Schmidt, W. and Turkel, E. (1981), "Numerical solutions of the Euler equations by finite volume methods using Runge-Kutta time stepping schemes", *AIAA-Paper No. 81-1259*, Reno, NV.

Karpel, M. (1982), "Design for active flutter suppression and gust alleviation using state-space aeroelastic modelling", *Journal of Aircraft*, Vol. 19 No. 3, pp. 221-7.

Kousen, K.A. and Bendiksen, O.O. (1988), "Non-linear aspects of the transonic aeroelastic stability problem", *AIAA Paper No. 88-2306, AIAA/ASME/ASCE/AHS 29th Structures, Structural Dynamics and Material Conference*, Denver, CO.

Kousen, K.A. and Bendiksen, O.O. (1994), "Limit cycle phenomena in computational transonic aeroelasticity", *Journal of Aircarft*, Vol. 31 No. 6, pp. 1257-63.

Kroll, N. and Jain, R.K. (1987), "Solution of two dimensional Euler equations – experience with a finite volume code", *DLR Report, DFVLR-FB 87-41*.

Librescu, L. (1965), "Aeroelastic stability of orthotropic heterogeneous thin panels in the vicinity of the flutter critical boundary (I)", *Journal de Mecanique*, Vol. 4 No. 1, pp. 51-76.

Librescu, L. (1967), "Aeroelastic stability of orthotropic heterogeneous thin panels in the vicinity of the flutter critical boundary (II)", *Journal de Mecanique*, Vol. 6 No. 1, pp. 133-52.

MacNeal Schwendler Corporation (1995), "MSC/NASTRAN aeroelastic analysis", *Seminar Notes Version 68*.

Meijer, J.J., Hounjet, M.H.L., Eussen, B.J.G. and Prananta, B.B. (1998), "NLR-TU Delft experience in unsteady aerodynamics and aeroelastic simulation applications", *AGARD Report No. 822, Numerical Unsteady Aerodynamic and Aeroelastic Simulation*, pp. 11.1-11.21.

Nissim, E. (1971), "Flutter suppression using active controls based on the concept of aerodynamic energy", *NASA TN D-6199*.

Nissim, E. (1977), "Recent advances in aerodynamic energy concept for flutter suppression and gust alleviation using active controls", *NASA TN D-8519*.

Nissim, E. (1990), "Design of control laws for flutter suppression based on the aerodynamic energy concept and comparisons with other design methods", *NASA TP 3056*.

Nissim, E. and Abel, I. (1978), "Development and application of an optimization procedure for flutter suppression using the aerodynamic energy concept", *NASA TP 1137*.

Nissim, E., Caspi, A. and Lottatti, I. (1978), "Application of the aerodynamic energy concept to flutter suppression and gust alleviation by use of active controls", *NASA TP 1137*.

Noll, T.E. (1993), "Aeroservoelasticity", in Noor, A.K. and Venneri, S.L. (Eds), *Flight-Vehicle Materials, Structures, and Dynamics-Assessment and Future Direction, Structural Dynamics and Aeroelasticity*, Chapter 3. Vol. 5, pp. 179-212.

Pak, C.G., Friedman, P.P. and Livne, E. (1991), "Transonic adaptive flutter suppression using approximate unsteady time domain aerodynamics", *AIAA-91-0986-CP*, Reno, NV.

Prananta, B.B. and Hounjet, M.H.L. (1996), "Aeroelastic simulation with advanced CFD methods in 2D and 3D transonic flow", *Symposium Unsteady Aerodynamics 1996, RAeS*, 17-18 July, London, UK.

Prananta, B.B., Hounjet, M.H.L. and Zwaan, R.J. (1995), "Thin layer Navier-Stokes solver and its application for aeroelastic analysis of an airfoil in transonic flow", *Proceedings International Forum on Aeroelasticity and Structural Dynamics*, June 1995, Manchester, pp. 1.1-1.9.

Robinson, B.A., Batina, J.T. and Yang, H.T.Y. (1991), "Aeroelastic analysis of wings using the Euler equations with s deforming mesh", *Journal of Aircraft*, Vol. 28 No. 11, pp. 781-8.

Scanlan, R.H. and Rosenbaum, R. (1951), *Introduction to the study of Aircraft Vibration and Flutter*, Macmillan, New York, NY.

Schulze, S. (1998), "Transonic aeroelastic simulation of a flexible wing section", *AGARD Report No. 822, Numerical Unsteady Aerodynamic and Aeroelastic Simulation*, pp. 10.1-11.20.

Schuster, D.M., Beran, P.S. and Huttsell, L.J. (1998), "Application of the ENS3DAE Euler/Navier-Stokes aeroelastic method", *AGARD Report No. 822, Numerical Unsteady Aerodynamic and Aeroelastic Simulation*, pp. 3.1-3.11.

Thomas, P.D. and Lombard, C.K. (1979), "Geometric conservation laws and its application to flow computations on moving grid", *AIAA Journal*, Vol. 17 No. 10, pp. 1030-7.

Whalley, R. and Ebrahimi, M. (1998), "Vibration and control of aircraft wings", *Proceedings of IMechE,* Part G, Vol. 212, pp. 353-65.

Received October 2001
Revised June 2003
Accepted August 2003

Numerical study of active shock control for transonic aerodynamics

N. Qin
Department of Mechanical Engineering, University of Sheffield, Sheffield, UK
Y. Zhu
Department of Mechanical Engineering, Brunel University, Uxbridge, UK
S.T. Shaw
College of Aeronautics, Cranfield University, Bedford, UK

Keywords *Aerodynamics, Waveforms, Flow, Differential equations, Numerical analysis*

Abstract *In this paper, the effectiveness of a number of active devices for the control of shock waves on transonic aerofoils is investigated using numerical solutions of the Reynolds-averaged Navier-Stokes equations. A brief description of the flow model and the numerical method is presented including, in particular, the boundary condition modelling and the numerical treatment for surface mass transfer. Comparisons with experimental data have been made where possible to validate the numerical study before some systematic numerical simulations for a parametric study. The effects of surface suction, blowing, and local modification of the surface contour (bump) on aerofoil aerodynamic performance have been studied extensively regarding the control location, the mass flow strength and the bump height. The numerical simulations highlight the benefits and drawbacks of the various control devices for transonic aerodynamic performance and identify the key design parameters for optimisation.*

1. Introduction

For aircraft flying at high subsonic Mach numbers, local pockets of supersonic flow develop over the lifting surfaces that are usually terminated by a shock wave. Associated with the appearance of the shock wave is an increase in drag, resulting from the entropy losses due to the shock wave itself (wave drag) and from the corresponding shock-boundary layer interaction (increase in skin friction). For large transport aircraft, control of the shock can reduce the drag substantially at the cruise condition with obvious implications for fuel economy and range. In addition, control of shock strength and buffet provides scope for noise reduction on rotorcraft and improved agility for military aircraft. The formation of shock waves, their interaction with the boundary layer and their control have been the subject of extensive research (Pearcey, 1961; Delery, 1985, 1999).

Early attempts to control the phenomena relied heavily on careful aerofoil design and the use of passive devices to re-energise the boundary layer ahead of the shock. Pearcey (1961) describes in detail the application of vane vortex

International Journal of Numerical Methods for Heat & Fluid Flow
Vol. 14 No. 4, 2004
pp. 444-466

0961-5539
DOI 10.1108/09615530410532240

generators to the problem of shock control on transonic wings. The control mechanism of vortex generators relies on the strong discrete vortices produced by the vanes to mix high-energy fluid from the freestream with the retarded fluid in the outer regions of the boundary layer. Using this technique shock induced boundary layer separation can be suppressed at the cost of a viscous drag penalty.

Alternatively, control of the shock can be achieved using the difference in pressure before and after the shock to produce natural flow circulation (Delery, 1999). This can be obtained by placing a cavity and porous plate at the foot of the shock. Experimental tests indicate that significant reductions in wave drag can be achieved due to the weakening of the shock wave by the pre-compression of the distorted displacement surface ahead of the shock position. However, in almost all of the cases studied, there is an increase in total drag due to the accompanying increase in skin friction in the control region.

While the use of passive devices for flow control has been demonstrated to improve the aerodynamic performance at the design point, the effect at off-design conditions is often detrimental. To overcome this problem, attention has recently shifted towards the use of active flow management techniques, in which the control device can be "switched on" to improve the performance locally within the flight envelope and "switched off" when not required. Two main control strategies can be identified; surface mass transfer and local modification of the surface contour.

1.1 Surface mass transfer

The basic principle underlying the control of shock boundary layer interaction is to increase the overall energy of the boundary layer, so that it is better able to negotiate the strong adverse pressure gradient across the shock. This can be achieved more readily by mass injection or mass removal. Mass removal by suction at the aerofoil surface was proposed by Regenscheit (1941) and has been studied extensively as a means of controlling shock wave-boundary layer interaction (Pearcey, 1961; Smith and Walker, 1960). Smith and Walker showed that lift could be increased by application of strong suction in the interaction region. More recently, computational studies by Qin and Zhu (1999) and Qin *et al.* (1999) have shown that application of suction in the strong adverse pressure gradient region delays separation and increases lift, however this is achieved with an increase in shock strength and increased drag.

Alternatively, momentum can be injected directly into the boundary layer through the surface of the aerofoil. This modifies the boundary layer displacement in such a way that the flow ahead of the shock must negotiate a "viscous ramp". The acceleration of the inviscid outer flow over the disturbed boundary layer ahead of the shock induces weak compression waves that soften the adverse pressure gradient experienced by the boundary layer in the interaction region. Mass injection for shock control was investigated

experimentally by Chen *et al.* (1989) and Wong (1977). Zhu (2000) and Zhu and Qin (1999) investigated the performance of slot blowing using solutions of the Navier-Stokes equations.

1.2 Local modification of the surface contour

Ashill and Fulker (1999) and Ashill *et al.* (1996) proposed devices which utilise local displacements of the aerofoil surface geometry for effective control of the shock and shock-boundary layer interaction. The surface bump can be viewed as a replacement of the "air bump" generated over the porous surface in the passive flow control case, mentioned earlier. Such devices accelerate the flow over the upstream face of the bump or ramp, inducing compression waves ahead of the shock. This results in a substantial reduction in wave drag, as the flow now negotiates a system of weaker compressions rather than a single strong normal shock. However, the presence of the device increases the momentum loss of the downstream boundary layer resulting in increased viscous drag, but this increase in skin-friction can be amply offset by the change in wave drag, leading to an overall drag reduction. Zhu (2000) performed an extensive parametric study on ramps and bumps using solutions of the Navier-Stokes equations. The shock bump can be viewed as being "active" in the sense that it may be deployed when required by active change of the local wing geometry although a fixed device may also prove to be beneficial.

2. Physical model and solution method

2.1 Governing equations

The physical problem under consideration is that of compressible viscous airflow involving shock waves, shear layers (including boundary layers) and their interactions. The mathematical model used is the two-dimensional compressible thin-layer Navier-Stokes equations. In turbulent cases, the Reynolds averaged Navier-Stokes equations are used with either the Baldwin and Lomax (1978) algebraic turbulence model or the two equation k-ω turbulence model.

The law of conservation of mass, momentum and energy over an area S bounded by a contour line l can be expressed in integral form as:

$$\frac{\partial}{\partial t}\int_S \mathbf{q}\,\mathrm{d}S + \int_l (\mathbf{H}\cdot\mathbf{n})\,\mathrm{d}l = 0 \tag{1}$$

where $\mathbf{q}$ is the conservative variable vector and $\mathbf{n}$ is the outward pointing unit vector normal to the line l. The flux tensor $\mathbf{H}$ can be written in terms of the Cartesian flux including inviscid and viscous contributions.

2.2 Surface mass transfer model

The effect of mass transfer at the wall is modelled in the Baldwin-Lomax turbulence model using the modification to the Van Driest factor proposed by Cebeci (1970).

$$A^+ = 26\left\{\exp\left(11.8v_{\mathrm{w}}^+\right) - \frac{p^+}{v_{\mathrm{w}}^+}\left[\exp\left(11.8v_{\mathrm{w}}^+\right) - 1\right]\right\}^{-1/2} \tag{2}$$

in which

$$p^+ = -\frac{(\mathrm{d}p/\mathrm{d}\xi)_{\mathrm{w}}\mu_{\mathrm{w}}}{\rho_{\mathrm{w}}^2(u_{\mathrm{w}}^*)^3} \tag{3}$$

and

$$v_{\mathrm{w}}^+ = \frac{v_{\mathrm{w}}}{u_{\mathrm{w}}^*} \tag{4}$$

$(\mathrm{d}p/\mathrm{d}\xi)_{\mathrm{w}}$ is the pressure gradient at the wall in the streamwise direction, μ_{w} is the molecular viscosity at the wall, and u_{w}^* is the friction velocity given.

2.3 Numerical method

The equations are discretised by a cell-centred finite-volume method, where numerical fluxes at each cell-cell interfaces are calculated and used to update the solution at the cell centres. Derivatives in the viscous flux at the interfaces are evaluated by creating auxiliary cells and implementing the Gauss theorem. The inviscid or convective fluxes need special attention for both shock waves and boundary layers. Shock waves are considered as discontinuities and therefore, are weak solutions of the governing equations. Conservative discretisation and approximate Riemann solvers for the convective flux evaluation provide a methodology for sharp shock capturing capability. The shock capturing method also needs to resolve the boundary layers by limiting the numerical dissipation so that the physical viscosity is properly modelled, rather than overshadowed by the numerical viscosity. Some details of the numerical aspects are given below and further details can be found in the study of Qin *et al.* (2000).

2.3.1 Approximate Riemann solver. The convective numerical flux at the cell interface is evaluated using Osher's approximate Riemann solver, which can be written as:

$$\tilde{E}_{i+\frac{1}{2},j} = \frac{1}{2}[\bar{E}(Q^{\mathrm{L}}) + \bar{E}(Q^{\mathrm{R}})] - \frac{1}{2}\int_{Q^{\mathrm{L}}}^{Q^{\mathrm{R}}}\left|\frac{\partial\bar{E}}{\partial Q}\right|\mathrm{d}Q \tag{5}$$

where $\bar{E}$ is the transformed flux in ξ direction and Q^{L}, Q^{R} the flow states on the left and right sides of the interface, respectively. The integration in the last term on the right hand side in the state space is carried out using a natural ordering of the sub-paths parallel to the eigenvectors of the flux Jacobian $\partial\bar{E}/\partial Q$.

2.3.2 High order variable extrapolation scheme. To attain higher order accuracy, the van Leer's variable extrapolation scheme is used. This means

that a linear or higher order approximation of the solution is used on each cell to calculate the interface values, rather than a piecewise constant solution.

In the equation below, Δ_- and Δ_+ are the forward and backward difference operators, respectively, and q is the column vector for the primitive variables. The parameter, κ, determines the spatial accuracy of the interpolation. Here, $\kappa = 1/3$ is chosen for a third order upwind biased scheme.

The scheme is implemented as:

$$q^{\mathrm{L}} = q_{i,j} + \left\{ \left(\frac{s}{4}\right)[(1 - \kappa s)\Delta_- + (1 + \kappa s)\Delta_+]q \right\}_{i,j} \tag{6}$$

$$q^{\mathrm{R}} = q_{i+l,j} - \left\{ \left(\frac{s}{4}\right)[(1 + \kappa s)\Delta_- + (1 - \kappa s)\Delta_+]q \right\}_{i+l,j} \tag{7}$$

Limiters need to be used in order to eliminate spurious wiggles at discontinuities, such as shock waves. In this paper, we have used a slope limiter, s as given below.

$$s = \frac{2(\Delta_+ Q)(\Delta_+ Q) + \varepsilon}{(\Delta_+ Q)^2 + (\Delta_- Q)^2 + \varepsilon}, \quad \text{where } \varepsilon \approx 10^{-7}. \tag{8}$$

The numerical time integration is carried out by either a Runge-Kutta four stage scheme or an implicit scheme (Qin *et al.*, 2000).

2.3.3 Boundary conditions. At the far field boundaries, characteristic boundary conditions are applied. In the present study of two-dimensional flows over aerofoils, this implies either a subsonic inflow or a subsonic outflow characteristic boundary condition.

At the aerofoil surface without mass transfer, a no-slip boundary condition is specified. At the surface with mass transfer, the normal velocity component is determined by

$$v_{\mathrm{w}} = \frac{C_Q \rho_\infty U_\infty c}{\sum\limits_{L_{\mathrm{suction}}} \rho_{\mathrm{w}} \Delta s}, \tag{9}$$

where the suction/blowing coefficient is defined as:

$$C_Q = \frac{\dot{m}}{\rho_\infty U_\infty c} = \frac{1}{\rho_\infty U_\infty c} \int_{s_1}^{s_2} \rho_{\mathrm{w}} v_{\mathrm{w}} \, \mathrm{d}s. \tag{10}$$

For the relatively weak suction and blowing considered in this study, the viscous boundary conditions can reasonably be applied. In addition to the above normal velocity component, the tangential velocity component is determined from the suction/blowing inclination angle.

2.4 Force calculation and system consideration

In the case of suction, mass is removed from the flow external to the aerofoil surface. Obviously, the same amount of mass has to be ejected somewhere from the aerofoil into the main flow to conserve mass. From the conservation of momentum, or Newton's second law, there will be an additional force acting on the aerofoil in addition to the pressure and skin-friction forces acting on the external surfaces of the aerofoil. However, this force will depend on how the sucked air is ejected into the main flow. These include factors such as where to eject, at what direction and at what speed. The ejection itself in turn will also influence the flowfield and, therefore, pressure and skin-friction forces on the aerofoil. Furthermore, for practical application, it is also necessary to consider the cost for the installation of the pipeline system inside the aircraft, the power required to run the pump and the losses in the pipe system. This highlights the importance of considering the system as a whole for successful implementation of flow control devices involving surface mass transfer.

The current study is limited to the study of the effect of suction control on the flowfield as an isolated factor. Therefore, system integration issues are not discussed further in this paper, although they would obviously have to be investigated in a more general study. It is assumed that the air sucked from the mainstream is ejected out through a pipeline normal to the aerofoil cross section at the pipe exit. Therefore, there is no contribution to the lift and drag forces from the ejected air. Similarly, for the cases of blowing, the present studies are limited only to isolated effects of blowing on the forces acting on the aerofoil.

3. Validation

3.1 NACA64A010 aerofoil with suction

The NACA64A010 aerofoil was tested extensively by Smith and Walker (1960) at transonic conditions with surface suction downstream of the hinge line of the trailing-edge flap. It is a 10 per cent c thick aerofoil, symmetric if the trailing edge flap is not deflected. The NACA six-series wing section was designated for profiles with substantial portion of laminar boundary layers due to favourable pressure gradient.

The flow conditions investigated in the experiment correspond a Reynolds number of 2.9 million based on aerofoil chord for a range of Mach numbers from 0.70 to 0.84 and a range of angles of incidence from -1 to 4°. Both suction parameter and flap angle were varied in the experiments.

The flow conditions chosen for computation were $M_\infty = 0.78$, $\alpha = 0.5°$ and $\mathrm{Re} = 2.9 \times 10^6$ corresponding to one of the wind tunnel experimental conditions. In the experiment, the suction region was located between 69 and 72.5 per cent of chord length from the leading edge, which is downstream of the shock position without suction. The suction coefficient was 0.00225, with a flap deflection of 1°. The suction angle β was chosen to be 84° to the aerofoil surface,

since the suction is normal to the chord line. The flow was assumed to be fully turbulent due to the high Reynolds number in the experiment. The 189×65 grid around the aerofoil is shown in Figure 1 with clustering near the surface, the leading and trailing edges, and the shock wave location.

For quantitative comparison, the pressure distributions from both computation and experiment, with and without suction, are compared in Figure 2. These figures show that the computation is in good agreement with the experimental data in both cases. The effect of the surface suction is captured quite well. The Mach contours (Figure 3) show the effects of suction on increasing the shock strength.

Table I shows the comparison of the lift and drag coefficients for the NACA64A010 aerofoil cases for a fixed incidence. The comparison between the experimental data and the computed results is reasonably good. However, in comparison with a rather good agreement in pressure distribution, the discrepancies are a little disappointing, which may be due to the grid sensitivity of the computation or the uncertainties in the experiments.

One can observe from the results that, for the present suction control downstream of the shock wave, both lift and drag are increased with a more substantial increase in the lift. These increases can be explained in the

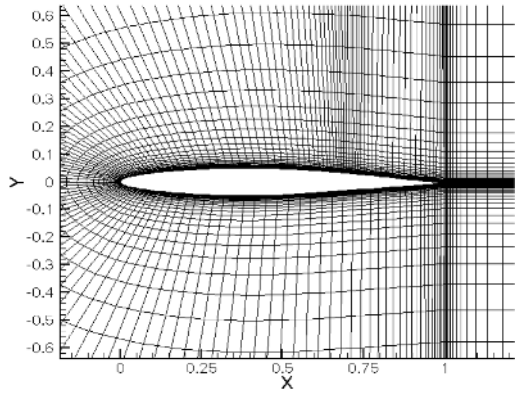

Figure 1.
NACA64A010 case grid

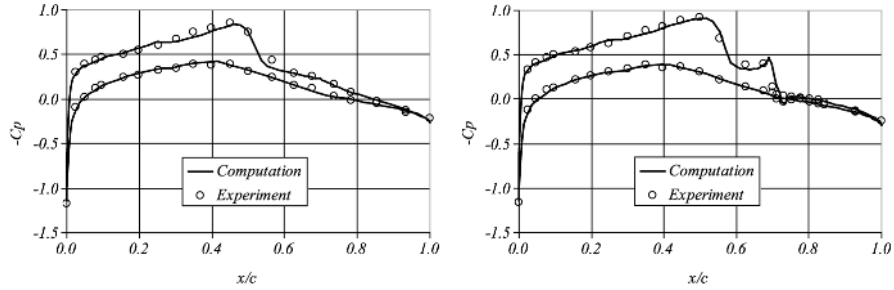

Figure 2.
Surface pressure distribution around NACA64A010 aerofoil: no suction (left) and with suction (right)

following analyses of the suction's effects on the boundary layers and the skin-friction.

Figure 4 shows the predicted boundary-layer displacement thickness, δ^*, both with and without suction. It shows that the displacement thickness has a sudden increase under the shock wave. Upstream of the shock, suction has little effect on the displacement thickness, except that the shock is displaced slightly downstream. Immediately downstream of the shock, the displacement thickness is increased by the suction, but only after a small distance further downstream this drops down below the corresponding "no-suction" value on

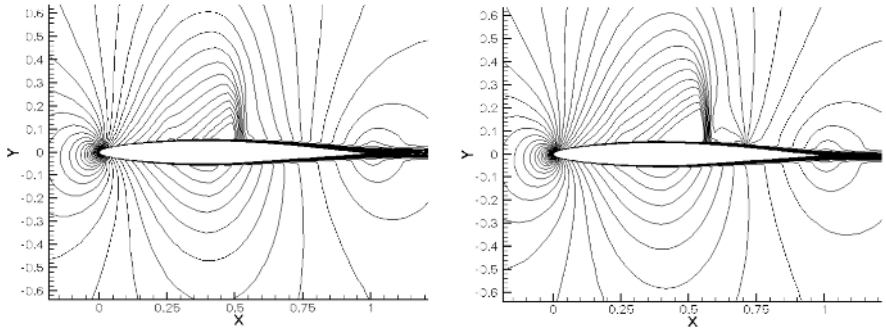

Figure 3.
Mach contours around NACA64A010 aerofoil: no suction (left) and with suction (right)

	C_L	C_D
No suction		
Experiment	0.20	0.013
Computation	0.2166	0.0111
With suction		
Experiment	0.24	0.014
Computation	0.2795	0.0138

Table I.
NACA64A010 aerofoil lift and drag coefficient without and with suction

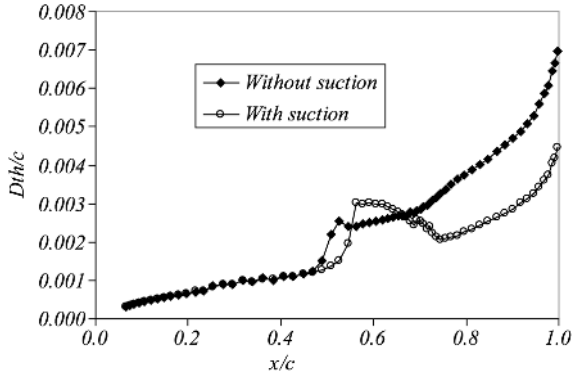

Figure 4.
Computed boundary-layer displacement thickness on NACA64A010 aerofoil

the last third of the aerofoil downstream of the suction region. This indicates that the suction increases the effective camber of the aerofoil and therefore the lift, shown earlier.

The skin-friction distributions on the upper surface of the aerofoil are plotted in Figure 5, for the cases with and without suction. Very high skin-friction over the suction region can be clearly observed, contributing to the skin-friction drag. This higher local skin-friction is due to the higher velocity gradient at the surface as part of the low energy flow in the boundary layer has been sucked in. The local high skin-friction was also observed in experimental tests, e.g. Ashill *et al.* (1996). For both cases, the skin-friction reduces to a value near zero, locally due to the effect of a strong adverse pressure distribution created by the shock wave. Since suction actually strengthens the shock in this case, the skin-friction becomes closer to the incipient separation condition with suction. This indicates that suction downstream can promote shock-induced separation locally (bubble type).

Note that in practical applications and experiments, suction control is mostly achieved through sucking through porous surfaces. In the simulation, this is modelled in the macro scale by distributed surface mass transfer as implemented in the numerical boundary condition (equation (10)). Strictly speaking, the skin-friction is only for the solid part of the porous surface. However, the porosity is practically rather small and therefore the local skin-friction can be reasonably represented by the local shear stress over the solid surface.

3.2 RAE5243 aerofoil with suction

The RAE5243 aerofoil with a maximum thickness-chord ratio of 14 per cent is a natural laminar flow (NLF) aerofoil with a pressure distribution on the upper surface having a favourable pressure gradient upstream of the shock at about 55 per cent chord. The aerofoil has a very slight blunt trailing edge (0.5 per cent c). The flow conditions were $M_\infty = 0.6799$, $\mathrm{Re} = 18.68 \times 10^6$, corresponding to the wind tunnel experiment by Fulker and Simmons (1994). The angles of incidence measured in the experiment for both cases (with and without suction) to be studied are $\alpha = 0.77°$. The suction region is located at 45-46 per cent chord

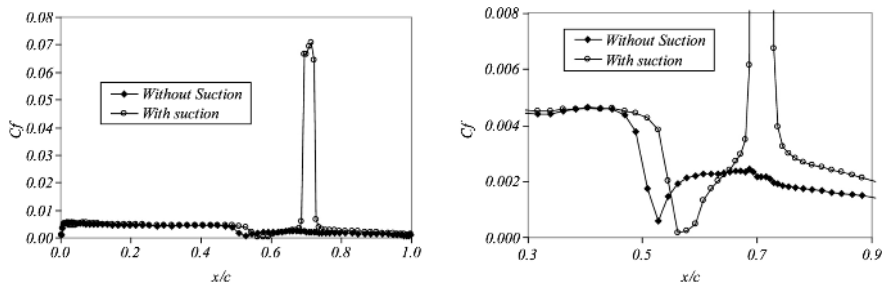

Figure 5.
Computed skin-friction distributions on NACA64A010 aerofoil: overview (left) and local (right)

length with suction coefficient $C_Q = 9 \times 10^{-5}$ and the suction angle $\beta = 89°$. It is a case of weak suction about 10 per cent chord upstream of the shock wave.

Initial studies revealed that a proper treatment of the trailing edge in the numerical model is crucial for the accurate prediction of aerofoil lift and drag. A multi-block solution approach has to be adopted to provide a precise simulation of the trailing edge flow although the bluntness is only 0.5 per cent chord. The grid is generated in two blocks, one around the aerofoil (189×65) and the other in the wake region (25×47) that is behind the blunt trailing edge as shown in Figure 6.

Computational and experimental pressure distributions for the RAE5243 aerofoil are shown in Figure 7, for cases without and with suction, respectively, at the same experimental normal force coefficient. The figures show that the computation is in excellent agreement with the experimental data for both cases. Note that the trailing edge pressure is slightly open due to the slight bluntness of the trailing edge.

Table II shows the lift and drag comparison between the experiment and the computation. One can observe an excellent agreement in lift while some discrepancies in drag remains. Unlike the previous case, the effects of suction are rather small, reducing both very slightly.

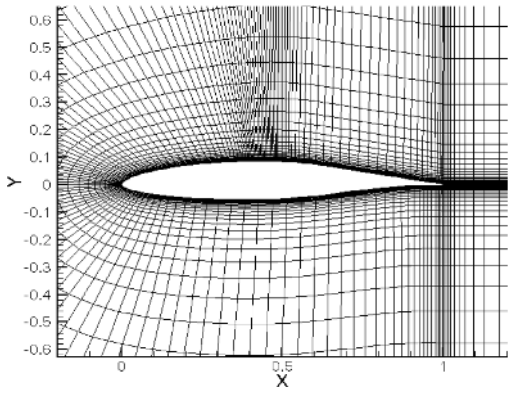

Figure 6.
RAE5243 two-block grid

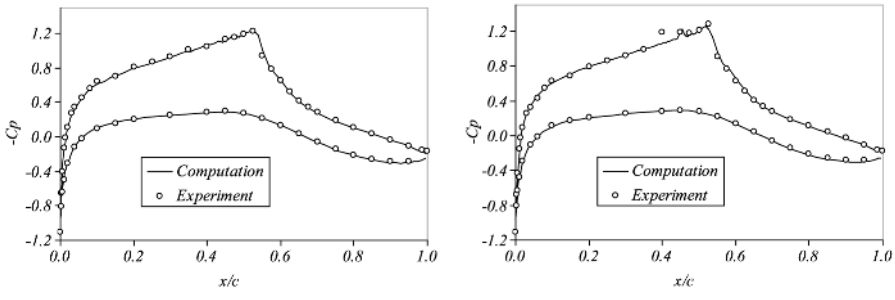

Figure 7.
Surface pressure distribution around RAE5243 aerofoil: no suction (left), suction (right)

Figure 8 shows the Mach number contours for the case with suction. The perturbation of the flowfield by suction can be seen ahead of the shock wave. However, this does not have an effect on reducing the shock's strength. This is also evident in the surface pressure distribution (Figure 7).

3.3 RAE5225 aerofoil with surface bump

The RAE5225 aerofoil is a supercritical aerofoil with a maximum thickness to chord ratio of 14 per cent. The characteristics of a supercritical aerofoil are quite different from those of an NLF aerofoil. While the NFL aerofoil tries to maintain a favourable pressure gradient to stabilise the boundary layer, the supercritical aerofoil is designed to delay the drag rise Mach number, which results in a much earlier onset of an adverse pressure gradient on the aerofoil.

The flow conditions chosen for the computational test were $M_\infty = 0.734$ and $\mathrm{Re} = 6.1 \times 10^6$ with transition fixed at 5 per cent chord on both upper and lower surfaces corresponding to the wind tunnel experiment by Fulker *et al.* (1993). A bump of circular-arc shape and of maximum height (relative to the upper surface of the datum aerofoil) of 0.175 per cent chord was fixed at 40-60 per cent chord position on the upper surface as shown in Figure 9 along with the grid.

Figure 10 shows the computational and the experimental pressure distributions for the RAE5225 aerofoil with 0.175 per cent chord length height bump at 40-60 per cent chord length from the leading edge at 2.95°

Table II.
RAE5243 aerofoil lift and drag coefficient without and with suction

	C_L	C_D
No suction		
Experiment	0.5154	0.0877
Computation	0.5142	0.0980
With suction		
Experiment	0.5146	0.0830
Computation	0.5144	0.0968

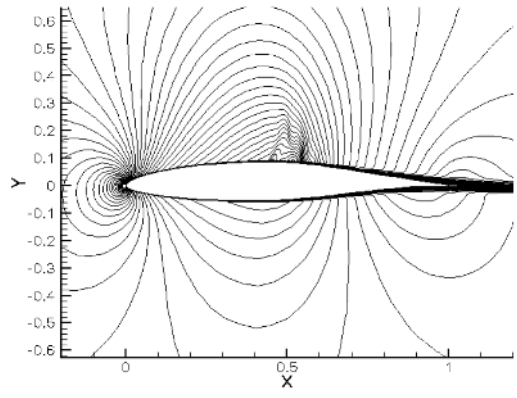

Figure 8.
Mach contours for RAE5243 suction case

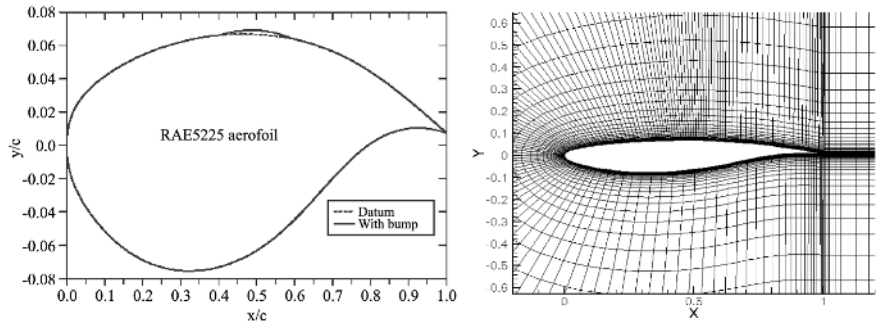

Figure 9.
RAE5225 aerofoil with bump and grid

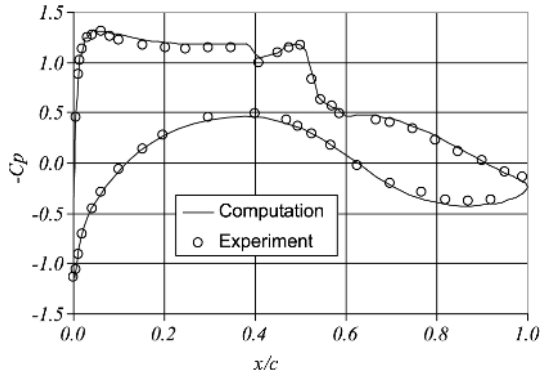

Figure 10.
Surface pressure distribution around RAE5225 aerofoil with surface bump

incidence. It shows that the computation is in good agreement with the measurement.

Table III shows the comparison of the computation with the experimental data for the given incidence of 2.95°. The difference between the lift, between the experiment and computation may come from the wall interference of the wind tunnel test, which generally has an effect of reducing the effective incidence of the aerofoil (Zhu, 2000). A more useful comparison for the force coefficient data is to compare the drag for a given lift coefficient. A reasonable comparison can then be achieved.

Figure 11 shows the flowfield in Mach number contours. It is clear that the compression waves ahead of the shock wave have the effect of reducing the shock strength and therefore the wave drag. The mechanism of the drag reduction is due to the reduction of the shock strength and the wave drag. It is

	C_L	C_D
Experiment	0.7200	0.0150
Computation	0.7523	0.0172

Table III.
RAE5225 aerofoil lift and drag coefficient with bump

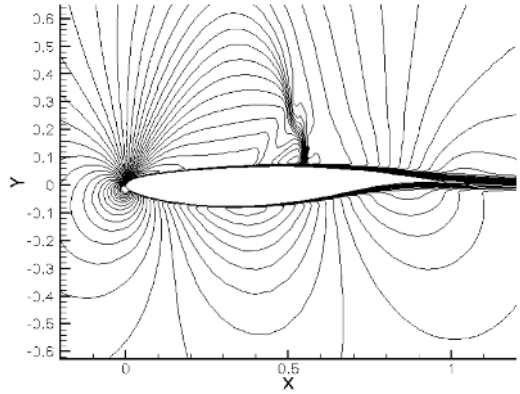

Figure 11.
Mach contours for RAE5225 aerofoil bump case

therefore concluded that the control is achieved through the inviscid flow behaviour rather than the viscous effects. Indeed, Euler solutions indicate that a more significant drag reduction can be achieved and the viscous effects tend to moderate such reductions and therefore the effectiveness of the bump control device.

4. Parametric studies

In this section, we study the influence of some parameters in the various control devices in order to identify the key ones affecting the aerodynamic performance of the aerofoil.

4.1 Suction

The effect of the position of suction regions relative to the shock position is shown in Figures 12 and 13 for the RAE5225 aerofoil case, where $M_\infty = 0.734$, $\alpha = 3°$ (for Figure 12 only), $C_Q = 5 \times 10^{-4}$. Apparently, suction changes the local pressure significantly. The aerofoil performance can be improved by suction located at or downstream of the shock position. However, when the

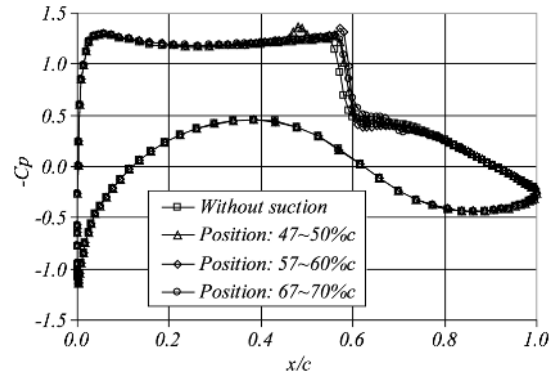

Figure 12.
Pressure distribution around RAE5225 aerofoil – effect of suction position at $M_\infty = 0.734$, $\alpha = 3°$

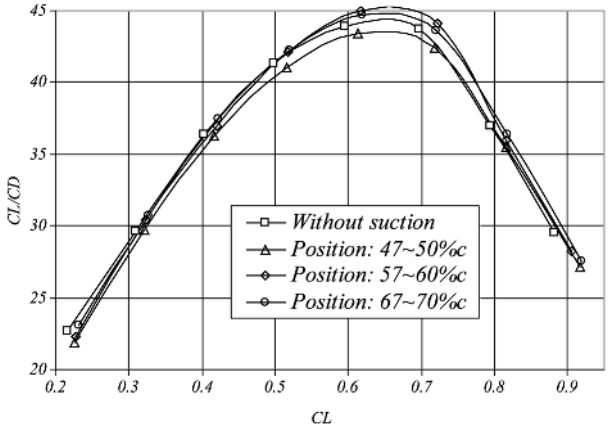

Figure 13.
Lift-drag ratio for RAE5225 aerofoil – effect of suction position

suction position is upstream of the shock position, the aerodynamic performance is degraded (Figure 13). This behaviour is consistent with the detailed analysis in Section 3. For a given incidence, suction downstream of the shock location has the effect of increasing both lift and friction drag but the L/D ratio is generally improved due to a more significant increase in lift. However, suction upstream of the shock wave has a relatively small effect on the lift but with a similar skin-friction penalty, which explains the degradation of the aerodynamic performance.

The suction strength also has a strong effect on the aerofoil surface pressure distribution and the L/D ratio. Figures 14 and 15 show the results for $M_\infty = 0.734$, $\alpha = 3°$ (for Figure 14 only) and suction position at 67-70 per cent c, downstream of the shock. Increasingly, stronger suction has an effect of pulling the shock further downstream (Figure 14) and shifting the L/D ratio curve to the right into the higher lift region (Figure 15). This indicates that while stronger

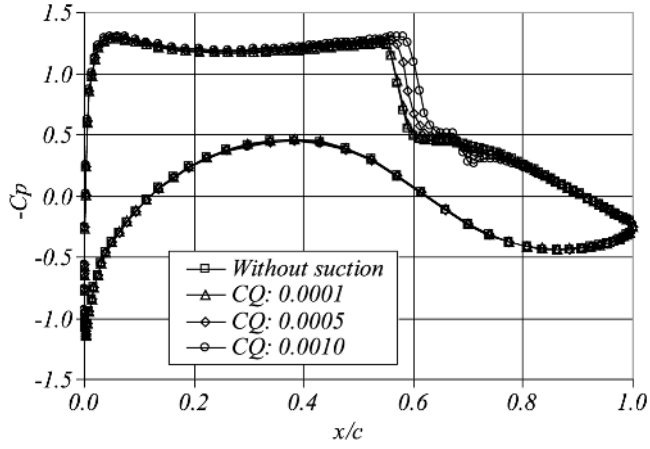

Figure 14.
Pressure distribution around RAE5225 aerofoil – effect of suction mass flow at M_∞=0.734, $\alpha = 3°$

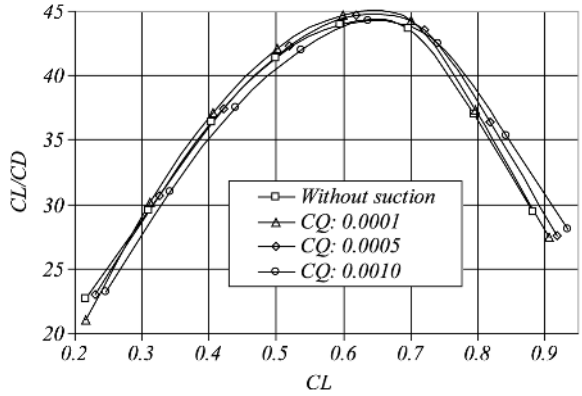

Figure 15.
Lift-drag ratio for RAE5225 aerofoil – effect of suction mass flow

suction can improve the performance in the high lift region, the performance in the low lift region can be degraded. For the relatively weaker suction, there is only a slight improvement around $C_L = 0.65$. The results indicate a strong dependency of the suction strength design on the design lift condition.

4.2 Blowing

As shown in Section 3, a local bump can improve the aerodynamic performance by moderating the shock wave on the upper surface of the aerofoil at transonic speeds. Similar effects may also be expected by blowing at the foot of the shock wave. It can thicken the local boundary layer so as to increase the boundary layer displacement. This in turn forms an effective local air ramp to moderate the shock wave by pre-compression (isentropic).

Three blowing positions, 45-50 per cent chord, 50-55 per cent chord, and 55-60 per cent chord near the foot of the shock wave, were selected to investigate the effects of the blowing position. The case is for $M_\infty = 0.68$, $C_Q = 4 \times 10^{-4}$, and the inclined blowing angle $\beta = 15°$. Figure 16 shows the aerofoil pressure distributions for three blowing positions at the same

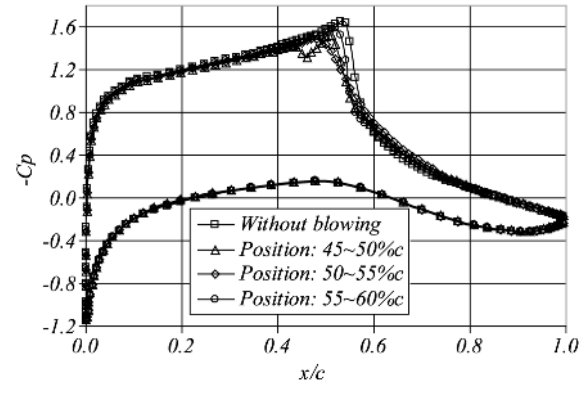

Figure 16.
Surface pressure distribution around RAE5243 aerofoil – effect of blowing position

incidence $\alpha = 3°$. It clearly shows that blowing changes the pressure distribution. The shock strength is reduced, and the shock wave moves upstream, the effect being particularly apparent when blowing is right underneath the shock wave. It is interesting to see that blowing slightly downstream of the original shock wave can also slightly reduce the shock strength by moving it upstream. Blowing at 50-55 per cent under the shock (at ~55 per cent) is most effective in reducing the shock strength with a similar effect as the solid bump.

Figures 17 and 18 show the boundary layer behaviour and the skin-friction with and without blowing. The blowing case is for the 50-55 per cent c position. They show that blowing increases the boundary-layer thickness and reduces the skin-friction drag for a fixed incidence. These are both due to the effect of

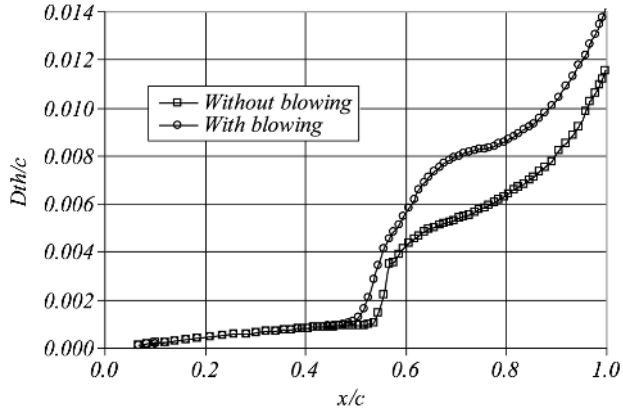

Figure 17.
Computed boundary-layer displacement thickness for RAE5243 aerofoil

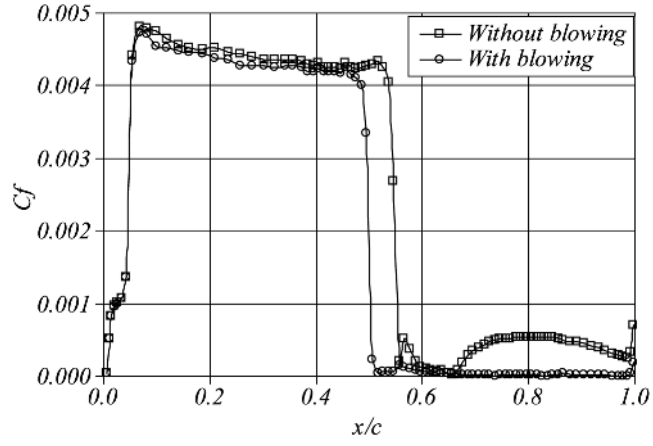

Figure 18.
Computed skin-friction for RAE5243 aerofoil

the blowing pushing the boundary layer outward, reducing the velocity gradient at the wall in the process.

Figure 19 shows the lift-drag ratio plotted against lift coefficient for the blowing cases, which reveals that the blowing reduces the lift-drag ratio significantly over the whole range of the lift coefficients studied, although the shock wave is weakened. The behaviour is in total contract with the suction cases, where the shock strength is increased with an increase in the lift-drag ratio.

The effects of the blowing angle were studied by investigating three inclination angles, 5, 15 and 45° with other parameters fixed. The angle is defined as the angle between the blowing flow direction and the local aerofoil surface tangent. The results were hardly distinguishable. This indicates that in the present investigation, the blowing control effects are from the effects of the mass flow injection and the boundary layer thickness change instead of the effects of the momentum injection (as often used to energize the boundary layer).

Blowing further away from the shock wave has also been studied for the RAE5225 aerofoil. It was found that appropriate blowing could increase the lift-drag ratio. Blowing near the trailing edge with small blowing coefficient indicated some improvement in L/D for the RAE5225 aerofoil. The blowing position in these calculations was taken to be near the trailing edge at 97.5-98 per cent chord, with the blowing coefficients $C_Q = 0.0005$ and 0.001 and $\beta = 5°$.

Figure 20 shows the pressure distributions for the RAE5225 aerofoil for $\alpha = 3°$ with blowing near the trailing edge. It shows that blowing far away the shock wave weakly can also weaken the shock wave, and move the shock wave upstream slightly. Figure 21 shows the lift-drag ratio against lift coefficient for the corresponding cases. It shows that weak blowing near trailing edge with

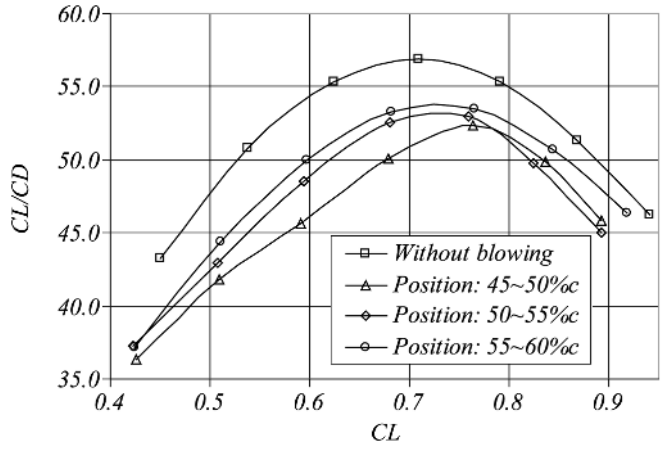

Figure 19.
Lift-drag ratio for RAE5243 aerofoil – effect of blowing position

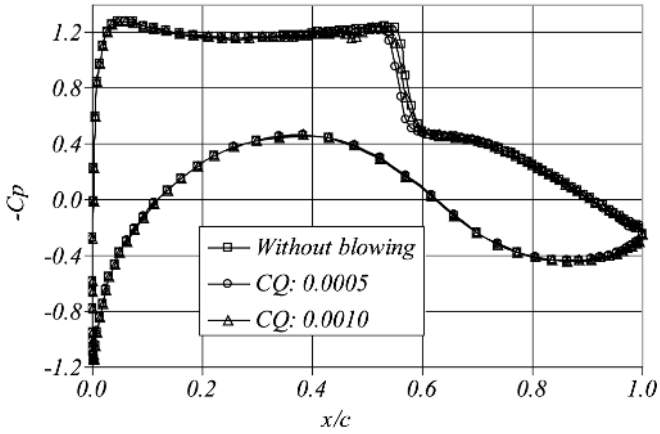

Figure 20.
Pressure distribution for RAE5225 – near trailing edge blowing

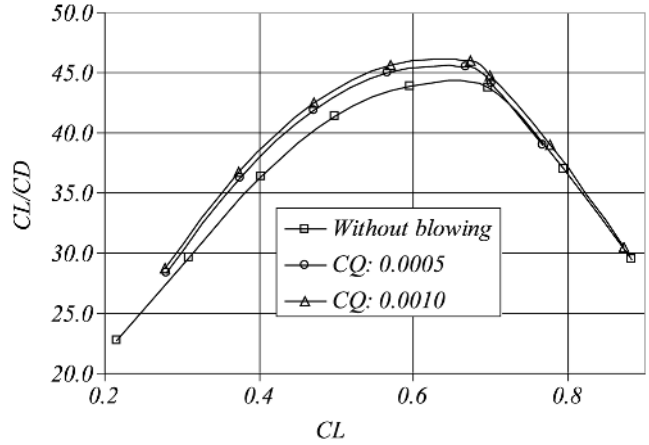

Figure 21.
Lift-drag ratio for RAE5225 – near trailing edge blowing

a small angle to the aerofoil surface can improve the aerodynamic performance of the aerofoil for $C_L < 0.7$. It is most beneficial in the maximum lift-drag ratio region. There is very little improvement for higher lift region. Unlike the suction and bump cases, this improvement is related to the modification of the trailing edge flow (similar to the jet flap for increasing circulation) rather than the near shock behaviour.

4.3 Surface bumps

Figure 22 shows the RAE5243 aerofoil datum section with 0.175 per cent chord high bump at 40-60 per cent chord. The bump is made of a circular arc, similar to Fulker *et al.* (1993), on top of the original datum aerofoil. The flow conditions are $M_\infty = 0.68$, $\mathrm{Re} = 19 \times 10^6$ with transition fixed at 5 per cent chord on both upper and lower surfaces. Figures 23 and 24 show the pressure distributions

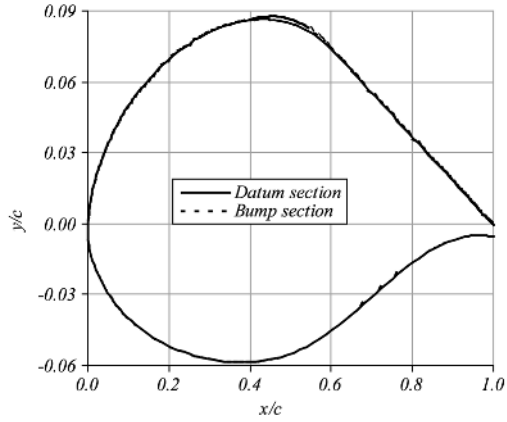

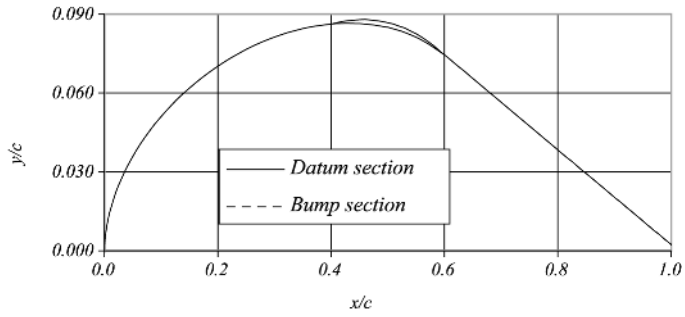

Figure 22.
RAE5243 aerofoil with bump

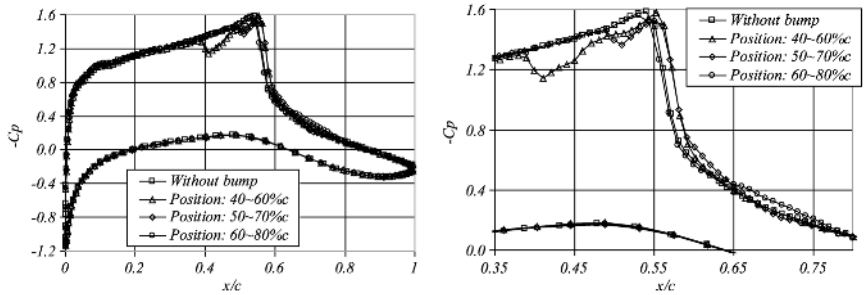

Figure 23.
Surface pressure distribution around RAE5243 aerofoil – effect of bump position

for the RAE5243 aerofoil at an angle of incidence $\alpha = 2.5°$, for three bump positions. The figure demonstrates the sensitivity of the pressure distribution to the bump location. When placed with its crest close to the shock the bump can serve well the purpose of reducing shock strength and hence wave drag.

It is particularly interesting to examine the effect of bump positions on L/D for a wide range of lift coefficients, as shown in Figure 24. This figure shows

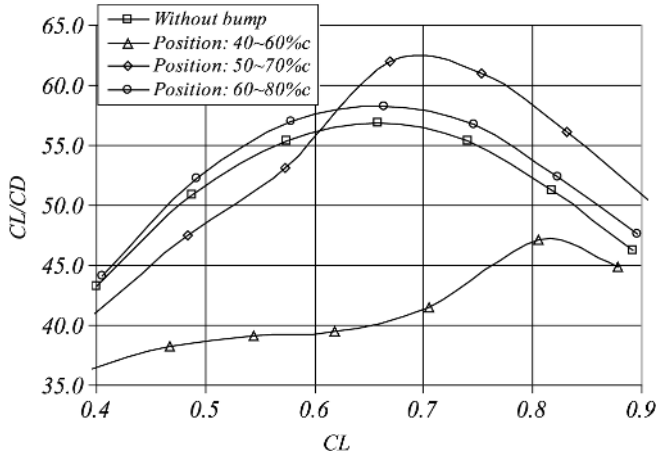

Figure 24.
Lift-drag ratio for RAE5243 aerofoil – effect of bump position

that a bump at 40-60 per cent chord (ahead of the shock) reduces the L/D ratio for the whole lift range considered, while a bump at 60-80 per cent chord (downstream the shock) increases the lift-drag ratio moderately over the same lift range. A bump at 50-70 per cent chord (under the original shock) increases the lift-to-drag ratio significantly for the high lift region but degrades the performance of the original aerofoil at the lower lift region (0.4-0.6). There is an interesting crossover at $C_L = 0.6$. Note that for NLF aerofoil the shock position is almost fixed at 55 per cent for the incidence (lift) range considered.

Another important parameter is the bump height as shown in Figure 25. This shows results for three different bump heights located at 50-70 per cent for the RAE5243 aerofoil. It demonstrates that the higher bump gives more significant gain at higher lift range and, at the same time, more degradation at the lower lift range. This can be attributed to the fact that higher lift cases

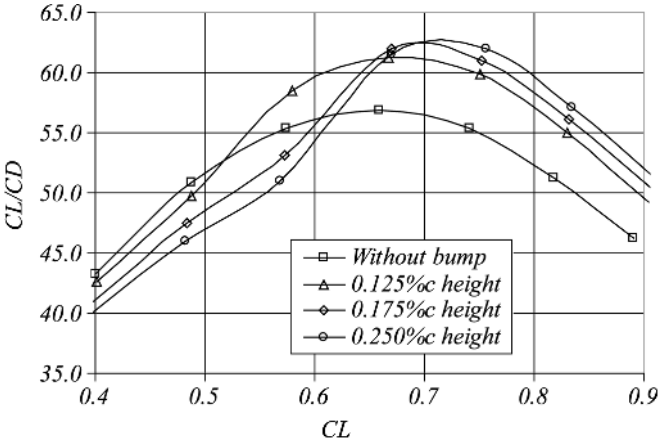

Figure 25.
Lift-drag ratio for RAE5243 aerofoil – effect of bump height (position: 50-70 per cent)

correspond to stronger shock waves. Higher bumps have a stronger effect in reducing the shock strength and therefore, the wave drag. We can also conclude from the results that the higher bump (0.25 per cent c) serves better as a device for delaying drag rise or buffet onset. However, for a wider operational range for beneficial effects, a lower bump (0.125 per cent c) may be better for both drag reduction and buffet delay.

5. Conclusions

A numerical study is presented based on a high-resolution solution of the Reynolds averaged Navier-Stokes equations using an algebraic turbulence model with surface mass transfer effects. Some validation work has been presented against available experimental data regarding surface pressure distribution and lift and drag coefficients.

A parametric study of shock control for transonic aerofoil flows using suction, blowing, and local changes to the local surface contour has been carried out.

Suction generally improves the aerofoil transonic aerodynamic performance through an increased lift-drag ratio. It achieves this, despite the tendency for suction to increase shock strength, while moving the shock wave downstream (indicative of an increase in wave drag). It was noted that the associated increase in lift is generally more than that in drag. However, as a shock control device, suction is ineffective in reducing the shock strength and the associated wave drag.

Blowing ahead of the shock was found to reduce the shock strength significantly by creating a λ-shock structure or a compression fan. Blowing downstream of the shock can also move the shock upstream and reduce the shock strength slightly. The angle of inclination of blowing has shown little effect on the control, with smaller angles showing a slightly better performance. Drag polars indicate that blowing near the foot of the shock (either just upstream or just downstream of the shock) does not provide a reduction in drag for a given lift. However, weak blowing near the trailing edge can improve the performance before the drag rise.

Bumps placed in the vicinity of the shock reduce shock strength and wave drag significantly with no substantial increase in viscous drag. The result is a significant increase in lift/drag ratio and a delay in buffet onset, confirming previous studies at DERA. The physical mechanisms for the improvement are highlighted by the flowfield simulations and provides further insight into the nature of the local flow interactions in the region of the shock. This provides the basis for optimising the bump arrangement. Among the three devices investigated, the bump is the only one that achieves a total drag reduction at a given lift condition through weakening the shock wave strength, giving the best performance. It can serve as a fixed device to an existing aerofoil or as an adaptive deployable device when required. Since the lower bump has a

relatively wider operational range, it may be used as a fixed device. On the other hand, active bumps may be adapted for best performance for the given operational point. Potential ideas for such bumps may be achieved by recent development in shape memory alloy diaphragms, piezoelectric patches and small inflatable blisters.

In practical applications, for all the shock control devices, the benefits need to be weighed against the cost associated with the devices through system integration studies. In this regard, controls involving surface mass transfer (both suction and blowing) may be more complicated and therefore more costly as compared to the bumps.

References

Ashill, P.R. and Fulker, J.L. (1999), "A review of flow control research at DERA", Private Communication.

Ashill, P.R., Fulker, J.L., Simmons, M.J. and Gaudet, I.M. (1996), "A review of research at DRA on active and passive control of shock waves", *Proceedings of the International Congress in Aeronautical Sciences*.

Baldwin, B.S. and Lomax, H. (1978), "Thin layer approximation and algebraic model for separated turbulent flows", AIAA Paper 78-0257.

Cebeci, T. (1970), "Behaviour of turbulent flow near a porous wall with pressure gradient", *AIAA J.*, Vol. 8 No. 12, pp. 2152-6.

Chen, C.L., Chow, C.Y., William, R. and Holst, T.L. (1989), "Computation of viscous transonic flow over porous airfoils", *J. Aircraft*, Vol. 26 No. 12, pp. 1067-75.

Delery, J.M. (1985), "Shock wave/turbulent boundary layer interaction and its control", *Progress in Aerospace Sciences*, Vol. 22 No. 4, pp. 209-80.

Delery, J.M. (1999), "Shock phenomena in high speed aerodynamics: still a source of major concern", *Aeronautical J.*, Vol. 103 No. 1019, pp. 19-34.

Fulker, J.L., Ashill, P.R. and Simmons, M.J. (1993), "Study of simulated active control of shock waves on aerofoil sections", DRA Technical Report TR93025.

Fulker, J.L. and Simmons, M.J. (1994), "An experimental study of shock control methods", RA/AS/HWA/TR94007/1.

Pearcey, H.H. (1961), "Shock-induced separation and its prevention by design and boundary layer control", *Boundary Layer and Flow Control*, Pergamon Press, New York, NY, Vol. 2.

Qin, N., Ludlow, D.K. and Shaw, S.T. (2000), "A matrix-free preconditioned Newton/GMRES method for unsteady Navier Stokes solutions", *International Journal of Numerical Methods in Fluids*, Vol. 33 No. 3, pp. 223-48.

Qin, N. and Zhu, Y. (1999), "Inclined suction and blowing for shock control at transonic speeds", *Proceedings of the 22nd International Symposium on Shockwaves*, London.

Qin, N., Zhu, Y. and Poll, D.I.A.P. (1999), "Surface suction on aerofoil aerodynamic characteristics at transonic speeds", *Proceedings of IMechE Part.G J. Aeronautical Engineering* Vol. 212, pp. 339-51.

Regenscheit, B. (1941), "Drag reduction by suction of the boundary layer separated behind shockwave formation and high Mach numbers", NACA TM 1168.

Smith, D.W. and Walker, J.H. (1960), "Test of an area suction flap on a NACA64A010 airfoil at high subsonic speeds", NASA TN D 310.

Wong, W.F. (1977), "Application of boundary layer blowing to suppress strong shock induced separation in a supersonic inlet", AIAA Paper 77-147.

Zhu, Y. (2000), "Computational study of shock control at transonic speed", PhD thesis, College of Aeronautics, Cranfield University.

Zhu, Y. and Qin, N. (1999), "Inclined slot blowing on transonic aerodynamics performance of the RAE 5243 and RAE 5225 aerofoils", CoA Report 9906, Cranfield University.

Further reading

Amitay, M. and Honohan, A. (1997), "Modification of the aerodynamic characteristics of bluff bodies using fluidic actuators", AIAA 97-2004.

Osher, S. and Solomon, F. (1982), "Upwind difference schemes for hyperbolic systems of conservation laws", *Mathematics of Computation*, Vol. 38 No. 158, pp. 339-74.

Dynamic modeling in large-eddy simulation of turbulent channel flow

Investigation of two-dimensional versus three-dimensional test filtering

Received April 2002
Revised August 2003
Accepted October 2003

Jessica Gullbrand
Center for Turbulence Research, Stanford University, Stanford, California, USA

Keywords *Simulation, Turbulent flow, Eddy currents, Tests and testing*

Abstract *Large-eddy simulation (LES) of a turbulent channel flow is performed using different subfilter-scale (SFS) models and test filter functions. The SFS models used are the dynamic Smagorinsky model (DSM) and the dynamic mixed model (DMM). The DMM is a linear combination between the scale-similarity model and the DSM. The test filter functions investigated are the sharp cut-off (in spectral space) and smooth filter that is commutative up to fourth-order. The filters are applied either in the homogeneous directions or in all three spatial directions. The governing equations are discretized using a fourth-order energy-conserving finite-difference scheme. The influence from the test filter function and the SFS model on the LES results are investigated and the effect of two-dimensional versus three-dimensional test filtering are investigated. The study shows that the combination of SFS model and filter function highly influences the computational results; even the effect on the zeroth-order moment is large.*

Introduction

In large-eddy simulation (LES), a low-pass filter is applied to the governing equations. This filtering procedure divides the flow field into resolved scale motions and subfilter-scale (SFS) motions. The SFS motions consist of scales that are damped by the filter function used and/or scales that are smaller than the smallest resolved length scale (Carati *et al.*, 2001; Gullbrand and Chow, 2003).

The most commonly used LES approach is the implicitly filtered approach. In implicitly filtered LES, the computational grid and the discretization operators are considered as the filtering of the governing equations. The advantage is that the procedure requires no implementation of filters. The drawback is that the filter function used cannot be determined, which can make SFS modeling more difficult.

The author wishes to thank Prof Oleg V. Vasliyev for providing the channel flow code and Prof Parviz Moin for his helpful discussions. He also thanks Fotini K. Chow for commenting on this paper.

International Journal of Numerical Methods for Heat & Fluid Flow
Vol. 14 No. 4, 2004
pp. 467-492

0961-5539
DOI 10.1108/09615530410532259

An alternative to implicitly filtered LES is to use explicit filtering. In the explicit approach, a filter function is chosen and applied in the simulations. Recently this approach has gained increased interest from the research community (Gullbrand, 2002; Gullbrand and Chow, 2003; Stolz *et al.*, 2001; Winckelmans *et al.*, 2001). The explicit filtering approach seems to be very promising as computer capacity is increasing, but further investigations are needed to make it applicable to flow fields of engineering interest.

In this paper, the implicitly filtered LES approach is used, since the study is aimed at investigating dynamic modeling for flow fields of engineering interest. The flow field investigated is the turbulent channel flow. The channel flow is a simplified turbulent flow field, but it serves as a good test case since it is well documented (Moser *et al.*, 1999) and has only one inhomogeneous direction. Traditionally, in channel flow simulations, the homogeneous directions of the flow field are used in the procedure for determining the contribution from the dynamic model. Flow fields of engineering interest usually involve complex geometries where there is no homogeneous direction. Therefore, an alternative procedure must be used where the three dimensionality of the flow field needs to be considered in the modeling procedure. This paper presents a detailed investigation of the effects of using a three-dimensional test filter in the dynamic procedure, as well as the effect of using the same filter as a local averaging of the dynamic coefficient to prevent numerical instability. The difficulty of creating a model for the resolved SFS motions in implicitly filtered LES is also addressed.

First, three-dimensional test filtering in the dynamic modeling of the SFS stresses is investigated. The influence of test filtering in the inhomogeneous direction is important to determine since, its effect also enters into the predicted results of more complex flow fields. The impact from three-dimensional test filtering is studied by comparing the results to those predicted by using two-dimensional filtering. To determine appropriate filter functions for filtering in inhomogeneous directions, special care is needed to avoid introducing commutation errors into the simulations (Ghosal, 1995; Ghosal and Moin, 1995). Therefore, a general theory for constructing discrete filters that commute up to desired order was developed by Vasilyev *et al.* (1998). To minimize the commutation error in the inhomogeneous direction, a filter function that is commutative to at least the same order as the numerical scheme used is needed. The effect of these high-order commutative filter functions on the LES results still needs to be determined. Earlier investigations on the influence of different filter functions on LES results focused on two-dimensional test filters which do not need to be commutative (Lund and Kaltenbach, 1995; Najjar and Tafti, 1996; Piomelli *et al.*, 1988; Sarghini *et al.*, 1999). A commutative test filter function is used in the simulations presented in this study to examine the effect of three-dimensional filtering without introducing commutation errors. Furthermore, the effect from the commutative

filters on the SFS stresses needs to be determined. This is investigated by performing a simulation applying a commonly used test filter function (the sharp cut-off filter) and comparing the results to those obtained using the commutative filter function.

Two dynamic SFS models are applied in this study: the dynamic Smagorinsky model (DSM) by Germano *et al.* (1991) and the dynamic mixed model (DMM). The DMM used here is a linear combination of the scale-similarity model (SSM) by Liu *et al.* (1994) and the DSM. In DSM, a test filter function is used to determine the dynamic coefficient, and the coefficient is traditionally averaged in the homogeneous directions of the channel flow. The test filter function commonly used is a sharp cut-off filter (in spectral space) in the homogeneous directions. Since a sharp cut-off filter is difficult to apply in more general flow cases, the influence of using a smooth test filter needs to be determined. Furthermore, the test filter function chosen is a reflection of the assumption of the implicit filter function. The dynamic procedure is based upon a similarity assumption which requires the test filter function to be similar to the implicit filter (Carati and Eijnden, 1997). The difficulty with the implicitly filtered LES approach is that the shape of the implicit filter function is unknown and therefore, an appropriate test filter function cannot be chosen. In the explicitly filtered LES approach, the filter function applied to the governing equations is known and the resolved SFS part can therefore be reconstructed (Gullbrand and Chow, 2003). This is not applicable in implicitly filtered LES and therefore a model is needed for the resolved SFS part. Note that an SFS model for the resolved stresses is only valid when assuming the implicit filter function to be a smooth filter function. When applying a sharp cut-off filter, all the motions that are larger than the cut-off length-scale are assumed to be resolved. In this paper, the SSM by Liu *et al.* (1994) is used as a first approximation of an appropriate SFS model for the resolved SFS part.

Finally, the effect of the averaging procedure applied to the dynamic model coefficient is evaluated. In DSM, the model coefficient is calculated dynamically during the entire simulation. However, the coefficient value may vary rapidly in the computational domain leading to numerical instability. To avoid this problem, Germano *et al.* (1991) suggested averaging the model coefficient in the homogeneous directions of the channel flow. This averaging procedure may not be feasible in flow fields of engineering interest and the coefficient may need to be averaged locally. Ghosal *et al.* (1995) proposed a dynamic localization model to avoid the problem. However, this is a rather complicated method, which involves solving an additional integral equation. Therefore, in the investigation presented, a simple approach is examined where the dynamic coefficient is averaged locally with the test filter function used. It is an easy approach which does not require implementation of any additional filter function or procedure. This averaging procedure was earlier proposed by

Zang *et al.* (1993), and applied to a recirculating flow field. However, the influence on the LES results from the locally averaged and homogeneously averaged model coefficient need to be determined.

The simulations presented in this paper are performed with a fourth-order finite-difference scheme in addition to using a fourth-order commutative filter function. The SFS models typically use information from the smallest resolved length scales to model the SFS contribution. It is therefore of great importance, that these resolved length scales are captured accurately. This requires that the numerical error of the scheme be sufficiently small and thereby the use of high-order discretization and a high-order commutative filter function. All the LES results are compared to DNS data by Moser *et al.* (1999).

Governing equations

In LES, the governing equations are filtered in space. The low-pass filter function G is applied to the flow variable f

$$\bar{f}(x, \Delta, t) = \int_{-\infty}^{\infty} G(x, x', \Delta) f(x', t)\, \mathrm{d}x' \tag{1}$$

where Δ is the filter width.

The governing equations for incompressible flows are the filtered continuity equation and the Navier-Stokes, written as

$$\frac{\partial \bar{u}_i}{\partial x_i} = 0 \tag{2}$$

$$\frac{\partial \bar{u}_i}{\partial t} + \frac{\partial \bar{u}_i \bar{u}_j}{\partial x_j} = -\frac{\partial \bar{p}}{\partial x_i} + \frac{1}{\mathrm{Re}_\tau} \frac{\partial^2 \bar{u}_i}{\partial x_j^2} - \frac{\partial \tau_{ij}}{\partial x_j} \tag{3}$$

where u_i denotes velocity vector, p pressure, and Re_τ the Reynolds number based upon the friction velocity and channel half-width. τ_{ij} is the SFS stress tensor defined as $\tau_{ij} = \overline{u_i u_j} - \bar{u}_i \bar{u}_j$.

The SFS stress tensor includes the turbulence motions from scales that are damped by the filter function and/or scales that are smaller than the grid size resolution (Carati *et al.*, 2001). In implicitly filtered LES, both damped turbulence motions and unresolved motions need to be modeled. This is done with SFS models.

Subfilter-scale models

Since implicitly filtered LES are used in the simulations presented, both resolved and unresolved SFS stresses need to be modeled. On the other hand, in explicitly filtered LES, the resolved SFS stresses can be reconstructed by an inverse filtering procedure. Different approximations in the inverse filtering

procedure have been proposed in the literature (Chow and Street, 2002; Stolz *et al.*, 2001), and one of the models that can be obtained from this procedure is the SSM by Bardina *et al.* (1980). In the explicit filtering approach, even though a model is used for the resolved SFS stresses, the unresolved SFS stresses must still be modeled. The unresolved SFS stresses contain motions that are smaller than the smallest resolved length scale. This term is usually denoted as the sub-grid scale (SGS) stresses. Note that the SSM by Bardina *et al.* (1980) requires the use of explicit filtering.

The SSM by Liu *et al.* (1994) is used in these simulations as the model for the resolved SFS stresses, while the DSM is used for the unresolved stresses. Since an SFS model cannot be reconstructed for the resolved stresses, the SSM by Liu *et al.* (1994) is chosen as it is similar to the model by Bardina *et al.* (1980). Both models are based upon a similarity assumption, but the model by Liu *et al.* (1994) uses information from length scales larger than in the model by Bardina *et al.* (1980). The SSM by Liu *et al.* is written as $\left(\widehat{\bar{u}_i\bar{u}_j} - \widehat{\bar{u}}_i\widehat{\bar{u}}_j\right)$, where the tophat symbol ($\widehat{\ }$) denotes filtering with a test filter function with larger filter width than the implicit filter. The total expression for the SFS stresses with both scale-similarity term and DSM is

$$\tau_{ij} = \widehat{\bar{u}_i\bar{u}_j} - \widehat{\bar{u}}_i\widehat{\bar{u}}_j - 2(C_s\Delta)^2|\bar{S}|\bar{S}_{ij},$$

where C_s is the dynamic model coefficient in the DSM and S_{ij}, is the strain rate tensor. A coefficient could be placed in front of the scale-similarity term, however this is not investigated in this work and is left for future studies.

The dynamic procedure in the DSM uses the same test filter function as in the SSM by Liu *et al.* (1994) to determine the model coefficient. In the simulations, it is the $(C_s\Delta)^2$ term that is calculated dynamically. The advantage of solving for $(C_s\Delta)^2$ instead of only C_s is to avoid the ambiguity in determining the filter width used in the DSM when stretched meshes are used (Scotti *et al.*, 1996). When solving for $(C_s\Delta)^2$, it is only the ratio between the test filter width and the implicit filter that is employed. The least-square approximation by Lilly (1992) is used to solve the six independent equations to obtain one model coefficient. To simplify the notation used in this paper, the $(C_s\Delta)^2$ term is hereafter denoted as C.

To avoid numerical instabilities, the dynamic model coefficient is usually averaged in the homogeneous directions of the channel flow (Germano *et al.*, 1991). This averaging procedure, denoted with $\langle C\rangle$, is compared to a locally averaged procedure. The local averaging is performed by filtering the coefficient using the test filter function ($\hat{C}$). This local averaging was earlier used by Zang *et al.* (1993), but they used another test filter function in their simulations. The local averaging of the coefficient is of interest when more complex flow fields are considered, and to the authors knowledge there has been no comparisons between the two methods in order to determine the impact on the LES results from each averaging procedure.

In the simulations, the total eddy viscosity is clipped, if the value from the DSM is largely negative. The criteria used is the same as applied by Zang *et al.* (1993) that prevents the total eddy viscosity from becoming negative:

$$\nu_{\text{total}} \leq \nu_{\text{DSM}} + \nu_{\text{molecular}}$$

Filters

Two test filters, i.e. one fourth-order commutative filter function and one sharp cut-off filter, are used in the simulations. The simulations are performed using a fourth-order finite-difference scheme and therefore, in order to minimize the commutation error, a filter function that is at least commutative up to fourth-order is needed. In the channel flow case, it is only in the inhomogeneous direction of the flow that a commutation error might be introduced. The fourth-order commutative filter was developed using the theory proposed by Vasilyev *et al.* (1998).

The two test filter functions are shown in spectral space in Figure 1. In physical space, the discrete fourth-order commutative filter is

$$\hat{\phi}_i = -\frac{1}{32}\phi_{i-3} + \frac{9}{32}\phi_{i-1} + \frac{1}{2}\phi_i + \frac{9}{32}\phi_{i+1} - \frac{1}{32}\phi_{i+3}, \tag{5}$$

where the filter weights for $\phi_{i\pm2}$ are zero.

In the simulations, the filter functions are employed only when calculating the SFS contribution. A test filter is used in the dynamic procedure of the DSM and when determining the contribution from the SSM part (Liu *et al.*, 1994). The commutative filter function is used both in two-dimensional test filter cases and three-dimensional ones. The sharp cut-off filter is used only in the two-dimensional filter studies. Note that when using the sharp cut-off filter in the DMM, the contribution from the SSM vanishes and only the contribution

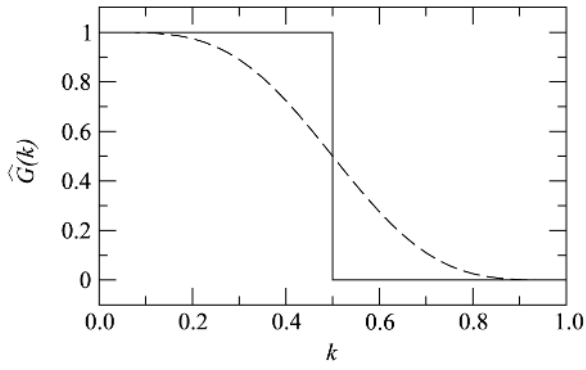

Figure 1.
Filter function $\hat{G}(k)$ as a function of the wavenumber k

from the DSM remains. Therefore, the DMM is not used with the sharp cut-off filter.

The ratio between the test filter width and the computational cell size is chosen to be $\Delta_{test}/\Delta_{grid} = 2$. This is the value that was recommended by Germano *et al.* (1991) for the test filter width in the DSM. For the fourth-order commutative filter function, the filter width is determined by where $\hat{G}(k) = 0.5$ and as seen in Figure 1, $k\Delta/\pi = 0.5$ at this location. This corresponds to an effective filter width of 2Δ (Lund, 1997).

Solution algorithm

The space derivatives in the governing equations are discretized using a fourth-order finite-difference scheme on a staggered grid. The convective terms are discretized in a skew-symmetric form to ensure conservation of turbulent kinetic energy (Morinishi *et al.*, 1998; Vasilyev, 2000). The equations are integrated in time with the third-order Runge-Kutta scheme described by Spalart *et al.* (1991). The diffusion terms in the wall-normal direction are treated implicitly with the Crank-Nicolson scheme to ease the constraint on the time step of the scheme. The splitting method of Dukowicz and Dvinsky (1992) is used to enforce the solenoidal condition. The resulting discrete Poisson equation of pressure is solved using a penta-diagonal direct matrix solver in the wall-normal direction and a discrete Fourier transform in the homogeneous/periodic directions. Periodic boundary conditions are applied in the streamwise and spanwise directions, while no slip conditions are applied at the walls. A fixed mean pressure gradient is used in the streamwise direction. An evaluation of the fourth-order energy-conserving scheme and a comparison with a second-order conservative scheme are reported by Gullbrand (2000) and Gullbrand and Chow (2003).

Turbulent channel flow simulations

The Reynolds number of the turbulent channel flow is $\mathrm{Re}_\tau = 395$ and the computational domain is $(2\pi h, 2h, \pi h)$ in the streamwise (x), wall-normal (y) and spanwise (z) directions, respectively. A computational grid resolution of (36, 37, 36) is used. The grid is stretched in the wall-normal (j) direction according to

$$y(j) = \frac{\tanh\left(\gamma\left(\frac{2j}{N_2} - 1\right)\right)}{\tanh(\gamma)}, \quad j = 0, \ldots, N_2 \tag{6}$$

where N_2 is the number of grid points in the j-direction and γ is the stretching parameter. In the simulations, $\gamma = 2.75$ is used. The grid resolution corresponds to $\Delta x^+ = 69$, $0.5 \leq \Delta y^+ \leq 56$ and $\Delta z^+ = 34$ when normalized with the friction velocity and the kinematic viscosity. This resolution is very coarse and is near the limit of where LES is expected to perform well. However,

the coarse resolution is chosen because of the additional challenge it brings to the SFS models. As the resolution decreases, an increased emphasis is put on the models as an increasing portion of the energy spectrum is not resolved and therefore has to be modeled. In flow fields of engineering interest, fine resolution is often not feasible due to the complexity of the flow and the long computational times associated with LES. By using a coarse computational grid, larger emphasis is also put on the numerical scheme. A statistically stationary solution is obtained after 60 dimensionless time units and thereafter, statistics are sampled during 30 time units. The time is normalized by the friction velocity and the channel half-width. The statistics are compared to the unfiltered DNS data of Moser *et al.* (1999). The LES results are averaged in time and in the homogeneous direction if not stated otherwise.

In order to verify that the results presented in this study is not an artifact of too coarse grid resolution, the same simulations were performed using a resolution of (64, 49, 48). This resolution is a quarter of the DNS resolution in each spatial direction. The same trends were observed in the LES results for both resolutions; (36, 37, 36) and (64, 49, 48). However, the differences in the results predicted by the different models were smaller on the finer grid resolution. As the resolution increases more length scales are resolved and therefore, less influence is expected from the models on the LES results.

Results

The LES results predicted by the DSM and the DMM are presented in this section. The test filtering is performed in two or three dimensions. The sharp cut-off filter is used only for the two-dimensional test filtering, while the fourth-order commutative filter function is applied in both two and three dimensions. The LES results are compared to DNS data for mean velocity profiles and reduced (deviatoric) turbulence intensities. Note that these turbulence intensities are adjusted by removing the trace from each tensor component, as discussed by Winckelmans *et al.* (2002). The values predicted by the SFS models are compared between the different simulations for the dynamic model coefficient, eddy viscosity, and modeled shear stress.

Two-dimensional test filtering

In this section, the test filter is applied only in the homogeneous directions (x, z). Both sharp cut-off filter and fourth-order commutative filter have been used to calculate the contribution from the SFS models.

The DSM versus the DMM. As seen in Figure 2, the mean velocity profiles predicted by the DSM with the sharp cut-off test filter and the DMM (commutative test filter) are relatively close to the the DNS data. The mean velocities predicted by the LES all over-predict the velocity in the log-law region. The difference between the DMM and the DSM with the sharp cut-off

filter is small. The largest over-prediction is predicted by the DSM with the commutative filter.

While the DSM with the sharp cut-off filter predicts the best velocity profile, the reduced turbulence intensities predicted by the DMM are closer to the DNS data (Figure 3). The absolute value of the intensities predicted by the LES are

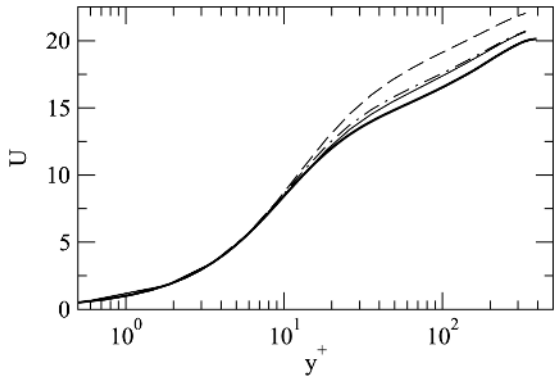

Note: —— : DNS data, —— : DSM using sharp cutoff filter, — — — : DSM using fourth-order commutative filter and · — · — : DMM using fourth-order commutative filter

Figure 2.
Mean velocity profiles using two-dimensional test filtering and grid resolution (36, 37, 36)

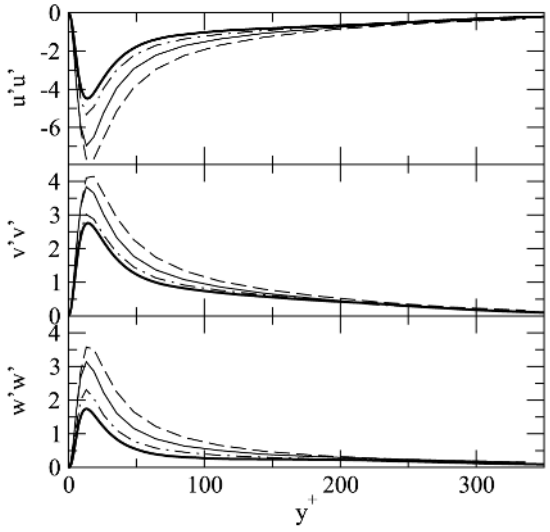

Note: —— : DNS data, —— : DSM using sharp cutoff filter, — — — : DSM using fourth-order commutative filter and · — · — : DMM using fourth-order commutative filter

Figure 3.
Reduced turbulence intensities in streamwise $u'u'$, wall-normal $v'v'$, and spanwise $w'w'$ directions using two-dimensional test filtering and grid resolution (36, 37, 36)

all larger than the DNS results. As shown for the mean velocity profiles, the worst results are predicted by the DSM when used with the commutative filter function.

Figure 4 shows the dynamic model coefficient predicted by the DSM. The value of the coefficient increases as the test filter function changes from the sharp cut-off filter to the commutative filter. Using the commutative test filter, the DSM predicts smaller coefficient values when used in combination with the SSM. The same trend as observed for $\langle C \rangle$ is also seen for the eddy viscosity, $\nu_{\mathrm{DSM}} = C|\bar{S}|$ (Figure 5). This indicates that the absolute value of the strain rate

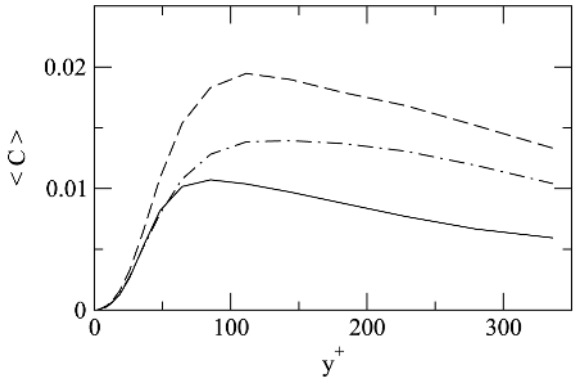

Note: —— : DSM using sharp cutoff filter, — — — : DSM using fourth-order commutative filter and · — · — : DMM using fourth-order commutative filter

Figure 4.
Model parameter $\langle C \rangle$ predicted by the DSM using two-dimensional test filtering and grid resolution (36, 37, 36)

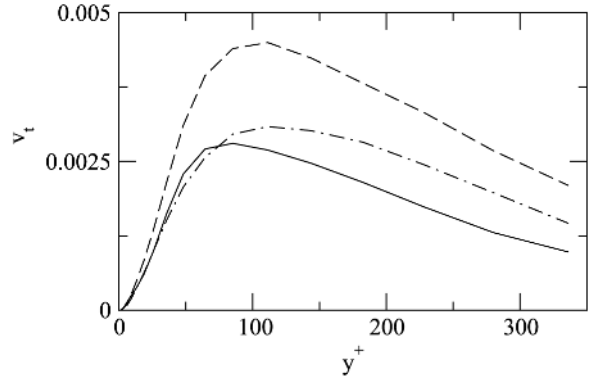

Note: —— : DSM using sharp cutoff filter, — — — : DSM using fourth-order commutative filter and · — · — : DMM using fourth-order commutative filter

Figure 5.
Eddy viscosity ν_t predicted by the DSM using two-dimensional test filtering and grid resolution (36, 37, 36)

is not very different in the simulations. Therefore, the increased eddy viscosity predicted by the DSM when used with the commutative test filter seems to be mainly an effect of the increased value of the model coefficient.

Figure 6 shows the modeled shear stress τ_{12}, where index 1 denotes the x-direction and 2 the y-direction. The DMM predicts the largest modeled shear stress and the SSM portion of the model contributes with the largest stress. Actually, the SSM stress is more than twice as large as the DSM contribution. When the DSM is used alone, the predicted shear stress increases, when used with the commutative test filter compared to the sharp cut-off filter.

The results presented in this section, indicate that the increased over-prediction of the mean velocity profile and reduced turbulence intensities predicted by the DSM are a result of the increased value of the dynamic model coefficient. The model coefficient increases when the test filter is smooth compared to when the sharp cut-off filter is used. The SSM seems to be a relatively good model of the resolved SFS stresses in the DMM. When studying the turbulence intensities, the DMM even predicts results better than the DSM when used with the sharp cut-off filter, despite the fact that the DSM with the sharp cut-off filter is a model that is known to predict good results in the channel flow simulations.

The DSM: homogeneous averaging versus local averaging. In this section, the concept of averaging the model coefficient in the DSM in either the homogeneous directions or locally (by using the test filter function) is studied. When averaging in the homogeneous directions, the computational data in the whole plane (streamwise and spanwise directions) are used. By using the test filter, only the closest computational grid points are used in the averaging procedure. The stencil of the filter function determines the number of grid

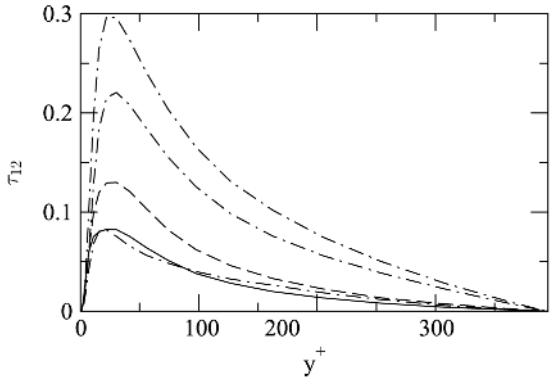

Note: —— : DSM using sharp cutoff filter, – – – : DSM using fourth-order commutative filter and · — · — · : DMM using fourth-order commutative filter. Lower curve: DSM contribution, middle curve: SSM contribution, and upper curve: total contribution

Figure 6.
Modeled shear stress τ_{12} using two-dimensional test filtering and grid resolution (36, 37, 36)

points that are involved in the averaging. Therefore, the test filter function results in a local averaging of the model coefficient. The term local averaging is used to describe the model coefficient averaged with the test filter function. The study is performed for the DSM when used with the commutative filter function only.

The comparison of the mean velocity profiles for the two different averaging procedures is shown in Figure 7. The mean velocity profile in the log-law region improves significantly when the local averaging of the model coefficient is applied. The results from using the local averaging are comparable to the ones predicted using the sharp cut-off filter shown in Figure 2.

The reduced turbulence intensities are also improved when local averaging is used compared to the homogeneous averaging (Figure 8). The peak value of the turbulence intensities when using local averaging are comparable to the DMM results in Figure 3, and both DSM local averaging and DMM are close to the DNS predictions. However, the peaks of the turbulence intensities are broader for the DSM with local averaging than for the DMM results.

An instantaneous spanwise profile of the model coefficient C in the DSM is shown in Figure 9. The data is calculated *a priori* from an instantaneous flow field where no SFS models have been used. Large fluctuations in the value of the model coefficient and large negative values may result in numerical instabilities. Therefore, it is of interest to reduce the peaks or smooth them out. The two procedures investigated here are filtering the coefficient using the test filter function or averaging the coefficient in the homogeneous directions. The results from both procedures is seen in Figure 9. In the simulations, small negative values are allowed while large negative values are clipped.

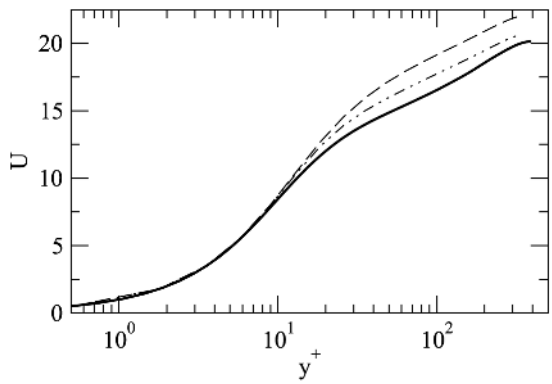

Note: —— : DNS data, – – – : DSM using fourth-order commutative filter and homogenous averaging, and ·–·–· : DSM using fourth-order commutative filter and local averaging

Figure 7.
Mean velocity profiles using two-dimensional test filtering and grid resolution (36, 37, 36)

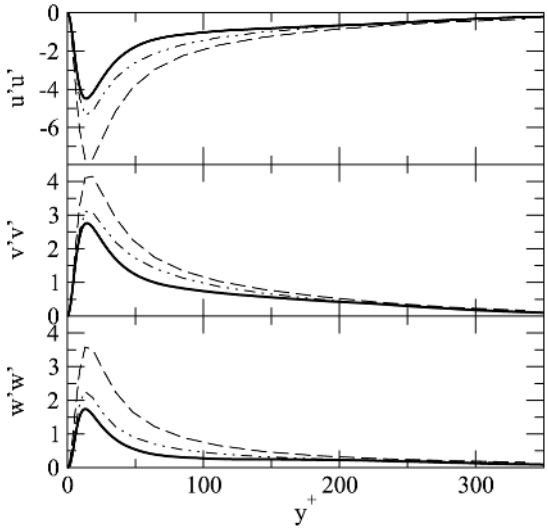

Note: ——— : DNS data, – – – : DSM using fourth-order commutative filter and homogenous averaging, and – · – · – : DSM using fourth-order commutative filter and local averaging

Figure 8.
Reduced turbulence intensities in streamwise $u'u'$, wall-normal $v'v'$ and spanwise $w'w'$ directions using two-dimensional test filtering and grid resolution (36, 37, 36)

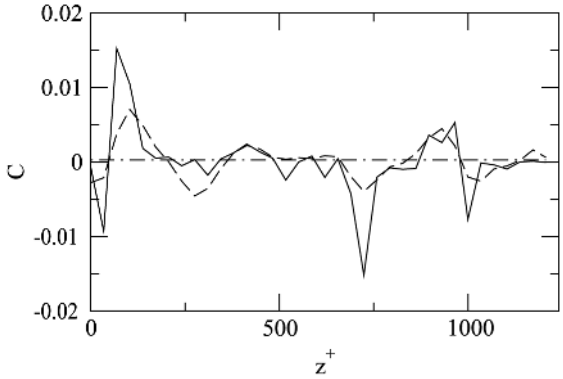

Note: ——— : C: DSM data using fourth-order commutative filter before averaging, – – – : $\widehat{C}$: DSM data using fourth-order commutative filter and local averaging, and – · – · – : $<\widehat{C}>$: DSM data using fourth-order commutative filter and homogeneous averaging ($<\widehat{C}>$=0.00028)

Figure 9.
Model parameter C in the DSM calculated from an instantaneous flow field in the center of the domain using two-dimensional test filtering and grid resolution (36, 37, 36)

The clipping value is chosen to be $-1/\mathrm{Re}_\tau$, in order to avoid negative dissipation in the momentum equations.

Variations of locally averaged model coefficient is shown in a horizontal cross-section in Figure 10. Regions of positive and negative values of the model coefficient are observed.

The value of the predicted eddy viscosity is larger when using local averaging (Figure 11). In the center part of the channel flow ($y^+ > 100$), an almost constant relation is observed between the two eddy viscosities, however, the curves deviate from each other close to the wall.

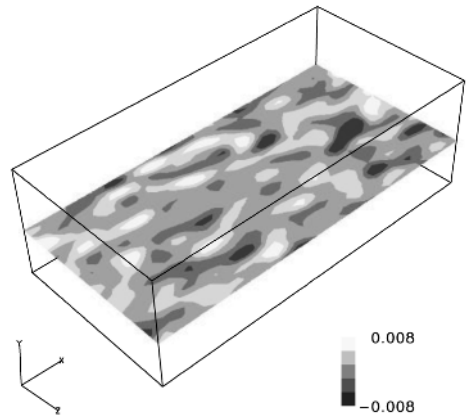

Note: Black contour represents negative values and white positive ones

Figure 10.
Model parameter C in the DSM in the center plane of the domain calculated from an instantaneous flow field using two-dimensional test filtering and grid resolution (36, 37, 36)

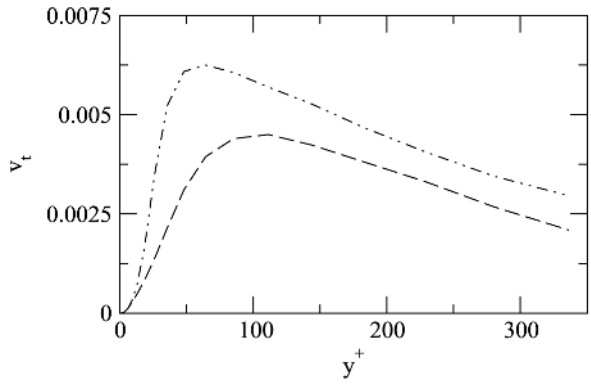

Note: − − − : DSM using fourth-order commutative filter and homogenous averaging, and ·−·−· : DSM using fourth-order commutative filter and local averaging

Figure 11.
Eddy viscosity ν_t from the DSM using two-dimensional test filtering and grid resolution (36, 37, 36)

Figure 12 shows a larger peak value of the modeled SFS shear stress when local averaging is used compared to the homogeneously averaged one. Otherwise, the shape of the curves are very similar.

By allowing the model coefficient to fluctuate in the plane, the locally averaged DSM predicts the mean velocity profile and peak values of turbulence intensities that are very similar to what is predicted by the DMM. Larger local fluctuations are introduced by the local averaging that seem to be comparable to the DMM results, even though the modeled shear stresses are very different between the two simulations.

Three-dimensional filtering

In this section, three-dimensional test filtering using a fourth-order commutative filter function is applied when calculating the SFS stresses.

The DSM versus the DMM. As shown in Figure 13, the DSM with the three-dimensional test filtering over-predicts the mean velocity profile in the log-law region, while the DMM is unable to capture the log-law behavior in the center of the channel. The mean velocity profile predicted by the DMM starts to deviate from the log-law just below $y^+ = 100$. This is due to the three-dimensional filtering of the SSM, indicating that the resolution in the wall-normal direction is too coarse in the center of the channel for the SSM. When the grid resolution is doubled in the wall-normal direction, the results are improved greatly. The results are also improved if the coarse grid resolution is used and the test filtering of the SSM is performed only in the two homogeneous directions. Using the finer grid resolution in the wall-normal direction or the two-dimensional filtering of the SSM, the mean velocity profile is very close to the DNS results. Since the LES results are expected to improve,

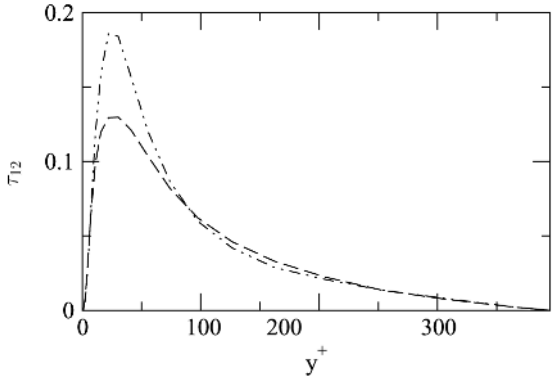

Note: – – – : DSM using fourth-order commutative filter and homogenous averaging, and – · · · – : DSM using fourth-order commutative filter and local averaging

Figure 12.
Modeled shear stress τ_{12} using two-dimensional test filtering and grid resolution (36, 37, 36)

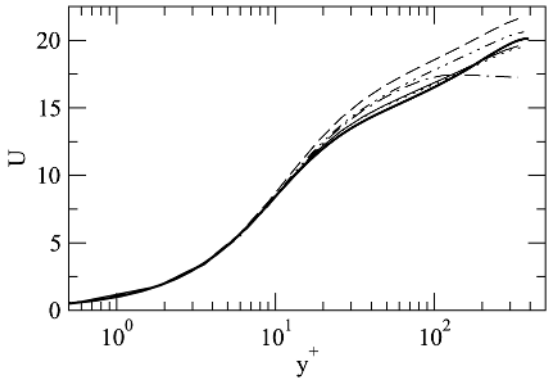

Note: ——— : DNS data, ——— : DMM using fourth-order commutative two-dimensional filtering of SSM and three-dimensional filtering of DSM and grid resolution (36,37,36), ····· : DMM using fourth-order commutative filter and grid resolution (36,73,36), – – – : DSM using fourth-order commutative filter and grid resolution (36,37,36), ·—·—· : DMM using fourth-order commutative filter and grid resolution (36,37,36), and ·–··–· : DSM using fourth-order commutative filter and grid resolution (36,73,36)

Figure 13.
Mean velocity profiles using three-dimensional test filtering

as the resolution is refined, the DSM with the finer grid resolution in the wall-normal direction is performed for comparison purposes. The DSM using the finer grid predicts a mean velocity profile that is similar to the DMM on the coarser grid in the near wall region. The DSM shows no difficulties in capturing the log-law region for either grid resolution. However, for the finer grid resolution the mean velocity profile predicted by the DMM is closer to the DNS data than the DSM results.

The peak values of the turbulence intensities are fairly well captured by the DMM (Figure 14), even though the DMM breaks down in the center of the channel. The turbulence intensities predicted by the DMM show a small bump after $y^+ = 100$, for all intensities. The bump is clearly seen in the predicted spanwise intensity. As for the DSM, the turbulence intensities in all three directions are very similar to the ones predicted using two-dimensional test filtering. The intensities predicted when using the DMM with the finer wall-normal resolution or the DMM using the coarse grid and two-dimensional test filtering of the SSM, both show good agreement with the DNS data. The DSM with the fine wall-normal resolution does not show large improvements in the turbulence intensities predicted. Therefore for the DSM, large over-prediction of the intensities seems to depend upon the resolution in the homogeneous directions to a larger degree, than the wall-normal resolution.

The value of the dynamic model coefficient is smaller when used in the DMM as shown in Figure 15. The same observation was made for the coefficient when two-dimensional test filtering was applied. However, the model

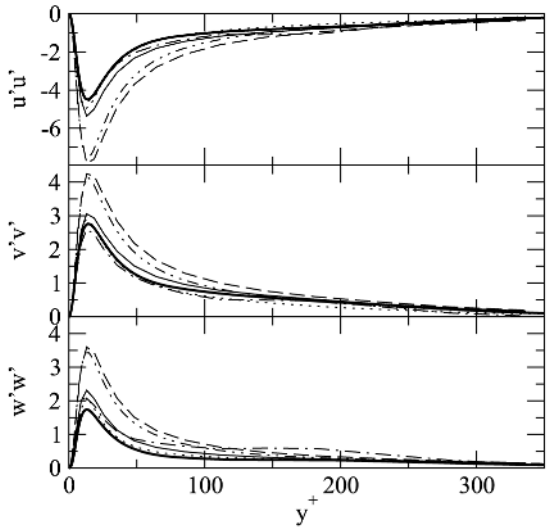

Note: —— : DNS data, —— : DMM using fourth-order commutative two-dimensional filtering of SSM and three-dimensional filtering of DSM and grid resolution (36,37,36), ····· : DMM using fourth-order commutative filter and grid resolution (36,73,36), – – – : DSM using fourth-order commutative filter and grid resolution (36,37,36), – · – · : DMM using fourth-order commutative filter and grid resolution (36,37,36), and – · · – · : DSM using fourth-order commutative filter with grid resolution (36,73,36)

Figure 14.
Reduced turbulence intensities in streamwise $u'u'$, wall-normal $v'v'$ and spanwise $w'w'$ directions using three-dimensional test filtering

coefficient for the DMM when using the coarse grid and three-dimensional filtering shows a rather strange behavior. The value of the coefficient becomes negative on an average. When the resolution is increased or two-dimensional filtering of the SSM is applied, the shape of the curves for the model coefficient are closer to those previously seen in Figure 4. By increasing the wall-normal resolution, the value of the model coefficient is decreased in the center of the channel and its predicted peak value is closer to the wall. Even though the value of the model coefficient is very similar in the two cases (increased grid resolution or filtering of the SSM in two dimensions), the finer resolution results in a smaller eddy viscosity (Figure 16). This is due to the fact that the finer grid resolution resolves more length scales and therefore, the effect from the SFS model is reduced. The same behavior is observed for the DSM as the grid resolution is increased in the wall-normal direction. The eddy viscosity predicted by the DMM shows the same peculiar behavior as observed for the model coefficient on the coarse resolution. The largest eddy viscosity is predicted by the DSM.

The largest contribution to the modeled shear stress is predicted by the DMM where the SSM part is considerably larger than the DSM portion as

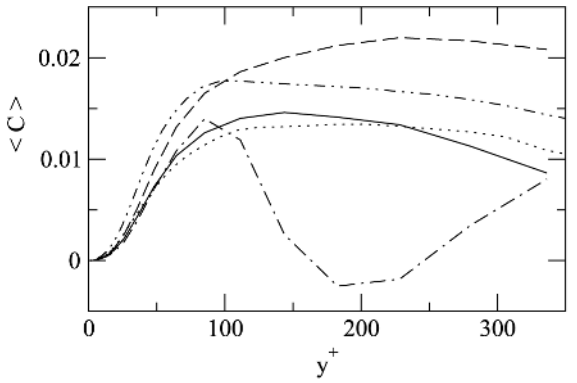

Note: —— : DMM using fourth-order commutative two-dimensional filtering of SSM and three-dimensional filtering of DSM and grid resolution (36,37,36), ····· : DMM using fourth-order commutative filter and grid resolution (36,73,36), – – – : DSM using fourth-order commutative filter and grid resolution (36,37,36), – · – · : DMM using fourth-order commutative filter and grid resolution (36,37,36), and – · · – · · : DSM using fourth-order commutative filter with grid resolution (36,73,36)

Figure 15.
Model parameter $\langle C \rangle$ from the DSM using three-dimensional test filtering

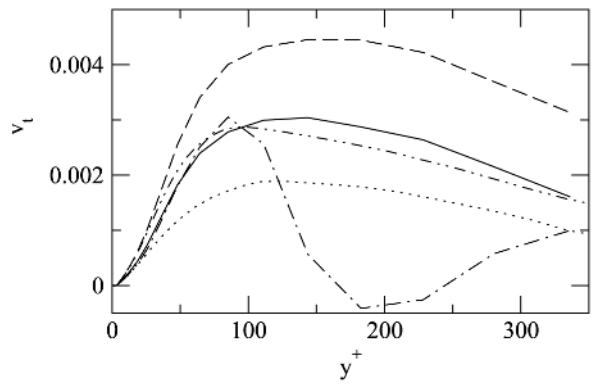

Note: —— : DMM using fourth-order commutative two-dimensional filtering of SSM and three-dimensional filtering of DSM and grid resolution (36,37,36), ····· : DMM using fourth-order commutative filter with grid resolution (36,73,36), – – – : DSM using fourth-order commutative filter and grid resolution (36,37,36), – · – · : DMM using fourth-order commutative filter and grid resolution (36,37,36), and – · · – · · : DSM using fourth-order commutative filter with grid resolution (36,73,36)

Figure 16.
Eddy viscosity contribution from the DSM using three-dimensional test filtering

shown in Figure 17. The figure explains the strange behavior of the model coefficient and the eddy viscosity, Figures 15 and 16, respectively, in the DMM for the coarse resolution and three-dimensional test filtering. The SSM predicts too large shear stress in the center of the flow field (above $y^+ = 100$). The shear stress predicted by the DSM rapidly decreases to reduce the total influence from the DMM. However, the reduction in the DSM is not enough to counteract the influence from the SSM. The eddy viscosity predicted is prevented from becoming largely negative because of the clipping procedure to avoid negative total viscosity. Therefore, the DSM is not able to fully counteract the behavior of the SSM or have a larger influence on the results. For the DSM used alone, the fine grid resolution in the wall-normal direction results in a smaller shear stress predicted.

The DSM: homogeneous averaging versus local averaging. Local averaging in three dimensions of the model coefficient in the DSM reduces the over-prediction of the mean velocity profile compared to homogeneous averaging (Figure 18). The same trend was observed in the results for the two-dimensional test filtering. However, for the three-dimensional test filtering, the relative improvement of the velocity profile when using local averaging is smaller, because the results of the DSM using homogeneous averaging are improved initially when three-dimensional test filtering is applied. The mean velocity profiles predicted using local averaging show very small dependence upon two-dimensional or three-dimensional test filtering (compare Figures 7 and 18).

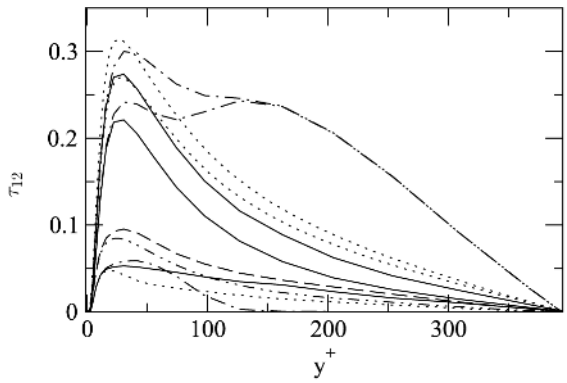

Note: ——— : DMM using fourth-order commutative two-dimensional filtering of SSM and three-dimensional filtering of DSM and grid resolution (36,37,36), ····· : DMM using fourth-order commutative filter and grid resolution (36,73,36), – – – : DSM using fourth-order commutative filter and grid resolution (36,37,36), – · – · : DMM using fourth-order commutative filter and grid resolution (36,37,36), and – · · – · · : DSM using fourth-order commutative filter with grid resolution (36,73,36)

Figure 17.
Modeled shear stress τ_{12} using three-dimensional test filtering

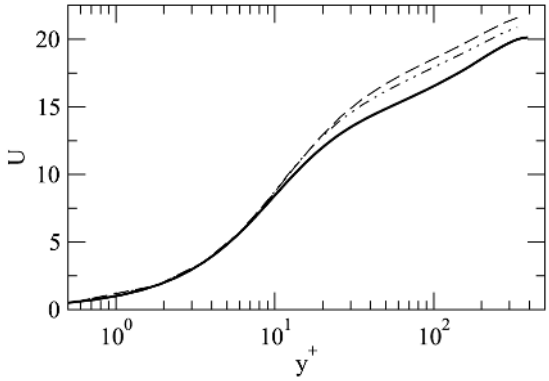

Note: —— : DNS data, – – – : DSM using fourth-order commutative filter and homogeneous averaging, and – · · · – : DSM using fourth-order commutative filter and local averaging

Figure 18.
Mean velocity profiles using three-dimensional test filtering and grid resolution (36, 37, 36)

The turbulence intensities are improved when using three-dimensional local averaging of the model coefficient in the DSM, (Figure 19). However, the turbulence intensities predicted by local averaging and test filtering in two dimensions (Figure 8) are closer to the DNS data than the results predicted by using three-dimensional test filtering. The peak values are higher and are

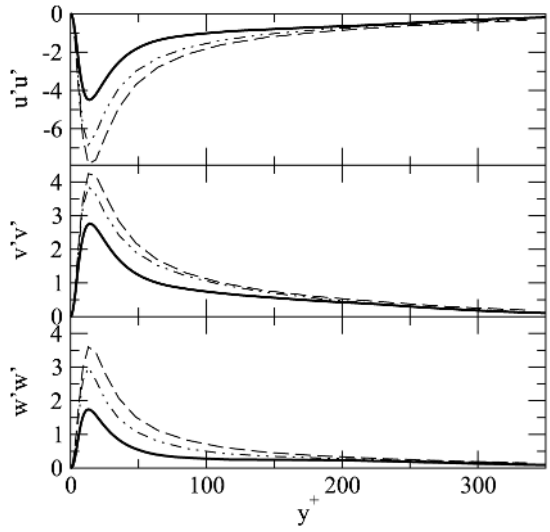

Note: —— : DNS data, – – – : DSM using fourth-order commutative filter and homogeneous averaging, and – · · · – : DSM using fourth-order commutative filter and local averaging

Figure 19.
Reduced turbulence intensities in streamwise $u'u'$, wall-normal $v'v'$ and spanwise $w'w'$ directions using three-dimensional test filtering and grid resolution (36, 37, 36)

broader when using local averaging and three-dimensional test filtering compared to the two-dimensional test filtered results. The turbulence intensities predicted by the DSM using homogeneous averaging of the model parameter are almost identical when test filtering is performed in either two dimensions or three dimensions.

The eddy viscosity predicted when using local averaging shows a sharper gradient in the near wall region (Figure 20). Otherwise, the maximum value of the eddy viscosity is not very different in the two simulations. The eddy viscosity predicted by the local averaging and two-dimensional test filtering is larger than the homogeneously averaged results (Figure 11), but this is not observed in the results when using three-dimensional test filtering. However, when the three-dimensional test filtering and local averaging are applied, the eddy viscosity fluctuates in the near wall region. This behavior was not observed for the two-dimensional filtering. The eddy viscosity increases in the first three grid points from the wall while lower viscosity is calculated in the next two points. In the first three grid points in the wall-normal direction, asymmetric commutative filter functions are used. A symmetric filter (equation (5)) is used in the rest of the flow field. The jump in the eddy viscosity corresponds to the change from the asymmetric filters to the symmetric one. This dependence is not observed when homogeneous averaging of the model parameter is used. However, the change from asymmetric to symmetric filter does not influence the computed results. A simulation was performed where the eddy viscosity was set to zero in the first three grid points. No effect was seen in the presented results. As long as the grid resolution is fine enough in the near wall region, the filters used there do not influence the results.

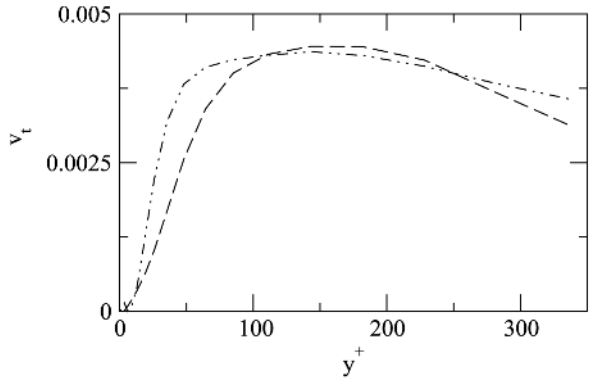

Note: – – – : DSM using fourth-order commutative filter and homogeneous averaging, and – · · · – : DSM using fourth-order commutative filter and local averaging

Figure 20.
Eddy viscosity ν_t contribution from the DSM using three-dimensional test filtering and grid resolution (36, 37, 36)

The peak value of the SFS shear stress is larger when local averaging is used (Figure 21). The near wall behavior observed in Figure 20 is also seen in the predicted shear stresses. For the shear stress, the same trend is observed for three-dimensional test filtering as for the two-dimensional one, that the peak value of the stresses predicted are larger when local averaging is used compared to the homogeneously averaged case. However, the values of the stresses are lower in the three-dimensional local averaging case when compared to the results using two-dimensional test filtering.

Discussion and conclusions

An investigation has been performed using dynamic modeling in LES using two- and three-dimensional test filtering in turbulent channel flow. The results of this study are intended for application to flow fields of engineering interest where it is of great importance to determine the influence of three-dimensional test filtering on the predicted LES results. The LES approach used is the implicitly filtered procedure, which is the most commonly used approach. In implicitly filtered LES, the computational grid and the discretization operators are considered to be the filtering of the governing equations. The test filtering is employed only in the dynamic modeling of the SFS stresses. Most test filtering in channel flow simulations has been performed only in the homogeneous directions, which is not applicable to complex geometries. In order to minimize the commutation error from test filtering in the inhomogeneous direction, a fourth-order commutative filter function is used. The commutative filter is a smooth filter function. A sharp cut-off filter is used in the investigation for comparison purposes. The implicit filter used in the simulations cannot be determined and the test filter function employed reflects the assumption of the shape of the implicit filter.

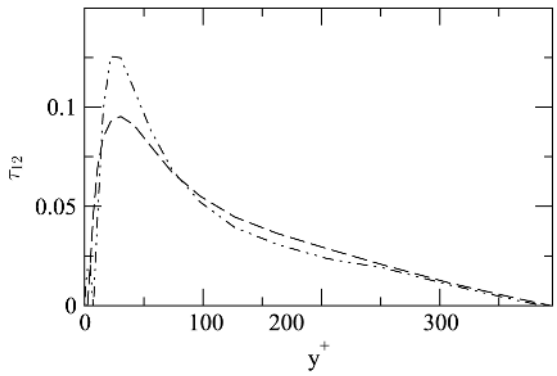

Note: – – – : DSM using fourth-order commutative filter and homogeneous averaging, and – · · · – · : DSM using fourth-order commutative filter and local averaging

Figure 21.
SGS shear stress τ_{12} from the DSM using three-dimensional test filtering and grid resolution (36, 37, 36)

The dynamic SFS models used in the simulations are the DSM by Germano *et al.* (1991) and the DMM, which is a linear combination of the SSM by Liu *et al.* (1994) and the DSM. The unresolved SFS stresses are modeled by the DSM, while the resolved SFS stresses are modeled by the SSM. Another aim of this work was to investigate whether the SSM by Liu *et al.* (1994) is an appropriate model for the resolved SFS stresses. The LES results predicted by the dynamic models using two- or three-dimensional test filtering are compared. The sharp cut-off filter is applied only in the two-dimensional test filtering, while the fourth-order commutative filter is applied using both two-dimensional and three-dimensional test filtering.

For two-dimensional test filtering, the DMM performs very well. The mean velocity profile predicted by the DMM is very similar to the profile by the DSM with the sharp cut-off filter. The DSM with the cut-off filter is known to produce good results in turbulent channel flows (Germano *et al.*, 1991; Piomelli *et al.*, 1988). Furthermore, a large improvement is observed for the turbulence intensities when using the DMM. The DSM with the commutative test filtering predicts results that deviate from the DNS data.

When using three-dimensional test filtering, the DMM also performs well as long as the grid resolution in the wall-normal direction is fine enough. The DMM requires a finer resolution in the wall-normal direction than the DSM to capture the log-law region of the mean velocity profile. It is the three-dimensional test filtering of the SSM portion that destroys the log-region. Even though the mean velocity profile is not correctly captured in the DMM results, the peak values of the turbulence intensities (in the near wall region) are well captured. The DSM again predicts results that differ to the DNS results when used with the three-dimensional commutative filter function. However, using a three-dimensional commutative test filter with the DSM, improves the mean velocity profiles when compared to the two-dimensional case. The improvements are not observed in the turbulence intensities which show almost no difference between two- or three-dimensional filtering.

The large deviation between the DNS data and the DSM results when using the fourth-order commutative filter function shows the need to use an SFS model for the resolved SFS stresses. The same trend is observed for both two- and three-dimensional test filtering. The increased value of the model coefficient in the DSM caused by using the smooth commutative test filter seems to be the reason for the increased disagreement between the LES results and the DNS data. The value of the model coefficient increases when used with the commutative test filter and this results in an increased eddy viscosity. The larger eddy viscosity enhances the over-prediction of both mean velocity profile and turbulence intensities.

The simulations using the DMM indicate that the SSM by Liu *et al.* (1994) is a very promising model for the resolved SFS stresses. The requirement for the

DMM to predict reasonable results is that the grid resolution is fine enough in the inhomogeneous direction. The concept of using a model parameter in the expression of the SSM needs to be investigated, but is left for future investigations.

The dynamic model coefficient is usually averaged in the homogeneous directions (Germano *et al.*, 1991), but since this averaging procedure is not always feasible, there is great interest to investigate how local averaging of the model coefficient affects the LES results. In this study, the local averaging was performed by filtering the coefficient using the commutative test filter function. The study is limited to the influence of the averaging procedure on the LES results predicted by the DSM when used with the fourth-order commutative test filter.

The simulations show that local averaging of the dynamic model coefficient improves the predicted LES results. The local averaging allows the coefficient to vary in the homogeneous directions, and it has a favorable impact on the predicted LES results. It is interesting to note that the use of a simple procedure such as local averaging has a significant impact on the results. Most likely, allowing the model coefficient to vary in the plane aids the break-up of large structures that are predicted in the near wall region. This allows the log-law region in the predicted mean velocity profile to approach the wall, thereby improving the results. The influence of local averaging with the DMM is also of interest, but is left for future studies.

In summary, the DMM performs best with the fourth-order commutative test filter function while the DSM with the same test filter shows the worst performance. Three-dimensional test filtering improves the results when compared to two-dimensional filtering. Using a smooth filter function with the DSM in implicitly filtered LES definitely shows the need for an SFS model for the resolved SFS stresses. The SSM by Liu *et al.* (1994) used as a model for the resolved SFS stresses gives reasonably good results as long as the grid resolution is fine enough in the inhomogeneous direction. Local averaging of the model coefficient in the DSM improves the predicted LES results when a smooth test filter function is used. This simple local averaging method seems to provide a promising alternative to more involved local models.

References

Bardina, J., Ferziger, J.H. and Reynolds, W.C. (1980), "Improved subgrid scale models for large eddy simulation", AIAA-80-1357.

Carati, D. and Eijnden, E.V. (1997), "On the self-similarity assumption in dynamic models for large eddy simulations", *Physics of Fluids*, Vol. 9, pp. 2165-7.

Carati, D., Winckelmans, G.S. and Jeanmart, H. (2001), "On the modelling of the subgrid-scale and filtered-scale stress tensors in large-eddy simulation", *Journal of Fluid Mechanics*, Vol. 441, pp. 119-38.

Chow, F.K. and Street, R.L. (2002), "Modeling unresolved motions in LES of field-scale flows", *American Meteorological Society, 15th Symposium on Boundary Layers and Turbulence*, pp. 432-5.

Dukowicz, J.K. and Dvinsky, A. (1992), "Approximation as a higher order splitting for the implicit incompressible flow equations", *Journal of Computational Physics*, Vol. 102, pp. 336-47.

Germano, M., Piomelli, U., Moin, P. and Cabot, W.H. (1991), "A dynamic subgrid-scale eddy viscosity model", *Physics of Fluids A*, Vol. 3, pp. 1760-5.

Ghosal, S. (1995), "An analysis of numerical errors in large-eddy simulations of turbulence", *Journal of Computational Physics*, Vol. 125, pp. 187-206.

Ghosal, S. and Moin, P. (1995), "The basic equations of the large eddy simulation of turbulent flows in complex geometry", *Journal of Computational Physics*, Vol. 118, pp. 24-37.

Ghosal, S., Lund, T.S., Moin, P. and Akselvoll, K. (1995), "A dynamic localization model for large-eddy simulation of turbulent flows", Vol. 286, pp. 229-55.

Gullbrand, J. (2000), "An evaluation of a conservative fourth order DNS code in turbulent channel flow", *Annual Research Briefs 2000*, Center for Turbulence Research, pp. 211-18.

Gullbrand, J. (2002), "Grid-independent large-eddy simulation in turbulent channel flow using three-dimensional explicit filtering", *Annual Research Briefs 2002*, Center for Turbulence Research, pp. 167-79.

Gullbrand, J. and Chow, F.K. (2003), "The effect of numerical errors and turbulence models in LES of channel flow, with and without explicit filtering", *Journal of Fluid Mechanics* (in press).

Lilly, D.K. (1992), "A proposed modification of the Germano subgrid-scale closure method", *Physics of Fluids A*, Vol. 4, pp. 633-5.

Liu, S., Meneveau, C. and Katz, J. (1994), "On the properties of similarity subgrid-scale models as deduced from measurements in a turbulent jet", *Journal of Fluid Mechanics*, Vol. 275, pp. 83-119.

Lund, T.S. (1997), "On the use of discrete filters for large eddy simulation", *Annual Research Briefs 1997*, Center for Turbulence Research, pp. 83-95.

Lund, T.S. and Kaltenbach, H-J. (1995), "Experiments with explicit filtering for LES using a finite-difference method", *Annual Research Briefs 1995*, Center for Turbulence Research, pp. 91-105.

Morinishi, Y., Lund, T.S., Vasilyev, O.V. and Moin, P. (1998), "Fully conservative higher order finite difference schemes for incompressible flow", *Journal of Computational Physics*, Vol. 143, pp. 90-124.

Moser, R.D., Kim, J. and Mansour, N.N. (1999), "Direct numerical simulation of turbulent channel flow up to $Re_\tau = 590$", *Physics of Fluids*, Vol. 11, pp. 943-5.

Najjar, F.M. and Tafti, D.K. (1996), "Study of discrete test filters and finite difference approximations for the dynamic subgrid-scale stress model", *Physics of Fluids*, Vol. 8, pp. 1076-88.

Piomelli, U., Moin, P. and Ferziger, J.H. (1988), "Model consistency in large eddy simulation of turbulent channel flows", *Physics of Fluids*, Vol. 31, pp. 1884-91.

Sarghini, F., Piomelli, U. and Balaras, E. (1999), "Scale-similar models for large-eddy simulations", *Physics of Fluids*, Vol. 11, pp. 1596-607.

Spalart, P., Moser, R. and Rogers, M. (1991), "Spectral methods for the Navier-Stokes equations with one infinite and two periodic directions", *Journal of Computational Physics*, Vol. 96, pp. 297-324.

Stolz, S., Adams, N.A. and Kleiser, L. (2001), "An approximate deconvolution model for large-eddy simulation with application to incompressible wall-bounded flows", *Physics of Fluids*, Vol. 13, pp. 997-1015.

Vasilyev, O.V. (2000), "High order finite difference schemes on non-uniform meshes with good conservation properties", *Journal of Computational Physics*, Vol. 157, pp. 746-61.

Vasilyev, O.V., Lund, T.S. and Moin, P. (1998), "A general class of commutative filters for LES in complex geometries", *Journal of Computational Physics*, Vol. 146, pp. 82-104.

Winckelmans, G.S., Jeanmart, H. and Carati, D. (2002), "On the comparison of turbulence intensities from large-eddy simulation with those from experiments or direct numerical simulation", *Physics of Fluids*, Vol. 14, pp. 1809-11.

Winckelmans, G.S., Wray, A.A., Vasilyev, O.V. and Jeanmart, H. (2001), "Explicit filtering large-eddy simulation using the tensor-diffusivity model supplemented by a dynamic smagorinsky term", *Physics of Fluids*, Vol. 13, pp. 1385-403.

Zang, Y., Street, R.L. and Koseff, J.R. (1993), "A dynamic mixed subgrid-scale model and its application to turbulent recirculating flows", *Physics of Fluids*, Vol. 5, pp. 3186-96.

The role of endothermic gasification in propellant ignition

Caroline Lowe

Department of Applied Mathematics and Theoretical Physics, Centre of Mathematical Sciences, Cambridge University, Cambridge, England, UK

Received February 2002
Revised May 2003
Accepted May 2003

Keywords *Compressible flow, Ignition systems, Differential equations, Gases*

Abstract *This study explores a reactor model designed to describe the decomposition, ignition and combustion of energetic materials in combination with real experimental data for these energetic materials. Spatial uniformity is initially assumed which reduces the system of partial-differential-equations to a system of ordinary-differential-equations that can be easily solved numerically. The phase-plane is explicitly presented and examined to illustrate how chemistry and temperature evolve in time. The computations provide an understanding of the vast different timescales that exist and illustrate the singularity structure. Following this the effect of including this chemical regime in an environment typically induced by the combustion of these materials, that is within a compressible fluid flow, is pursued.*

Introduction

Energetic materials are the fuel source used in propulsion systems, such as rocket motors, ballistic weapons and explosive devices. During combustion, these materials rapidly release large quantities of chemical energy. The transport and handling of these materials is hazardous and extremely sensitive to local thermal conditions and mechanical shock. This danger has lead to the development of insensitive munitions that are more stable during handling. However, making these materials less volatile in "normal" conditions has also made them harder to ignite reliably during use.

Experiments on these materials have indicated a number of distinct stages in the combustion process. These stages include an initial gasification of the solid, that can be either endothermic or mildly exothermic; what is worth noting is that insensitive munitions display a distinct endothermic gasification process. The gasification produces gaseous reactants that at some point ignite and burn in a very exothermic reaction. A model of a simple chemical system to describe these stages and numerical solutions of single and multi-phase fluids that included this chemistry was presented by Clarke and Lowe (1996) and Lowe and Clarke (1999).

A reactor model for ignition and combustion, presented by Clarke (1996), follows a simple reaction scheme and investigates an endothermic gasification process that provides a supply of gaseous reactive species. The model, as it will be referred herein, assumes that both gasification and gas-phase reactions can be described as Arrhenius-type reactions. This chemical combination

International Journal of Numerical Methods for Heat & Fluid Flow
Vol. 14 No. 4, 2004
pp. 493-511

0961-5539
DOI 10.1108/09615530410532268

illustrates two distinctly different classes of solution depending on the relation between the characteristic times of the chemical reactions. The behaviour of these reduced chemical systems appears to display the attributes of various successful and unsuccessful ignition processes that are known to exist.

If spatial uniformity is assumed then spatial variations can be neglected in the model – a so-called "well-stirred reactor". Consequently, the system is mathematically described by a system of ordinary-differential-equations that describe how the density, reactants and energy change over time. Some simplifications enable the system to be reduced to a single equation that describes the change in one reactant species with temperature. This enables the mathematician to obtain singular points and explore their nature.

Two areas of interest will be pursued in this account: the previous study of the combustion model was able to identify singular points and sketch the nature of the solution. However, the complete solution in the phase plane can only be provided by numerical integration of the system of equations. Further, simplifications assumed in the earlier work – needed to provide an analytically tractable system – will be relaxed with the objective of studying a more "realistic" problem. In this case, the nature of the solution can only be explored by adopting numerics; direct comparisons between the "realistic" and simplified systems will be made.

The second part of the study will focus on non-linear wave interaction with this chemical sequence. The reactor model adopts chemical data obtained from experiments on HMX explosive. The fluid flows created from the combustion of such highly energetic fuels in closed conditions are often of high Mach number. Consequently, the one-dimensional form of the reactive compressible Euler equations are presented and solved using appropriate numerical techniques. The research focuses on how wave motion couples with the chemical behaviour in a closed vessel and the suitability of computational schemes.

The reactor model

A closed container holds inert gas that is hotter than the ambient initial temperature. The hot conditions cause a reactive solid to gasify, creating reactive species P. The requirement of latent heat of vaporisation means that the gasification is an endothermic process. P reacts to produce a further reactant A in a thermally neutral process. Finally, A reacts to provide heat and inert product gas B. The sequence can be summarised:

$$\text{solid fuel} \xrightarrow{\dot{m}} P \xrightarrow{k_1} A \xrightarrow{k_2} B + \text{heat} \tag{1}$$

with reaction rates k_n $(n = 0, 1)$ presumed to be of the form:

$$k_n = \mathscr{A}_n \exp(-E_n/RT). \tag{2}$$

Equation (2) is a typical Arrhenius form with T temperature, E_n activation energy, R gas constant and $\mathscr{A}_n$ is a pre-exponential factor (assumed to be

constant in this study) of dimensions s^{-1}. The gasification is assumed to behave according to a surface pyrolysis in which the rate of gaseous mass addition $\dot{m}$ is a function of surface temperature which is itself a function of gas temperature, such that:

$$v\dot{m} = \mathscr{B} \exp(-E_S/RT) \tag{3}$$

where $v = 1/\rho$ is the specific volume.

The specific total energy E is defined as:

$$E = e + \frac{1}{2}u^2; \quad e = \sum_{i=1}^{N} c_i e_i \tag{4}$$

where u is the gas velocity, c_i is the mass-fraction of each chemical species i, and e_i is the corresponding specific internal energy. Assume that the specific heats at constant volume C_v are constant and the same for all species and the gases are ideal, then the internal energies for the gaseous components are:

$$e_P = e_A = e^{\text{th}} + Q; \qquad e_B = e^{\text{th}}; \quad \text{where } e^{\text{th}} = C_v T; \tag{5}$$

e^{th} is thermal energy per unit mass of each species, T is temperature and Q is the energy of formation. It follows that

$$e = \sum_{i=1}^{N} c_i e_i = e^{\text{th}} + (c_P + c_A)Q$$

and the total energy may then be simplified and given as:

$$E = e^{\text{th}} + (c_P + c_A)Q + \frac{1}{2}u^2. \tag{6}$$

The ideal gas assumption implies that

$$p = \rho RT; \qquad a^2 = \gamma RT = \gamma pv \tag{7}$$

where ρ is density, $v = 1/\rho$ is specific volume, p is pressure, γ is the ratio of specific heats, $R = \mathscr{R}/\mathscr{W}$ is a constant where $\mathscr{R}$ is the universal gas constant, $\mathscr{W}$ is the molecular weight of each gas (which again for simplicity will be assumed to be the same for both oxidant and fuel and by implication for product also) and a is sound-speed.

The equations that govern one-dimensional unsteady behaviour of a compressible gas that reacts according to the scheme given in equation (1) can be put together from information by Clarke and Lowe (1996), as follows:

$$\mathbf{U}_t + \mathbf{F}_x(\mathbf{U}) = \mathbf{S}(\mathbf{U}) \tag{8}$$

where

$$\mathbf{U} = \begin{pmatrix} \rho \\ \rho c_P \\ \rho c_A \\ \rho u \\ \rho E \end{pmatrix}, \qquad \mathbf{F}(\mathbf{U}) = \begin{pmatrix} \rho u \\ \rho u c_P \\ \rho u c_A \\ \rho u^2 + p \\ up(E + pv) \end{pmatrix},$$

$$\mathbf{S}(\mathbf{U}) = \begin{pmatrix} \dot{m} \\ \dot{m} - \rho k_1 c_P \\ \rho k_1 c_P - \rho k_2 c_A \\ \dot{m} u \\ \dot{m}(e_{\text{th}} + pv + k) + \dot{m}(Q - L) \end{pmatrix}.$$

Note that there is no explicit equation necessary for mass fraction c_B, since $c_A + c_P + c_B = 1$.

Summary of ODE form

The spatially uniform equations derived from equation (8) are a system of four ODEs in time. Define quantities $\mathscr{D}_n$ as Damköhler numbers that denote the ratio between the reaction rate and the local flow of gasifying material ($v\dot{m}$):

$$\mathscr{D}_n = k_n / v\dot{m}. \tag{9}$$

In the earlier work, it was assumed that the rate of reaction k_1 is such that $\mathscr{D}_1$ is constant; for this choice of parameter values the equation for c_P can be analytically integrated to give:

$$c_P = (1 + \mathscr{D}_1)^{-1}\{1 - \exp[-(1 + \mathscr{D}_1)]\tau\} \tag{10}$$

where the new independent variable $\tau = \ln[1 + m/\rho_0)]$ and m is the total mass of propellant that has gasified in time t (that is τ is the transformed non-dimensional time).

If it is further assumed that:

$$c_P(0) \equiv (1 + \mathscr{D}_1)^{-1} \tag{11}$$

then c_P will remain constant as long as there is a supply of reactant species. The study by Gray and Scott has examined models of this type (c_P constant – described as "pool-reactant" models), both with mathematics and in the laboratory (Gray and Scott, 1990). It was shown that by making the pool reactant assumption, the model reduced to one single autonomous ODE.

For comparison with earlier study, this single autonomous equation will be presented; define the following non-dimensional system:

$$\theta \equiv \frac{T - T_{\mathrm{a}}}{\sigma T_{\mathrm{a}}}, \qquad \alpha \equiv \frac{c_A}{c_{\mathrm{ref}}} \tag{12}$$

where

$$\tilde{Q} = \frac{Q}{C_v T_{\mathrm{a}}}, \qquad \sigma = \frac{RT_{\mathrm{a}}}{E_2}, \qquad \kappa = \mathscr{D}_2(0), \qquad c_{\mathrm{ref}} = \frac{\sigma}{\kappa \tilde{Q}}$$

and T_{a} is the ambient temperature.

Using these new variables and assumption (equation (11)), the spatially uniform version of system (equation (8)) can be reduced to the following single equation:

$$\frac{\mathrm{d}\alpha}{\mathrm{d}\theta} = \frac{\mu - \kappa\alpha f(\theta) - \alpha}{\alpha f(\theta) - \mathscr{L}_{\mathrm{a}} + (\gamma - 1)\theta} \tag{13}$$

where

$$\nu = E_{\mathrm{S}}/E_2, \qquad f(\theta) = \exp\left[\frac{-(\nu - 1)\theta}{1 + \sigma\theta}\right], \qquad \sigma\mathscr{L}_{\mathrm{a}} \equiv \frac{L}{C_v T_{\mathrm{a}}} - (\gamma - 1),$$

$$\mu \equiv \mathscr{D}_1 c_P / c_{\mathrm{ref}}.$$

This single equation has the capacity to provide two different classes of solution, *providing* the gasification process is indeed endothermic. It should be observed that different regimes provided by the combustion model *only* exist if the combustion process includes an endothermic stage. If no endothermic phase exists then the denominator of equation (13) is always greater than 0; therefore, there will be no singular points of the ODE. Consequently, the combustion model will always eventually result in a successful ignition due to the fact that the exothermic reaction rate k_2 is always non-zero, in this case, the ignition delay will depend on the activation energy E_2. It is only through the introduction of latent heat requirements that failure to ignite and a"slow burn" mechanism (that will be illustrated below) can emerge. This study is not aimed towards characterising how the size of the latent heat effects the combustion; what is of interest are how the opposing endothermic and exothermic reactions and their relative timescales control the ignition and combustion processes. In summary, the role of the endothermic reaction is to enrich the combustion model in terms of providing new mechanisms of ignition and burning that are not available in a model that includes only exothermic behaviour. Therefore, the study assumes constant endothermic latent energy (L(J/kg)) and exothermic combustion energy (Q(J/kg)) but varies the activation energy of these reactions.

The two classes of solution depend on the ratio of the chemical times of the endothermic and exothermic reactions, ν, that is defined in relation to equation (13). Let us reintroduce the initial-value problem defined by Clarke (1996) in which reaction rate data were approximated from the experimental data of Tarver and McGuire on HMX explosive (Table I). Equivalent values of the dimensionless variables are also defined in Table I.

Numerically derived phase planes will be presented using these data for different values of the parameter ν. Two different initial value problems will be pursued.

The first, for comparison and validation purposes, corresponds to the pool reactant model in which c_P remains constant – and non-zero – for all times and $c_A(0) \equiv 0$, that is the solution to equation (13). Recall that earlier studies have sketched the nature of this solution; here the full solution is presented.

The second explores a more realistic problem in which both reactant species $c_P(0) \equiv 0$ and $c_A(0) \equiv 0$. These equations do not reduce to an autonomous form and therefore, the complete solution and all singular points can only be identified numerically. The emphasis will be to clarify whether there is similar behaviour between this solution and the one described in the previous paragraph.

It is easy to show that the system of equations is stiff due to different timescales involved. Consequently, the system of equations was numerically integrated with a semi-implicit algorithm detailed by Press *et al.* (1992).

Case A: $0 \leq \nu \leq 1$

Initial-value-problem $c_P(0) \equiv (1 + \mathscr{D}_1)^{-1}$. For this initial value of c_P the concentration of reactant P remains constant for all time and the system of

T_a	300 K
γ	1.27
$\mathscr{W}$	21 kg/mol
Q	5,000,000 J/kg
$\mathscr{A}_2$	$3.5 \times 10^{19}\,s^{-1}$
$\mathscr{B}$	$1.156 \times 10^{18}\,s^{-1}$
$\mathscr{A}_1 = 9\mathscr{B}$	–
p_0	101,400 Pa
$\mathscr{R}$	8,313 J/kmol
L	416,447 J/kg
E_2	142 kJ
$E_S = \nu E_2$	–
$E_1 = \nu E_2$	–
σ	0.0175
μ	58.47
κ	0.1
$\mathscr{L}_a$	38.78

Table I.
Input parameters

ODEs reduces to equation (13). There is an unstable singularity, namely a saddle-point, in the θ-α plane. For $\nu = 0.9$ this saddle point was predicted to be located at position (0, 53.141). Define locii y_1 and y_2 that follow the nullclines of equation (13) (that is y_1 and y_2 should locate the turning points of the solutions to equation (13) and the intersection of y_1 and y_2 should locate the singular point).

Figure 1 shows the numerical solutions for $T_0 = 395,\ 396,\ 400\,\mathrm{K}$ and $c_A(0) \equiv 0$. Define the critical initial dimensionless temperature as θ_{crit} that separates a successful ignition from an unsuccessful ignition. This is located at the dimensional temperature $T_{\mathrm{crit}} \approx 395\,\mathrm{K}$: when $\theta_0 = \theta_{\mathrm{crit}} - \Delta\theta$, where $\Delta\theta$ is some small change in θ, the temperature continues to decrease as the reactant mass-fraction increases – this corresponds to the physical situation in which latent heat requirements are always greater than the exothermic activity in the gas-phase and ignition of the gas-phase fails. Over time, the temperature will continue to decrease and the reactant mass increases.

For $\theta_0 = \theta_{\mathrm{crit}} + \Delta\theta$, the temperature initially decreases, again due to latent heat requirements. However, as the reactant gases accumulate in the chamber, eventually sufficient exothermic activity arises for the reactant mass to decrease, due to consumption of the reactant, temperature starts to increase and eventually thermal runaway (ignition) is established. In this study, the time taken between time zero and thermal runaway will be described as the induction time t_{ind}.

Equivalent behaviour has been seen before for a simpler chemical scheme, as detailed by Clarke and Lowe (1996). Consider the timescales associated with these solutions; for $T_0 \equiv 400\,\mathrm{K}$, the history of the temperature and mass-fraction c_A is shown in Figure 2(b). For this initial temperature, the

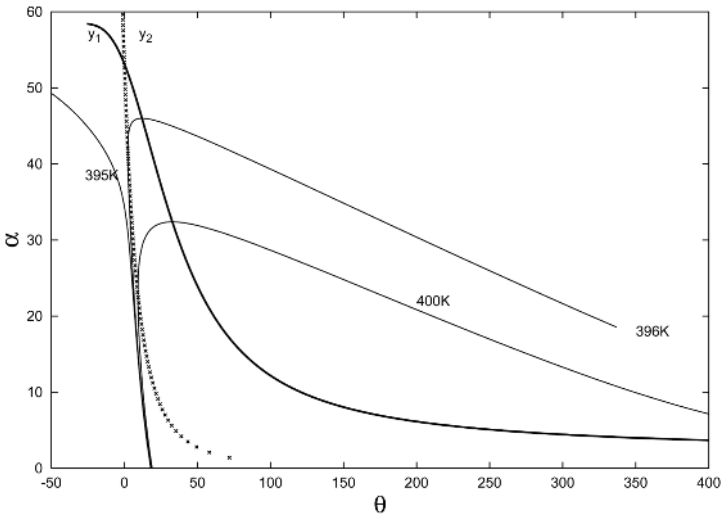

Figure 1.
Phase plane for the reactor model with $\nu = 0.9$ and $c_P(0) \equiv (1 + \mathscr{D}_1)^{-1}$

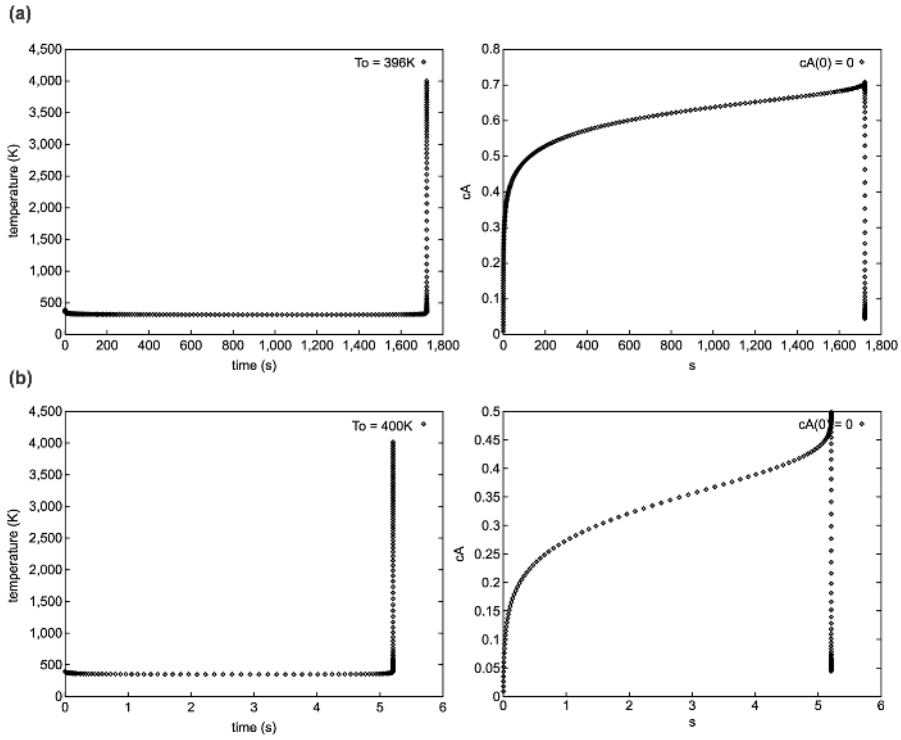

Figure 2.
Temperature and mass-fraction c_A histories for the reactor model with $\nu = 0.9$ and $c_P(0) \equiv (1 + \mathscr{D}_1)^{-1}$. Initial conditions
(a) $T_0 = 396\,\mathrm{K}$,
(b) $T_0 = 400\,\mathrm{K}$

time to ignition is $t_{\mathrm{ind}} \approx 6\,\mathrm{s}$; this is much longer than would be desirable in an actual propulsion system for example, in a ballistic device the complete combustion event (i.e. from ignition to material completely burning out) should last for about 10 ms. As the trajectories in the phase plane approach the singular point time increases by several orders of magnitude, as shown in Figure 2(a) for $T_0 = 396\,\mathrm{K}$. It was speculated that trajectories close to the saddle point describe a "hang-fire" situation in which ignition occurs, but only after an unacceptably long delay.

Initial-value-problem $c_P(0) \equiv 0.0$. In this case, the variation in c_P over time means that the type of analysis seen above, in which the system of equations can be reduced to one single equation, is no longer possible. Figure 3 shows three-dimensional numerical solutions for $T_0 = 400$ and 420 K and $c_A(0) = 0$ with corresponding θ-α plane. It can be seen that the behaviour is broadly similar to that shown in Figure 1, only the critical temperature has increased, for the case in which $T_0 = 400\,\mathrm{K}$ there is no successful ignition. The similarity of the solution is not surprising on examination of the corresponding c_P history for $T_0 = 420\,\mathrm{K}$ (Figure 4); c_P rapidly attains the final value 0.1 and other than this, initial short transient behaves as a pool-reactant.

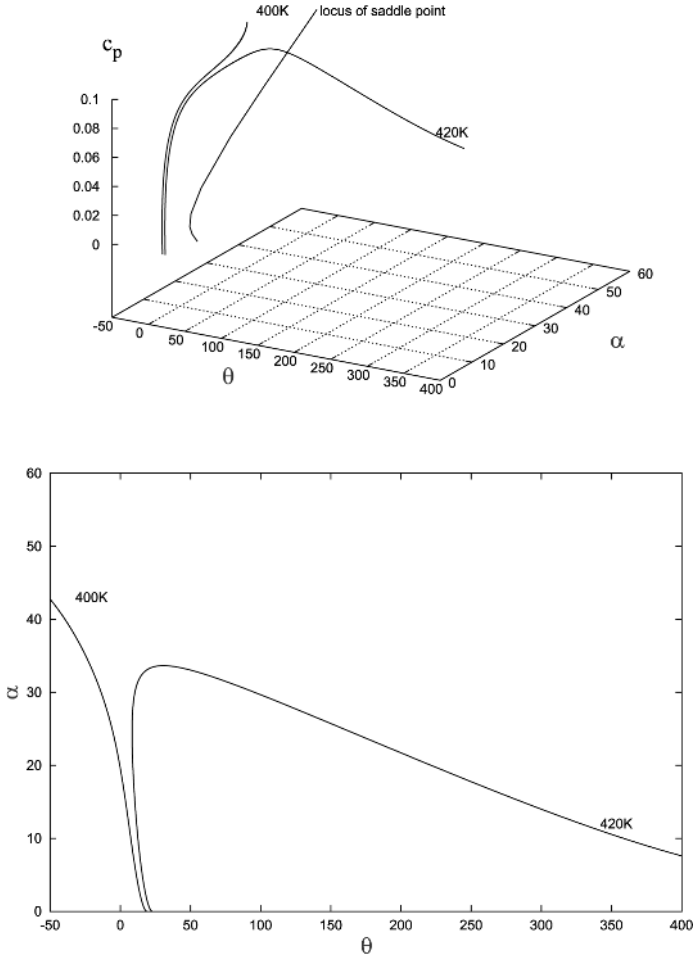

Figure 3.
Phase plane for the reactor model with $\nu = 0.9$ and $c_P(0) = 0$

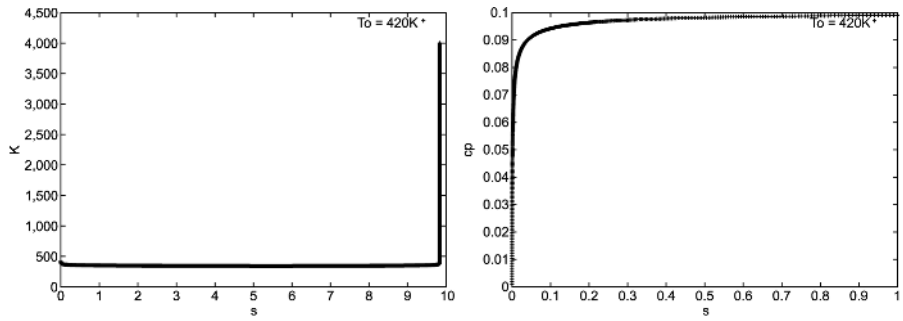

Figure 4.
T and c_P for the reactor model with $\nu = 0.9$, $c_P(0) = 0$ and initial conditions $T_0 = 420\,\mathrm{K}$

It is seen that for the choice of parameters made in this study, the relaxed more general system behaves in a similar manner to the reduced system in the section previous. The rate of increase of c_P relies on the rate of change of dimensionless variable τ (equation (10)) which depends on $\dot{m}$. If the parameter values were such that the rate of increase of c_P were much slower, then μ would increase slowly with c_P thus perturbing the ODE (equation (13)) over longer times. The saddle point is no longer fixed in (θ, α) space but varies with c_P (Figure 3). Figure 4 shows that for $T_0 = 420\,\mathrm{K}$, the ignition time is $\approx 10\,\mathrm{s}$; for the case in which c_p is constant throughout, the ignition time is only 0.03 s – almost three-orders of magnitude smaller. Although the qualitative behaviour of the complete and reduced systems of ODEs is similar, the quantitative behaviour differs enormously.

Case B: $1 < \nu$

Initial-value-problem $c_P(0) \equiv (1 + \mathscr{D}_1)^{-1}$. For the pool-reactant model, there are two singular points for these values of ν. The first is, as above, located at position (0, 53.141), but corresponds to a stable node. The second singularity is located at (194.21, 58.39) and is an unstable saddle point.

Figure 5 shows the phase-plane including trajectories corresponding to initial conditions $T_0 = 1,328\,\mathrm{K}, 1,329\,\mathrm{K}, c_A(0) = 0$ along with curves y_1 and y_2. Note that the curve y_2 is a continuous curve that leaves the picture at position (3, 70), attains a maximum and then re-enters the picture at (195, 70). In this case, the critical temperature θ_{crit} is much higher; corresponding to a temperature of approximately 1,328 K.

If the initial temperature is such that $\theta = \theta_{\mathrm{crit}} + \Delta\theta$, then thermal runaway will eventually occur. However, if $\theta = \theta_{\mathrm{crit}} - \Delta\theta$, then the temperature decreases and the reactant mass-fraction grows. As before, the system fails to

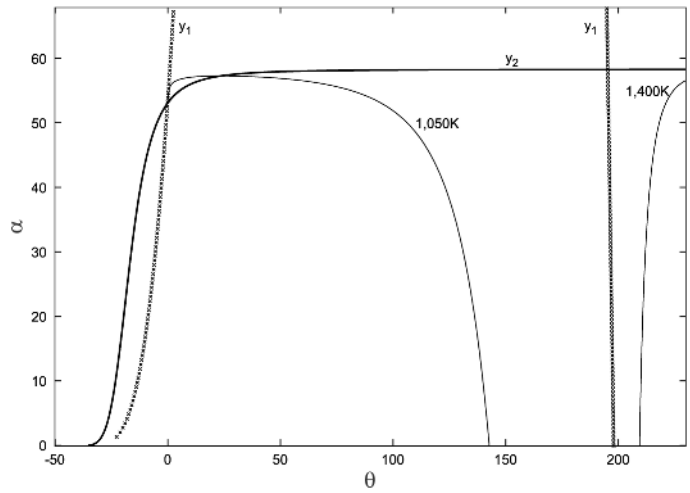

Figure 5.
Phase plane for the reactor model with $\nu = 1.1$ and $c_P(0) \equiv (1 + \mathscr{D}_1)^{-1}$

ignite but in this case, all integral curves will approach a minimum temperature, namely 300 K, and maximum mass-fraction $c_A = 0.9$ at the node (note that the remaining gas will be composed of the pool reactant $c_P = 0.1$). Let us focus on the additional feature which is the history of trajectories in the phase plane that approach the stable node. Figure 6 shows the timescales for this process that are composed of two distinct stages. The first stage consists of an extremely rapid reduction in temperature from 1,328 K to approximately 420 K in approximately 1 s followed by a slow decline to 330 K that takes more than a day! Again, it was suggested that this would adequately represent a "misfire" situation in which thermal runaway does not occur but nevertheless, the material is gasifying and "cooking" over a prolonged time until the point at which the supply of solid material has been completely gasified. The mass-fraction c_A rapidly increases to 0.9 and then starts to decline slowly; for this problem, the reactor system gas is composed of mostly c_A and pool reactant $c_P = 0.1$ indicating that the secondary exothermic reaction is occurring very slowly.

Initial-value-problem $c_P(0) \equiv 0$. Figure 7 shows the equivalent simulation that now sets c_p to zero initially – included are the locii of node and saddle points. In this case, there is negligible difference between the ignition time associated with the initial condition $T_0 = 1,400\,\mathrm{K}$ whether $c_P(0) \equiv 0$ or $c_P(0) \equiv (1 + \mathscr{D}_1)^{-1}$. Similarly, the times associated with the path towards the stable node for the case in which $T_0 = 1{,}050\,\mathrm{K}$ remain virtually the same. On examination, the close similarity – both qualitative and quantitative – between the phase planes in (θ, α) space for the complete and reduced systems is associated with a very rapid increase of c_P to the pool-reactant value.

The one-dimensional problem

It is of interest to identify under what fluid flow regime it may be possible to induce ignition for the reactor model explored earlier. Compressible flows involve shocks, expansion waves and contacts; a test problem that involves all of these features is a standard shock tube problem. The inert shock tube problem is given by equation (8) in which all the terms on the right-hand side

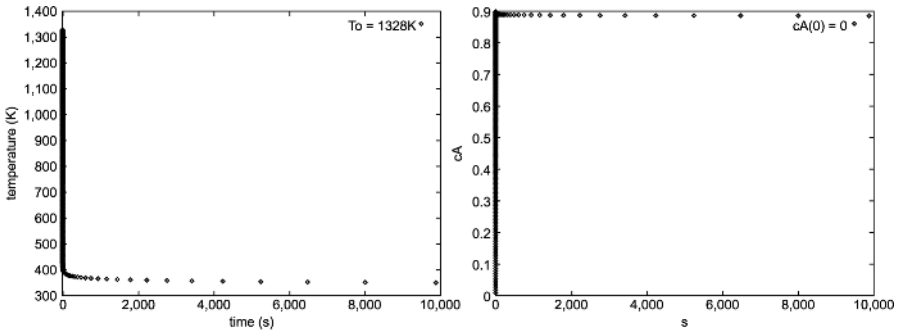

Figure 6.
Temperature and mass-fraction c_A histories approaching the stable-node. Initial conditions $T_0 = 1{,}328\,\mathrm{K}$ and $c_P(0) \equiv (1 + \mathscr{D}_1)^{-1}$

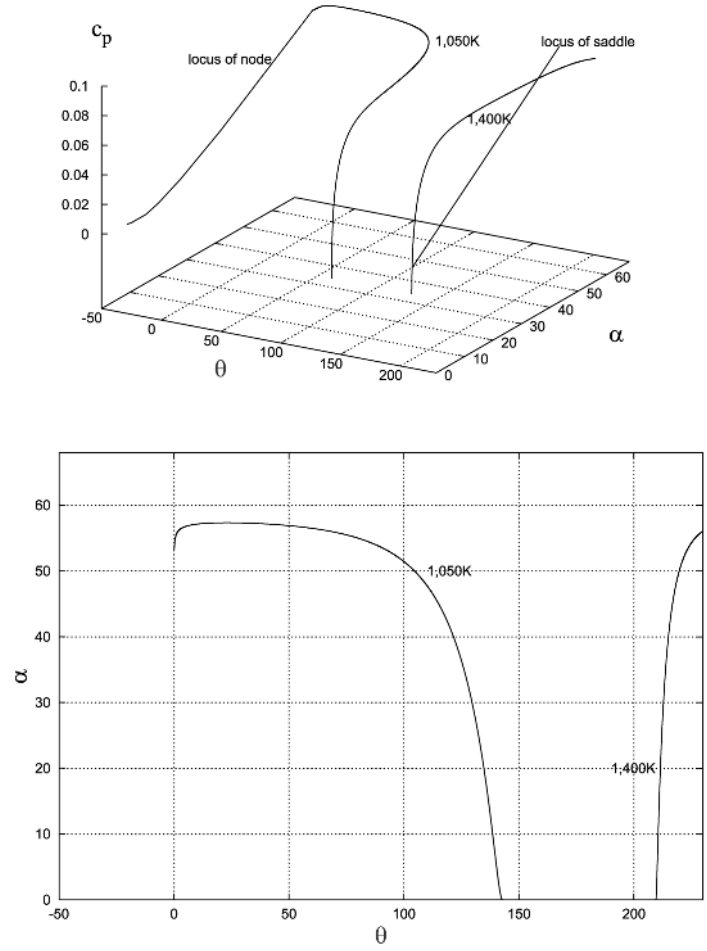

Figure 7.
Phase plane for the reactor model with $\nu = 1.1$ and $c_P(0) \equiv 0$

(source terms) are set to zero. The reactive system of equations is given by equation (8) including the source terms.

The standard technique of time-operator splitting will be employed to solve equation (8). This involves splitting this non-homogeneous hyperbolic problem into two sub-problems, a system of ordinary-differential-equations and a homogeneous hyperbolic system. The former can be solved as above and the latter using shock-capturing methods (Lowe, 1996).

Test problem for $\nu = 0.9$

Initially, explore the case in which $\nu = 0.9$. Consider a domain of length 1 m with initial conditions:

$$T(x,0) = 355\,\mathrm{K}, \qquad c_A(x,0) = 0, \qquad c_P(x,0) = 0,$$
$$p = \begin{cases} 101,400, & x \le 0.5\,\mathrm{m}; \\ 5 \times 101,400, & x > 0.5\,\mathrm{m}. \end{cases} \tag{14}$$

For reference purposes, Figure 8 shows two solution profiles for the inert shock tube problem with a mesh of 1,000 cells. The graphs include the density and temperature at 0.7 and 0.95 ms. At $t = 0.7$ ms, the standard solution consists of an expansion wave that is travelling to the left with head at location $x \approx 0.2$ m and tail at $x \approx 0.43$ m at this time. Similarly, a shock wave is travelling to the right and is at position $x \approx 0.92$ m and a contact discontinuity is at $x \approx 0.69$ m. The temperature ahead of the contact discontinuity and behind the shock, location $0.69 < x < 0.92$, is approximately 421 K. Consequently, it might be expected that the reactive system would result in a successful ignition since this is above the critical ignition temperature. The domain is closed, which means that when the shock wave meets the right boundary at about 0.84 ms it reflects; the solution at time $t = 0.95$ ms illustrates how the temperature behind the reflected shock jumps to $T \approx 493$ K.

Figure 9 shows the flow variables for the reactive case at 0.7 and 0.847 ms. Included are the additional variables that describe the chemical progress c_P, c_A and Damköhler number $\mathscr{D}_2$. The growth in mass-fraction c_P indicates that gasification has been initiated due to the elevated temperature between the contact and shock, $0.69 < x < 0.92$. The profile for c_A indicates that some of this reactant has been converted from c_P to c_A within this region. The endothermic gasification process required to create c_P has a direct effect on the temperature in this region – it is no longer constant as in the inert case – due to latent heat requirements. The temperature does not experience runaway at this time; the reason for this is the induction time associated with this initial temperature (Figure 4). It takes approximately 10 s for the reactor with initial conditions $T_0 = 421$ K, $c_P(x,0) = 0$, $c_A(x,0) = 0$ to ignite under uniform conditions. Some exothermic activity is occurring as seen from the increase in $\mathscr{D}_2$ from zero. If the chamber was not closed, then the wave motion would be sustained and it would take about 10 s for ignition to occur.

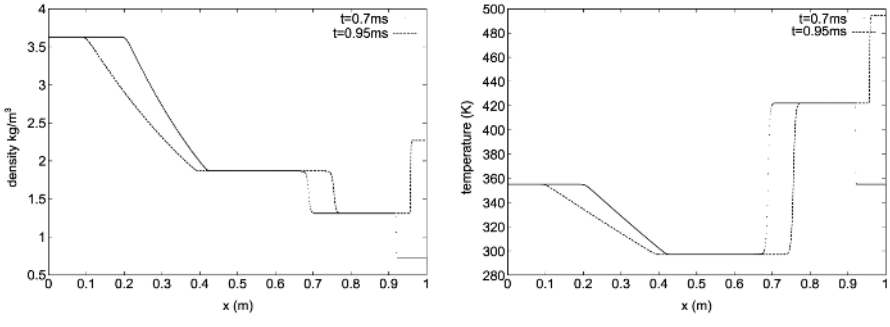

Figure 8.
Profiles at $t = 0.7$ and 0.95 ms for the inert shock-tube problem $T_0 = 355$ K

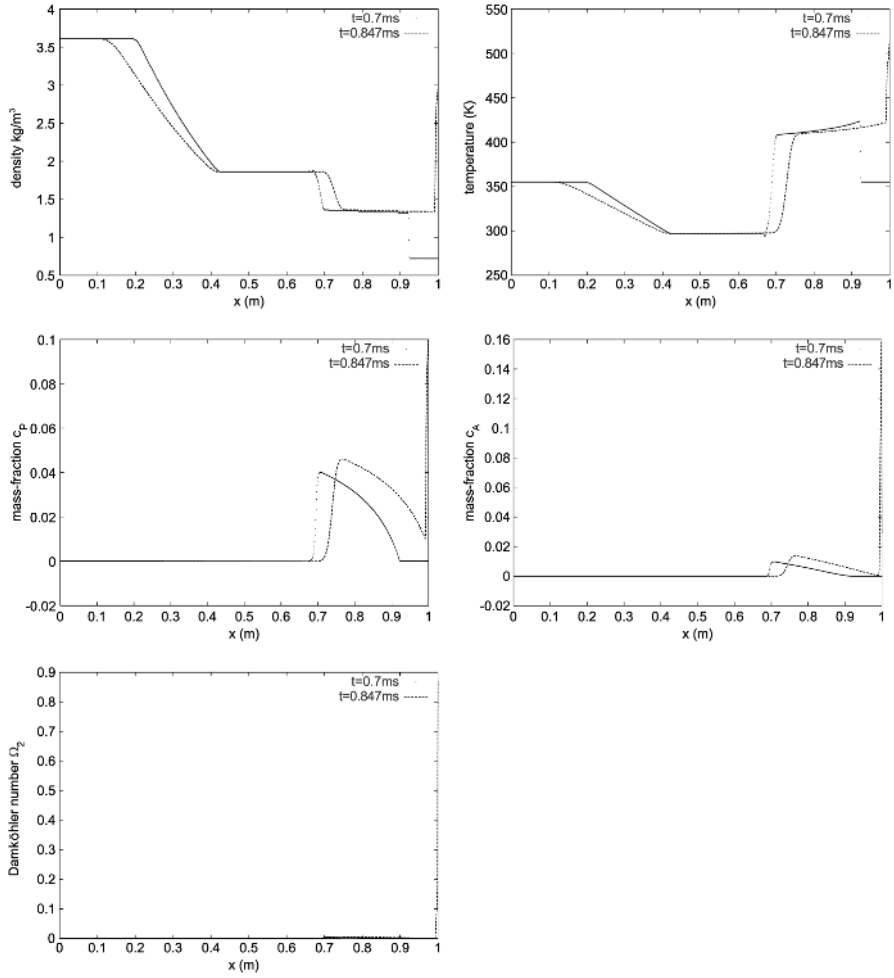

Figure 9.
Profiles at $t = 0.7$ and 0.847 ms for the reactor model with $\nu = 0.9$, $T_0 = 355$ K

Consider the later events at 0.847 ms. c_P is only non-zero ahead of the contact that has moved from 0.69 to 0.72 m. The reason for this is two-fold; reactant c_P that existed between $0.69 < x < 0.72$ at time $t = 0.7$ ms has been carried by the local velocity ahead of the contact. Further c_P can no longer be locally created between $0.69 < x < 0.72$ m as at 0.847 ms, the temperature here is 300 K – at this temperature, negligible gasification occurs. Ahead of the contact and behind the shock, c_P continues to increase due to the combined effect of convected c_P along with local production due to the high temperatures immediately ahead of the contact. There is no c_P ahead of the shock wave as the local temperatures are too low and convected material is travelling slower than the shock wave. Since the shock reflects from the right-hand boundary, the

temperature at the boundary experiences a step increase to $T \approx 490\,\mathrm{K}$. The increased temperature at this boundary will change the course of events: referring back to the phase plane for some insight of chemical timescales at these temperatures; for initial conditions $T_0 = 490\,\mathrm{K}$, $c_P(x,0) = 0$, $c_A(x,0) = 0$, numerical simulations have indicated that the induction time is approximately 0.06 ms and it will also take approximately the same time for the mass-fraction c_P to attain its maximum, $c_P = 0.1$. These events are translated to the history of events at the right-hand boundary (Figure 10). After the shock has reflected, c_P starts to rapidly increase whilst the temperature starts to decrease first due to latent heat requirements. It actually takes much less than 0.06 ms after the reflection, for ignition to be induced since the reflected shock is interacting with convected mass-fractions c_P and c_A still travelling towards the right-hand boundary (as these lag behind the shock). After this time, the timescale of the chemical reaction is much smaller than that associated with convection; the characteristic time of the chemical reaction is approximately $t_{\mathrm{reac}} = O(10^{-11})$ whilst the wave motion timestep associated with the Courant condition is $t_{\mathrm{conv}} = O(10^{-6})$. Computing much further after this point would not only take many computational hours but also it is likely that discontinuous waves would not be captured correctly – the difficulty associated with numerical solutions for these types of problems will be explored further in the next section. Any practical computation would benefit from assuming that the

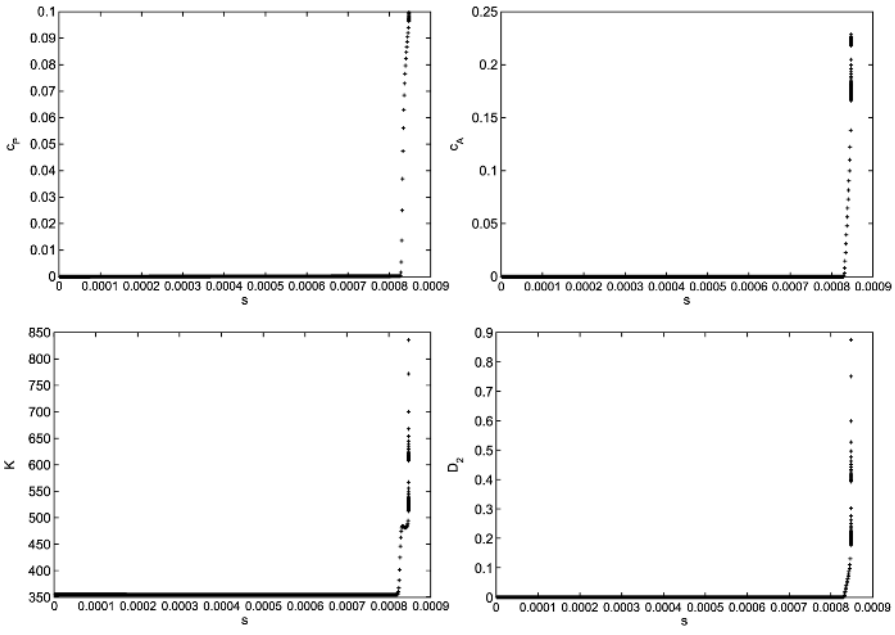

Figure 10.
History at right-hand boundary for $\nu = 0.9$ and $T_0 = 355\,\mathrm{K}$

chemistry is occurring so fast that equilibrium conditions could be assumed, as examined by Clarke and Lowe (1996) and Lowe and Clarke (1999).

The case above involved conditions such that one shock reflection was sufficient to provoke ignition. Generally, the location of the saddle point (Figure 3) controls the go/no-go criteria and how many shock reflections (from the sides of the chamber) are necessary before ignition will occur will depend on this saddle point. *If* the system is completely adiabatic (as assumed) there is an infinite supply of solid reactant, eventually the gas must ignite. However, this would not necessarily be the case if additional physics, such as heat-loss from the reactor, were included in the calculation.

Test problem for $\nu = 1.1$

Initial conditions for the shock-tube problem will be given as:

$$T(x,0) = 1,050\,\mathrm{K}, \qquad c_A(x,0) = 0, \qquad c_P(x,0) = 0,$$

$$p = \begin{cases} 101,400, & x \leq 0.5\,\mathrm{m}; \\ 1,014,000, & x > 0.5\,\mathrm{m}. \end{cases} \tag{15}$$

As above, we wish to explore the case in which local flow conditions provide temperatures above the critical temperature; to achieve this the initial temperature of the shock-tube problem is higher and so is the initial pressure ratio compared to the earlier section. In the case $\nu = 1.1$, recall that the critical temperature for ignition is $T_{\mathrm{crit}} \approx 1,328\,\mathrm{K}$. In Figure 11, the inert solution indicates that the local temperature ahead of the contact is above T_{crit} and one might therefore expect a successful ignition at some point during the wave propagation.

Figure 12(a) and (b) shows the temperature and mass-fraction c_A for the reactive problem at 0.05 and 0.1 ms, respectively. At 0.05 ms, it is clear that the temperature has radically fallen to about half the initial temperature throughout most of the domain. This occurs due to the rapid timescales associated with the chemical rates for initial conditions $T_0 = 1,050\,\mathrm{K}$ – this is

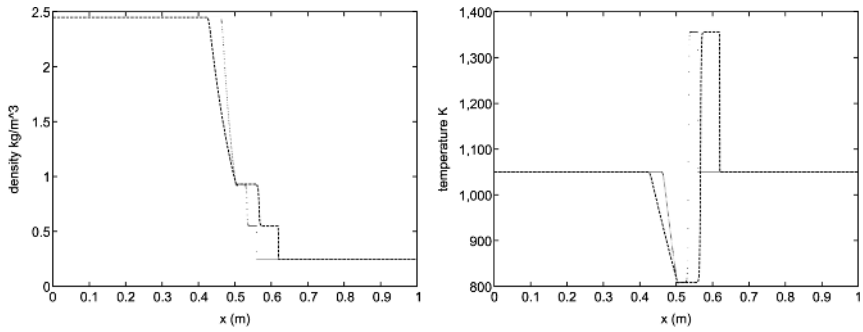

Figure 11.
Profiles at $t = 0.05$ and 0.1 ms for the inert shock-tube problem $T_0 = 1{,}050\,\mathrm{K}$

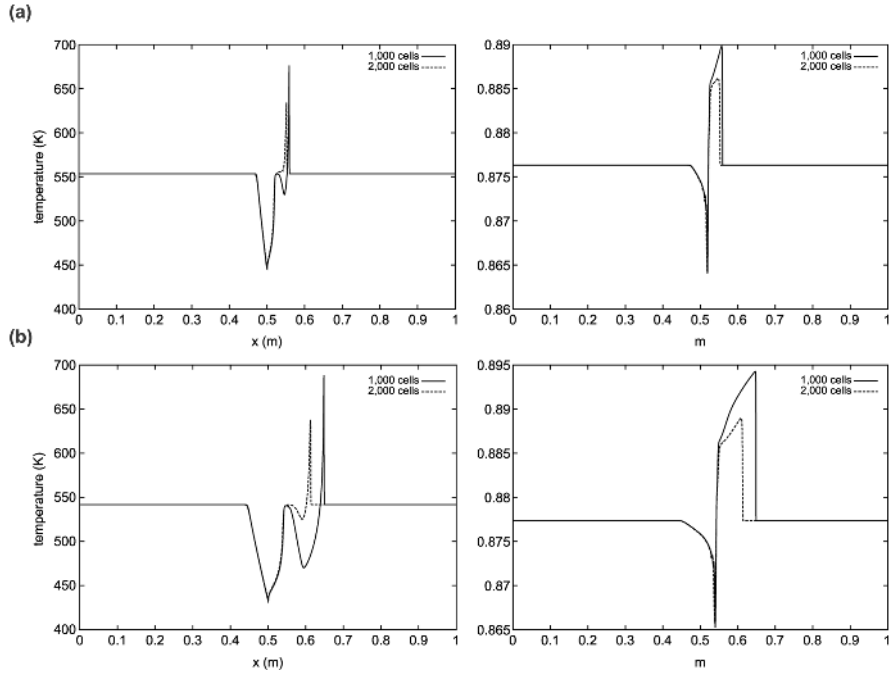

Figure 12.
Temperature and mass-fraction c_A profiles at (a) 0.05 ms and (b) 0.1 ms for the reactor model with $\nu = 1.1$, $T_0 = 1{,}050$ K

similar to the behaviour shown in Figure 6 in which the temperature reduces by half in less than 1 μs. At this time, mass-fraction c_P has already arrived at the theoretical maximum $c_P = 0.1$ and it can be seen from the plot c_A (Figure 12(a)) that most of the remaining gas in the chamber is composed of reactant mass-fraction c_A – at these low temperatures negligible amounts of c_A are reacting to give product gas.

After this dramatic behaviour the solution follows a much slower progress towards the stable node but perturbed by wave motion. In this situation, reactant gasification is continuing but at temperatures which are too low and therefore prevent gas-phase thermal runaway from occurring.

However, in this case there were problems with gaining convergence in the solution of the propagating shock. Figure 12(a) and (b) compares solution for a 1,000 cell mesh and 2,000 cell mesh; the fine mesh solutions indicate a different shock wave location – this is particularly visible at time $t > 0.05$ ms.

Numerical experiments indicate that the shock position depends on both space and time discretisations. This type of phenomenon is well documented in the literature for problems that involve non-equilibrium chemistry. More generally, hyperbolic systems that include stiff source terms (that is the timescales associated with the source terms are much shorter than those associated with the homogeneous hyperbolic system) are difficult to solve numerically. As discussed by LeVeque and Yee (1990), the non-physical

propagation of discontinuous features is *not* associated with either the use of an explicit shock-capturing methods or time-operator splitting – the chosen method of solution adopted here. Leveque compared an implicit predictor-corrector method, that did not require any splitting, with an explicit split method – both provided non-physical grid dependent shock-speeds. In fact, the reason for the problem is associated with the intrinsic numerical diffusion that is an attribute of *all* shock-capturing methods. Solution points that fall within the numerical "discontinuity" (due to numerical diffusion) will be rapidly taken to some (non-physical) equilibrium value due to the source terms. The effect of this is a shock moving at a grid-dependent speed since the number and position of points within the numerical discontinuity depend on the mesh size.

A shock-tracking method that explicitly tracks discontinuous features is a possible solution to this problem however, the extension of these methods to general multidimensional systems is still unproven. This study suggests that since the timescales associated with the chemistry are so much faster than the times associated with acoustic wave propagation it may be possible to derive a quasi-steady theory or ignition sub-model to make the application of this model practical.

Conclusions

The reactor model has been analysed for two different types of initial value problem. The first in the spatially uniform regime in which the singular points have been numerically located and the system integrated to provide the complete phase plane. The phase plane diagrams differ depending on the ratio of the activation energies of the endothermic gasification and the exothermic gas-phase combustion. The more realistic problem that cannot be analytically examined, that is the case in which there is initially neither reactant species P nor A in the vessel, has also been pursued and compared with earlier analytical studies. The effect of this additional degree of freedom does not qualitatively change the nature of the solution for the parameter set adopted, but the actual size of the timescales can change significantly. The model displays a number of different initiation events that could represent both successful and unsuccessful ignition processes that is known to occur.

The second type of initial value problem has involved the solution to the Euler equations including the source terms defined by the reactor model. Consequently, the solution combines chemical timescales associated with the rapidly changing source terms in combination with normal compressible flow dynamics. The work involved developing numerical solutions of what is a difficult problem due to the vastly different timescales involved – an understanding of the simple phase plane has been very valuable in this process. The role of singularities and different timescales that exist in the phase plane

(associated with the chemistry alone) has been translated to a more complex problem that involves coupling with the local flow conditions.

Future work must resolve the difficulties associated with these different timescales. The study suggests that numerical methods that explicitly track interfaces might prevent the difficulties associated with mesh convergence however, the radically different scales between the chemistry and the flow imply that asymptotic techniques might be a better solution methodology for this parameter set that involves chemical reactions of high activation energy. Clearly, if this is relaxed and the activation energies were reduced then the numerical solution described above would be the preferred choice as this methodology is easily extendible to more general multidimensional systems.

In this particular study, assumptions associated with the Damköhler number $\mathscr{D}_1$ were made to help make direct comparisons with the earlier theoretical study – this could be relaxed in further work. The effect of heat-loss on the reactor model would be interesting to deduce whether a greater range of solution is possible.

This study does not take explicit account of volume-fraction associated with the gasification of solid material, that is two-phase effects. A more sophisticated model for the solid gasification might include the computation of the solid-surface temperature T_s. This would mean that the gasification rate would be an Arrhenius expression based on T_s, rather than inferring that an Arrhenius rate based on gas temperature is sufficient.

References

Clarke, J.F. (1996), "A reactor model for ignition and burning of a gasifying solid", *Journal of the Chemical Society: Faraday Transactions*, Vol. 92 No. 16, pp. 2951-8.

Clarke, J.F. and Lowe, C.A. (1996), "Combustion with source flows", *Mathematical and Computer Modelling*, Vol. 24 No. 8, pp. 95-104.

Gray, P. and Scott, S.K. (1990), *Chemical Oscillations and Instabilities: Non-linear Chemical Kinetics*, Clarendon Press, Oxford.

Lowe, C.A. (1996), *CFD Modelling of Solid Propellant Ignition*, PhD thesis, Cranfield University Press, Cranfield, Bedfordshire.

Lowe, C.A. and Clarke, J.F. (1999), "Aspects of solid propellant combustion", *Philosophical Transactions of the Royal Society*, Vol. 357 No. 1764, pp. 3639-54.

Press, W.H., Teukolsky, S.A. and Vetterling, W.T. (1992), *Numerical Recipes in Fortran: The Art of Scientific Computing*, 2nd ed., Cambridge University Press, Cambridge.

LeVeque, R.J. and Yee, H.C. (1990), "A study of numerical methods for hyperbolic conservation laws with stiff source terms", *Journal of Computational Physics*, Vol. 86, pp. 187-210.

Further reading

Lowe, C.A. and Clarke, J.F. (2001), "The Euler equations with source terms revisited", *Godunov Methods: Theory and Applications*, Kluwer Academic/Plenum, Dordrecht/New York, NY.

Received February 2002
Revised March 2003
Accepted May 2003

Rarefied, superorbital flows in an expansion tube

V. Wheatley, H.S. Chiu, P.A. Jacobs, M.N. Macrossan, D.J. Mee and R.G. Morgan

Department of Mechanical Engineering, Centre for Hypersonics, The University of Queensland, Brisbane, Australia

Keywords *Rarefied flow, Expansion tube, Computational modelling, Modelling, Flow, Numerical analysis*

Abstract *This paper describes a free-piston driven expansion tube and its instrumentation. The facility is used to generate rarefied flows at speeds of approximately 10 km/s. Although the flow in the tube itself is in the continuum regime, rarefied flow conditions are achieved by allowing the test gas to further expand as a free jet into the facility's test section. The test flow is surveyed to provide bar-gauge pressure measurements. Numerical simulation is then used to describe more fully the test flow properties. The flows produced are suitable for the aerodynamic testing of small models at superorbital speeds and should provide data that are suitable for the calibration of Direct Simulation Monte-Carlo codes.*

Introduction

In the past decade, there has been a resurgence of interest in rarefied, hypervelocity flows. This interest can be chiefly attributed to two factors; the increasing use of aerobraking maneuvers to save fuel on interplanetary missions (Moss, 1995), and the fact that a greater understanding of rarefied hypervelocity flows is required to optimise the design of re-entry vehicles (Gupta *et al.*, 1997). In particular, accurate predictions of the surface heating, temperature, and flow field quantities during re-entry are required so that the weight of the thermal protection system can be minimised in order to increase the payload capacity. Obtaining accurate predictions by computational fluid dynamics (CFD) methods requires accurate modelling of the flow field chemistry, gas-surface interaction, body and shock slip and the thermochemical nature of the flow field (Gupta, 1996).

Owing to the extreme conditions encountered during re-entry, and the associated modelling difficulties, it becomes essential to calibrate the CFD codes against the experimental data for a wide range of flow conditions. While some codes have proven to be accurate for the flows that can be obtained in present ground based test facilities, calibration for the high energy, rarefied hypervelocity flows encountered during re-entry has only been possible using relatively scarce flight data. The most suitable numerical technique for the

The experimental work was supported by Australian Research Council Grant 97/ARCL99. The computer time was provided by the High Performance Computing Unit at The University of Queensland.

International Journal of Numerical Methods for Heat & Fluid Flow
Vol. 14 No. 4, 2004
pp. 512-537

0961-5539
DOI 10.1108/09615530410532277

calculation of the flow properties is the Direct Simulation Monte Carlo (DSMC) method (Bird, 1994), in which the motions and collisions of the gas molecules are simulated on a computer. Gupta *et al.* (1997) compared the results from DSMC and a number of continuum CFD codes with the flight data from the Japanese Orbital Re-entry Experiment (OREX) vehicle. While the flight data agreed quite well with the DSMC predictions for altitudes greater than 84 km, there were still significant discrepancies at altitudes of around 95 km.

To remedy this situation an experimental validation of DSMC for hypervelocity conditions should be undertaken. Unfortunately, present experimental facilities that produce rarefied gas flows (such as the DLR Göttingen continuous operation hypersonic vacuum wind tunnel (Dankert, 1996) and the SR3 low density facility (Allegre, 1992)) are limited to stagnation temperatures of around 2,500 K and hence test speeds of under 2.5 km/s, whereas a flow speed of the order of 10 km/s is required to simulate the conditions encountered during an aerobraking maneuver.

One possible method for generating rarefied hypervelocity flows is to modify an expansion tube (Morgan, 1997). In 1998, a pilot study was conducted on the development of a rarefied hypervelocity test facility using the X1 expansion tube at The University of Queensland (Wendt *et al.*, 1998). In the pilot study rarefied flow was generated by operating the tube at low densities and then expanding the flow into the dump tank via a conical nozzle attached to the exit of the tube. This generated a flow of argon in the transitional regime at 8.8 km/s, with a test flow duration of 60 μs. A 50 mm diameter central core flow was produced with a spanwise Pitot pressure variation of 30 per cent. Unfortunately, these variations make the flow unsuitable for most experiments, where a nominally uniform core flow is required. Another problem identified in the pilot study was the unacceptable large amount of time-variation in the experimental data. In addition to this, there were found to be significant differences between the experimental data and the results from a CFD simulation, pointing to inadequacies in the simulation technique.

To continue the study into developing a rarefied hypervelocity test facility, a new series of experiments has been conducted using a free jet to expand a flow of nitrogen into the dump tank (Macrossan *et al.*, 2000). The results of these experiments consist of Pitot pressure histories at discrete locations throughout the dump tank and static pressure histories at several points along the expansion tube from which shock speeds can be calculated. More information on the flow field is required before precise testing can be carried out in the facility. This information could be obtained from an accurate CFD model of the flow through the facility.

This paper presents the experimental data in conjunction with computational estimates. Once the accuracy of the CFD model has been verified, more detailed information can be extracted from the simulation data that is available from the experimental data. Most importantly, it is possible to

quantify the variation of flow parameters across the test flow; this determines whether or not the flow is suitable for experiments. The divergence of the core flow can also be determined along with the degree of rarefaction of the flow. The final CFD model can also be used to predict the performance of the experimental facility at different operating conditions. This enables the establishment of a tentative range of rarefied flows that can be produced in the facility.

Experimental facility

The X1 expansion tube at the University of Queensland is a small scale, free piston-driven expansion tube (Paull *et al.*, 1988). X1 was the first expansion tube to be driven by a free piston driver and could be used to produce superorbital flows (i.e. flight speed above 8 km/s or total enthalpy over 30 MJ/kg), with test speeds of up to 13 km/s.

The layout of X1 configured with a simple free-piston driver is shown in Figure 1. The facility consists of the following components: a high pressure cylinder called the compression tube, which initially contains the driver gas and the 3.4 kg free piston; an annular reservoir which stores the compressed air that is used to drive the free piston; a lower pressure cylinder referred to as the shock tube, which initially contains the test gas; a cylinder referred to as the acceleration tube, which is initially filled with very low pressure acceleration gas; and finally, a large dump tank/test section with a volume of 0.15 m^3 which is also initially filled with low pressure acceleration gas. The geometries of sections were: compression tube length of 2.30 m and internal diameter of 100 mm; shock tube length of 2.09 m and diameter of 38.1 mm; acceleration tube length of 2.91 m and diameter of 38.1 mm.

The driver and shock tube are separated by a steel diaphragm known as the primary diaphragm. During operation of the facility, the compressed air in the annular reservoir propels the free piston down the compression tube, compressing the driver gas. At some point, the pressure of the driver gas exceeds the burst pressure of the primary diaphragm, causing it to rupture. The high pressure driver gas then expands into the shock tube and generates a shock wave that rapidly compresses the low pressure test gas. This shock wave, which is referred to as the primary shock, propagates along the length of

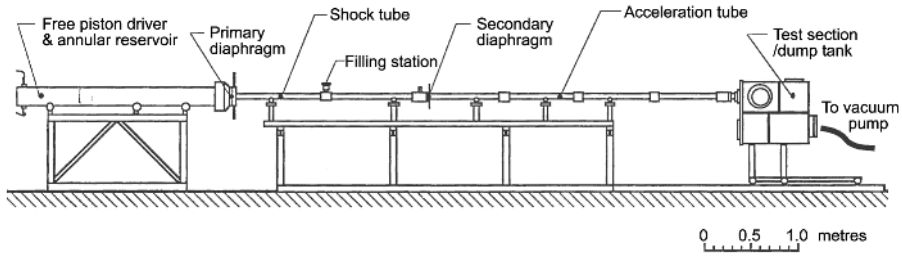

Figure 1.
Layout of the X1 expansion tube

the shock tube compressing and accelerating the test gas. This process is illustrated via the distance-time (x-t) wave diagram in Figure 2, along with the other processes that occur in X1.

Upon reaching the end of the shock tube, the primary shock ruptures the light plastic secondary diaphragm, which initially separates the test gas from the acceleration gas. For ideal expansion tube operation, the secondary diaphragm is assumed to be massless and to rupture instantaneously, (Figure 2). The compressed test gas is then processed by an unsteady expansion and begins to expand into the acceleration tube generating the secondary shock, which compresses and accelerates the low pressure acceleration gas. The unsteady expansion that propagates upstream through the test gas (downstream in the laboratory reference frame as expansion waves travel at velocity u-a and the shock compressed test gas is supersonic) serves to expand it to the desired test conditions. The test flow begins with the passage of the contact surface between the acceleration and the test gas past the model location. The test flow at the model location is terminated by one of the following two events; the arrival of the tail of the unsteady expansion, or the arrival of the disturbance caused by the reflection of the head of the expansion off the contact surface between the driver and the test gas.

Usually, the expansion tube facilities are operated in such a way as to produce flows with high static and total pressures. To generate a rarefied hypervelocity test flow in X1, relatively low initial fill pressures were used in the shock and acceleration tubes. The resultant flow at the end of the acceleration tube was then further expanded as a free jet into the dump tank. Helium was used as the driver gas and nitrogen was used as both test and acceleration gases. The set of nominal fill conditions used in the experiments include 536 Torr of helium in the compression tube, 14.5 Torr nitrogen in the shock tube and 15 Pa nitrogen in the acceleration tube and dump tank. It is assumed that the gas temperatures, after filling, were same as the ambient temperature of 296 K. The primary steel diaphragm had a thickness of 0.55 mm and a burst pressure of approximately 19.3 MPa. The light, secondary diaphragm consisted of 23 μm thickness cellophane with an approximate burst pressure of 100 kPa.

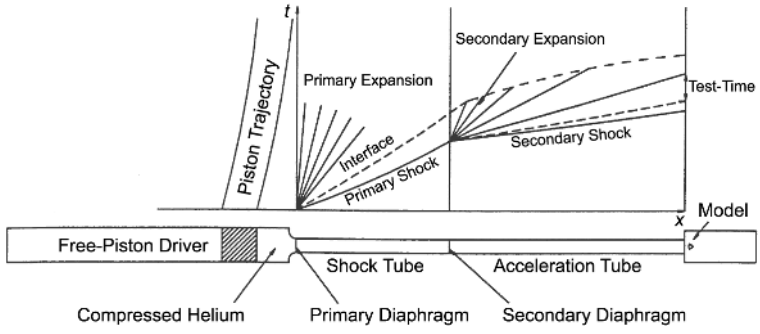

Figure 2.
Ideal wave diagram of the shock and expansion processes that produce the test flow in X1

Instrumentation

The flow field in the dump tank was surveyed using bar gauges specifically designed to give fast response Pitot pressure measurements in the impulsively started flow. Surveys of the radial Pitot pressure distribution were made at six axial locations between 25 and 340 mm from the exit of the acceleration tube. Bar gauges were used in preference to conventional Pitot probes with piezoelectric pressure transducers due to slow response of such probes in low-density, short duration flows. This poor performance was due to the shielding that was used to protect the pressure transducer from erosion caused by diaphragm fragments travelling at high speeds with the flow. The bar gauges used during low density operation of X1 are shown in Figure 3. They are a modified form of the conventional bar gauge. To improve the aerodynamic shielding of the bar and the survivability of the gauge, a steel disc of 9 mm diameter and 1 mm thickness was attached to the front of each bar. Although the addition of the disc slows the response of the bar gauge, its rise time is still only around 5 μs.

Two types of strain sensing elements were used in the bar gauges during the program of low-density testing in X1: piezoelectric polymer films (Smith and Mee, 1996) and semiconductor strain gauges (Kulite type ACP-120-300). Piezoelectric film with an axial length of 10 mm was wrapped around each bar, with its most sensitive axis aligned with the bar axis. Two strain gauges were mounted on opposite sides of each bar in a bending compensation arrangement allowing the axial strain in the bar to be measured. The strain gauge amplifier had a rise time of 1 μs.

The calibration of the bar gauges using PCB impact hammers (type 086-C04 and 086-D80) is described by Macrossan *et al.* (2000). The accuracy of this calibration was estimated to be ± 5 per cent. The calibration of the bar gauges was then checked by placing it in a known flow produced by a shock tube. This was done to account for the curved bow shock that forms in front of the gauge, causing the pressure on the disc to vary from close to the Pitot pressure at the center, to lower values near the edge of the disc. From the shock tube tests, the overall uncertainty in the measured disc average pressure was estimated to be ± 7 per cent for average pressures of the same order as those at the exit of the expansion tube. Away from the exit of the tube in the expansion tube tests, the Pitot pressure drops to as low as 3 per cent of the value at the acceleration tube exit causing the uncertainty in the bar gauge measurements to increase. At the most, distant locations included in the flow field survey, the uncertainty

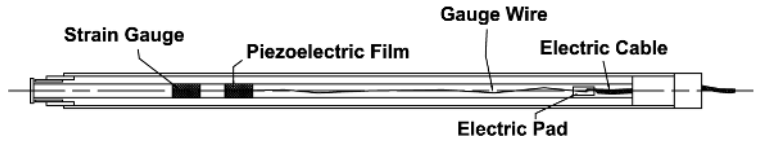

Figure 3.
Bar gauge design for low-density, impulsively started flows

in the disc average pressure was estimated to increase to a maximum of ± 15 per cent.

During the low-density experiments in X1, a large spike in the signal from the strain sensing devices was recorded upon arrival of the flow at the bar gauge locations. The spike duration was typically around 10 μs and was attributed to ionization of the flow as it is stagnated at the front of the bar gauge. The spike was separated from the pressure signal by positioning the strain sensing devices on the bar such that the spike had subsided by the time the stress waves generated by the flow arrived at the transducer locations.

Static wall pressure was monitored at a number of locations along the expansion tube using commercially available PCB piezoelectric transducers (111, 112 and 113 series). These transducers have a diameter of 5.5 mm and a response time of between 1 and 2 μs. The transducers were mounted flush to the tube wall to minimise the response time. The manufacturer's calibration factors were used to convert the recorded voltages to pressures. The designations, locations (distances from the acceleration tube exit), sensitivities, types and serial numbers of the active static pressure transducers in X1s shock tube and acceleration tube are presented in Table I. The static pressure traces from these transducers are used to calculate the primary and secondary shock speeds.

Experimental data

For each test, the static pressures along the tube were recorded at the transducer locations (Table I) and bar gauge pressures were recorded at up to three discrete locations in the dump tank. The data acquired during shot S5_157 are presented here as an example of the data obtained during a typical test. Chiu (2000) gives the report for the full set of experimental data. The static pressure histories measured during this shot by the transducers in the shock tube are shown in Figure 4. Note that the signal from transducer ST2 becomes saturated before any steady level is reached and the recorded traces terminate at the transducer locations before the arrival of the unsteady expansion. The primary shock speed was calculated to be 5.24 km/s from the shock arrival times at the transducer locations. Using this shock speed and assuming

Transducer	Location (mm)	Sensitivity (V/kPa)	Serial number	Transducer type
ST1	3,585	1.508×10^{-4}	8487	111A22
ST2	3,410	1.670×10^{-2}	15290	112A22
ST3	3,233	1.460×10^{-4}	9533	111A22
AT1	2,718	7.304×10^{-3}	14534	112A21
AT3	2,018	1.500×10^{-2}	15292	112A22
AT5	1,076	7.562×10^{-3}	14536	112A21
AT7	376	4.120×10^{-3}	9569	113A21
AT8	120	1.624×10^{-2}	10633	112A22

Table I. Active static pressure transducers in the shock and acceleration tubes. Distances are measured upstream of the acceleration tube exit

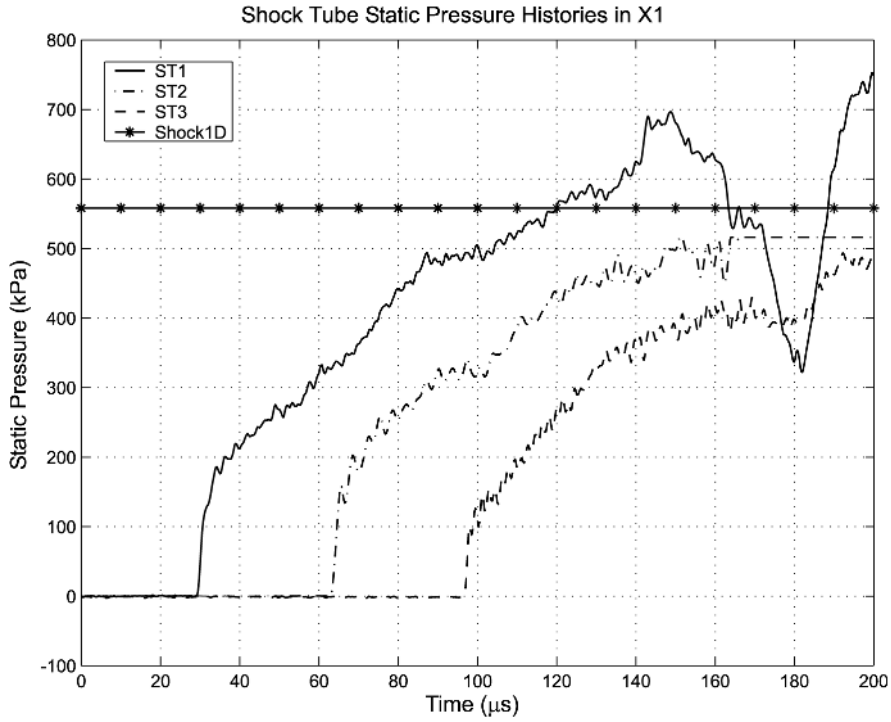

Figure 4.
Measured static pressure traces from transducers in the shock tube during shot S5_157

a one-dimensional shock processing of the test gas (Shock1D), the flow conditions following the passage of the primary shock wave were estimated as: static pressure of 558 kPa, temperature of 7,040 K and a flow speed of 4.79 km/s.

The measured static pressures upstream of the secondary diaphragm show an initial jump with the arrival of the primary shock followed by a gradual rise until reaching the calculated value, approximately 100 μs, after the passage of the shock (Figure 4). Three factors that may contribute to the slow pressure rise behind the primary shock are: non-ideal rupture of the primary diaphragm; piston dynamics; and the geometry of the compression tube. The duration of the pressure rise, approximately 100 μs, is of the same order as the opening time of the diaphragm and it is expected that pressure waves will be generated as the diaphragm opens (Petrie-Repar and Jacobs, 1998). Upon the rupture of the primary diaphragm, an unsteady expansion travels back into the driver gas and, when the expansion propagates into the larger diameter section of the compression tube, compression waves form which travel downstream, gradually raising the pressure in the shock tube above the level behind the primary shock. Assuming quasi-steady flows and given fixed driver gas conditions, the area change in the driver tube may cause a factor of three difference in the driven gas pressure when compared to a constant-area driver. This geometric effect was further explored by Wheatley (2000). The driver and

shock tube transition was modelled with a quasi-one-dimensional CFD code, L1D (Jacobs, 1999). When the unsteady expansion traversed the area change in the driver section, a pressure increase was produced behind the primary shock as expected, however, the pressure rise was small compared with that across the primary shock. Although it was a good candidate, the area change in the driver did not appear to be the cause of the gradual pressure rise observed in the experimental data. The simulations also indicated that the piston dynamics was not the cause either. This issue remains unresolved.

The static pressure histories from four of the transducers in the acceleration tube are shown in Figure 5. It can be seen that, prior to the arrival of the shock, the pressure indicated by the transducers is non-zero in some cases and shows some drift. This is associated with the acceleration sensitivity of the pressure transducers. The effects of transducer drift are most obvious in the low pressure traces near the exit of the acceleration tube. The transducers indicate pressures near the lower limit of their range in these traces. For example, transducer AT7 indicates about 10 kPa but the PCB type 113A21 pressure transducer has a calibrated range of 0.345-1,330 kPa. The reason the gauges are operated near the low end of their range is that they need to be able to

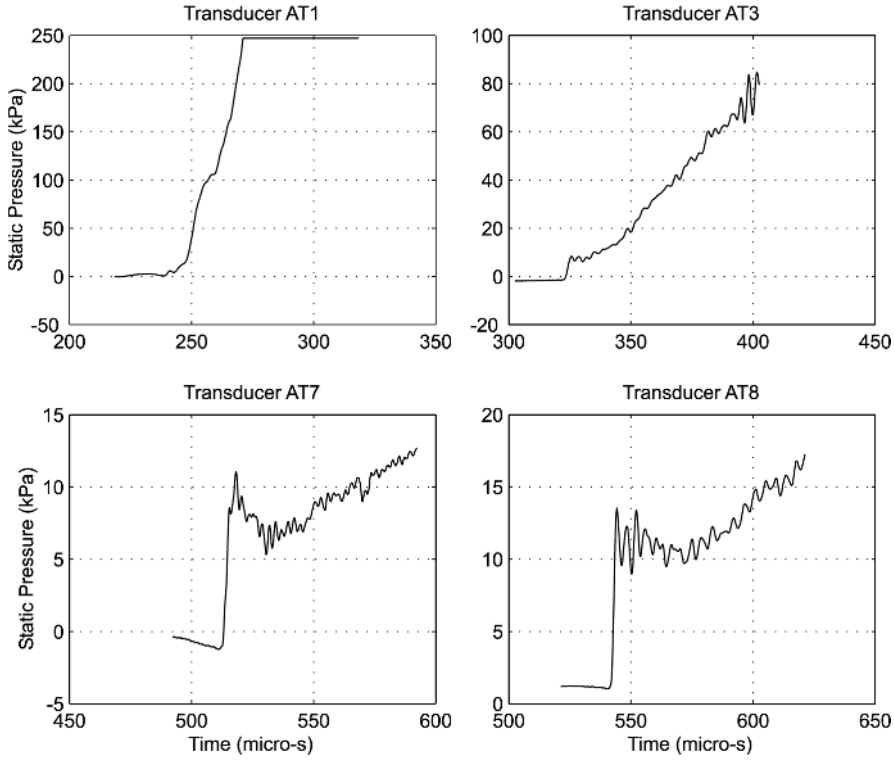

Figure 5.
Measured static pressure traces from transducers in the acceleration tube during shot S5_157

withstand the very high pressure associated with the arrival of the unsteady expansion and, a little later, the arrival of the driver gas. The acceleration effects can be minimised by carefully mounting the transducers in the tube. This was done in the present experiments and the drifts shown in Figure 5 are the smallest that could be achieved with the current transducers. The speed of the secondary shock near the exit of the acceleration tube was estimated to be 8.98 km/s, from the difference between the shock arrival times at transducers AT7 and AT8. The estimated uncertainty in the measured shock speeds is ± 1 per cent. During shot S5_157, three bar gauge pressure histories were recorded at an axial distance of 125 mm from the acceleration tube exit (Figure 6). The histories were recorded on the centerline and at a radius of 28 mm, both above and below the centerline. The noise caused by the ionization of the flow when it first impacts on the bar gauges can be seen in the histories shown in Figure 6 at a time of around 350 μs. To account for shot-to-shot variations from the nominal conditions, the bar gauge pressure histories were normalised by an estimate of the test gas Pitot pressure at the exit of the acceleration tube, $P_{\text{pitot,e}}$, for each particular shot. Estimates of the test gas Pitot pressure at the exit plane of the acceleration tube were calculated using the TUBE program (R.G. Morgan, personal communication). TUBE computes the state of the test flow from the fill conditions and experimentally measured shock speeds

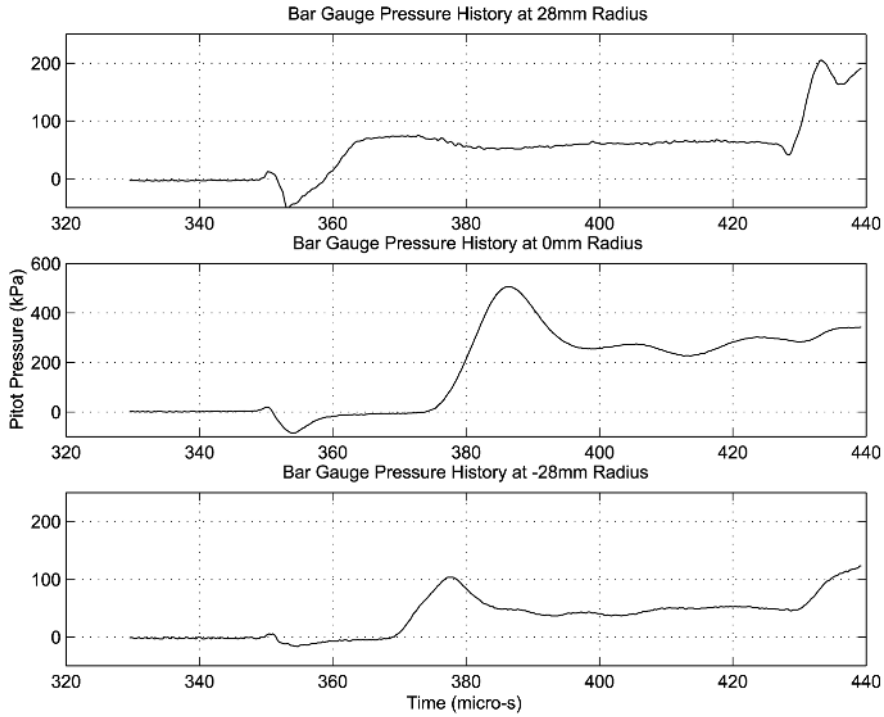

Figure 6.
Measured bar gauge pressure histories from shot S5_157 at 125 mm from the acceleration tube exit

assuming inviscid, one-dimensional flow which is either chemically frozen or in equilibrium. The nominal value of the Pitot pressure at the acceleration tube exit was computed to be 627 kPa. This value was used to normalise the CFD results. The uncertainty in the calculated Pitot pressure is dominated by the ± 1 per cent uncertainty in the secondary shock speed and was estimated to be ± 10 per cent.

The results of the flow field survey at all six axial locations and nine different radii are plotted (Figure 7). The values, $(P_{bar}/P_{pitot,e})_{av}$, are the nominally steady bar gauge pressures of the test gas, which have been normalised by the estimated Pitot pressure at the acceleration tube exit and averaged over a number of tests. For the region within 175 mm of the tube exit plane, the Pitot pressure profile is non-uniform, with a large peak near the centerline. By 225 mm, the Pitot pressure is uniform within experimental uncertainty. Even at this distance, the strong axial gradient of Pitot pressure near the centerline limits the suitability of the flow to the testing of blunt-body models with small axial lengths. From the Pitot pressure histories, it was determined that a nominally steady test time of 50 μs is available at 225 mm from the acceleration tube exit.

It was mentioned previously that the pressure measured using the bar gauges differs from the Pitot pressure due to the pressure variation over the

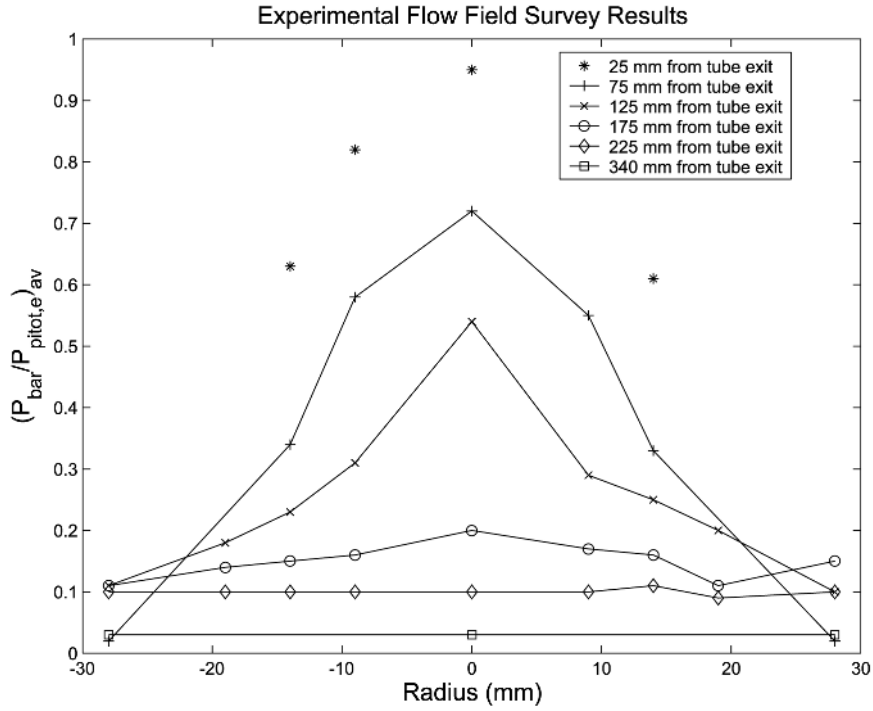

Figure 7.
Experimentally determined profiles of normalised, average bar gauge pressure at several axial locations in the dump tank

face of the disc attached to the front of the bar gauge. CFD simulations of nitrogen, impacting on a disc, normal to the flow, were run to determine the pressure distribution on the face of the disc. Both continuum and rarefied gas dynamics codes (Borque, 1999) were used. From these simulations, it was determined that the ratio of the average pressure on the disc to the Pitot pressure varies from around 0.9 or less for continuum flow, to around 0.95, depending on the Knudsen number. As an average adjustment, Pitot pressures computed using the continuum CFD code are multiplied by a factor of 0.93 for comparison with the bar gauge pressures.

Simulation of the acceleration tube flow

The MB_CNS code (Jacobs, 1998) was used to model the hypervelocity flow through the X1 facility. MB_CNS was built to simulate high-enthalpy transient-flow facilities and performs a time-integration of the Navier-Stokes equations for two-dimensional (planar or axisymmetric) compressible flows on a multiple-block structured mesh. The integral form of the governing equations is used, with the flow field being recorded as cell-averaged values. An explicit time-stepping scheme is used to update the conserved quantities within each cell. The code has a shock-capturing capability that is provided by a limited reconstruction of the flow-field data using quadratic patches combined with an adaptive flux calculator that is suitable for flows with very strong shocks. This flux calculator switches between the equilibrium-flux method (EFM) (Macrossan, 1989) and the AUSMDV flux calculator (Wada and Liou, 1994), with the more dissipative EFM, selected for cell interfaces that are near a shock. The code includes thermochemical models for a variety of gas, including nitrogen in chemical equilibrium.

The high speeds of shock waves in the shock tube of the X1 facility cause the shock-processed test gas to reach very high static temperatures, around 10,000 K in some cases. This results in parts of the flow having high levels of dissociation and possibly some ionisation. The test gas cools again as it is processed by the unsteady expansion in the acceleration tube. To determine the conditions of the test gas at the end of the acceleration tube, an ideal (but very expensive) calculation would include the finite-rate chemistry of the shock-compressed and then expanded test gas. Other possibilities are to use equilibrium chemistry or to assume that the test gas chemistry remains frozen at the state behind the primary shock. Neely and Morgan (1994) found that equilibrium chemistry calculations through the unsteady expansion gave results in reasonable agreement with experiments in X1, while frozen chemistry calculations did not. Equilibrium chemistry modelling has been used for the present simulations.

As a shock travels down the acceleration tube, a boundary layer grows in the flow behind it. As this boundary layer becomes quite thick at the end of the tube, it will have a significant influence on the flow field in the dump tank

during the test time. A boundary layer also grows behind the primary shock as it travels down the shock tube. For the operating condition discussed here, this boundary layer will have little effect on the test flow for two reasons. First, the flow in the shock tube has a much higher density and lower velocity than that in the acceleration tube, resulting in a much thinner boundary layer. Second, when the primary shock arrives at the secondary diaphragm, the gas that comprises the test flow is located immediately behind the primary shock where a boundary layer has just begun to grow. The thicker boundary layers further upstream of the secondary diaphragm should have little influence on the test gas as it is expanded down the acceleration tube. The net result of this is that the cross-stream variation in the test gas as it exits the acceleration tube is chiefly due to two-dimensional effects in the acceleration tube. This implies that only the acceleration tube and dump tank must be modelled two-dimensionally, provided an inflow condition at the secondary diaphragm station can be accurately determined from either experimental data or a one-dimensional flow calculation.

The dump tank is actually a rectangular prism, but has been modelled as a cylinder with a radius equal to the minimum distance from the centerline to one of the dump tank walls (Figure 8). Since the simulation time expires before any waves reflected from the modelled dump tank wall encroach on the test flow, this approximation should not affect the estimate of the test conditions. In the simulations, the length of the acceleration tube was taken to be 2.91 m. For convenience, the co-ordinate x is defined as being the axial distance from the exit of the acceleration tube, and the co-ordinate r as being the radial distance from the axis of the acceleration tube.

Inflow conditions

Since the MB_CNS model of the X1 facility is truncated upstream of the secondary diaphragm, an acceleration tube inflow condition is needed. It is possible to make a purely analytical estimation of the performance of an expansion tube, and hence the acceleration tube inflow condition, based on the facility dimensions, fill states and the expected driver performance. Such an

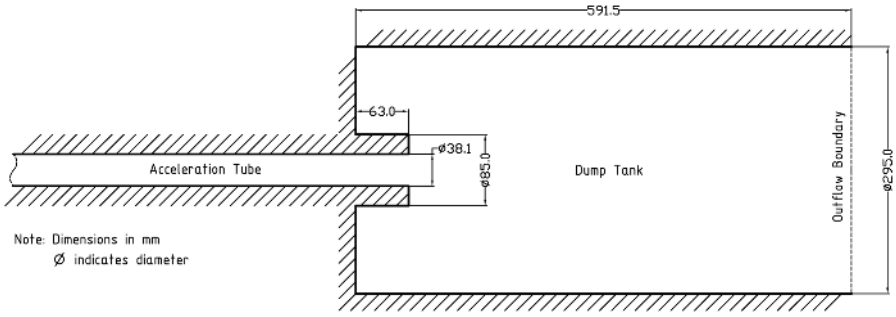

Figure 8.
Modelled geometry of the end of X1's acceleration tube and dump tank. The acceleration tube diameter is 38.1 mm and the dump tank diameter is 295 mm

analysis was carried out by Trimpi (1962) for dissociating air assuming ideal diaphragm rupture. However, experimental investigations have revealed that this approach is inaccurate (Jones, 1965; Shinn and Miller, 1978). Neely (1995) cites viscous effects on the flow, due to the low quiescent gas pressures in the shock and acceleration tubes, as the primary source of the inadequacies of such analytical predictive techniques. He goes on to state that one technique to minimise this complication, and any non-ideal driver effects, is to use the shock speeds observed during the operation of the expansion tube to calculate the shock strengths in the test and acceleration gas. This approach of using experimentally observed shock speeds is adopted to calculate the state of the gas flowing into the acceleration tube, which is initially taken to be the conditions behind the primary shock as it arrives at the secondary diaphragm. Even though the cause of the gradual pressure rise in the shock tube is not known (Figure 4), the flow in the acceleration tube is simulated using a fixed set of post-shock conditions, obtained shortly before the shock arrives at the secondary diaphragm.

Using the conditions behind the primary shock, our inflow conditions assumes that the secondary diaphragm operates ideally. This implies that when the primary shock arrives, the diaphragm material is instantly removed from the flow path so that a reflected shock is not generated. The effects of non-ideal diaphragm rupture were examined by Wheatley (2000) and it was found that the experimental conditions in X1 could be better simulated with the inclusion of a non-ideal diaphragm rupture model. The holding time model used by Wilson (1992) was incorporated into the simulation because the more realistic diaphragm-inertia model (Morgan and Stalker, 1992) could not be easily implemented in a fixed-grid CFD code such as MB_CNS. Equilibrium chemistry modelling was used in preference to a frozen composition as it was shown that this provides a solution in reasonable agreement with that computed using the finite-rate chemistry modelling (Wheatley, 2000).

To implement the holding time model in the MB_CNS simulation, two blocks were added to the computational grid. The first block extends from a location in the shock tube at $x = -3.11$ m to the location of the shock reflected from the secondary diaphragm at the expiration of the holding time. This block initially contains gas with the conditions behind the primary shock.

Roberts *et al.* (1997) calculated effective holding times for a number of light diaphragms used in an expansion tube. This was done by constructing an x-t wave diagram from heat flux signals recorded in the region of the diaphragm, and extrapolating to determine the delay between the impact of the primary shock and the time at which the secondary shock is transmitted into the acceleration tube. For a planar polyethylene diaphragm that is 13 μm (similar to the diaphragms used during low-density testing in X1), the holding time was found to be of the order of 10 μs, over a range of operating conditions. For this

reason, a holding time of 10 μs was adopted and the reflected shock was calculated to be at $x = -2.9185$ m, after this the holding time expired.

The second block extends from the reflected shock location to the secondary diaphragm station at $x = -2.91$ m, and initially contains gas with the conditions behind the reflected shock. These are a static pressure of 6.83 MPa and temperature of 10,280 K. At these conditions, dissociated nitrogen atoms comprise nearly 42 per cent of the gas mixture and there is a small amount of ionisation.

When this simulation was initiated, there was no barrier to prevent the gas behind the reflected shock from suddenly expanding into the acceleration tube, thus simulating an instantaneous rupture of the secondary diaphragm after the 10 μs holding time.

Grid definition and resolution

The computational models extend from the location $x = -3.11$ m in the downstream end of the shock tube to a plane part way along the dump tank at $x = 0.5285$ m. At the inflow plane, the flow condition is the test-gas condition after the passage of the primary shock. The other end of the computational domain is modelled as a supersonic outflow boundary. This assumes that waves do not reflect off the downstream end wall of the dump tank and affect the flow within the simulation time. The computational grid for the acceleration tube has 3,900 cells in the axial direction and 30 cells in the cross-flow direction. The cells are radially clustered towards the wall in order to adequately capture the boundary layer growth. This can be seen in Figure 9, which shows a sample of the computational grid near the exit of the acceleration tube. For the most part, the computational grid for the dump tank has 300 cells in the axial

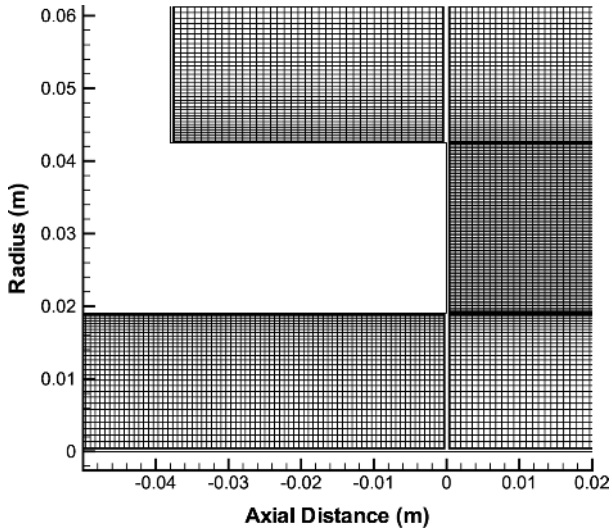

Figure 9.
Sample of the computational grid at the entrance of the dump tank

direction and 210 cells in the cross-flow direction. The cells are initially filled with ambient temperature nitrogen with a pressure of 15 Pa.

This arrangement for the computational grid was arrived after a number of simulations were run on coarser grids, in which some of the flow features did not appear to be adequately resolved. By refining the grid to the current level, the flow features around the shocks and contact surfaces were sharpened, but the overall solution appeared to be grid independent. The final simulation required approximately 100 days of CPU time to solve on an SGI Origin 2000 supercomputer. The physical time taken to run the simulations was considerably less than this, around 30 days, as the simulation was run in parallel on several processors.

Simulation results compared with experimental data

Figure 10 shows a comparison of the computed static pressure histories at four transducer locations along the acceleration tube and the experimental pressure histories from these transducers. The experimental data have been shifted to align the arrival times of the shock. The computed shock speed was found to be 8.1 per cent, greater than the experimental value of 9.06 km/s. This error is significant and may be caused by the use of an equilibrium thermochemical

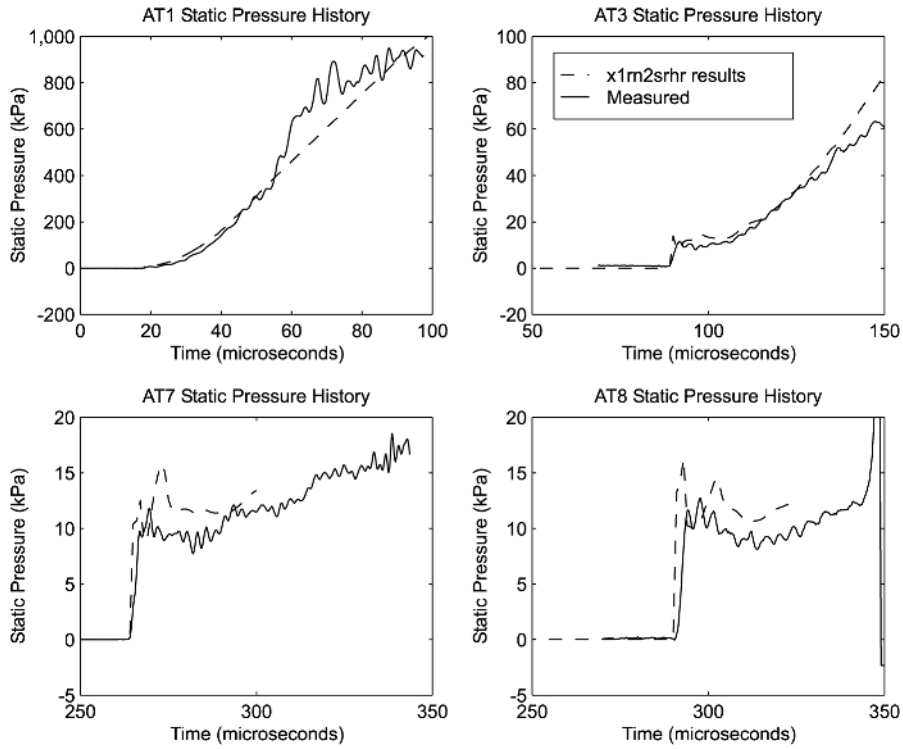

Figure 10.
Aligned computed and experimental static pressure histories in the acceleration tube of X1 at transducer locations AT1 ($x = -2.718$ m), AT3 ($x = -2.018$ m), AT7 ($x = -0.376$ m) and AT8 ($x = -0.120$ m). Experimental values are from shot S7_26

model. A frozen chemistry model produced a significantly lower shock speed so that one can expect a finite-rate chemistry model to perform better.

Despite the difference in shock speed, there is a very good agreement between the shape of the computational and experimental traces at early times (which are relevant to the expanded test flow conditions). The agreement between magnitudes of the computed and experimentally measured pressure histories is also quite good, with the higher pressures behind the shock which is caused by the overestimate of the shock speed. The pressure gradient in the latter part of the simulated expansion may be greater than that which is measured experimentally, because of the unmodelled effects of piston motion and shock tube dynamics. In the results of simulations, without the holding time model (Wheatley, 2000), it was seen that at transducer AT1, the experimental pressure continued to rise after the computed history had leveled off. This problem has been resolved by the inclusion of the holding time model, confirming that a reflected shock is generated during the rupture of the secondary diaphragm.

Figure 11 shows a comparison of the computed and experimental bar gauge pressure histories 175 mm from the exit of the acceleration tube at a radius of 14 mm. It can be seen that the agreement between the nominally steady levels

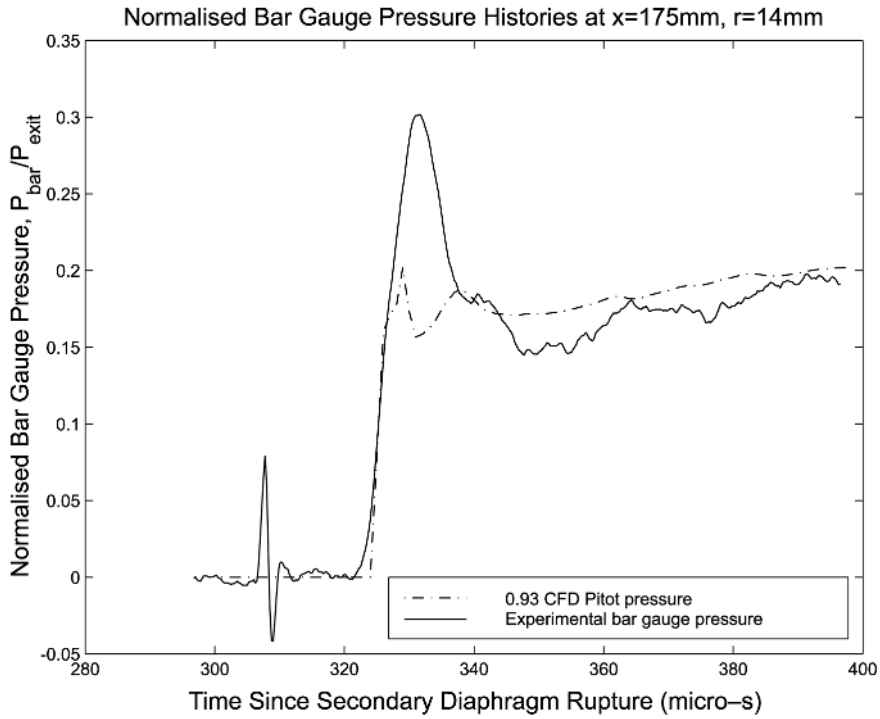

Figure 11.
Normalised bar gauge pressure histories 175 mm from the exit of the acceleration tube at a radius of 14 mm

of the two histories is quite good, however, in this case the magnitude of the Pitot pressure spike due to the reverse shock is far greater in the experimental history.

In Figure 12, a number of Mach number contour plots are presented that show the evolution of the flow field in the dump tank. At the time of the last frame of this figure, $t = 0.34$ ms, the test flow has just arrived at the nominal test location at $x = 225$ mm.

Figures 13-15 show a comparison of the full set of experimental bar gauge pressure profiles in the dump tank and the results of the simulation during the passage of the test gas. The agreement between both the shape and magnitude

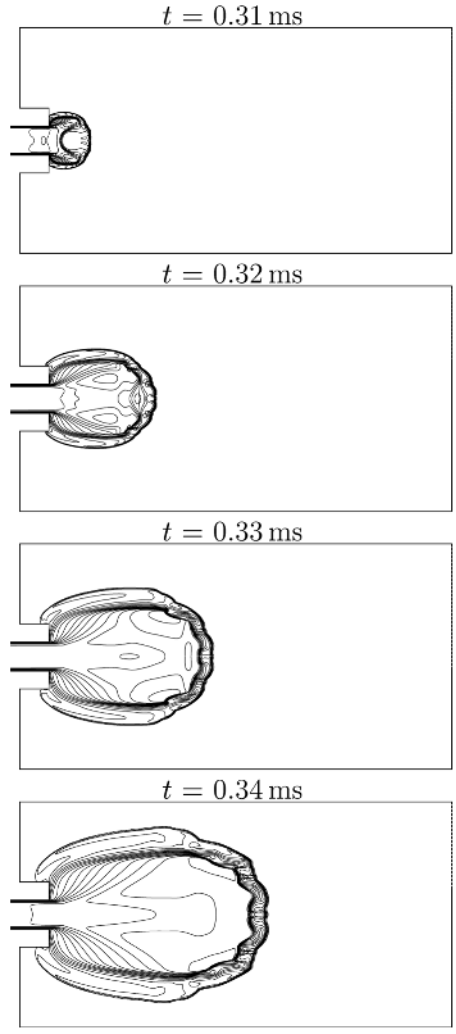

Figure 12.
Contour plots of Mach number showing the evolution of the flow field in the dump tank. Time t is the time since secondary diaphragm rupture

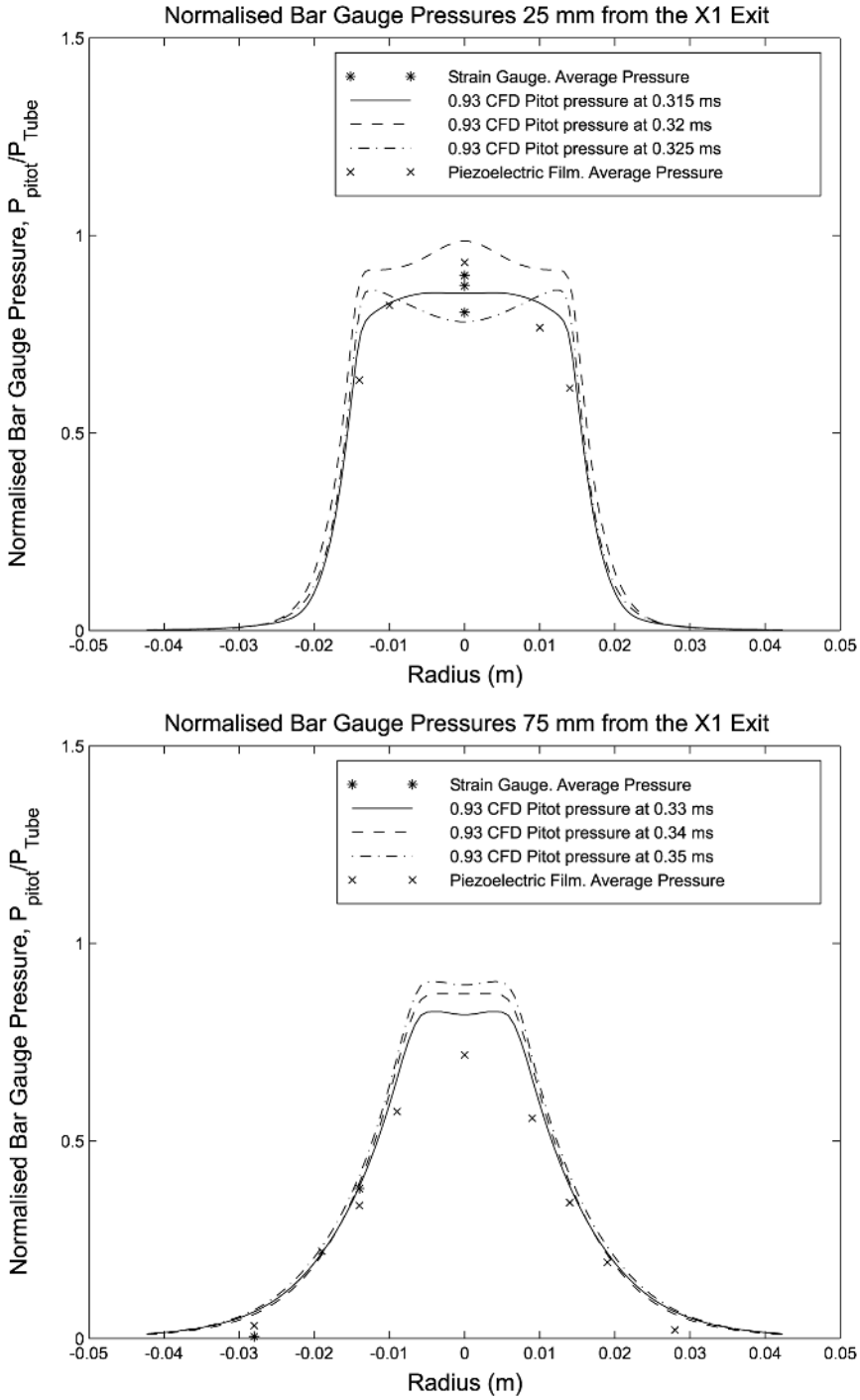

Figure 13.
Normalised bar gauge pressure profiles in the X1 dump tank at 25 and 75 mm from acceleration tube exit during the passage of the test gas

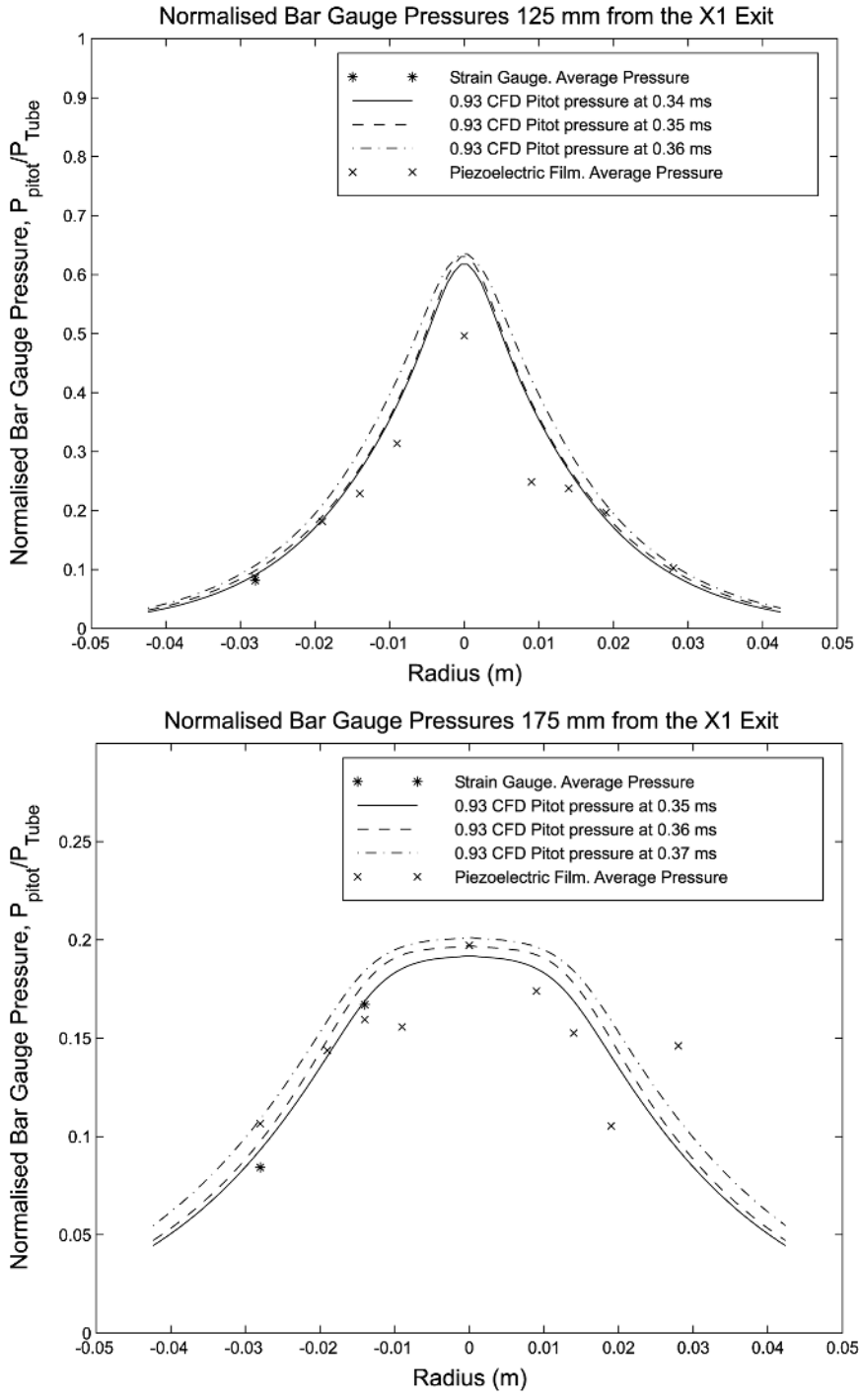

Figure 14.
Normalised bar gauge pressure profiles in the X1 dump tank at 125 and 175 mm from acceleration tube exit during the passage of the test gas

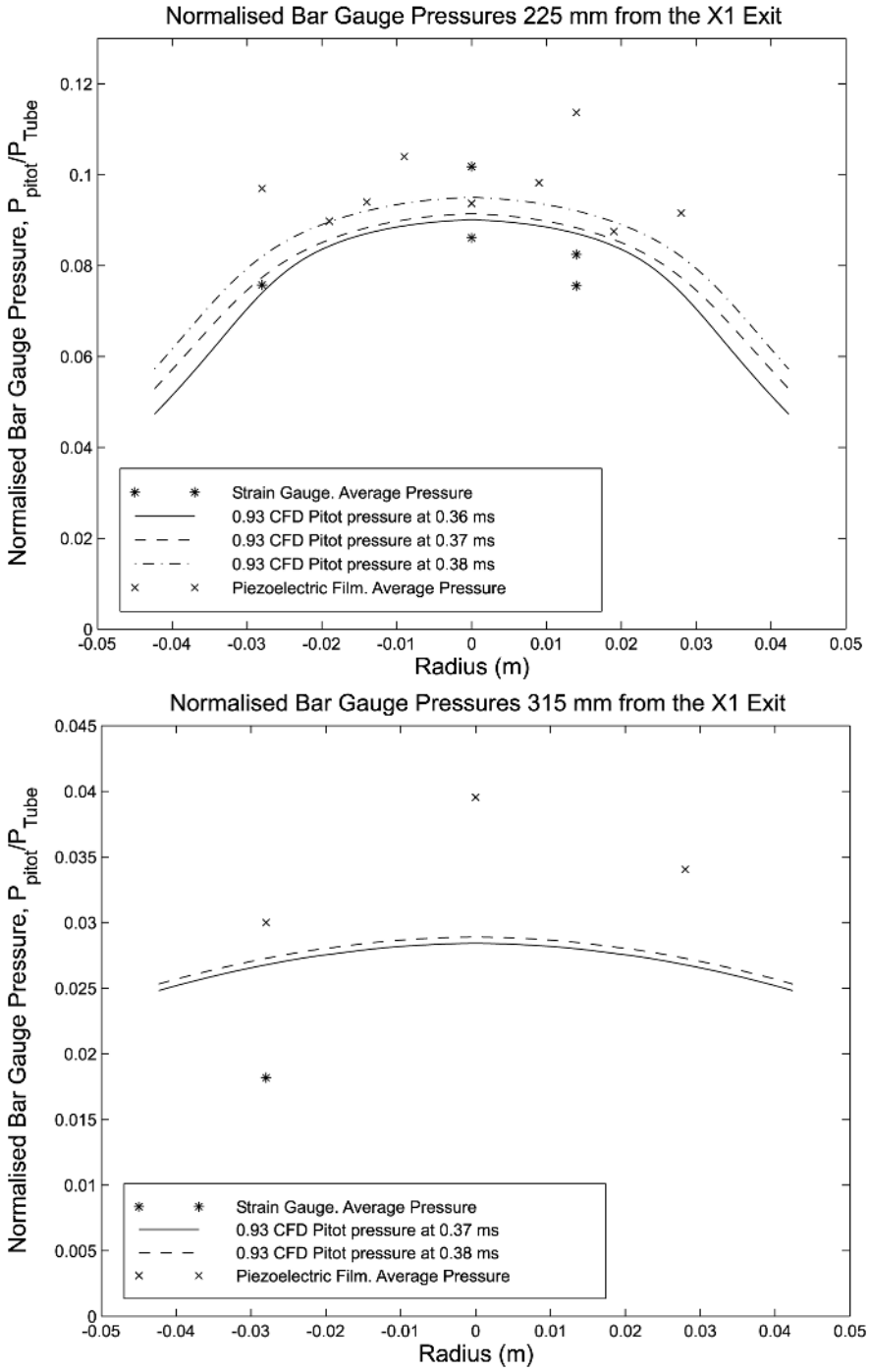

Figure 15.
Normalised bar gauge pressure profiles in the X1 dump tank at 225 and 340 mm from acceleration tube exit during the passage of the test gas

of the computed and experimental profiles is relatively good and, when compared with other simulation results (Wheatley, 2000), confirms that it is important to include the effects of non-ideal secondary diaphragm rupture in a computational model of the facility. From the profiles at 75 and 125 mm from the acceleration tube exit, it can be seen that the computed Pitot pressures near the centerline are slightly overestimated due to the secondary shock speed being overestimated by 8.1 per cent. At $x = 175$ mm, the divergence of the test flow has caused the core of high Pitot pressure flow to be somewhat spread across the dump tank. At the nominal test location, $x = 225$ mm, the Pitot pressure is reasonably uniform near the centerline, indicating that it would be suitable for experiments. The agreement between the computed and experimental profiles is quite good, considering the amount of scatter in the experimental data. In contrast, the experimental values at $x = 340$ mm are considerably higher than the computational results. This may be due to the high degree of rarefaction at axial locations, so far into the dump tank.

Breakdown parameter

For the operating condition used in this study, it was expected that the flow through the majority of facility would be in the continuum regime, only becoming rarefied as it expanded into the dump tank. The validity of using a continuum CFD code (such as MB_CNS) to simulate the low-density flow through X1 is assessed by evaluating the breakdown parameter, P, throughout the facility (Bird, 1994). The breakdown parameter is defined as,

$$P = \frac{\sqrt{\pi}}{2} S \frac{\lambda}{\rho} \left| \frac{\partial \rho}{\partial x} \right|$$

where ρ is the density and S the speed ratio, $u/(2RT)^{0.5}$. Physically, this parameter corresponds to the ratio of the mean time between molecular collisions, τ_c, and the time taken for the flow to traverse a length scale based on the macroscopic gradient of density. In any region of an expanding flow where the breakdown parameter is greater than 0.04, it is probable that the Navier-Stokes equations with no-slip boundary conditions will not give an accurate description of the flow (Bird, 1994). At the instant considered (350 μs), the breakdown parameter only exceeds 0.04 within the free jet into the dump tank. The computed contours of P in this region are shown in Figure 16. It can be seen that the core of the test flow is in the continuum regime, as P is well below 0.04, near the centerline. The high values of P in the flow that has expanded around the corner at the acceleration tube exit indicate that this region of the flow will be subjected to fairly strong non-continuum effects; the characteristic temperatures of the three thermal velocity components will be significantly different. It is expected that the flow in this region will not greatly affect the properties of the test flow near the centerline. The only other regions where the critical

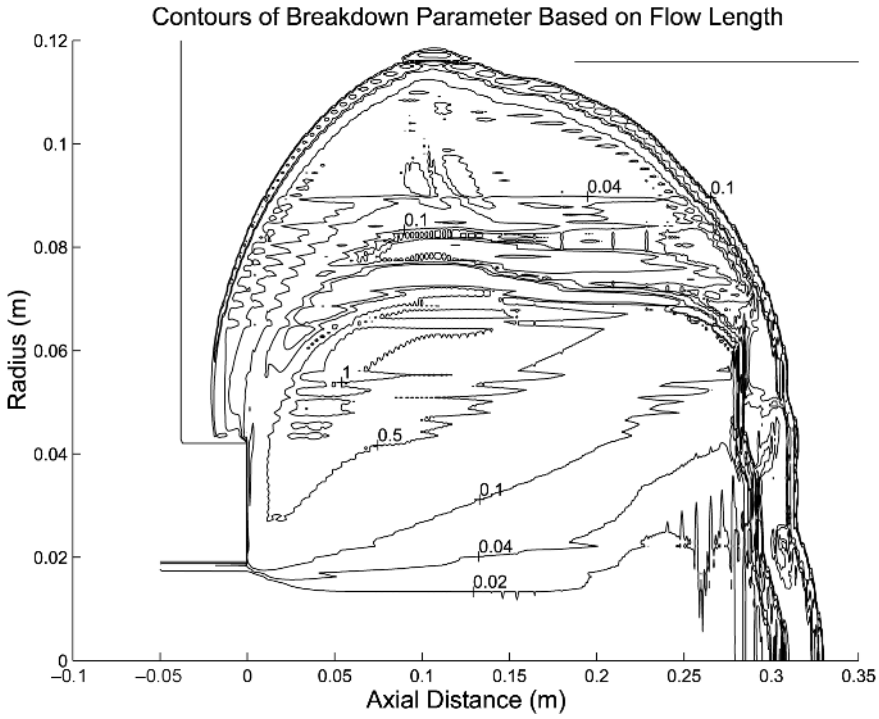

Figure 16.
Computed contours of the breakdown parameter, P, based on the macroscopic gradient of density at $t = 350\ \mu$s

value of P is exceeded are within the shocks, however, the accuracy of shock capturing Navier-Stokes solvers is not significantly affected by the non-continuum effects that occur within shocks (Cheng and Emanuel, 1995). Overall, it appears that the accuracy of the estimated core flow conditions from MB_CNS should not be severely affected by the non-continuum effects.

One of the goals of this study is to produce a test flow where the breakdown parameter based on model size, P_D, is of the order of 0.04. The value of P (the breakdown parameter based on macroscopic flow gradients) being less than 0.04 in the core flow does not compromise this goal because the size of the model should be considerably less than the length scale based on the macroscopic flow gradients. This is required to ensure that the flow over the model is approximately uniform.

Test-section flow properties

The profiles of some important flow properties at the nominal test location, $x = 225$ mm, are shown in Figure 17. The profiles shown are from $t = 370\ \mu$s, at which time the test flow is nominally steady. It is believed that the most significant errors in the estimated conditions are those in the flow speed, and hence the Pitot pressure and Mach number. It appears that other quantities

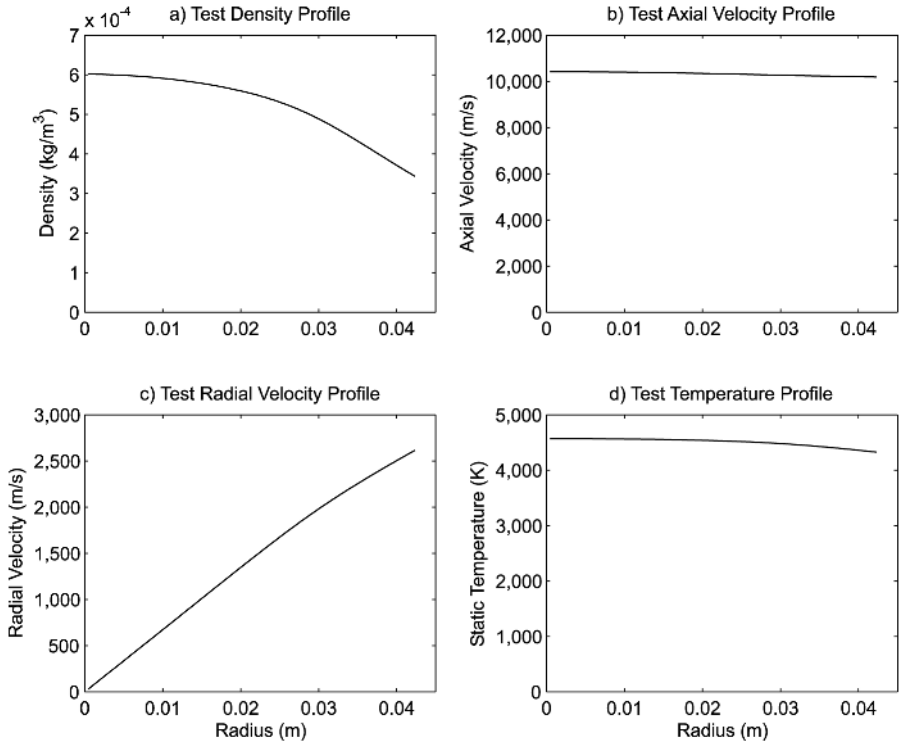

Figure 17.
Computed profiles of density, axial velocity, radial velocity and static temperature at the nominal test location in X1, 225 mm from acceleration tube exit. Profiles are from $t = 370\ \mu$s

have been estimated more accurately for the following reasons: the error of around 17 per cent in Pitot pressure near the centerline at $x = 75$ mm is approximately what is expected for an 8 per cent error in flow speed, which indicates that the estimate of density must be fairly accurate; the static pressure traces from near the exit of the acceleration tube indicated that the static pressure of the flow has been estimated with reasonable accuracy. It can be seen that the axial velocity is fairly constant across the test flow (Figure 17). The variation in Pitot pressure seen in Figure 15 is due to the variation in density across the test flow. The profile of radial velocity shows that the flow angularity increases linearly with radius. This may pose a problem for researchers who wish to test models with large widths.

Figure 18 shows the variation of rarefaction parameters, axial velocity and density in the test flow ($t = 370\ \mu$s and $x = 225$ mm) along the centerline of the dump tank. From the axial profile of the breakdown parameter based on an object size of 10 mm, it can be seen that at the nominal test location $P_D \approx 0.1$, so we could expect strong non-continuum effects in the flow over a model of this size. The large axial gradient of density is problematic for testing models with large axial lengths (Figure 18). Overall, the computational data presented in Figures 17 and 18 indicated that the test flow produced during low-density

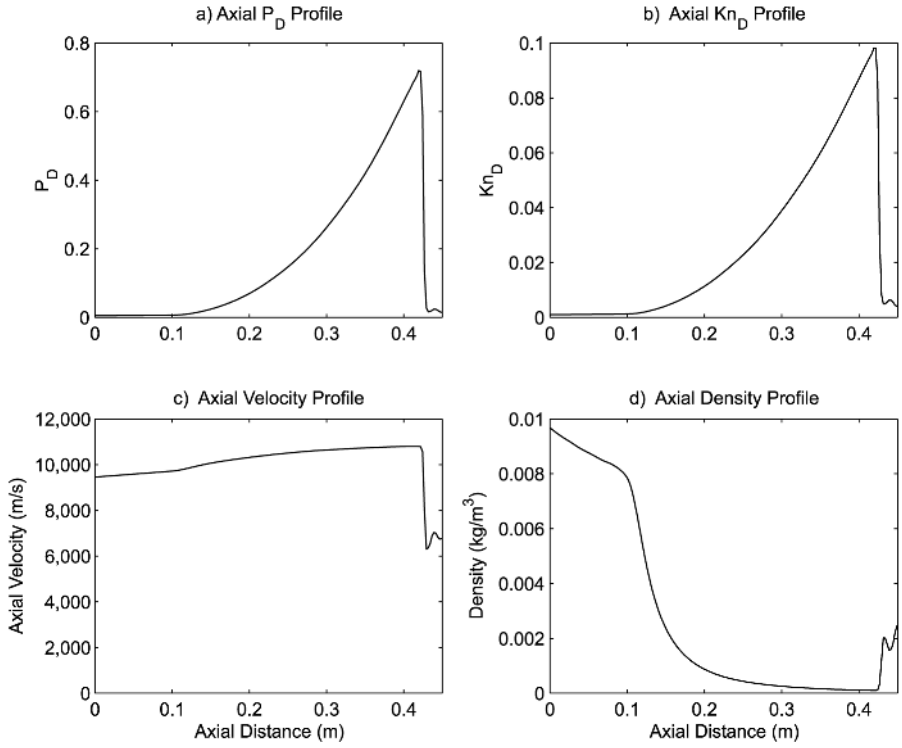

Figure 18.
Computed profiles of breakdown parameter, P_D, Knudsen number, Kn_D (based on $D = 10$ mm), axial velocity and density along the centerline in the dump tank. Profiles are from $t = 370\ \mu$s when the secondary contact surface is located at $x \approx 425$ mm

operation of X1 is suitable for the testing of relatively compact models with small diameters and that the flow conditions are similar to those encountered during an aerobraking maneuver. This similarity will allow computational techniques such as DSMC to be experimentally calibrated at high-enthalpy flow conditions.

Conclusions

By using an expansion tube and further expanding the test gas as a free jet, rarefied flows at superorbital speeds can be produced in a laboratory facility. The flows produced in the X1 facility have been surveyed using bar-gauge pressure transducers and further details have been obtained via numerical simulation. There is good agreement between most of the experimental data and the simulation results; however, some of the simulation results, such as shock speed, should be better estimated using a non-equilibrium thermochemical model. The test section flows, as produced for this study, were reasonably uniform and could be used to test small aerodynamic models. Data from these tests could then be used to calibrate other CFD codes for high enthalpy rarefied flow.

References

Allegre, J. (1992), "The SR3 low density wind-tunnel: facility capabilities and research development", AIAA Paper 92-3972.

Bird, G.A. (1994), *Rarefied Gas Dynamics and the Direct Simulation of Gas Flows*, Claredon Press, Oxford.

Borque, B. (1999) "Development of hypervelocity wind tunnel for rarefied flow", Undergraduate Thesis, University of Queensland.

Cheng, H.K. and Emanuel, G. (1995), "Perspective on hypersonic nonequilibrium flow", *AIAA Journal*, Vol. 33 No. 3, pp. 385-400.

Chiu, H.H. (2000), "Development of a test facility for hypervelocity rarefied flows", Departmental Report 2000/09, Department of Mechanical Engineering, University of Queensland.

Dankert, C. (1996), "DLR Göttingen hypersonic vacuum wind tunnels V1G and V2G and high vacuum wind tunnel V3G", Brochure, DLR, SM-SK-ATD, Bunsenstrasse 10, D-37073 Göttingen, Germany.

Gupta, R.N. (1996), "Viscous shock-layer study of thermochemical nonequilibrium", *Journal of Thermophysics and Heat Transfer*, Vol. 10 No. 2, pp. 257-66.

Gupta, R.N., Moss, J.N. and Price, J.M. (1997), "Assessment of thermochemical nonequilibrium and slip effects for orbital re-entry experiment", *Journal of Thermophysics and Heat Transfer*, Vol. 11 No. 4, pp. 562-9.

Jacobs, P.A. (1998), "MB-CNS: a computer program for the simulation of transient compressible flows", 1998 Update, Department of Mechanical Engineering Report 7/98, The University of Queensland, Brisbane, available at: http://www.mech.uq.edu.au/staff/jacobs/cfd/mb_cns/doc/mb_cns.html

Jacobs, P.A. (1999), "L1d: a computer code for the quasi-one-dimensional modelling of transient-flow facilities", Technical Report 1/99, Department of Mechanical Engineering, The University of Queensland.

Jones, J.J. (1965), "Some performance characteristics of the LRC 33/4-inch pilot tube using and unheated hydrogen driver", *4th Hypervelocity Techniques Symposium*.

Macrossan, M.N. (1989), "The equilibrium flux method for the calculation of flows with non-equilibrium chemical reactions", *Journal of Computational Physics*, Vol. 80 No. 1, pp. 204-31.

Macrossan, M.M., Chiu, H.H. and Mee, D.J. (2000), "A test facility for hypervelocity rarefied flow", in Gallis, B. (Ed.), *Proceedings of the 22nd International Symposium on Rarefied Gas Dynamics*, American Institute of Physics, New York, NY, p. 772.

Morgan, R.G. (1997), "A review of the use of expansion tubes for creating superorbital flows", AIAA Paper 97-0279.

Morgan, R.G. and Stalker, R.J. (1992), "Double diaphragm driven free piston expansion tube", *Proceedings of the 18th International Symposium on Shock Tubes and Waves*.

Moss, J.N. (1995), "Rarefied hypersonic flows: simulation, experiments and applications", *Proceedings of the 19th International Symposium on Rarefied Gas Dynamics*.

Neely, A.J. (1995) "Experimental and analytical study of a pilot superorbital expansion tube for aerothermodynamic testing to 13 km/s in air", PhD thesis, University of Queensland.

Neely, A.J. and Morgan, R.G. (1994), "The superorbital expansion tube concept, experiment and analysis", *The Aeronautical Journal*, Vol. 98 No. 973, pp. 97-105.

Paull, A., Stalker, R.J. and Stringer, I.A. (1988), "Experiments on an expansion tube with a free piston driver", *AIAA 15th Aero. Testing Conference*.

Petrie-Repar, P.J. and Jacobs, P.A. (1998), "A computational study of shock speeds in high performance shock tubes", *Shock Waves*, Vol. 8 No. 2, pp. 79-91.

Roberts, G.T., Kendall, M.A. and Morgan, R.G. (1997), "Shock-diaphragm interaction in expansion tubes", *21st International Symposium on Shock Waves*.

Shinn, J.L. and Miller, C.G. (1978), "Experimental perfect-gas study of expansion-tube flow characteristics", NASA Technical Paper 1317.

Smith, A.L. and Mee, D.J. (1996), "Dynamic strain measurement using piezoelectric polymer film", *Journal of Strain Analysis*, Vol. 31 No. 6, pp. 463-5.

Trimpi, R.L. (1962), "A preliminary theoretical study of the expansion tube, a new device for producing high-enthalpy short-duration hypersonic gas flows", NASA Technical Report R-133.

Wada, Y. and Liou, M.S. (1994), "A flux splitting scheme with high-resolution and robustness for discontinuities", AIAA Paper 94-0083.

Wendt, M., Macrossan, M., Jacobs, P.A. and Mee, D.J. (1998), "Pilot study for a rarefied hypervelocity test facility", *13th Australasian Fluid Mechanics, Conference*.

Wheatley, V. (2000) "Modelling low-density flow in hypersonic impulse facilities", Masters of Engineering Science Thesis, The University of Queensland.

Wilson, G.J. (1992), "Time dependent quasi-one dimensional simulations of high enthalpy pulse facilities", *AIAA 4th International Aerospace Planes Conference*.

Received January 2002
Revised May 2003
Accepted May 2003

Numerical simulation of inductively coupled plasma flows under chemical non-equilibrium

Gérard Degrez and David Vanden Abeele
von Karman Institute for Fluid Dynamics (VKI), Rhode St-Gense, Belgium
Service de Mécanique des Fluides, Université Libre de Bruxelles (ULB), Bruxelles, Belgium
Paolo Barbante
von Karman Institute for Fluid Dynamics (VKI), Rhode St-Gense, Belgium
Dipartimento di Matematica, Politecnico di Milano, Milano, Italy
Benot Bottin
von Karman Institute for Fluid Dynamics (VKI), Rhode St-Gense, Belgium
Institut Suprieur Industriel de Bruxelles (ISIB), Bruxelles, Belgium

Keywords *Numerical analysis, Plasma physics, Flow, Equilibrium methods*

Abstract *This paper presents a detailed review of the numerical modeling of inductively coupled air plasmas under local thermodynamic equilibrium and under chemical non-equilibrium. First, the physico-chemical models are described, i.e. the thermodynamics, transport phenomena and chemical kinetics models. Particular attention is given to the correct modelling of ambipolar diffusion in multi-component chemical non-equilibrium plasmas. Then, the numerical aspects are discussed, i.e. the space discretization and iterative solution strategies. Finally, computed results are presented for the flow, temperature and chemical concentration fields in an air inductively coupled plasma torch. Calculations are performed assuming local thermodynamic equilibrium and under chemical non-equilibrium, where two different finite-rate chemistry models are used. Besides important non-equilibrium effects, we observe significant demixing of oxygen and nitrogen nuclei, which occurs due to diffusion regardless of the degree of non-equilibrium in the plasma.*

The second author was supported by a grant from the Flemish Institute for the Promotion of Scientific-Technological Research in the Industry (IWT). The third author was supported by a Marie Curie Grant in the TMR program of the European Union. This work was partially supported by the INTAS Research Grant RFBR-95-1329 and benefited from fruitful discussions with Project Coordinator Dr G.S.R. Sarma (DLR, Germany) and Project partner Dr A.F. Kolesnikov (Institute for Problems in Mechanics, Moscow).

International Journal of Numerical Methods for Heat & Fluid Flow
Vol. 14 No. 4, 2004
pp. 538-558

0961-5539
DOI 10.1108/09615530410532286

1. Introduction

During their entry in atmosphere, space (re-)entry vehicles, whether manned such as the space shuttle or unmanned such as planetary probes, are exposed to very high temperature flows and are therefore protected against excessive heating by heat shields made out of thermal protection materials (TPMs). Before their actual use in space vehicles, the performance of TPMs must be tested in ground facilities. It is precisely for this purpose that the European Space Agency recently financed, together with the Belgian Federal Office of Scientific, Technical and Cultural affairs, the construction at the von Karman Institute (VKI) of a large scale (1.2 MW) inductively coupled plasma (ICP) flow wind tunnel (Plasmatron) (Bottin *et al.*, 1999a).

In this kind of facility (Figure 1), the operating gas (air or any other mixture of gases reproducing a particular planetary atmosphere) is heated in an electrodeless manner to a partially ionized plasma state with peak temperatures around 10,000 K. The gas is injected into a quartz tube surrounded by a copper inductor. A radio-frequency electrical current runs through the inductor and induces a secondary current through the gas inside the quartz tube, which heats up by means of ohmic dissipation.

A key characteristic of TPMs is their catalytic properties. For a given wall temperature and free stream properties (total enthalpy, pressure and velocity), the wall heat flux can depend strongly on the wall catalycity if the boundary layer developing around the body is far from chemical equilibrium. Contrary to arc heated wind tunnels, in which the flow is polluted by metallic impurities produced by electrode erosion, inductively heated wind tunnels produce plasma jets of high chemical purity and are therefore, particularly, suited for the determination of material catalycity.

Except in very special conditions (e.g. at very low pressures), material catalycity cannot be measured directly, but has to be determined indirectly

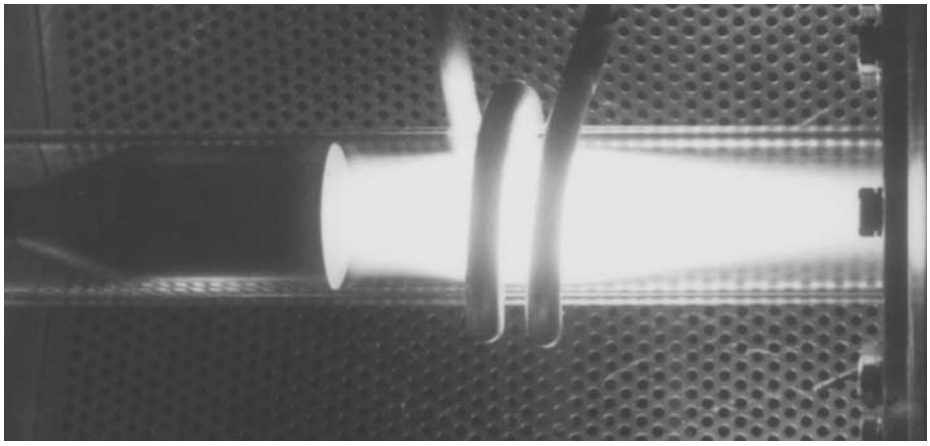

Figure 1.
Small ICP torch in operation (VKI mini-torch, argon, 1 atm, 3 kW, 27 MHz)

through its effect on wall heat flux. A methodology to determine wall catalycity, which relies on both experimental and computational results, has been developed by Russian researchers (Kolesnikov, 1999; Kolesnikov *et al.*, 1998). The implementation of this methodology at the VKI has motivated the development of a series of computational tools for the simulation of inductively coupled plasma flows and hypersonic (re-)entry flows, to be used in conjunction with experimental techniques for the characterization of the flow in the VKI Plasmatron and of TPM catalycity. This paper describes the developed numerical model of high-pressure air ICPs under local thermodynamic equilibrium (LTE) and under chemical non-equilibrium (but at thermal equilibrium).

Air ICPs under LTE have been intensively studied by Vasil'evskii *et al.* (1996). Models of high-pressure ICPs under both thermal and chemical non-equilibrium have been presented earlier by Benoy (1993), Kulumbaev (1999), Mostaghimi *et al.* (1987) and Semin (1991). However, these models only dealt with the relatively straightforward case of argon plasmas and cannot be easily extended to more complex mixtures, such as air, for two main reasons. First, the modeling of thermodynamic and transport phenomena in multi-component molecular plasmas is considerably more complex than for argon, which is a three-component (Ar, Ar^+, e^-) atomic plasma. In particular, one should provide an adequate model of diffusion processes between the numerous species in the plasma. Secondly, when switching from argon to molecular plasmas, the increased number of species and the need to include stiff chemistry drives up the computational cost of the numerical simulations. To obtain converged results in reasonable computation times, the use of efficient iterative methods then becomes essential.

2. Governing equations

ICP flows can be described by an axisymmetric model in which the outer inductor is modelled by a series of parallel current-carrying rings, assumed infinitely thin for simplicity (Figure 2). The governing equations consist of the conservation equations of gas dynamics supplemented by a magnetohydrodynamic induction equation for the induced electric field.

2.1 Conservation equations of gas dynamics

Despite small amplitude oscillations due to the high frequency electromagnetic (EM) field, ICP flows may be considered quasi-steady (Vanden Abeele and Degrez, 2000). Indicating the axial, radial and azimuthal coordinates by, respectively, z, r and θ, the set of conservation equations may be written in a compact axisymmetric form:

$$\frac{\partial(r\mathbf{F}^{c})}{\partial z}+\frac{\partial(r\mathbf{G}^{c})}{\partial r}=\frac{\partial(r\mathbf{F}^{d})}{\partial z}+\frac{\partial(r\mathbf{G}^{d})}{\partial r}+\mathbf{S}, \tag{1}$$

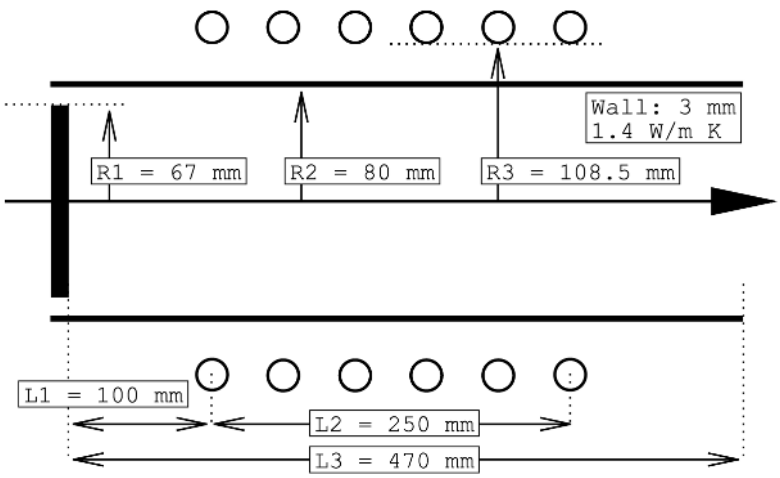

Figure 2.
VKI plasmatron torch geometry

where $\mathbf{F}^{c}$, $\mathbf{G}^{c}$ and $\mathbf{F}^{d}$, $\mathbf{G}^{d}$ are the convective and diffusive fluxes, respectively, and $\mathbf{S}$ represents the source terms in the equations. Because ICP flows are characterized by low Mach numbers ($M < 0.1$), we may neglect the contribution of kinetic energy (negligible with respect to the plasma enthalpy) as well as the work of the shear stresses (negligible with respect to the heat fluxes). Since Reynolds numbers are low as well ($Re \sim 500$), the flow field is laminar and no modelling of turbulence is needed. Assuming thermal equilibrium (single temperature problem), then the precise expressions of the various fluxes are:

$$\mathbf{F}^{c} = (\rho u, \rho y_s u, \rho u^2 + p, \rho uv, \rho uw, \rho uh)^t \tag{2}$$

$$\mathbf{G}^{c} = (\rho v, \rho y_s v, \rho uv, \rho v^2 + p, \rho vw, \rho vh)^t \tag{3}$$

$$\mathbf{F}^{d} = \left(0, -J_{zs}, \tau_{zz}, \tau_{zr}, \tau_{z\theta}, -\sum_{s=1}^{n_s} J_{zs} h_s - q_z\right)^t \tag{4}$$

$$\mathbf{G}^{d} = \left(0, -J_{rs}, \tau_{zr}, \tau_{rr}, \tau_{r\theta}, -\sum_{s=1}^{n_s} J_{rs} h_s - q_r\right)^t \tag{5}$$

$$\mathbf{S} = (0, r\dot{m}_s, rF_z, p + \rho w^2 - \tau_{\theta\theta} + rF_r, -\rho vw + \tau_{r\theta}, r\dot{Q})^t, \tag{6}$$

where ρ is the global density, y_s the species mass fractions ($s = 1, \ldots, n_s$), p the pressure, u, v and w the axial, radial and azimuthal velocity components, h the internal enthalpy, $\vec{J}_s$ the diffusive mass flux of species s, h_s the species

enthalpies per unit mass, τ_{ij} the viscous stresses, $\vec{q}$ the conduction heat flux, $\dot{m}_s$ the chemical source terms, and $\vec{F}$ and $\dot{Q}$ are the body force and volume heat sources/sinks, respectively, which are specified in Section 2.2 (equation (11)). While the considered flows are axisymmetric, they may contain a significant amount of "swirl" (transverse velocity component w), which serves to stabilize the flow field.

The shear stresses may be further expressed as

$$\begin{aligned}
&\tau_{zz} = \mu\left(2\frac{\partial u}{\partial z} - \frac{2}{3}\nabla\cdot\vec{u}\right) \quad \tau_{zr} = \mu\left(\frac{\partial u}{\partial r} + \frac{\partial v}{\partial z}\right) \quad \tau_{rr} = \mu\left(2\frac{\partial v}{\partial r} - \frac{2}{3}\nabla\cdot\vec{u}\right)\\
&\tau_{z\theta} = \mu\frac{\partial w}{\partial z} \quad \tau_{r\theta} = \mu\left(\frac{\partial w}{\partial r} - \frac{w}{r}\right) \quad \tau_{\theta\theta} = \mu\left(2\frac{v}{r} - \frac{2}{3}\nabla\cdot\vec{u}\right)\\
&\nabla\cdot\vec{u} = \frac{\partial u}{\partial z} + \frac{\partial v}{\partial r} + \frac{v}{r},
\end{aligned} \tag{7}$$

where Stokes' hypothesis has been used, and the heat flux vector components are expressed as

$$q_z = -\kappa\frac{\partial T}{\partial z} \quad q_r = -\kappa\frac{\partial T}{\partial r}. \tag{8}$$

The expression for the diffusion fluxes $\vec{J}_s$ is discussed later (equation (15)). The source term $\dot{Q}$ may be decomposed into a Joule heating term and a radiative cooling term ($\dot{Q} = \dot{Q}_{\text{Joule}} - \dot{Q}_{\text{rad}}$, assuming optically thin radiation). For the air ICP flows at subatmospheric pressures considered in this paper, radiative losses can be safely neglected (Dresvin *et al.*, 1977).

In order to close the system of governing equations, a set of thermodynamic, transport and chemical kinetics models are required. These models, which are to be described in Sections 3-5, have been implemented in a common software library (PEGASE) used by all VKI high-temperature CFD solvers (Bottin *et al.*, 1999b).

2.2 Magnetohydrodynamic induction equation

Owing to the axial symmetry of the problem, all electromagnetic phenomena may be expressed in terms of the azimuthal electric field, which consists of a single Fourier mode:

$$\vec{E} = E\exp(\mathrm{i}2\pi ft)\vec{e}_\theta, \tag{9}$$

where f represents the operating frequency of the torch. To consider phase-differences within the plasma, the electric field amplitude $E(r,z)$ stands for a complex variable. The electric field amplitude can be shown to satisfy the following fully resistive axisymmetric MHD induction equation, both inside the

torch and on a far field domain which covers the space around the torch (Mekideche, 1993):

$$\frac{\partial^2 E}{\partial z^2} + \frac{1}{r}\,\frac{\partial}{\partial r}\left(r\,\frac{\partial E}{\partial r}\right) - \frac{E}{r^2} - \mathrm{i}2\pi\mu_0\sigma f\,E = -\mathrm{i}\mu_0 2\pi f \sum_{j=1}^{n_c} \delta(\vec{r} - \vec{r}_j) I_{\mathrm{C}}, \quad (10)$$

where σ is the electrical conductivity of the plasma. The Dirac δ distribution in the right hand side takes care of the singular current density in the n_c (infinitely thin) inductor rings. For the radio-frequency currents used in high-pressure ICPs, it is reasonable to assume that a single coil current with amplitude I_{C} oscillates at phase angle zero through each coil ring (Jaeger *et al.*, 1995). The electric currents in the ICP are generating Lorentz body forces and Joule heat sources in the gas dynamics equations (equation (6)), whose expression is (Vanden Abeele and Degrez, 2000):

$$\begin{aligned} F_r &= \frac{\sigma}{4\pi f}\left(\frac{E_{\mathrm{R}}}{r}\,\frac{\partial r E_{\mathrm{I}}}{\partial z} - \frac{E_{\mathrm{I}}}{r}\,\frac{\partial r E_{\mathrm{R}}}{\partial z}\right) \\ F_z &= \frac{\sigma}{4\pi f}\left(\frac{E_{\mathrm{R}}}{r}\,\frac{\partial r E_{\mathrm{I}}}{\partial r} - \frac{E_{\mathrm{I}}}{r}\,\frac{\partial r E_{\mathrm{R}}}{\partial r}\right) \\ \dot{Q}_{\mathrm{Joule}} &= \frac{\sigma}{2}\left(E_{\mathrm{R}}^2 + E_{\mathrm{I}}^2\right), \end{aligned} \quad (11)$$

where E_{R} and E_{I} are the real and imaginary parts of the electric field amplitude.

3. Modeling of thermodynamic properties

In the present computational models, we consider mixtures of thermally perfect gases in thermal equilibrium for which the pressure is related to the temperature and the species densities by Dalton's law

$$p = \sum_{s=1}^{n_s} \rho y_s R_s T. \quad (12)$$

The other required thermodynamic relation relates the internal energy to the species densities and temperature:

$$\tilde{\varepsilon} = \sum_{s=1}^{n_s} \rho y_s \varepsilon_s(T) \quad (13)$$

where $\tilde{\varepsilon}$ is the mixture internal energy per unit volume and $\varepsilon_{\mathrm{s}}(T)$ are the species internal energies per unit mass.

For monoatomic or diatomic species such as the major constituents of air between 250 and 15,000 K, the thermodynamic properties can be directly calculated from statistical mechanics (Anderson, 1989; Vincenti and Kruger, 1965), provided assumptions are made concerning the number of electronic

levels to be considered in the expressions, and the modelling of vibration/rotation coupling. Both issues were thoroughly investigated (Bottin *et al.*, 1999b). For each species under consideration, the influence of the number of electronic levels was assessed by comparing the computed enthalpies over the temperature range of interest for number of electronic levels within a reasonable range. Such a comparison is shown in Figure 3 for the N^+ ion. One observes that the curves corresponding to six or more electronic levels are superimposed, from which it is concluded that it suffices to take six electronic levels into account to accurately compute the thermodynamic properties of the N^+ ion. The number of levels to be considered for the constituents of the 13-species air model is given by Bottin *et al.* (1999b).

In the simplest (rigid rotator/harmonic oscillator) model for diatomic molecules, rotation and vibration energy modes are decoupled. In reality though, molecules stretch while rotating and vibrations alter the moment of inertia, so that rotation and vibration are coupled and should be treated together. First-order anharmonicity correction models which consider rotation/vibration (Mayer and Mayer, 1946) or full rotation/vibration/electronic (Drellishak *et al.*, 1965) coupling have been compared to literature data based on the direct summation method (Gurvich *et al.*, 1989), as shown in Figure 4 for the O_2 molecule (number of electronic levels ranging between 5 and 18). Although the full coupling model provides better agreement with literature data up to 8,000 K, it appears to be totally inadequate beyond this point. This phenomenon is due to the fact that the oxygen molecule has many excited levels in the low energy range. In contrast, for the nitrogen molecule, first-order corrections remain accurate up to 15,000 K. In any event, inaccuracies in the anharmonicity corrections are in practice unimportant because molecules

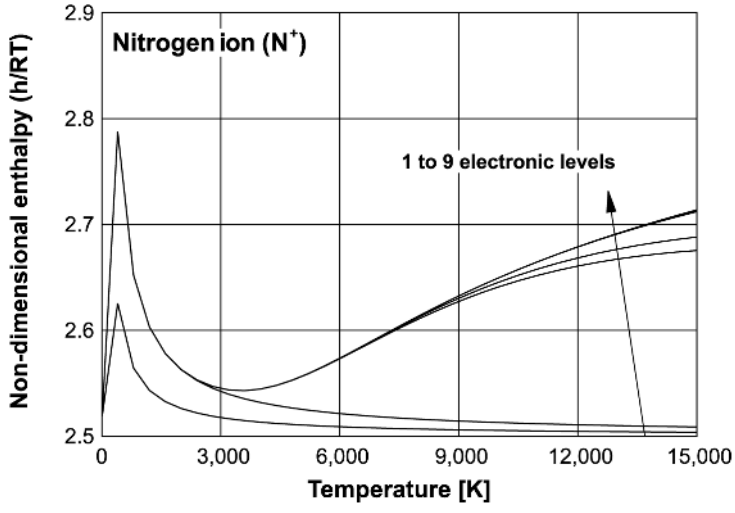

Figure 3.
Enthalpy of N^+ ion as a function of the number of electronic levels

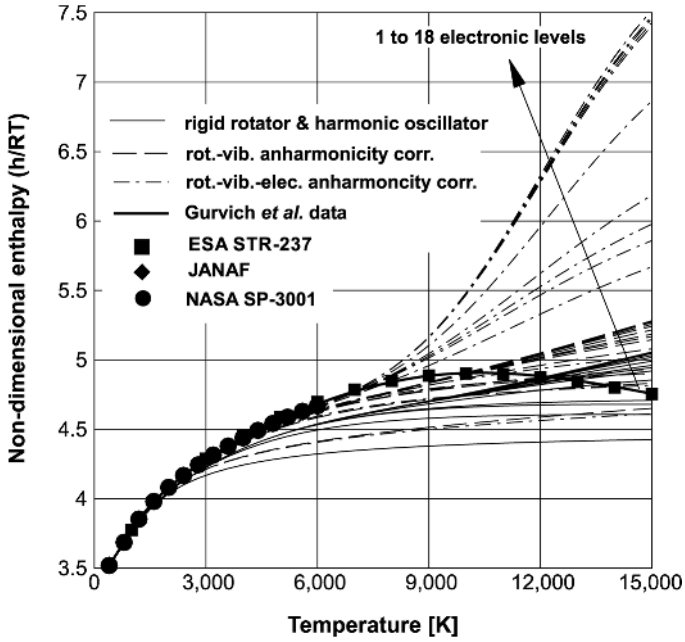

Figure 4.
Comparison of anharmonicity correction models for the O_2 molecule at 1 bar

dissociate at temperatures where the basic decoupled model is still accurate. As a result, the mass fraction of molecules and ionized molecules is so small at higher temperatures that inaccuracies in the anharmonicity corrections have essentially no influence on the computational results. In conclusion, it appears that the gain in accuracy of computed thermodynamic quantities provided by anharmonicity corrections does not justify the additional computational cost.

For equilibrium flows, the thermodynamic relations (12 and 13) are complemented by n_r equilibrium and n_c nuclei/charge conservation equations (with $n_r + n_c = n_s$) so that the number of independent thermodynamic variables reduces to two, e.g. pressure and temperature. The mixture composition is computed as a function of these independent variables using an original, partly analytical, partly numerical method based on a Schur-complement approach (Bottin *et al.*, 1999b). Basically, its principle is to solve for the logarithms of mass or mole fractions using a Newton iterative method. In terms of these variables, the equilibrium relations are *linear* so that n_r unknowns can be eliminated analytically, leaving only a system of n_c equations in n_c unknowns [1] to solve numerically. As the number of nuclei is much smaller than the number of species in complex gas mixtures such as air, the computational cost is dramatically reduced, which is an important feature for a CFD application since the composition calculation routine has to be called for each mesh point and at each iterative (time) step.

4. Modeling of transport phenomena

4.1 Transport coefficients

Transport properties are computed by the method of Chapman-Enskog as a function of the chemical composition, the temperature, pressure and the interaction potentials between the various colliding plasma particles (Hirschfelder *et al.*, 1967). The first-order correction to the equilibrium Maxwell-Boltzmann solution is obtained in terms of a series of Sonine polynomials. Usually, taking the first non-vanishing Sonine contribution in the expression for the transport coefficients provides sufficiently accurate results.

Whereas the expressions for binary diffusion coefficients are simple, the rigourous expressions for mixture transport properties such as viscosity and thermal conductivity derived by Hirschfelder *et al.* (1967) involve ratios of $n_s \times n_s$ determinants, and are consequently, prohibitively expensive for CFD applications. Therefore, approximations to these formulas, commonly referred to as mixture rules, have been derived by several researchers.

The accuracy of mixture rules for various transport properties has been investigated in detail (Bottin *et al.*, 1999b). For the viscosity, the mixture rule by Yos (1963) was found to provide accurate results. For the thermal conductivity, the heavy particles translational contribution was found to also be accurately evaluated by Yos' mixture rule, whereas the contribution of the internal degrees of freedom is adequately modelled by an Eucken-type approximation (Gupta *et al.*, 1990). To evaluate the electron contribution on the one hand, and all electron transport properties in general, higher order terms need to be kept in the expansion of Sonine polynomials. The formulas by Devoto (1967) and Kolesnikov and Tirsky (1984) with two non-vanishing Sonine polynomials were found to be equivalently accurate and efficient (Bottin *et al.*, 1999b). Finally, for equilibrium flows, the contribution to the heat flux due to the diffusion fluxes $\left(\sum_s \vec{J}_s h_s\right)$, which is spelled out for chemical non-equilibrium flows, can be conveniently modelled by means of a reactive thermal conductivity:

$$\sum_s \vec{J}_s h_s \approx -\nabla \cdot (\kappa_r \nabla T). \tag{14}$$

The above expression has been derived by Butler and Brokaw (1957) for neutral reactive gas mixtures, based on the assumption that no diffusion of elements ("demixing") occurs. It was shown (Bottin *et al.*, 1999b) that this expression is also valid for quasi-neutral mixtures of ionized gases under conditions of vanishing electric current. This expression was found to be more accurate than the mixture rule by Yos (1963) (see also Gupta *et al.*, 1990) when the degree of ionization is significant, as shown in Figure 5, which shows the various contributions to the thermal conductivity of equilibrium air up to 15,000 K. It is observed that the present results obtained using the expression by Butler and Brokaw are in excellent agreement with the results of

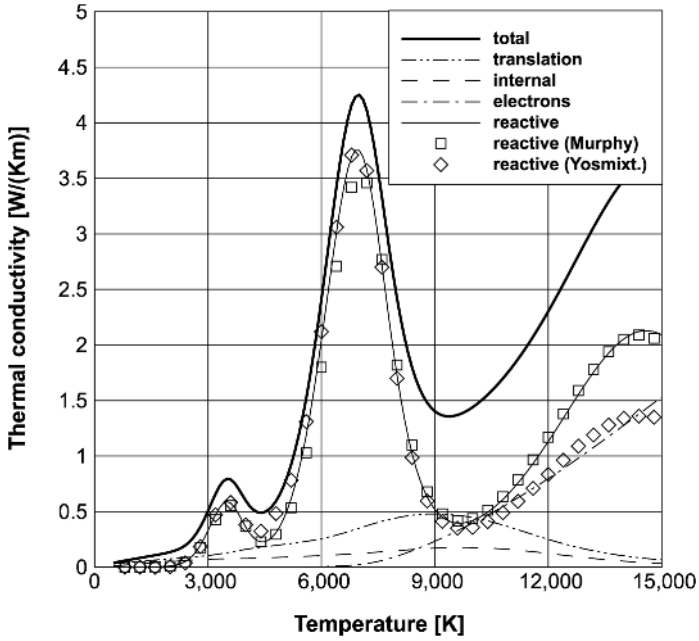

Figure 5.
Contributions to the thermal conductivity of equilibrium air at 1 atm

Murphy (1995) based on the rigourous expressions by Hirschfelder *et al.*, while Yos' mixture rule under-predicts the reactive thermal conductivity above 9,000 K.

The electrical conductivity, which is due entirely to the electrons, is accurately computed using the simplified expressions by Devoto (1967) or by Kolesnikov and Tirsky (1984).

4.2 Multi-component diffusion

Special care has been taken to the computation of the mass diffusion fluxes $\vec{J}_s$. These fluxes are commonly evaluated using the Fick's law approximation $\vec{J}_s = -\rho D_s \nabla c_s$, which has the advantage of an easy implementation, but violates mass conservation

$$\sum_s \vec{J}_s = 0.$$

In the present computational models, diffusion fluxes are evaluated using the full Stefan-Maxwell equations, which are equivalent to the Chapman-Enskog multi-component diffusion expressions (Hirschfelder *et al.*, 1967). Neglecting pressure and thermal diffusion as well as the effect of the magnetic field, we have

$$\frac{M}{\rho}\sum_{t=1}^{n_s}\left(\frac{x_s M_s \vec{J}_t - x_t M_t \vec{J}_s}{M_s M_t \mathscr{D}_{st}}\right) = \nabla x_s - \frac{\rho y_s \mathscr{Q}_s}{p}\vec{E}_{\text{amb}} \tag{15}$$

where M_s is the species molar masses, M the mixture molar mass, x_s the molar fractions, $\mathscr{D}_{st}$ the binary diffusion coefficients, and $\mathscr{Q}_s$ the species charge per unit mass. It can be proven that no net electric current flows in the poloidal (r, z) plane under conditions of thermal equilibrium (Vanden Abeele, 2000). The "ambipolar" electric field $\vec{E}_{\text{amb}}$ is then determined by imposing the additional constraint

$$\sum_{s=1}^{n_s} \mathscr{Q}_s \vec{J}_s = 0. \tag{16}$$

Equations (15) and (16) represent linear systems (one in each coordinate direction) in $n_s + 1$ unknowns, the diffusion fluxes and the ambipolar electric field, which are solved using an iterative method recently proposed by Sutton and Gnoffo (1998), adapted to the case of diffusion in ionized mixtures.

Different physics takes place in the azimuthal direction, where strong electric currents flow. Diffusion is driven by the induced electric field (equation (9)) rather than the ambipolar field and equation (15) simplify to Ohm's law

$$\mathscr{Q}_{\text{e}} \vec{J}_{\text{e}} = \sigma \vec{E}, \tag{17}$$

which has been used to derive equation (10).

5. Chemical reactions

Chemical source terms $\dot{m}_s$ are expressed according to the law of mass action, i.e.

$$\dot{m}_s = M_s \sum_{r=1}^{n_r} (\nu''_{sr} - \nu'_{sr}) \left\{ k_{\text{f}r} \prod_{t=1}^{n_s} \left(\frac{\rho_t}{M_t} \right)^{\nu'_{tr}} - k_{\text{b}r} \prod_{t=1}^{n_s} \left(\frac{\rho_t}{M_t} \right)^{\nu''_{tr}} \right\} \tag{18}$$

where n_r is the total number of reactions that involve species s, ν'_{sr} and ν''_{sr} are the stoichiometric coefficients for reactants and products, respectively, and $k_{\text{f}r}$ and $k_{\text{b}r}$ are the forward and backward reaction rates of reaction r. We recall that the previous expression is valid only if the n_r reactions considered are elementary reactions, i.e. reactions that take place in one single step. The forward reaction rates $k_{\text{f}r}$ are taken from Arrhenius data fits available in literature (Gnoffo *et al.*, 1989; Selle and Riedel, 2000). The backward reaction rates are computed from $k_{\text{f}r}$ and the equilibrium constant K_{cr}: $k_{\text{b}r} = k_{\text{f}r}/K_{cr}$. The equilibrium constant, which is related to the Gibbs free energy, is computed from statistical mechanics (Bottin *et al.*, 1999b) together with thermodynamic quantities.

6. Discretization and iterative solution procedure

6.1 Space discretization

The governing equations (1 and 10) are discretized using a co-located cell-centred finite volume method on structured meshes.

6.1.1 Gas dynamics equations. In ICP flowfields that are being characterized by low Mach numbers and therefore, low compressibility effects, the discrete equations are written in terms of the set of primitive variables $\mathbf{U} = (p, x_s, \rho\vec{u}, T)^t$. For such low speed flows, central discretizations on co-located grids are known to be subject to pressure stability problems. This is the reason why the vast majority of ICP models in the literature are based on a staggered grid arrangement. In the present study, we adopted a pressure-stabilized co-located grid approach (Ferziger and Perić, 1996) whose main advantage is a much simpler data structure.

Spurious pressure oscillations are suppressed in a conservative manner by adding a small dissipative pressure term to the convective mass flux, i.e. denoting the flowfield variables on both sides of a cell edge by the subscripts L and R, the pressure-stabilized normal mass flux at the cell edge (subscript E) is computed as

$$\tilde{f}_{m,E} = \frac{(\rho u_n)_L + (\rho u_n)_R}{2} - \frac{\Lambda}{\beta}(p_R - p_L) \tag{19}$$

where β is an estimate of the maximum velocity in the flow and Λ a factor to scale the pressure dissipation properly in regions of low cell Reynolds number:

$$\Lambda = \frac{\mathrm{Re}_h}{1 + \mathrm{Re}_h} \quad \mathrm{Re}_h = \frac{\rho\beta h}{\mu} \tag{20}$$

where h is some cell characteristic length. The previous definition indeed satisfies the asymptotic scalings $\Lambda/\beta \rightarrow h/\nu$ in the diffusion-dominated limit and $\Lambda/\beta \rightarrow 1/\beta$ in the advection-dominated limit.

At high Reynolds numbers, central discretizations also suffer from velocity oscillation problems. In the present model, these oscillations are controlled by introducing upwinding in the evaluation of the convective fluxes, i.e. the convective flux vector across the cell edge E with normal $\vec{n}$ is expressed as

$$\mathbf{F}_n^{\mathrm{c}} = \left(\tilde{f}_{m,E}, \tilde{f}_{m,E} y_{s,E} \tilde{f}_{m,E} u_E + \frac{p_L + p_R}{2} n_x, \tilde{f}_{m,E} v_E + \frac{p_L + p_R}{2} n_y, \tilde{f}_{m,E} w_E, \tilde{f}_{m,E} h_E\right)^t \tag{21}$$

where for any quantity q

$$q_E = \frac{q_L + q_R}{2} - \mathrm{sign}\left(\tilde{f}_{m,E}\right) \frac{q_R - \mathrm{q}_L}{2} \tag{22}$$

and $q_{L,R}$ are calculated from the neighbouring cell values using a linear or non-linear reconstruction (Hirsh, 1988). Non-linear positive reconstruction is needed for the energy and species mass fluxes whereas linear reconstruction is

sufficient for the momentum fluxes. Diffusive fluxes are computed using a central discretization.

6.1.2 MHD induction equation. The MHD induction equation (10) being linear, was found convenient to decompose the electric field between the contribution of the coil rings E_V, which can be computed analytically using the Biot-Savart law, and the plasma-induced part E_P (Vanden Abeele and Degrez, 2000). Substracting the equation for the contribution of the coil rings from equation (10), one then obtains the induction equation for the plasma contribution:

$$\frac{\partial^2 E_P}{\partial z^2} + \frac{1}{r}\frac{\partial}{\partial r}\left(r\frac{\partial E_P}{\partial r}\right) - \frac{E_P}{r^2} - \mathrm{i}2\pi\mu_0\sigma f(E_P + E_V) = 0. \tag{23}$$

A straightforward central discretization is sufficient to ensure numerical stability for this Helmholtz-type equation. Contrary to most existing high pressure ICP models, the induction equation is discretized on a far-field mesh which extends beyond the torch. The main advantage of this approach is the simple far-field boundary conditions which preserve the sparsity of the algebraic system, in contrast with the integral boundary condition used in most existing models (Vanden Abeele and Degrez, 2000; Van Dijk *et al.*, 2002).

6.2 Iterative solution strategy

To solve the discretized system of equations (1) and (23), we use a set of damped quasi-Newton strategies, together with a modern preconditioned Krylov subspace iterative technique (Saad, 1995), viz. the preconditioned GMRES algorithm, for the linear systems solved. The main reasons for selecting this type of iterative strategies lies in their ability to handle stiff systems and their fast iterative convergence, which is essential for the flow problems under consideration because of the high CPU cost per iteration associated to the evaluation of thermodynamic and transport properties.

In the initial iterations, a robust damped Picard strategy is used. Denoting by U and E the vectors of flowfield and EM variables, respectively, they are updated by solving separately the linear systems

$$J_P(U^{k+1} - U^k) = -R_U^k \tag{24}$$

$$J_E(E^{k+1} - E^k) = -R_E^k \tag{25}$$

where R_U and R_E are the space discretization residuals and J_E, J_P approximate jacobians. To ensure the robustness of the method, the flowfield jacobian is computed based on a first-order upwind reconstruction and by freezing the convective mass flux and ρ at iterative level k in the evaluation of the momentum, species and energy convective flux jacobians (Picard approximation). Specifically, at the interface between cells (i, j) and $(i + 1, j)$,

the convective flux jacobians of the terms $\tilde{f}_{m,E}q_E$ are approximated by (see equation (21))

$$\frac{\partial \tilde{f}_{m,EqE}}{\partial \mathbf{U}_{i,j}} \approx \frac{(1+\mathrm{sign}\tilde{f}_{m,E})}{2}\tilde{f}^{k}_{m,E}\left(\frac{\partial q}{\partial \mathbf{U}}\right)_{i,j}$$
$$\frac{\partial \tilde{f}_{m,EqE}}{\partial \mathbf{U}_{i+1,j}} \approx \frac{(1-\mathrm{sign}\tilde{f}_{m,E})}{2}\tilde{f}^{k}_{m,E}\left(\frac{\partial q}{\partial \mathbf{U}}\right)_{i+1,j} \quad (26)$$

Damping is, in general, necessary to ensure convergence. It is achieved by multiplying the diagonal entries in the Picard jacobian by a factor $(1 + 1/\mathrm{CFL})$ where the damping parameter CFL resembles the Courant number used in time-stepping schemes. Furthermore, solution updates are multiplied by an under-relaxation factor $\alpha = 0.7$.

Later, when the Picard method has converged around one order of magnitude, it switches to a damped quasi-Newton method, which differs from the Picard approach only by the evaluation of the flowfield jacobian. It is still computed based on a first-order reconstruction, but without freezing the convective mass flux, using a finite difference method.

The above Picard and quasi-Newton methods both solve for the flow and EM fields in a loosely coupled manner. A full Newton method, in which all equations are solved in a fully coupled manner, has also been considered. However, it was found that the important non-linear convergence gains obtained by full coupling are offset by a significant decrease in speed of convergence at the linear level (Vanden Abeele and Degrez, 2000).

7. Numerical results

7.1 ICP geometry, computation parameters

We simulate the heating chamber of the VKI Plasmatron wind tunnel (Bottin *et al.*, 1999a) to investigate the importance of chemical non-equilibrium effects in air ICPs. The problem geometry and operating conditions for the calculation are shown in Figure 2. Computations are performed using an 11-species air model (N_2, O_2, N, O, NO, NO^+, N^+, O^+, N_2^+, O_2^+, e^-). All thermodynamic and transport data (collision integrals) used for the simulations may be found in the work of Bottin (1999) and Vanden Abeele (2000). We model chemistry in the plasma in three different manners:

(1) assuming LTE, where we force the elemental composition plasma to be constant in space (79 per cent nitrogen, 21 oxygen elements per volume) by assuming vanishing nuclei diffusion fluxes (assumption also needed to apply equation (14));

(2) using the chemical kinetics model of Selle and Riedel (2000); and

(3) using the chemical kinetics model of Park as published by Gnoffo *et al.* (1989).

7.2 Convergence history

Calculations are run on a contemporary PC with a 900 MHz processor. A highly stretched 70×48 gas dynamics mesh and a 110×100 EM field mesh are used; an extensive mesh-refinement study has shown that this resolution is sufficient refined to obtain grid-converged results (Vanden Abeele *et al.*, 1999). The convergence history obtained for the calculations is shown in Figure 6. First, the LTE calculation is performed; after 50 Picard iterations, the quasi-Newton method is switched on and rapid convergence is observed. Next, the obtained LTE result serves as an initial solution for the subsequent non-equilibrium calculations. Usually, the LTE solution is sufficiently good to allow to immediately restart with the quasi-Newton method. The LTE calculations easily converge to machine accuracy; for the non-equilibrium calculations on fine meshes considered here, the residual norm is reduced by six orders of magnitude, after which convergence stagnates. We found that this convergence problem could be overcome by using lower values for the under-relaxation parameters CFL and α. For the LTE calculations, the required memory is 52 MB, where each iteration takes ~ 30 s; for the non-equilibrium calculations, 160 MB is needed and computation times increase sixfold to ~ 3 min per iteration.

7.3 Comparison of results

In Figures 7-9, we compare the computed results for the temperature, flow and electron concentration fields, obtained for the cases (a)-(c). For all cases, the flowfield pattern is a typical backward facing step flow pattern influenced by Lorentz forces and centrifugal forces due to the swirling flow injection. It is

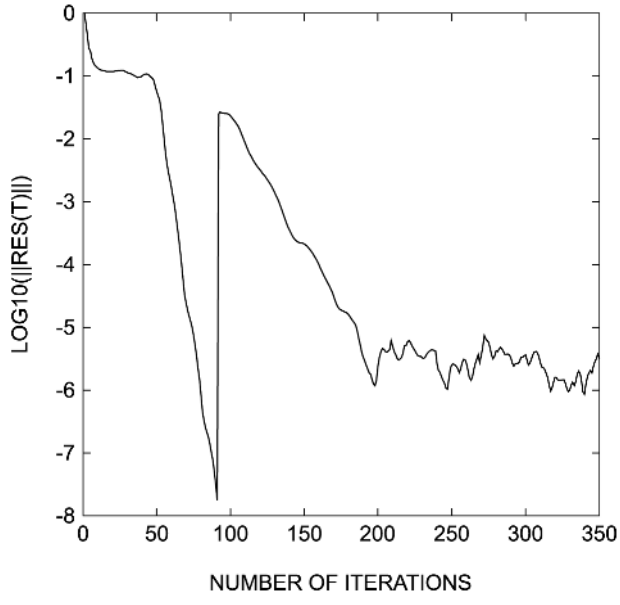

Figure 6.
Convergence histories of air ICP flow computations in the VKI Plasmatron torch

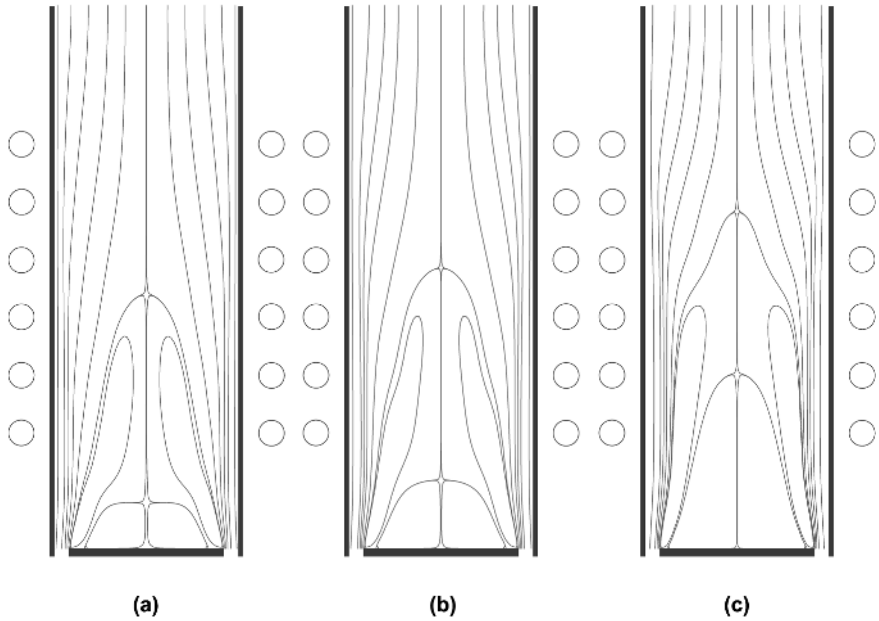

Figure 7.
Computed streamline patterns in the VKI Plasmatron torch: (a) LTE; (b) model of Selle and Riedel; and (c) model of Park

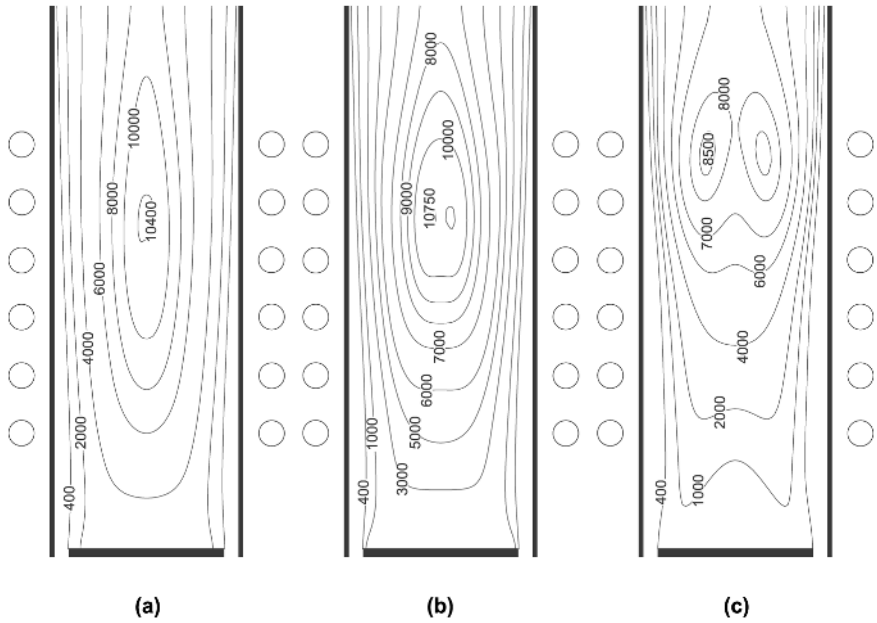

Figure 8.
Computed temperature contours in the VKI Plasmatron torch: (a) LTE; (b) model of Selle and Riedel; and (c) model of Park

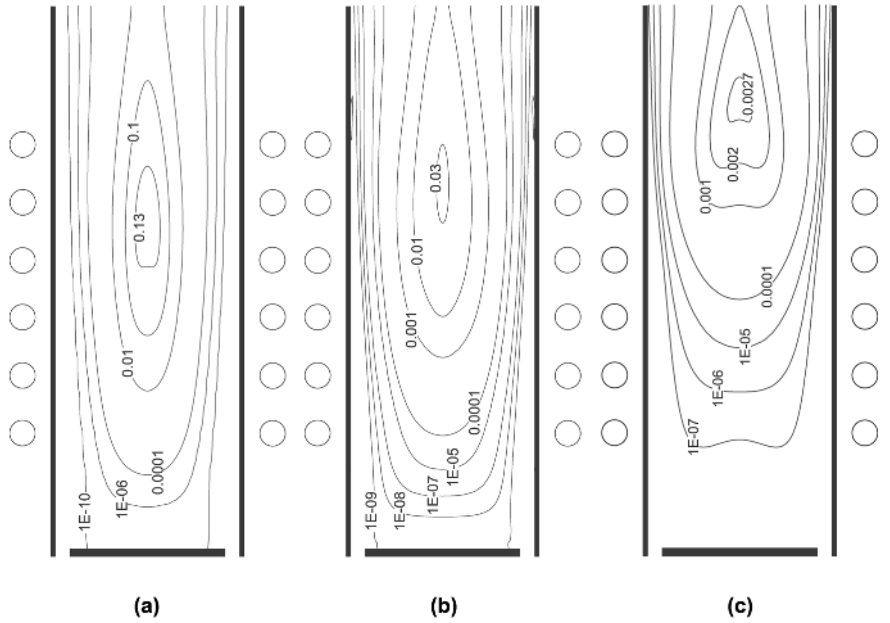

Figure 9.
Computed electron mole fraction contours in the VKI Plasmatron torch: (a) LTE; (b) model of Selle and Riedel; and (c) model of Park

seen that the non-equilibrium effects have a minor effect upon the obtained flow field.

Similar temperature fields with peak temperatures ~10,500 K on the axis are obtained when assuming LTE and when using the finite-rate chemistry model of Selle and Riedel (2000). However, important differences are observed in the corresponding electron concentration fields. As a result of convective quenching, the peak electron mole fraction ~0.03 found with the model of Selle and Riedel is more than four times smaller than the maximal LTE fraction ~0.13.

Far stronger non-equilibrium effects are found when using the model of Park (Gnoffo *et al.*, 1989). Peak temperatures ~8,500 K are found at a distinctive off-axis location. The maximal value of the electron mole fraction amounts to only ~0.003, which lies yet an order of magnitude beneath the value found using the model of Selle and Riedel. The fact that the peak in electron concentration does not coincide with the temperature maximum is entirely due to chemical non-equilibrium effects.

It should be noted that the temperatures and electron concentrations obtained when using Park's model are unrealistically low. In addition, the ionised gas itself lies behind the downstream end of the inductor, which indicates poor incoupling of energy. To obtain more physical results, thermal non-equilibrium effects should be added to the model. The temperature of free electrons rises faster than the equilibrium temperature used in our current simulations. Consequently, when a separate electron temperature is included,

the onset of ionisation will occur closer to the upstream end of the inductor and the overall degree of ionisation may be substantially higher.

7.4 Nuclei demixing

Figure 10 shows the computed contours of oxygen nuclei fractions (volumetric) obtained using the model of Selle and Riedel. It is seen that important demixing of oxygen and nitrogen elements occurs due to diffusive effects in the plasma. By multiplying the different species equations by the number of oxygen nuclei ξ_s^{O} in the respective species and summing over s, we obtain an advection-diffusion equation for the mass fraction of oxygen elements in the plasma:

$$\nabla\cdot\left[\rho\vec{u}\left(\sum_{s=1}^{n_s} y_s\xi_s^{\mathrm{O}}\right)\right] + \nabla\cdot\left[\sum_{s=1}^{n_s}\vec{J}_s\xi_s^{\mathrm{O}}\right] = 0. \tag{27}$$

The right hand side of the above result is zero because no nuclei are created in chemical reactions. The absence of chemistry terms implies that demixing occurs even for plasmas under LTE. The assumption of constant nuclei fractions and vanishing nuclei fluxes, commonly used in LTE simulations of multi-component plasma flows (Vasil'evskii *et al.*, 1996) is therefore, not always justified. In general, the usual set of LTE flow field equations should be complemented with an advection-diffusion equation (27) for each element in the plasma.

8. Conclusions

In this paper, we have presented the model for high-pressure air ICPs developed at the von Karman Institute over the past few years. Great care has been taken to ensure good accuracy and efficiency of the model.

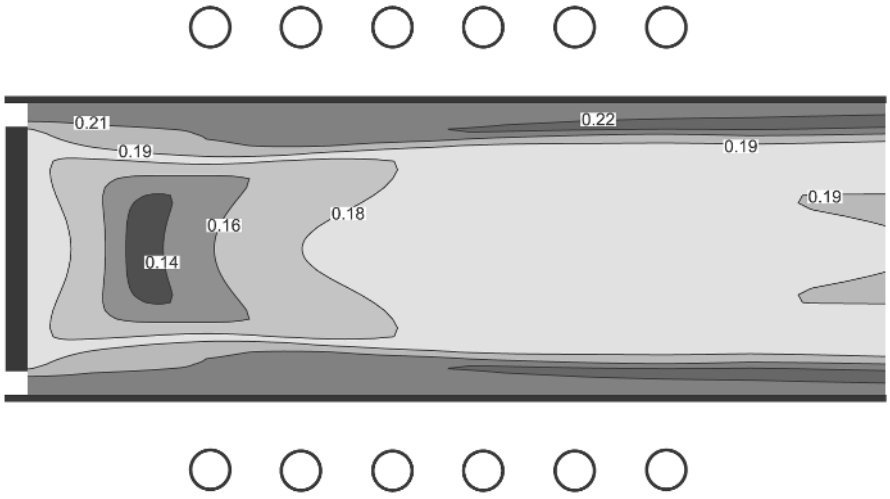

Figure 10.
Volumetric fraction of oxygen elements in the VKI Plasmatron torch (model of Selle and Riedel)

- Thermodynamic quantities are computed directly from statistical mechanics, using electronic cutoff criteria determined from systematic numerical experiments.
- Transport properties are computed from the Chapman-Enskog theory and validated mixture rules (two non-vanishing Sonine contributions are retained for electron properties).
- Diffusion fluxes in the poloidal plane are computed using the Stefan-Maxwell equations under the additional constraint of vanishing electric currents.
- The ICP model is based on the induction equation for the plasma-induced electric field only, which is solved for on a far-field mesh extending outside of the torch.
- The discrete equations are solved using efficient damped Picard and quasi-Newton techniques which allow fast computations of near equilibrium as well as non-equilibrium flows.

We have demonstrated the capabilities of the model by computing LTE and non-equilibrium air ICP flows inside the VKI Plasmatron torch. From the computed results, we may conclude the following.

- Chemical non-equilibrium effects may lead to significant deviations of LTE in the air ICPs typically used for TPM testing.
- The inadequacy of the air chemistry models currently available in the literature is clear, as very different results are obtained depending on the selected model.
- Inclusion of thermal NEQ effects is needed to obtain more physical results.
- Important demixing of oxygen and nitrogen nuclei occurs due to diffusion. As demixing takes place regardless of the degree of chemical non-equilibrium in the plasma, correct LTE models of chemically reacting viscous flows should include an additional advection-diffusion equation for each different element in the gas mixture.

It is clear that, before reliable quantitative predictions can be made, a very considerable effort remains to be invested in the development of a more adequate air chemistry model.

Note

1. There is actually one additional unknown (the total number of moles per unit volume) and one additional equation when solving for mole fractions.

References

Anderson, J.D. Jr (1989), *Hypersonics and High Temperature Gas Dynamics*, McGraw-Hill, New York, NY.

Benoy, D.A. (1993), "Modeling of thermal argon plasmas", PhD thesis, Technical University of Eindhoven, Eindhoven, The Netherlands.

Bottin, B. (1999) "Aerothermodynamic model of an inductively coupled plasma wind tunnel", PhD thesis, Université de Liège, Liège, Belgium.

Bottin, B., Chazot, O., Carbonaro, M., Van der Haegen, V. and Paris, S. (1999a), "The VKI Plasmatron characteristics and performance", in Charbonnier, J.M. and Sarma, G.S.R. (Eds), *Measurement Techniques for High Temperature and Plasma Flows*, NATO-RTO-EN 8.

Bottin, B., Vanden Abeele, D., Carbonaro, M., Degrez, G. and Sarma, G.S.R. (1999b), "Thermodynamic and transport properties for inductive plasma modelling", *Journal of Thermophysics and Heat Transfer*, Vol. 13 No. 3, pp. 343-50.

Butler, J.N. and Brokaw, R.S. (1957), "Thermal conductivity of gas mixtures, in chemical equilibrium", *Journal of Chemical Physics*, Vol. 26 No. 6, pp. 1636-43.

Devoto, R.S. (1967), "Simplified expression for the transport properties of ionized monoatomic gases", *Physics of fluids*, Vol. 10 No. 10, pp. 2105-12.

Drellishak, K.S., Aeschliman, D.P. and Cambel, A.B. (1965), "Partition functions and thermodynamic properties of nitrogen and oxygen plasmas", *Physics of Fluids*, Vol. 8 No. 9, pp. 1590-600.

Dresvin, S.V., Donskoi, A.V., Goldfarb, V.M. and Klubnikin, V.S. (1977) *Physics and Technology of Low-Temperature Plasmas*, in, Eckert, H.V. (Ed.), translated from Russian, Iowa State University Press, Ames, IA.

Ferziger, J.H. and Perić, M. (1996), *Computational Method for Fluid Dynamics*, Springer, Berlin.

Gnoffo, P.A., Gupta, R.N. and Shinn, J.L. (1989), "Conservation equations and physical models for hypersonic air flows in thermal and chemical nonequilibrium", *TP* 2867, NASA.

Gupta, R.N., Yos, J.M., Thompson, R.A. and Lee, K.P. (1990), "A review of reaction rates and thermodynamic and transport properties for an 11-species air model for chemical and thermal nonequilibrium calculations to 30,000 K", *RP* 1232, NASA.

Gurvich, L.V., Veyts, I.V. and Alcock, C.B. (1989), *Thermodynamic Properties of Individual Substances*, Part 2: Tables, Vol. 1, Hemisphere, New York, NY.

Hirsch, C. (1988), "Numierical computation of internal and external flows", *Computational Methods for Inviscid and Viscous Flows*, Vol. 2, Wiley, Chichester.

Hirschfelder, J.O., Curtiss, C.F. and Bird, R.B. (1967), *Molecular Theory of Gases and Liquids*, Wiley, New York, NY.

Jaeger, E.F., Berry, L.A., Tolliver, J.S. and Batchelor, D.B. (1995), "Power deposition in high-density inductively coupled plasma tools for semiconductor processing", *Physics of Plasmas*, Vol. 2 No. 6, pp. 2597-604.

Kolesnikov, A.F. (1999), "Combined measurements and computations of high enthalpy and plasma flows for determination of TPM surface catalycity", in Charbonnier, J.M. and Sarma, G.S.R. (Eds), *Measurement Techniques for High Temperature and Plasma Flows*, NATO-RTO-EN 8.

Kolesnikov, A.F. and Tirsky, G.A. (1984), "Hydrodynamics equations for partially ionised multicomponent gas mixtures with higher order approximations for transport coefficients", *Fluid Mechanics – Soviet Research*, Vol. 13 No. 4, pp. 70-97.

Kolesnikov, A.F., Pershin, I.S., Vasil'evskii, S.A. and Yakushin, M.I. (1998), "Study of quartz surface catalycity in dissociated carbon dioxide subsonic flows", AIAA Paper 98-2847.

Kulumbaev, E.B. (1999), "Development of thermochemical models of arc, induction, microwave and optical discharges", PhD thesis, Kyrgiz-Slavic University, Bishkek, Kyrgizstan (in Russian).

Mayer, J.E. and Mayer, M.G. (1946), *Statistical Mechanics*, Wiley, New York, NY.

Mekideche, M.R. (1993), "Contribution à la modélisation numérique de torches à plasma d'induction", PhD Thesis, École doctorale de Sicences pour, l'Ingénieur de Nantes, Saint-Nazaire, France.

Mostaghimi, J., Proulx, P. and Boulos, M.I. (1987), "A two-temperature model of the inductively coupled RF plasma", *Journal of Applied Physics*, Vol. 61 No. 5, pp. 1753-60.

Murphy, A.B. (1995), "Transport coefficients of air, argon-air, nitrogen-air and oxygen-air plasma", *Plasma Chemistry and Plasma Procession*, Vol. 15 No. 2, pp. 279-307.

Saad, Y. (1995), "Preconditioned Krylov subspace methods: an overview", in Hafez, M. and Oshima, K. (Eds), *Computational Fluid Dynamics Review*, Wiley, New York, NY.

Selle, S. and Riedel, U. (2000), "Transport coefficients of reacting air at high temperatures", *Technical Paper 2000-0211*, AIAA, Reno, Nevada.

Semin, V.A. (1991), "Theory of nonequilibrium inductive high-frequency discharge in a gas flow", *Mechanics of fluids and gases*, (translated from Russian), Vol. 26 No. 2, pp. 282-8.

Sutton, K. and Gnoffo, P. (1998), "Multi-component diffusion with application to computational aerothermodynamics", AIAA Paper 98-2575.

Van Dijk, J., van der Velden, M. and van der Mullen, J. (2002), "A multidomain boundary-relaxation technique for the calculation of the electromagnetic field in ferrite-code inductive plasmas", *Journal of Physics D: Applied Physics*, Vol. 35, pp. 2748-59.

Vanden Abeele, D. (2000), "An efficient computational model of inductively coupled air plasma flows under thermal and chemical non-equilibrium", PhD thesis, von Karman Institute for Fluid Dynamics/Katholieke Universiteit Leuven, Leuven, Belgium.

Vanden Abeele, D. and Degrez, G. (2000), "Efficient computational model for inductive plasma flows", *AIAA Journal*, Vol. 38 No. 2, pp. 234-42.

Vanden Abeele, D., Vasil'evskii, S.A., Kolesnikov, A.F., Degrez, G. and Bottin, B. (1999), "Code-to-code validation of inductive plasma computations", *VKI TN 197*, von Karman Institute for Fluid dynamics, St. Genesius-Rode, Belgium.

Vasil'evskii, S.A., Kolesnikov, A.F. and Yakushin, M.I. (1996), "Mathematical models for plasma and gas flows in induction plasmatrons", in Capitelli, M. (Ed.), *Molecular Physics and Hypersonic Flows*, Kluwer, Dordrecht, The Netherlands, pp. 495-504.

Vincenti, W.G. and Kruger, C.H. Jr (1965), *Introduction to Physical Gas Dynamics*, Wiley, New York, NY.

Yos, J.M. (1963), "Transport properties of nitrogen, hydrogen, oxygen and air to 30,000 K", RAD-TM-63-7, AVCO Corp., Wilmington, MA.

Discretization of the magnetic field in MPD thrusters

Jörg Heiermann and Monika Auweter-Kurtz
Institut für Raumfahrtsysteme, Universität Stuttgart, Stuttgart, Germany

Keywords *Plasma physics, Aerodynamics, Flow, Electromagnetic radiation*

Received February 2002
Revised November 2002
Accepted November 2002

Abstract *For the numerical simulation of magnetoplasmadynamic (MPD) self-field thruster flow, the solution of one of the two dynamical Maxwell equations – Faraday's law – is required. The Maxwell equations and Ohm's law for plasmas can be summarized in one equation for the stream function so that the two-dimensional, axisymmetric magnetic field can be calculated. The finite volume (FV) discretization of the equation on unstructured, adaptive meshes is presented in detail and solutions for different thruster currents are shown. The calculated thrust is compared with the experimental data.*

Introduction

Magnetoplasmadynamic (MPD) self-field thrusters are candidates for propelling manned spacecraft to Mars because they can achieve a high exhaust velocity combined with a high thrust density (Auweter-Kurtz, 1992; Bennett *et al.*, 1990; Jahn, 1968). The basic principle of self-field MPD propulsion is shown in Figure 1. Fuel is injected with a mass flow rate $\dot{m}$. It is heated and ionized by the electric discharge between anode and cathode so that a plasma is created. The plasma temperature can reach more than 40,000 K in the nozzle throat region. The electric current density $\vec{j}$ induces an azimuthal magnetic self-field $\vec{B}$ so that the plasma is accelerated by thermal expansion in the divergent nozzle as well as by the Lorentz force $\vec{j} \times \vec{B}$.

Since the early 1980s, MPD thrusters have been investigated at the Institut für Raumfahrtsysteme (IRS) experimentally, theoretically and numerically (Auweter-Kurtz *et al.*, 1998; Boie, 1999; Sleziona, 1998). Engineering aspects as well as basic plasma processes are considered in order to achieve higher efficiency and to avoid power-limiting plasma instabilities which are identified by voltage oscillations and increasing anode losses.

Numerical methods have been developed worldwide (Choueiri, 1999; Fujita, 1996; Minakuchi and Kuriki, 1984; Niewood and Martinez-Sanchez, 1991; Sankaran *et al.*, 2000; Turchi *et al.*, 1995) with the complexity of the discretized conservation equations increasing with the available computing power.

This work has been supported by the German Research Foundation DFG (Deutsche Forschungsgemeinschaft) through the project "Conservation Equations and Numerical Solutions for Technically Relevant Magneto-Plasmas" (Au 85/9-1,2,3), which belongs to the German Priority Research Program (Schwerpunktprogramm) "Analysis and Numerics for Conservation Laws".

International Journal of Numerical Methods for Heat & Fluid Flow
Vol. 14 No. 4, 2004
pp. 559-572

0961-5539
DOI 10.1108/09615530410532295

A new FV solver has been developed at the IRS for solving the conservation equations describing a continuum-mechanical, turbulent axisymmetric argon plasma flow under the influence of an arc discharge in thermal and reaction non-equilibrium (Heiermann and Auweter-Kurtz, 2001).

A novelty is the time-stabilized FV solution of the stream function which describes the distribution of the electric current on adaptive unstructured meshes. The formulation of the stream function equation and its discretization are explained in detail in the following sections.

Results are discussed for the thruster with hot anode HAT which has been built (Figure 2) and is being operated (Figure 3) at the IRS.

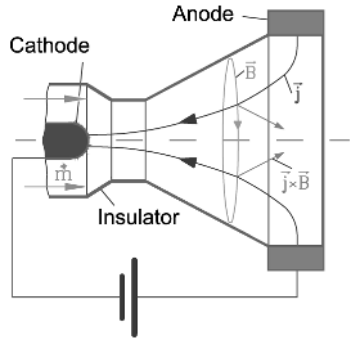

Figure 1.
Basic principle of self-field MPD propulsion

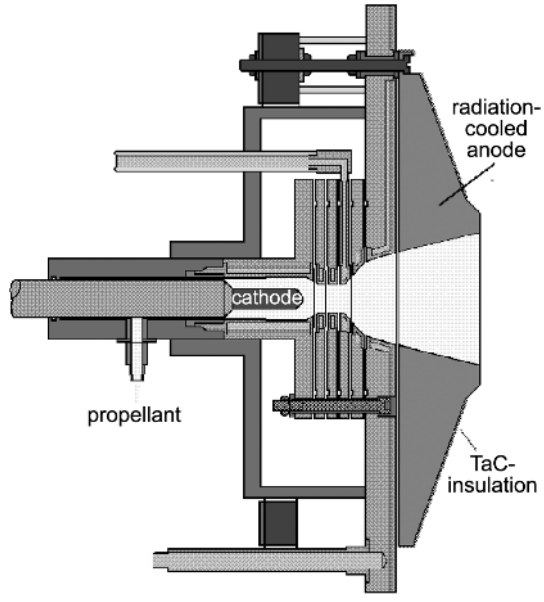

Figure 2.
The self-field MPD thruster with hot anode HAT

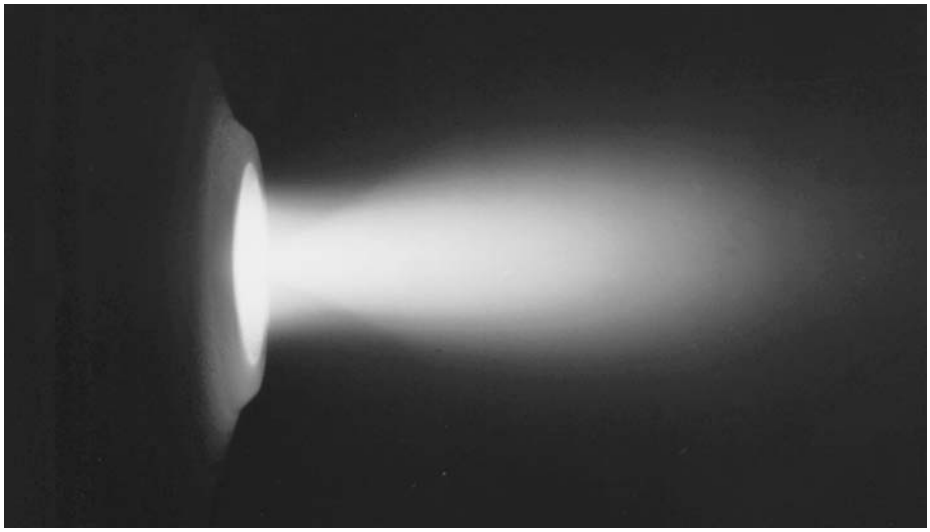

Figure 3.
HAT, firing, 2000 A, 0.8 g/s argon

Conservation equation for the magnetic field

For the derivation of the conservation equation for the magnetic field the Maxwell equations (Jackson, 1962) are required:

$$\text{rot}\,\vec{B} = \mu_0 \vec{j} + \frac{1}{c^2}\frac{\partial \vec{E}}{\partial t}, \tag{1}$$

$$\text{rot}\,\vec{E} = -\frac{\partial \vec{B}}{\partial t}, \tag{2}$$

$$\text{div}\,\vec{B} = 0 \tag{3}$$

and

$$\text{div}\,\vec{E} = \frac{\rho_{el}}{\varepsilon_0}. \tag{4}$$

Since a stationary solution shall be achieved and since no high frequency oscillations are considered, the Galilei-invariant formulation of equation (1) is used, neglecting the displacement current. Equation (3) is automatically fulfilled because of axisymmetry. In general, equation (4) can be used to calculate the charge density ρ_{el}. However, the plasmas considered can be assumed to be quasineutral so that ρ_{el} is zero.

Ohm's law for plasmas is given by (Cap, 1994)

$$\vec{E} = \frac{\vec{j}}{\sigma} - \vec{v} \times \vec{B} + \beta \vec{j} \times \vec{B} - \beta \nabla p_e. \tag{5}$$

It includes the electric conductivity σ (Devoto, 1973), the convection velocity $\vec{v}$ and the electron pressure p_e.

The Hall parameter

$$\beta = \frac{1}{en_e} \tag{6}$$

includes the electron density n_e.

The equations (1), (2) and (5) can be used to write the conservation equation for the magnetic field in cylindrical coordinates

$$\vec{B} = \begin{bmatrix} 0 \\ \mathrm{B} \\ 0 \end{bmatrix} \tag{7}$$

with the azimuthal component B:

$$\frac{\partial B}{\partial t} = -\mathrm{div}(B\vec{v}) + \frac{Bv_r}{r} - \mathrm{rot}\left(\frac{\mathrm{rot}\,\vec{B}}{\mu_0\sigma} + \frac{\beta}{\mu_0}\mathrm{rot}\,\vec{B}\times\vec{B} - \beta\nabla p_e\right)_\varphi . \tag{8}$$

The first term on the right hand side describes the convective transport of the magnetic field, the second term appears because of the use of cylindrical coordinates. The third term describes the change of the magnetic field by the electric current density $\vec{j}$ by the Hall current and by the ∇p_e term. Finally, the magnetic field B in equation (8) can be substituted by the stream function

$$\Psi = rB \tag{9}$$

and subsequently, the conservation equation for the magnetic field becomes

$$\frac{1}{r}\frac{\partial \Psi}{\partial t} = -\mathrm{div}\left(\frac{\Psi}{r}\vec{v}\right) + \frac{\Psi v_r}{r^2} - \mathrm{rot}\left(\frac{1}{\mu_0\sigma}\mathrm{rot}\begin{bmatrix} 0 \\ \Psi/r \\ 0 \end{bmatrix} + \frac{\beta}{\mu_0}\mathrm{rot}\begin{bmatrix} 0 \\ \Psi/r \\ 0 \end{bmatrix} \times \begin{bmatrix} 0 \\ \Psi/r \\ 0 \end{bmatrix} - \beta\nabla p_e\right). \tag{10}$$

This equation shall be iterated until a steady-state solution for the stream function is achieved. The contour lines of the stream function represent the stream lines of the electrons which carry the electric current. Hence, a constant electric current flows between two neighboring contour lines of the stream function.

The boundary condition on the eletrodes is that the electric field vector only has a component perpendicular to the electrode surfaces. Ampére's law is applied everywhere else as Dirichlet condition for Ψ:

$$\Psi = \frac{\mu_0 I}{2\pi}, \tag{11}$$

where I is the thruster current.

Discretization

Owing to the complex geometry of MPD thrusters, the spatial discretization is done on unstructured meshes. Appropriate adaptation (Iben *et al.*, 2000) of coarse initial meshes reduces the amount of computational time significantly. An advancing front algorithm is used to create a primary triangulation of the computational domain. The geometric centers of mass of the triangles are connected to create the so-called dual cells, see Figure 4. The connection of the centers of mass $\vec{x}_m$ of the dual cells creates the so-called "dual triangles". The dual triangles are the result of the choice of cylindrical coordinates; the centers of mass of the dual cells are not the geometric centers of mass.

A toroidal cell face is defined by its area ΔA_{ik}, the normal unit vector $\vec{n}_{ik}$ and the Gauß point $\vec{x}_{ik}$. Additionally, the dual triangles $\mathcal{T}_{ijk}$ and $\mathcal{T}_{ikl}$ and the physical states left (l) and right (r) of the cell face are attached to the cell face.

For the discretization of equation (10) the theorems of Gauß

$$\int_{\Delta V_\omega} \operatorname{div} \vec{a}\, \mathrm{d}\Delta V_\omega = \int_{\Delta A_{\omega k}} \vec{a}\, \mathrm{d}\Delta \vec{A}_{\omega k} \tag{12}$$

and Stokes

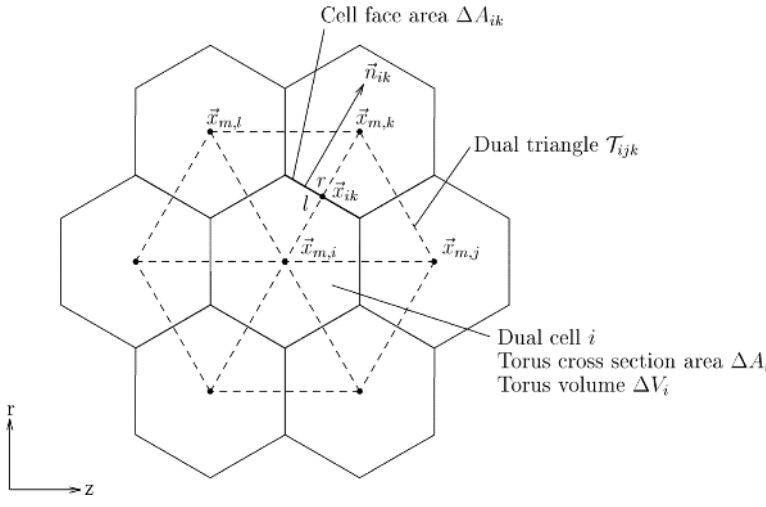

Figure 4.
Dual cells as control volumes

$$\int_{\Delta A_\omega} \mathrm{rot}\,\vec{E}\,\mathrm{d}\Delta\vec{A}_\omega = \oint_{\partial\omega} \vec{E}\,\mathrm{d}\vec{l}_{\partial\omega} \tag{13}$$

are needed on each dual cell ω.

The theorem of Gauß is applied to the convective part, and the theorem of Stokes to the rest of the right hand side of equation (10). The discretized right hand side is written as:

$$\begin{aligned}\mathrm{RHS}^B = &-\frac{1}{\Delta V_\omega}\sum_{k=1}^{K} F^B_{WENO}(\vec{x}_{\omega k})\Delta A_{\omega k} + \frac{\frac{\Psi}{r_{m,\omega}}v_r}{\left(\frac{1}{K+1}\sum_{\substack{k=1\\k=\omega}}^{K} r^3_{m,k}\right)^{1/3}} \\ &-\frac{1}{\Delta A_\omega}\sum_{k=1}^{K}\frac{1}{2}\left[\frac{(\mathrm{rot}\,\vec{B})_{\mathcal{T}_{\omega jk}}}{\mu_0\overline{\sigma_{\omega jk}}} + \frac{(\mathrm{rot}\,\vec{B})_{\mathcal{T}_{\omega kl}}}{\mu_0\overline{\sigma_{\omega kl}}} + \frac{\overline{\beta_{\omega jk}}}{\mu_0}(\mathrm{rot}\,\vec{B})_{\mathcal{T}_{\omega jk}}\times\overline{\vec{B}_{\omega jk}}\right. \\ &\left. + \frac{\overline{\beta_{\omega kl}}}{\mu_0}(\mathrm{rot}\,\vec{\beta})_{\mathcal{T}_{\omega kl}}\times\overline{\vec{B}_{\omega kl}} - \overline{\beta_{\omega jk}}(\nabla p_\mathrm{e})_{\mathcal{T}_{\omega jk}} - \overline{\beta_{\omega kl}}(\nabla p_\mathrm{e})_{\mathcal{T}_{\omega kl}}\right]\left[\overline{\vec{x}_{\omega kl}} - \overline{\vec{x}_{\omega jk}}\right].\end{aligned} \tag{14}$$

$\mathrm{F}^B_{\mathrm{WENO}}(\vec{x}_{\omega k})$ denotes the convective flux of the magnetic field for which the variables have been linearly reconstructed on each dual cell by a weighted essentially non-oscillatory (WENO) scheme (Friedrich, 1998). The WENO scheme assures second-order accuracy of the spatial solution.

The flux $\mathrm{F}^B_{\mathrm{WENO}}(\vec{x}_{\omega k})$ at the Gauß point $\vec{x}_{\omega k}$ is computed with a flux vector splitting scheme. The magnetoacoustic speed is defined as

$$\mathrm{c} = \sqrt{\frac{\gamma(p_\mathrm{h}+p_\mathrm{e})}{\rho} + \frac{B^2}{\mu_0\rho}}. \tag{15}$$

One now defines a new reference speed

$$\mathrm{s} = \sqrt{\alpha c^2 + q^2\left(1 - 2\alpha + \alpha\frac{q^2}{c^2}\right)}, \tag{16}$$

with

$$q^2 = \min\left(c^2, \mathrm{q}_n^2\right). \tag{17}$$

α is chosen as

$$\alpha = \frac{2}{\gamma\phi} \tag{18}$$

with $\gamma = 5/3$ being the adiabatic coefficient. The velocity normal to the cell face of two neighbouring dual cells is

$$q_n = v_z n_z + v_r n_r. \tag{19}$$

The eigenvalues are defined as

$$\begin{aligned} \lambda_0 &= q_n, \\ \lambda_1 &= \lambda_0 + s, \\ \lambda_2 &= \lambda_0 - s. \end{aligned} \tag{20}$$

With the physical states left (l) and right (r) of a cell face the following equations are chosen for the splitting:

$$h_{1l} = \frac{1}{4}(\lambda_{1l} + |\lambda_{1l}|), \tag{21}$$

$$h_{1r} = \frac{1}{4}(\lambda_{1r} - |\lambda_{1r}|), \tag{22}$$

$$h_{2l} = \frac{1}{4}(\lambda_{2l} + |\lambda_{2l}|), \tag{23}$$

$$h_{2r} = \frac{1}{4}(\lambda_{2r} - |\lambda_{2r}|). \tag{24}$$

The upwind flux function for the magnetic field is

$$F^B = B_l(h_{1l} + h_{2l}) + B_r(h_{1r} + h_{2r}). \tag{25}$$

In the source term in equation (10) an averaged radius is used to preserve symmetry in the discrete case. Overlined values represent average values on a dual triangle.

The remaining parts of equation (10) are discretized in a central manner. The distances

$$\left[\overline{\vec{x}_{\omega kl}} - \overline{\vec{x}_{\omega jk}}\right]$$

represent the border of the toroidal cross section ΔA_ω of a dual cell ω. The average values $\overline{\vec{x}_{\omega kl}}$ and $\overline{\vec{x}_{\omega jk}}$ are calculated on the primary triangles and represent the corners of a dual cell ω.

The current density $\vec{j}$ is calculated by

$$(\mathrm{rot}\,\vec{B})_{\mathcal{T}_{\omega jk}} = \mu_0 \begin{bmatrix} j_z \\ [0.5ex] \\ j_r \end{bmatrix}_{\mathcal{T}_{\omega jk}} = \mu_0 \begin{bmatrix} \dfrac{1}{\overline{\overline{r_{m,\omega jk}}}} \left(\dfrac{\partial \Psi}{\partial r}\right)_{\mathcal{T}_{\omega jk}} \\ [0.5ex] \\ -\dfrac{1}{\overline{\overline{r_{m,\omega jk}}}} \left(\dfrac{\partial \Psi}{\partial z}\right)_{\mathcal{T}_{\omega jk}} \end{bmatrix}. \tag{26}$$

Since a steady-state solution is required, an explicit first-order time stepping scheme is employed for time-stabilization. The calculation of the explicit local time step for equation (10) considers the magnetic diffusion which is in some sense comparable with a classical heat conduction problem. All K neighbouring cells are included:

$$\Delta t_B = \mathrm{CFL}_B \frac{\mu_0}{2} \frac{1}{K+1} \sum_{\substack{k=1 \\ k=\omega}}^{K} \sigma_k \left(\frac{1}{K} \sum_{k=1}^{K} |\vec{x}_{m,k} - \vec{x}_{m,\omega}| \right)^2. \tag{27}$$

The CFL_B number dampens the other mechanisms in Ohm's law, which are not considered in equation (27).

Before the actual time stepping is performed, all local time steps are multiplied with different random numbers RND between 0 and 1:

$$\Delta t_{B,\mathrm{RND}} = \Delta t_B \mathrm{RND}_B. \tag{28}$$

The time integration for the stream function Ψ

$$\Psi^{n+1} - \Psi^n = \Delta t_{B,\mathrm{RND}} \left[\left(1 - \frac{1}{K}\right) \mathrm{RHS}_{\omega}^{B} r_{m,\omega} + \frac{1}{K} \frac{\sum_{k=1}^{K} \mathrm{RHS}_{k}^{B} r_{m,k}}{K} \right]. \tag{29}$$

includes local residual smoothing.

The requirement of robustness is the reason for the choice of first-order time-stepping. Higher-order schemes like Runge-Kutta schemes generally accelerate convergence as long as the right hand sides are relatively simple. In the case of the complex non-linear right hand side presented here, they tend to produce numerical oscillations.

The random time stepping also adds stability. It allows an increase of the CFL_B number by about an order of magnitude. Although its mathematical properties are not yet understood, it is clear that it introduces a non-linear, dampening dissipation which disappears once the steady-state solution is

achieved. It should be mentioned here that the results obtained with and without random time steps are similar.

Results

A typical discretization of the computational domain is shown in Figure 5. In the nozzle area, the mesh is highly refined for a good resolution of the boundary layers and for capturing the oblique shock (Figures 6 and 7) which is visible during the experiment when the HAT is being fired in one of the test chambers in the IRS laboratory (Figure 3).

While the shock is clearly visible in the heavy particle temperature T_h, it cannot be seen in the current distribution (Figure 8). Obviously, the convective

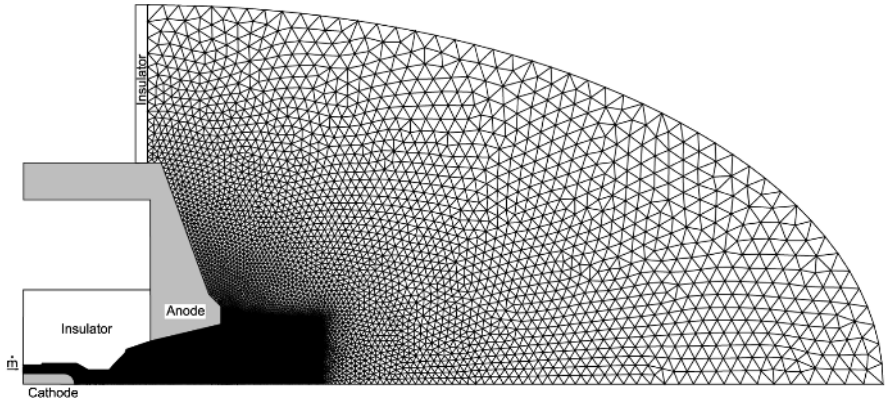

Figure 5.
HAT, entire adapted mesh with 28,034 cells, 2,000 A, 0.8 g/s argon

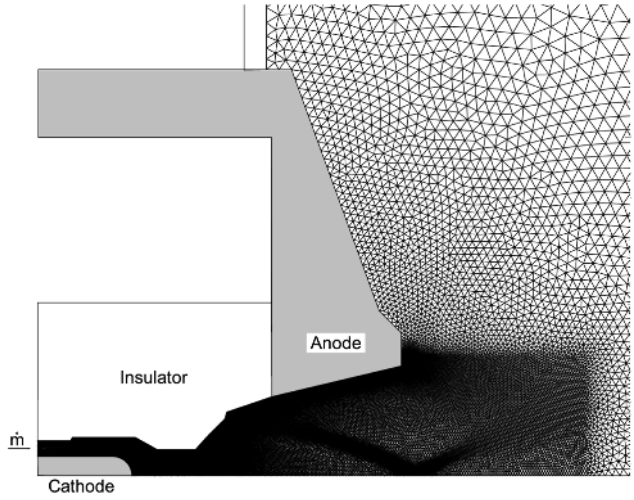

Figure 6.
HAT, adapted mesh with highly resolved boundary layers and oblique shock, 2,000 A, 0.8 g/s argon

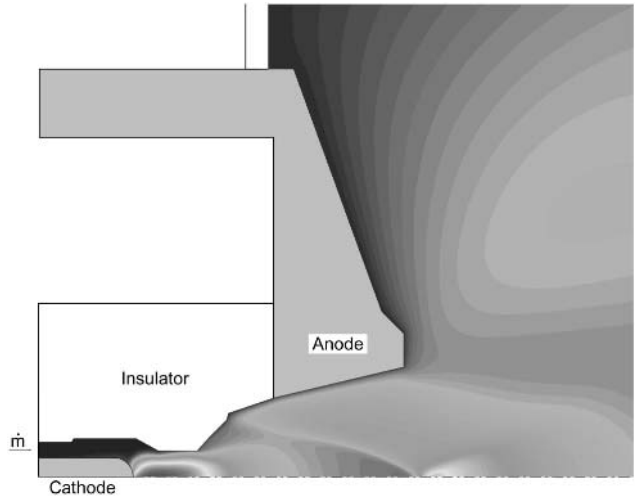

Figure 7.
HAT, heavy particle temperature, 2,000 A, 0.8 g/s argon

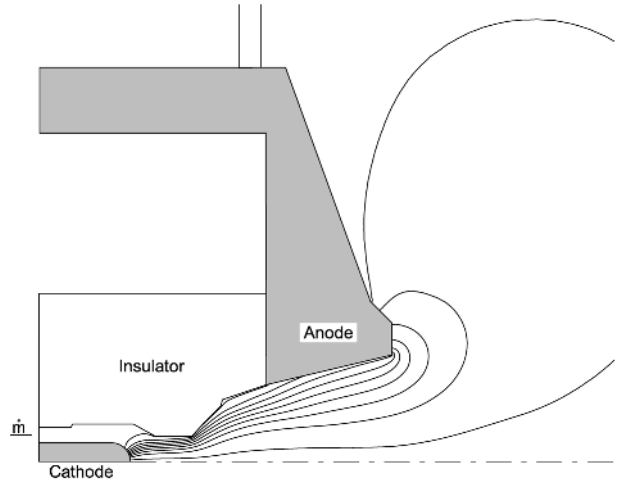

Figure 8.
HAT, stream function Ψ (250 A between two isolines), 2,000 A, 0.8 g/s argon

term in equation (10) is dominated by the other terms and the physical mechanisms they represent.

The evolution of the current distribution with increasing thruster current (Figures 8-11) shows that, beginning at about 4,000 A, the electric arc starts to constrict downstream of the nozzle throat because of the pinch effect.

Also, the arc attachment on the anode surface varies strongly with changing thruster current. The detailed analysis of the plasma/electrode interaction (Goodfellow, 1996; Hügel, 1980) is part of the current work at the IRS. The distribution of Ψ is mostly smooth, and slight oscillations only appear for

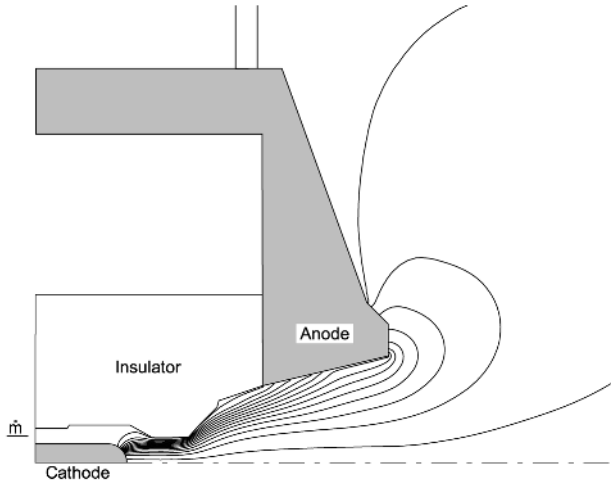

Figure 9.
HAT, stream function Ψ (250 A between two isolines), 3,000 A, 0.8 g/s argon

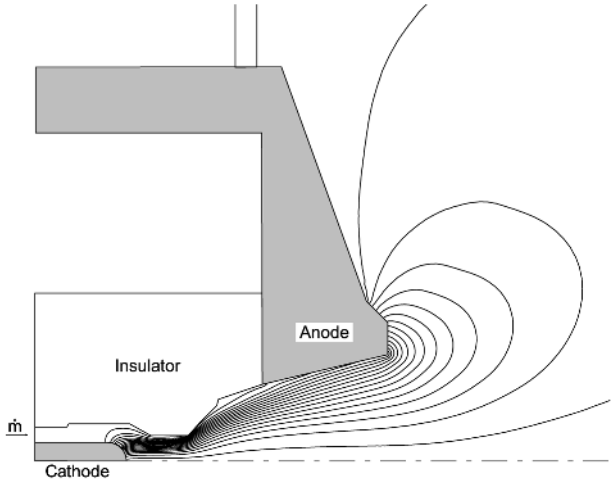

Figure 10.
HAT, stream function Ψ (250 A between two isolines), 4,000 A, 0.8 g/s argon

5,000 A where the pinch effect reduces the particle density downstream of the nozzle throat drastically.

The discretization is very robust and efficient. The results for Ψ deliver source terms in the conservation equations which are not discussed here. For example, the Lorentz force acceleration of the heavy particles and the Ohmic heating of the electron gas require smooth solutions of Ψ which is guaranteed by the discretization presented here.

The thrust can be calculated in the anode cross section as

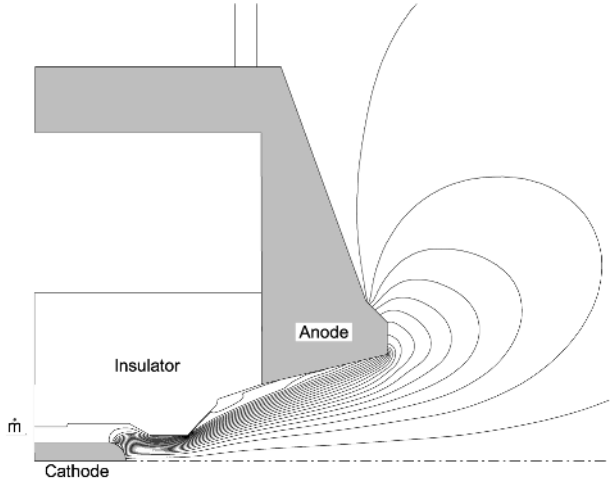

Figure 11.
HAT, stream function Ψ (250 A between two isolines), 5,000 A, 0.8 g/s argon

$$F = \sum_{\Delta A} \left(p_{\mathrm{h}} + p_{\mathrm{e}} + \frac{B^2}{2\mu_0} + \rho v_z^2 \right) \Delta A. \tag{30}$$

Results are given in Table I. The thruster is mounted on a thrust measurement stand in the test chamber to measure the thrust force. Since the thrust stand is being thermally heated in a non-uniform way during the thruster firings, the experimentally measured thrust data show some drifting. However, there is a good agreement between numerical and experimental data. A further evaluation of numerical and experimental results will be possible when electrode phenomena are included so that, for example, the voltage can be compared.

Conclusion

A new FV discretization for the conservation equation of the magnetic field in self-field MPD thrusters has been developed for unstructured adaptive meshes. Proper second-order upwinding and central discretization and explicit first-order stepping including randomization and residual smoothing deliver smooth steady-state solutions in a quick and robust way.

Table I.
Thrust data for the HAT (num.: numerical, exp.: experimental)

I(A)	$\dot{m}$ (g/s)	F(N) num.	F(N) exp.
2,000	0.8	4.3	3.7-4.7
3,000	0.8	5.9	5.7-7.0
4,000	0.8	8.5	7.8-9.4
5,000	0.8	10.1	11.1

Numerical and experimental data for the thrust agree well. In the next step, the plasma/electrode interaction will be investigated.

References

Auweter-Kurtz, M. (1992), *Lichtbogenantriebe für Weltraumaufgaben*, B.G. Teubner, Stuttgart.

Auweter-Kurtz, M., Boie, C., Habiger, H., Kaeppeler, H.J., Kurtz, H.L., Sleziona, P.C., Wegmann, T. and Winter, M.W. (1998), "Numerische Simulation von MPD–Triebwerken und Vergleich mit durchzuführenden experimentellen Untersuchungen", Universität Stuttgart, Stuttgart, Final Report of the DFG project Au85/5-2, Institut für Raumfahrtsysteme.

Bennett, G.L., Watkins, M.A., Byers, D.C. and Barnett, J.W. (1990), "Enhancing space transportation: the NASA program to develop electric propulsion", *IEPC-91-004, 21st AIAA/DGLR/JSASS International Electric Propulsion Conference*, Orlando, FL.

Boie, C. (1999), "Numerische Simulation magnetoplasmadynamischer Eigenfeldtriebwerke mit hochauflösenden adaptiven Verfahren", PhD thesis, Institut für Raumfahrtsysteme, Fakultät Luft- und Raumfahrttechnik, Universität Stuttgart, Stuttgart.

Cap, F. (1994), *Lehrbuch der Plasmaphysik und Magnetohydrodynamik*, Springer, Wien, NY.

Choueiri, E.Y. (1999), "Anomalous resistivity and heating in current-driven plasma thrusters", *Physics of Plasmas*, Vol. 6 No. 5, pp. 2290-306.

Devoto, R.S. (1973), "Transport coefficients of ionized argon", *The Physics of Fluids*, Vol. 16 No. 5, pp. 616-23.

Friedrich, O. (1998), "Weighted essentially non-oscillatory schemes for the interpolation of mean values on unstructured grids", *Journal of Computational Physics*, Vol. 144, pp. 194-212.

Fujita, K. (1996), "Performance computation of a low-power hydrogen arcjet", *AIAA-96-3183, 32nd Joint Propulsion Conference*, Lake Buena Vista, FL.

Goodfellow, K.D. (1996), "A theoretical and experimental investigation of cathode processes in electric thrusters", PhD thesis, Faculty of the Graduate School, University of Southern California, CA.

Heiermann, J. and Auweter-Kurtz, M. (2001), "Numerical simulation of high power steady state MPD thrusters", *IEPC-01-128, 27th International Electric Propulsion Conference*, Pasadena, CA.

Hügel, H. (1980), "Zur Funktionsweise der Anode im Eigenfeldbeschleuniger", Habilitation thesis, Fakultät Luft- und Raumfahrttechnik, Universität Stuttgart, DFVLR Research Report, 80-20 Stuttgart.

Iben, U., Warnecke, G., Heiermann, J. and Auweter-Kurtz, M. (2000), "Adaptive numerics for the simulation of magneto-plasmadynamic rocket thrusters", in Neittaanmäki, P., Tiihonen, T. and Tarvainen, P. (Eds), *Proceedings of The Third European Conference on Numerical Mathematics and Advanced Applications*, World Scientific, Singapore, Jyväskylä, Finland, pp. 121-30.

Jackson, J.D. (1962), *Classical Electrodynamics*, Wiley, New York, NY.

Jahn, R.G. (1968), *Physics of Electric Propulsion*, McGraw-Hill Series in Missile and Space Technology, USA.

Minakuchi, H. and Kuriki, K. (1984), "Magnetoplasmadynamic analysis of plasma acceleration", *AIAA-84-06, Proceedings of the 17th International Electric Propulsion Conference*, Tokyo, Japan.

Niewood, E.H. and Martinez-Sanchez, M. (1991), "A two-dimensional model of an MPD thruster", *AIAA 91-2344, 27th AIAA/SAE/ASME Joint Propulsion Conference*, Sacramento, CA.

Sankaran, K., Choueiri, E.Y. and Jardin, S.C. (2000), "Application of a new numerical solver to the simulation of MPD flows", *AIAA-2000-3537, 36th AIAA/ASME/SAE/ASEE Joint Propulsion Conference*, Huntsville, AL.

Sleziona, P.C. (1998), "Hochenthalpieströmungen für Raumfahrtanwendungen", Habilitation thesis, Fakultät Luft- und Raumfahrttechnik, Universität Stuttgart, Stuttgart.

Turchi, P.J., Mikellides, P.G., Hohman, K.W., Leiweke, R.J., Mikellides, I.G., Schmahl, C.S., Roderick, N.F. and Peterkin, R.E. Jr (1995), "Progress in modeling plasma thrusters and related plasma flows", *IEPC-95-159, Proceedings of the 24th International Electric Propulsion Conference*, Moscow, Russia.